2008

Growth and properties of metal-on-metal nanostructures: Ag on Cu(110) and Co on Ag(110)

Indrajith Chandima Senevirathne
Louisiana State University and Agricultural and Mechanical College

GROWTH AND PROPERTIES OF METAL-ON-METAL NANOSTRUCTURES: Ag ON Cu(110) AND Co ON Ag(110)

A Dissertation

Submitted to the Graduate Faculty of the
Louisiana State University and
Agricultural and Mechanical College
in partial fulfillment of the
requirements for the degree of
Doctor of Philosophy

in

The Department of Physics and Astronomy

by
Indrajith Senevirathne
B.Sc., University of Sri Jayewardenepura, 2000
August 2008

Dedication

To my father, Mr. Vajira Senevirathne, you taught me how to love and to be kind, not by words, but by example. You bought me my first book and you were patient and encouraging when I read it to you. You were there when I first counted to hundred sitting on your table, your eyes filled with pride and love, taking a moment off from writing your beloved books. You gave me constant, unconditional love and guidance all these years. I owe you more than I can ever say.

To my mother, Mrs. Anula Senevirathne, you taught me to value perseverance, you taught me to be a leader, and to trust myself. By example you showed me to appreciate and treasure the kindness we receive. You showed me a person can be soft and hard at the same time. I owe you more than I can ever say.

To the love of my life, my wife Reshani Senevirathne, you are my light in the darkness. Since high school you have been my best friend and confidant. You will always be my northern star. I owe you and love you more than I can ever say.

Acknowledgements

My tenure at LSU has been a wonderful and productive experience because of the many individuals I have known. Humans are social creatures, and this is how we learn and live.

First and foremost I thank Dr. Phillip Sprunger for being a wonderful advisor, mentor and friend. He was always positive, enthusiastic and passionate about the research enterprise. When things did not work out the way we planned in the lab, which is usually the case in research, I witnessed with admiration his dogged determination to complete the experiment. His extraordinary example was better than words.

I am thankful to Dr. Richard Kurtz for being a wonderful advisor, for his help and patience in so many ways when I had questions about interpretation and data analysis. From him I learned enormously by observing his attention to detail and his controlled and methodical approach to solving problems.

I am thankful to Dr. Roger Stockbauer, my previous advisor, who motivated me to choose Solid State Physics over Astrophysics. He is one of the most wonderful, caring and passionate human beings I have ever met, apart from being a great mentor and an advisor. I remember well his first comments he had for me when I came to the Surface Science Lab: "IC, everything is doable, but some things take a little more time!" That was seven years ago, and had he known then how true he was I wonder.

I am thankful to Dr. Ravi Rao for being a wonderful mentor and friend. From the first Quantum Mechanics course I took with him, he was always patient and available to discuss issues, and to answer questions, not only from me, but from all of the students at hand. I am thankful to Dr. Dana Brown for being patient with my never-ending enquires about assistantships and departmental policies. I am very thankful for being a great mentor, for being kind and

patient, and for his participation on my thesis committee. I am also thankful for the Dean's Representative, Dr. Dorel Moldovan, for being patient with me in the completion of the dissertation. I am thankful to Graduate Secretary Ms. Arnell Dangerfield for her patience and her kind help, not only for me, but also for all the graduate students in our department.

I am thankful to Ms. Virginia and Dr. Charles Grenier for their continuous love and support throughout our lives in Baton Rouge. I and my wife have been so very fortunate to have such wonderful and caring friends who made us feel Baton Rouge is our home away from home.

I am thankful to all my colleagues, brothers in arms and dear friends in our lab. Thanks to Frank Womack, with whom it is never boring to talk on any topic, leaving with something significant to take home. Thanks to Fei Wang, the quintessential loyal friend, always caring and ready to help. Thanks to Brendon Watson who was a helping hand on numerous occasions in the lab with a repertoire of hunting stories to tell. Thanks to Justin Runnel who has the biggest heart I have ever known, and who will always be a brother to me. Thanks to Matthew Patterson for being kind enough to proof read portions of the dissertation, even with his busy schedule. Thanks Weiwei Mou who made the sleepless nights less painful when we took EELS data all through the night. Thanks to Dr. Weichang Zao, who graduated from our group, for his patience in showing me the way when I had questions in experiments at the beginning of my career. Thanks to Dr. Asoka Sekharan, our postdoc, with whom I discussed everything from Angle Resolved Photo Emission to Asian politics. And finally, thanks to my dear friend, Dr. Orhan Kizilkaya from CAMD, for his passion for physics, for being a caring and true friend.

The United States is a unique country when one can meet so many people from very diverse cultures, nationalities and countries, I am thankful to all of whom I have met for enriching my life, particularly the people of Louisiana where I have lived the past years. In the end, I wish to thank my Father Mr. Vajira Chaminda Senevirathne, my first teacher, my dear

friend without whose guidance I could never have been the person I am today. I am thankful to you for introducing me to books for being there always, all the years, showing me how to be a kind and compassionate man. I wish to thank my mother Mrs. Anula Senevirathne for showing and encouraging me to work outside of books and to develop as an individual. Finally, I wish to thank my wife Reshani Senevirathne for being there all these years giving me so much selfless love, affection and joy. You make my world every second of the day.

- Indrajith Senevirathne

Table of Contents

Dedication ii

Acknowledgements iii

Acronyms Used viii

Abstract ix

1 Introduction 1
1.1 Overview 1
1.2 Systems to be Investigated 3
1.3 Organization 7

2 Experimental Principles and Instrumentation 8
2.1 Introduction 8
2.2 Low Energy Electron Microscopy (LEEM) 11
2.2.1 Principles 11
2.2.2 Device 24
2.3 Scanning Tunneling Microscopy (STM) 30
2.3.1 Principles 30
2.3.2 Aarhus (Scideco I/S) Scanning Tunneling Microscope 34
2.4 Auger Electron Spectroscopy (AES) 41
2.4.1 Principles 41
2.4.2 CMA (Cylindrical Mirror Analyzer) type AES 45
2.5 Electron Energy Loss Spectroscopy (EELS) 46
2.5.1 Principles 46
2.5.2 Dipolar Scattering 47
2.5.3 Impact Scattering 48
2.5.4 Instrumentation 49
2.5.5 Device 50

3 Dynamical Evolution of Ag Nanowires on Clean Cu(1 1 0) 53
3.1 Introduction 53
3.2 Experimental Procedure 59
3.3 Data and Observations 60
3.3.1 Preliminary Features 60
3.3.2 Observations in the Initial Stage 64
3.3.3 Observations in the Intermediate Stage 69
3.3.4 Observations in the Final Stage 74
3.4 Analysis and Discussion 90
3.4.1 Initial Stage 90
3.4.2 Intermediate Stage 95
3.4.3 Final Stage 117

3.4.4 Summary 128

4 Study of Co Nanodots on Clean Single Crystal Ag (1 1 0) Surface 131
4.1 Introduction 131
4.2 Experimental Procedure 135
4.3 Data and Observations 136
4.3.1 Preliminary Features 136
4.3.2 LEED Investigation of Co on Ag(1 1 0) 137
4.3.3 Auger Electron Spectra for the Co on Ag(1 1 0) 141
4.3.4 STM Analysis of Co on Ag(1 1 0) 152
4.4 Analysis and Discussion 166
4.5 Summary 173

5 Anisotropic Plasmon Dispersion of Ag Nanowires on Cu(1 1 0) 175
5.1 Introduction 175
5.2 Experimental Procedure 177
5.3 Data and Observations 179
5.3.1 Preliminary Features 179
5.3.2 Observations 180
5.4 Analysis and Discussion 183
5.5 Summary 195

6 Summary 196

Bibliography 200

Appendix 1 Measured Nanowire End Coordinates 209

Appendix 2 Nanowire - End Evolution Code in IGOR 216

Appendix 3 Time Variation of Gibbs Free Energy and Number of Critical Nuclei 221

Vita 222

Acronyms Used

AES	Auger Electron Spectroscopy
AFM	Atomic Force Microscopy
ARUPS	Angle Resolved Ultraviolet Photoemission Spectroscopy
CMA	Cylindrical Mirror analyzer
EDS	Energy-Dispersive X-ray Spectroscopy
EELS	Electron Energy Loss Spectroscopy
ES	Ehrlich - Schwoebel
FM	Frank - van der Merve growth mode
FOV	Field of View
HREELS	High Resolution Electron Energy Loss Spectroscopy
LEED	Low Electron Energy Diffraction
LEEM	Low Electron Energy Microscopy
MBE	Molecular Beam Epitaxy
MEIS	Medium Energy Ion Scattering
SEM	Scanning Electron Microscopy
SEXAFS	Surface Extended X-Ray Absorption Fine Structure
SK	Stranski Krastanov growth mode
STM	Scanning Tunneling Microscopy
TEM	Transmission Electron Microscopy
UHV	Ultra High Vacuum
UPS	Ultraviolet Photoemission Spectroscopy
VW	Volmer Weber growth mode
XPS	X-Ray Photoemission Spectroscopy

Abstract

Heteroepitaxial nanostructures have a diverse array of applications and show novel phenomena that arise from the exotic physics exhibited in reduced dimensions. We have investigated two nano-structured systems in order to gain insights into the dynamics of their nucleation, growth and have observed striking differences, due in part to a competition between lattice strain, surface and interfacial free energies.

When Ag is deposited on clean, single-crystal Cu(110), it initially wets the surface with a (111) monolayer, and spontaneously nucleates nanowires as the coverage is increased. The nanowires nucleate at defects and step edges and grow aligned along the $[1\bar{1}0]$ direction. In the initial stages of growth, they extend from step edges onto the lower terrace but as their height increases they extend along on the upper terrace as well, growing ~10nm wide and ~2.5nm high. The growth rate for any particular nanowire is found to be nearly independent of its separation from nearby nanowires, indicating that surface diffusion is facile. At elevated temperature (T > ~700K) and in the absence of the Ag flux, the nanowires Ostwald ripen into larger nanobars with widths of 400-800nm where surface adatom diffusion results in the disappearance of smaller nanowires.

Collective excitation of the electron gas within these nanowires reflects their distinct quasi-1D structural anisotropy. The dispersion of Ag plasmons has been obtained and along the nanowire axis we find that the plasmon dispersion is linear with momentum transfer and remains constant beyond 0.3Å^{-1}. No dispersion is found for the plasmon perpendicular to the nanowire axis, reminiscent of the localized Mie resonance found in clusters. In distinct contrast to Ag grown on Cu(110), where the surface free energy of Ag is smaller than that of the substrate, the

structures formed when Co is grown on Ag(110) arise due to the larger surface free energy of the adsorbate. Co prefers to cluster, and grows in the form of nanodots ~0.6nm high and ~2.5nm wide, embedded in Ag to minimize its energy. Upon annealing the Co nanodots sinter and agglomerate and into super-clusters while a portion migrates into the Ag bulk.

1 Introduction

1.1 Overview

If "semiconductor technology" was the buzzword of the last three decades of materials research, "nanotechnology" has become the new buzzword and will remain so for the foreseeable future. Merton C. Flemings' (Bensaude-Vincent and Hessenbruch 2004) description of the tetrahedron of interaction between *structure, properties, performances, and process* in materials research is as important as it has ever been, whether exploring the promise of nanomaterials for sheer curiosity, or applying them to solve problems for the benefit of humanity.

Materials containing the same elemental composition behave dramatically differently on the nanoscale compared with their properties in the bulk. Ag and Au, which have been known to humanity for millennia, are inert metals in their bulk form but become efficient catalysts and bioactive agents (anti-microbial activity and interfacing with DNA with Ag_{55} particles), respectively, when they are in the form of nanoparticles. As opposed to diamond and graphite, graphene and carbon nanotubes show a plethora of completely different and exotic behaviors including size, dependent conductance, Dirac Fermions (Nature Nanotechnology Editorial 2007), a Quantum Hall effect at room temperature, and Single Electron Transistor (SET) and Superconducting Transistor (Brink 2007) behaviors. Interest in nanomaterials has soared due to the rich and complex properties that arise due to quantum size effects (QSE), giving new functionality and fascinating physics.

From the application and characterization standpoints, it is important to develop new ways to create these nanoparticles, since different techniques can produce variations in nanoparticle characteristics. *Bottom up design* and *top down design* are the two methods being

used in both industry and research. Each has its own merits, but in the case of bottom up design of nanomaterials, understanding the dynamics involved in material growth is paramount. Particularly in the case of self-assembly (which falls into the domain of *bottom up design*), thermodynamics and kinetics of the system will govern reaction rates and the ultimate outcome. What are reaction rates? What mechanisms and pathways are taken during the process? What physical parameters govern the rate of change? Has the system reached equilibrium, is it in a kinetically limited local equilibrium, or is it unstable to forming other states? These are extremely important questions to ask, and to obtain answers to, for a self assembling system.

One of the most fundamental properties of a nano-material is its structure and morphology. Reduced dimensionality modifies the electronic and atomic structure, giving rise to exotic properties. Therefore elucidation of the atomic and electronic structure, and how it varies with elemental composition and morphology, is of utmost importance. In a nanoscale system these properties will determine the thermodynamic stability of the material. Variations in chemical composition can also provide a driving force to form new structures. Can there be alloying? In bond formation one may be concerned about the electro - negativities and free energies of the species involved. In terms of surface structures, one may be interested in the competition between surface, interface, and bulk free energies. Do the materials form thin films? Does the competition give rise to cluster or nanowire formation? Answering these questions will allow us to understand how structure, morphology and overall material stability are interrelated.

Understanding the new functionality of how new physical properties can be controlled and developed for applications is also extremely important. As stated earlier, reduced dimensionality gives rise to peculiar properties in nano structured systems and in many instances these properties are not expected by extrapolating a simple reduction in size. Thermal and electrical conductivity, optical reflectance, elasticity and mechanical strength to mention a few

are properties that may exhibit surprising changes as dimensions approach nanometers. It is also important to measure these material properties under varying eternal perturbations like temperature, since this can drive transitions into new states. This can provide hints to the state of the system at a particular time and will broaden extensibility, scalability and applicability of the system of nanostructures. As stated before, these properties give hints to electronic and physical states of systems, and also indirectly will provide hints to their thermodynamic stability.

1.2 Systems to be Investigated

Evaluating the issues discussed above will provide important insight in understanding the physics of reduced dimensional systems. The two systems studied in this thesis are reduced-dimensional metals in the form of nanowires, and nanoclusters grown on a single-crystal substrate. They consist of elementally well known metals: Ag, Cu and Co, and will act as model systems for improving our understanding of the physics of hetero-epitaxial metal-on-metal systems in reduced dimensions.

Our investigation starts with a study of the kinetics of formation of the different structures that Ag forms when deposited on clean single crystal Cu(1 1 0) at ~373K using Molecular Beam Epitaxy (MBE). The morphology of the phases that form have been previously studied in our group (Zhao 2005) (Kizilkaya 2003). Here we extend those studies to investigate the kinetic and thermodynamic aspects with some extended structural information as well. We have used Dr. Gary Kellogg's state of the art LEEM (Low Energy Electron Microscope) facility based in Sandia National Laboratory in Albuquerque, NM, to study the real-time in situ formation of the wetting Ag(1 1 1) layer and subsequent self assembly of anisotropic Ag nanowires oriented along the ΓX direction on Cu(1 1 0). Upon annealing, the system Ostwald ripens into a stable state where the Ag forms micro-clusters. The process of self assembly is

found to be of the (SK) Stranski - Krastanov type where the growth of the Ag wetting layer is followed by Ag islanding in the form of nanowires. In the simplest form this can be explained by Bauer's capillary theory of nanostructure formation (Bauer, Interactions on Metal Surfaces 1975). According to the capillary theory, growth progresses along the path that it does, first because the Ag surface free energy is lower than that of Cu, and second because the lattice mismatch of 11% induces a large strain into the system. The LEEM measurements focus on the point where the Ag(1 1 1) wetting layer becomes saturated at which point nanowires spontaneously nucleate. We then follow the dynamics involved in Ag nanowire formation. These studies conclusively prove that the wires nucleate on defect sites such as step edges and impurity centers. Wires initially nucleate at the bottom edge of a step but as they become larger they eventually grow across steps, and seem to be unimpeded by step presence. The initial rate of the nucleation of nanowires is high but drops of exponentially as the existing nanowires lengthen. The growth rate is independent of nanowire length and also independent of the edge to edge separation of the nanowires, indicating ample diffusion of Ag on Ag(1 1 1)/Cu(1 1 0). For individual nanowires, the growth rate also slows down gradually. One important observation that we make is that of an oscillatory growth rate with respect to nanowire length, which is reminiscent of oscillatory systems in far from equilibrium conditions. This is an indication that the state of the system is far from equilibrium even though the Ag flux is continuous. To the best of author's knowledge, this is the first time self-assembling nano structured systems has been observed to exhibit this phenomenon.

When the Ag flux is stopped and the nanowires are annealed at ~ 600K, Ostwald ripening sets in and cluster size measurements indicate that there is an attachment/detachment process that transforms the nanowires into micro clusters of Ag. These clusters are preferentially oriented in the ΓX direction but the aspect ratios are considerably lower than those of the nanowires and the

strain confinement effects are also reduced and the clusters increase in width considerably. This new state of Ag is a more thermodynamically stable than the Ag nanowire state, and forms the final state of the system in the annealing range that we have studied. Cluster statistics indicate widths have two different sets of values hinting at possible quantum size effects.

In a second study we have evaluated the structure and morphology of Co deposited via MBE on clean Ag(1 1 0) at ~273K (RT). In the bulk, Co is ferromagnetic metal with very high Curie temperature (~1388K) as opposed to Ag, which is non-magnetic. When combined in thin films they exhibit Giant Magneto-Resistance (GMR) (Binasch, et al. 1986) (Pratt Jr., et al. 1991) which makes the system appealing for its technological importance. It is notable that granular GMR (one of three types of GMR) has been only shown in Co clusters embedded in Cu (Berkowitz, et al. 1992), also nonmagnetic. If Co can be embedded in the Ag substrate it may also show granular GMR.

We have found that Co deposited at RT self assembles in to clusters/nanodots of 3Å to 6Å in height and ~25Å in width. These clusters show increased uniformity at higher coverage, likely due to lower diffusion lengths. The self assembly of these Co nanodots can be categorized as a Vollmer – Weber growth system, as islanding and cluster formation starts abruptly without a wetting layer. This is due to the fact Ag and Co have very different surface free energies [$\sigma_{Ag\ (1\ 1\ 0)}$ = 1.238Jm^{-2} (Vitos, et al. 1998) (Mezey and Giber 1982) and $\sigma_{Co\ (0001)}$ = 2.775 Jm^{-2}. High surface free energy of Co relative to Ag, annealing the system results in super clustering and agglomeration. Accumulation/agglomeration of clusters is rare in surface nanostructure literature as opposed to agglomeration of atoms to make even bigger clusters. At the same time annealing will drive a portion of Co in to the Ag matrix. When one species is driven to a matrix of another species by annealing and they have different lattice constants (there is 13% lattice mismatch in

the case of Ag and Co) this will introduce strain into the system. Yet in this system, free energy minimization dominates over the increased strain. We have evaluated the structure, morphology, and subsurface migration of these Co nanodots on Ag(1 1 0) using STM, Auger and LEED.

Finally, in the third topic, we study the plasmon dispersion relations of Ag nanowires on Cu(1 1 0). Plasmons are normal modes of the collective oscillations of the conduction band electron gas. Depending on the geometry of the material, they can be categorized into different states. In the bulk, conduction band electrons give bulk plasmons, while at the surface, they are surface plasmons (Raether 1988) and colloids with spherical geometries give rise to Mie plasmons (Mie 1908). With the intense interest in nanoparticles, plasmon resonances occur which are identified as nanoparticle plasmons (NPP) (Sonnichsen, et al. 2002). The field of plasmonics at the nanoscale has exploded due to the promise of nanophotonics. Nanowire waveguides, biosensors, high-resolution microscopy and ultra high density data storage are, to name a few, promising applications that have already been shown in the laboratory setting, giving rise to new concepts for devices that might revolutionize the world as we know it (Shalaev and Kawata 2007). Understanding the fundamental properties of nanoparticle plasmons lie at the heart of all these discoveries. There are numerous studies about plasmons in nanowires and nanoparticles but majority of them are about surface plasmon polaritons (SPP) where the excitation of the modes are achieved by means of photons. Further, almost all of them are lithographically patterned (*top down approach*) nanowires with considerably higher dimensions than the materials that we have produced (~8 times in width and ~30 times in height) (Schider, et al. 2003) (Ditlbacher, et al. 2005). Our approach is unique and distinct since it is the first time that a self-assembled metal on metal nanowire system was studied for plasmon dispersion.

We have identified a plasmon resonance that is unique compared to these other systems (bulk, surface and Mie). For Ag nanowires on Cu(1 1 0), the dispersion relation have been found

to exhibit clear anisotropy along and across the nanowire: there is a linear plasmon dispersion along the nanowire axis ([$1\bar{1}0$] direction) but no dispersion across the nanowire ([0 0 1] direction). Interestingly, none of the other systems (bulk, surface and Mie) show this kind of dispersion. With increasing coverage, we see no change in the dispersion relation indicating the property is representative of a single wire. Our dispersion relation is linear in energy vs. momentum transfer, and abruptly flattens out soon after. This indicates the existence of plasmon modes, essentially oscillations of the electron gas, along the wire but no modes across the wire. This nanowire system has been shown to have anisotropic band dispersion making it conductive along and insulating across (Zhao 2005). In these studies, we have used HREELS (High resolution Electron Energy Loss Spectroscopy) combined with Auger Spectroscopy and LEED (Low Energy Electron Diffraction) to study these various properties.

1.3 Organization

This thesis is organized with an introduction to the instrumentation, methodology, and theoretical principles in Chapter 2 *Experimental Principles and Instrumentation*, followed by the Chapter 3 *Dynamical Evolution of Ag nanowires on Clean Cu(1 1 0)* which describes the kinetic and thermodynamics of the Ag nanowire phase on Cu(1 1 0). These experiments were Surface Imaging Laboratory, Sandia National Laboratory in New Mexico. Then we investigate Co self assembly into nanodots and their evolution in Chapter 4 *Study of Co Nanodots on Clean Ag (1 1 0).* Finally we discuss the plasmon dispersion of Ag nanowires in Chapter 5 *Anisotropic Plasmon dispersion of Ag nanowires on Cu(1 1 0).*Experiments on both these sections were carried out in the Surface Science Lab in the Department of Physics and Astronomy at Louisiana State University.

2 Experimental Principles and Instrumentation

2.1 Introduction

In this chapter the theoretical basis, experimental equipment, and methodology will be explained. Experiments were conducted with the clean and metal evaporated Ag(1 1 0) and Cu(1 1 0) surfaces. One Ag and one Cu crystal used were from Monocrystals Company, Ohio, and two Cu crystals, which were used for LEEM, were from Dr. Gary Kellog. Ag and Cu crystals were of the purity 99.999^{+}%, orientation <1 1 0>, thickness 3-5mm, length across 5-9mm. Geometrically, Ag and three of Cu crystals used were circular, and a single Cu crystal was rectangular. Crystals used were single crystals with one side electro polished. Co for evaporation on the substrate was from a Co wire from *Alfa Aesar*, diameter 1.5mm, purity 99.995%, and Ag for evaporation was from a wire from *Goodfellow*, diameter 0.5mm, purity 99.99%. The crystals were mounted polished side up on a 1.6cm x 2.2cm x 1mm tantalum sample holder.

A Ag(1 1 0) crystal mounted on the sample holder is shown in Figure 2.1. The polished side of the crystal is facing up as seen in the left image of Figure 2.1. Thermocouple connectors are attached to the bottom of the holder through a MACOR block as seen in the right image of the Figure 2.1.

Thermocouple connectors are K type – Chromel (Nickel-Chromium Alloy) / Alumel (Nickel-Aluminum) (Veneklasen 1992), with a sensitivity of ~41 μV/°C (NIST, National Institute of Standards and Technology (NIST) NIST ITS-90 Thermocouple Database 2007). Experiments in Chapter 4 and 5 were carried out in the UHV (Ultra High Vacuum) chamber (Figure 2.2) in the Surface Science Lab, where the base pressure is ~$1x10^{-10}$Torr. UHV conditions are required to keep the surface clean for the duration of the experiment. By the Langmuir definition, 1 monolayer of molecular coverage on the surface is attained at a given

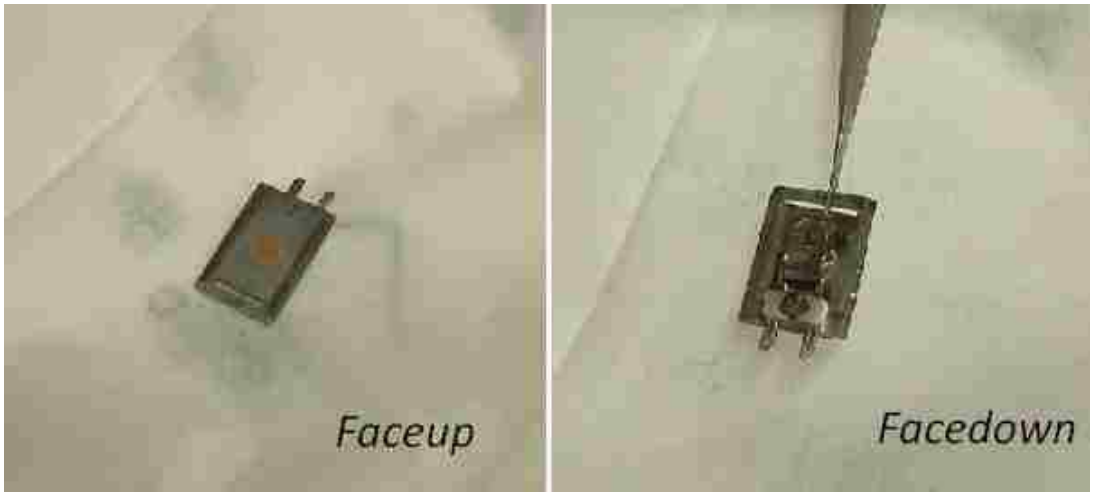

Figure 2.2 Ag(1 1 0) sample mounted on the sample holder.

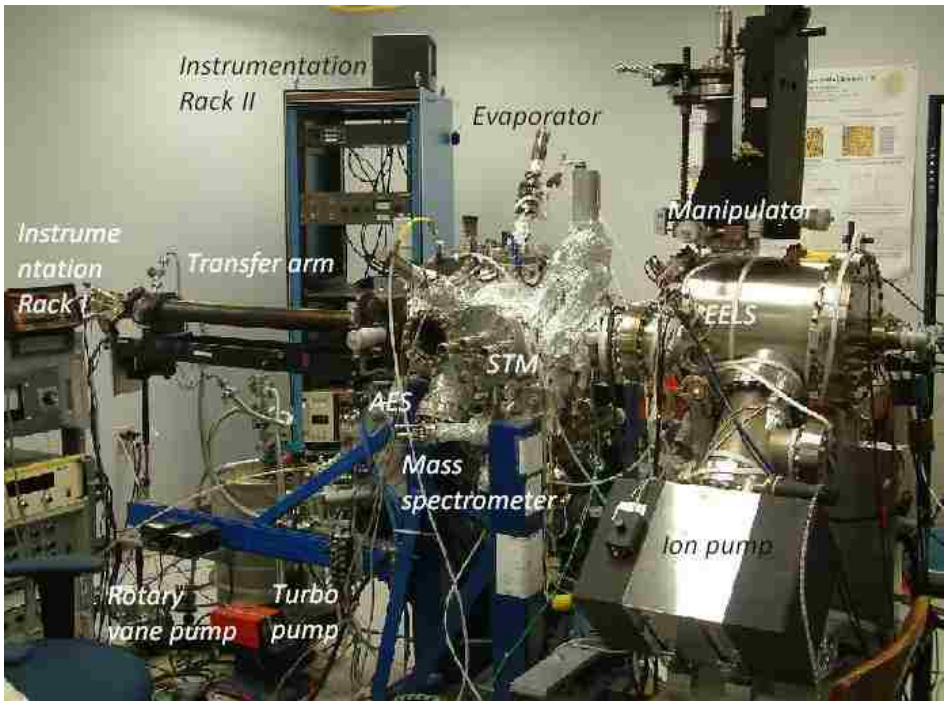

Figure 2.1 Experiments carried out in this UHV chamber in Surface Science Laboratory at the Department of Physics and Astronomy, LSU

molecular gas pressure of $1x10^{-6}$Torr within 1 second, assuming a sticking coefficient of unity (all molecules that collide with the surface will stick to the surface). This is the upper limit of surface contamination. Therefore, by reducing the pressure to ~$1x10^{-10}$Torr, it is possible to increase the time allocated for an experiment to ~3hours (~10^4s). Because typical sticking coefficients of clean metal surfaces are lower than 1, it is possible to have a finite but useful amount of time to perform an experiment.

UHV conditions are maintained by the constant pumping of two ion pumps (Varian – Star Cell, *VacIon* plus 300) and a turbo molecular pump (*Leybold* - TurboVac 151) backed by another turbo molecular pump (*Leybold* - TurboVac 50) backed by a rotary vane pump (*Leybold* – Trivac D 8 B). The chamber is also equipped with a Titanium Sublimation Pump (TSP) attached to a liquid N_2 reservoir, which increases the pumping speed via increased sticking coefficient attained by liquid N_2 cooled surface of the trap. The crystal samples were cleaned in the chamber under vacuum by cycles of sputtering and annealing. Sputtering was carried out by ultra clean Ne+ (by Airgas) beam of 0.5– 1.5KeV (Ion Gun and Controller – *PerkinElmer*). To get a cleaner stream of Ne, the gas was passed through a liquid N_2 filled flask prior to entering the chamber. Sputter current of ~15μA on the sample at a Ne pressure of at $5x10^{-5}$Torr was maintained while sputtering. Typical sputter runs lasted 30 minutes with time range varied according to the substrate surface. Sample transfer to preparation positions and STM position was carried out via a transfer arm going through the center of the chamber (Z axis) with rotational freedom about the Z axis. At the same time it was capable of limited mobility on X and Y axes, perpendicular to the Z axis. Altogether, the sample holder had 4 degrees of freedom: X, Y, Z and φ. This required a differential pumping stage at the connection edge. The sample holder consists of a filament with possibility to apply high voltage toe beam anneal. Annealing at

873K for Cu(1 1 0) and at 823K for Ag(1 1 0) was typically carried out for ten minutes. Typical cleaning consisted of 2 cycles, where one cycle is a sputter followed by an annealing. The chamber has directly attached SPECS er-LEED and AES. To establish surface cleanliness and integrity, LEED and AES analysis were performed on the sample, demonstrating less than 1% surface contamination. The UHV Chamber in the surface science lab is shown in Figure 2.2.

2.2 Low Energy Electron Microscopy (LEEM)

2.2.1 Principles

LEEM is a relatively new technique in electron microscopy with an achievable lateral resolution of ~5nm. What sets it apart from other microscopes is its ability to obtain video images in large fields of view of surfaces and interfaces in real time and in situ. These video data contain vast amounts of information, making it possible to do quantitative analysis on the system. The high rate of data acquisition and relatively low resolution (compared to the angstrom resolution of the STM) makes it a complementary tool to use concurrently with an STM, but gives unparalleled information with respect to the dynamics of a system. Systems studied by the LEEM are thin film, nano& microstructure growth, and strain relief on surfaces, but the strength of the device lies in its ability to provide dynamical information. The evolution of LEEM is parallel to that of the history of electron spectroscopy. Contributing technologies came from such diverse backgrounds as CRT technology and biology. Immersing the sample/surface in order to achieve rapid deceleration of the primary e-beam was used in thermionic and photoemission microscopic technologies, and incoming and outgoing e-beam split via a magnetic prism was used in mirror microscopy. Objective lens apertures were used in TEM and earlier mirror microscopes (Scheibner, Germer and Hartmann 1960). Although several equipments attempted and somewhat succeeded in using a display type LEED for real time

analysis of surfaces (Ehrenberg 1934) (Lander, Morrison and Unterwald 1962) (Bauer 1962), the invention of LEEM is credited to Ernest Bauer (Telieps and Bauer 1985). Due to the improvements needed in the development of low energy electron optics, the versatility of the LEEM greatly improved after 1985, where it was successfully demonstrated for the first time by Bauer and Teliep.

LEEM depends on low energy electrons to probe surfaces. Low energy electrons are highly susceptible to residual fields of the environment, which in the final sense degrades the image resolution and operational robustness. The modern approach is to shield completely the electron pathways by electrostatic/magnetic lenses, similar to a TEM (Transmission Electron Microscope). The general path of the electrons in the LEEM is straight forward.

Electrons emerge from the gun at high beam energy (~10–20 keV) and travel through the gun–lens system, initially through the focusing and condensing lenses and then through a bending field that is generated by the prism array system. The beam then passes the objective lens and probes the surface. Back-scattered return flux again passes through the objective, back to the imaging lens system via the prism array system deflecting to the opposite direction of the gun–lens system. Finally, the image projects on the channel plate screen system/detector (Figure 2.3). This can be imaged by a CCD camera and recorded in real time. The sequence of lenses/apertures and placement of them vary depending on the different LEEMs. Higher energy spread of the electron gun is a significant factor in lowering the resolution. Chromatic aberration is directly connected to the δE of the primary beam. For a hot emitter, energy spread is generally higher (~0.75 eV); for a cold cathode, it is relatively smaller (~0.25 eV) (R. M. Tromp 2000). The gun lens system guides the beam while reducing the spread of electrons on the cross section. This helps to reduce the scatter of the primary beam, which leads to minimal spherical

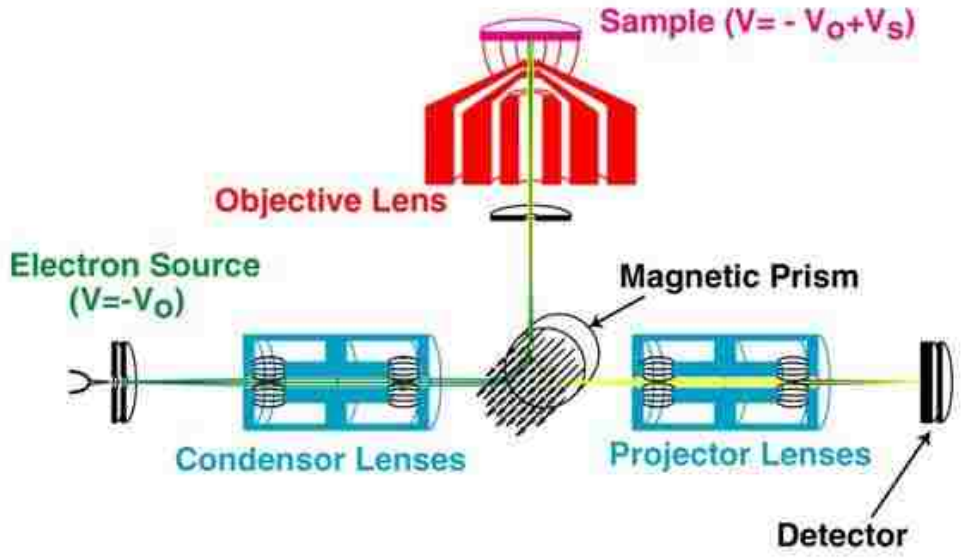

Figure 2.3 A typical LEEM schematics. (R. M. Tromp 2000)

aberrations in later stages. Electrons then move in to the beam separator, which is a lens/prism system that is unique to the LEEM. This helps in spatially separating the incoming primary beam from the outgoing secondary beam. An initial design was with a uniform magnetic field over circular region with prudently placed D cutouts (Archard and Mulvey 1958). This is a non-focusing field for the electron as it just deflects the beam. The application gave the behavior of an astigmatic lens, but this resulted in an unequal in plane and out of plane magnification. Eventual developments led to the introduction of magnetic prism arrays (Kolarik, Mankos and Veneklasen 1991), where in plane and out of plane focusing was obtained. Eventually, incorporation of the magnetic prism array into the microscope markedly improved the performance (Veneklasen 1991). Present day prism array systems are capable of deflecting and transferring both image and diffraction pattern with unit magnification and zero distortion (Tromp, Mankos, et al. 1998).

Electrons then pass the objective lens, followed by rapid deceleration coming to the sample surface. This is achieved by applying a static potential on the sample to keep the sample energy almost equal to the electron gun. Therefore the electrons interact and back scatter at energies ~0–100eV (low energies). At the initial pass, the objective lens behaves similar to a condenser, enabling the LEEM operator to manipulate the impinging angle and the location of the electron beam on the sample (Tromp and Reuter 1993). On the return path, electrons re-accelerate to gun energy by the field acting backward. The return electron flux again passes through the objective back to the imaging lens system via the prism array system, which deflects the beam to the opposite direction of the gun–lens system. The objective lens is an electrostatic immersion lens that is placed in the neighborhood of the sample holder. This gives rise to extreme fields up to ~5–10kV/mm, requiring severe design requirements on the sample holder and the stage. High fields could give rise to spherical and chromatic aberrations, and it is of

extreme importance to make the field as uniform as possible, as the performance ultimately depends on it. This is also of particular importance in cases like real time MBE (molecular beam epitaxy) and annealing, where there is a possibility of local and surface pressure increments giving rise to breakdown arcing. The author got firsthand experience of this as the lens edge and sample arced in several instances, requiring multiple cleaning cycles to restore the sample surface. Typically, high field strength results in high resolution, but at UHV, breakdown across objective lens and sample surface occurs at 10kV/mm, and it could happen for even lower fields when the pressure is high.

Finally, electrons traverse the imaging lens system after passing through the prism array system. Electrons eventually impinge on the detector/channel plate system. Plates are usually a CCD camera which will record the image. LEEM technique depends heavily on the *intensity* of the back scattered electrons. 180° scattering for particles requires head on collisions, which in the case of long wavelength electrons is not satisfied. Fast electron scattering {like in the case of TEM (Transmission Electron Microscope)} can be modeled by first Born approximation, yet this fails for slow electrons, and the use of better approximations such as partial wave analysis is obligatory. In this approximation, incoming and scattered waves are expanded in spherical harmonics centered at the atom. In the non-relativistic case, the scattering cross section is given by

$$f(\theta, k) = \frac{1}{2ik}\sum_{l=0}^{\infty}(2l+1)[\exp(2i\eta_l - 1)]P_l(\cos\theta), \quad -(2.1)$$

Where k is the wave vector, the calculated phase difference between the incoming and outgoing waves isη_l, and P_l are the Legendre polynomials (Bauer 1998). The intensity distribution is, therefore, $|\boldsymbol{f(\theta,k)}|^2$. Yet, from the relativistic and non-relativistic calculations already carried out (Fink, Martin and Somorjai n.d.) (NIST, NIST Electron Elastic Scattering

Cross Section Database - Standard Reference Data Base 64 1996), the accuracy falls rapidly with primary beam energy. Under 100eV, they become useless due to the fact the potentials of the free atoms extend further than the potentials of atoms in the solids, where the potentials are cut off at the nearest neighbor distances. Initial low back scattering intensities at low electron energies cast doubt on the applicability and feasibility of proposed low energy microscopy. When considering the self-consistent solid-state potentials, it was found that different elements have different back scattering intensities around zero energy (Bauer, Interactions on Metal Surfaces 1975), indicating that the process is considerably different from high energy forward scattering mediated via nuclear charge. Therefore, a case for a viable LEEM that takes into account the finite low energy back scattering was made. An important point is these calculations as later proven correct with high values of reflectivity of the Cu(1 0 0) and W(1 1 0) surfaces. It has been shown that the best fit of the theory is obtained for the exponential surface barriers with image potential tail (Andersson 1969) (Herlt, Feder, et al. 1981). Surface modification due to epitaxial growth, adsorbates, and temperature variations can readily change the reflected intensity, as seen in H dosed W(1 0 0), which has increased reflection due to the H monolayer (Herlt and Bauer 1986). A reflected intensity decrease has also been shown on surfaces coated with O (Herlt, Ph.D. Dissertation 1982). This is a further indication that low energy back scattering is independent of atomic cores. Although for crystalline specimens the reflection intensity is ample for the imaging purposes, amorphous specimens produce less reflected intensity with low energy electrons, as observed with Si(1 1 1) and amorphous Si (Dietzel, Meister and Bauer 1982).

Viability of LEEM depends also on the achievable *resolution*. In a typical electron microscope, the resolution is limited mainly by the aberration of the objective lens. This is extremely important in cathode objective lenses when the other lenses do not have design

imperfections and misalignments in LEEM setup. Consider chromatic aberration (δ_c), which depends on the initial angle α_o by the relation$\delta_c \propto \alpha_o$, and spherical aberration (δ_s), which depends on the initial angle α_o by the relation $\delta_s \propto \alpha_o^3$; these are results of the geometrical optics. But reduction of α_o by reducing the contrast aperture in order to minimize δ_c and δ_s will lead to resolution limitation due to diffraction aberration (δ_d) at the contrast aperture. The resolution peak is considering the minimization of the sum of squares of the respective aberration disks,

$$\delta^2 = \delta_c^2 + \delta_s^2 + \delta_d^2. \quad -(2.2)$$

The relationship is derived from geometrical optics arguments (Bauer 1994); and may not be compatible with wave optics. But wave optical calculations carried out later confirmed that the wave optics approach is not significantly different from the geometrical optics calculations (Shao and Crewe 1989) in the case of aberration disks. In the case of low energy electron microscopy, the cathode lens is crucial for the overall resolution of the device. Estimating the net resolution is simpler when the cathode lens is divided into a homogeneous field region and an ideal lens region, ignoring the electrode aperture separating them. Impinging beams pass the aperture (r_B), propagate into the ideal lens, pass through the electrode aperture (r_A), then in the homogeneous field, (**E**) where the specimen (cathode) is in the potential(-$\boldsymbol{U_o}$) (Figure 2.4) (Telieps 1987).

A virtual image is formed behind the specimen, which in turn acts as an object to the ideal lens. Analytical calculations of the aberrations are possible, resulting a limiting value for the resolution (Bauer 1985) (Figure 2.5). In the chromatic aberration dominating limit, a better approximation is (Bauer 1998):

$$\delta \cong 1.2(\Delta V\sqrt{F})^{1/2} V^{-1/4}. \quad -(2.3)$$

Here V is the energy,ΔV is the energy spread of the primary beam, F is the field strength

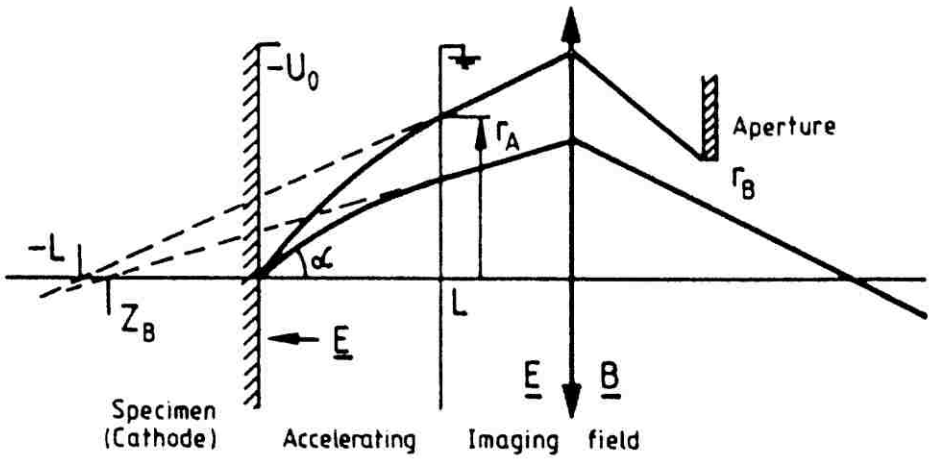

Figure 2.5 Schematics of the cathode lens optics, two regions are

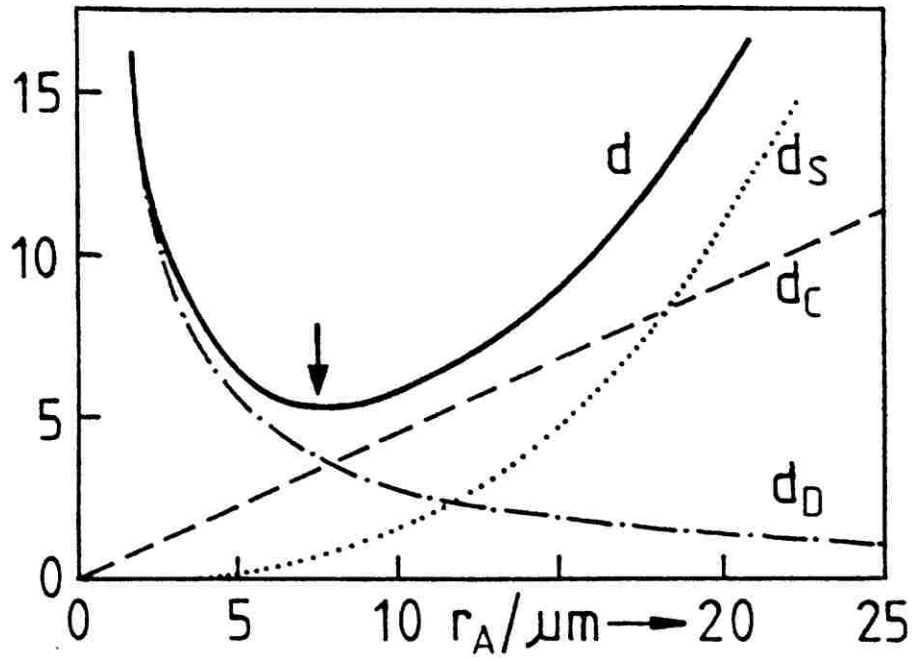

Figure 2.4 Variation of the net resolution (solid line) with various aberrations (dotted lines).

(units V/nm) at the sample, and δ is given in nanometers. A better approximation requires the layout of the lenses. Results of such a calculation are given in the Figure 2.6, where different cathode lens types with the same energy spread of 0.5eV are plotted with initial energy against the resolution (Chmelik, Veneklasen and Marks 1989). Further studies with variable energy spread (ΔE) curves of resolution versus initial energy shows clearly that lower spread gives higher resolution. Furthermore, the resolution limit (theoretical) for homogeneous field at the specimen currently stands at ~2nm. Yet the resolution achieved in experiments using LEEM is usually several times worse due to a multitude of reasons, which include but are not limited to high voltage instability, local charging, vibrations, specimen drift, etc.

When identifying surface features through LEEM, *contrast* is also a very important property. Typical contrast disparities are due to local variations of reflectivity *R(E)*that stem from differences of physical properties on the surface. One example is surface crystal symmetry variation that could occur locally, as in the case of W(1 1 0) versus W(1 0 0), where two orientations have clear differences in *R(E)* for different selective energies (Bauer 1994).

Surface reconstruction as in the case of Si (1 1 1) - (1×1) and Si (1 1 1) – (7×7) (Telieps and Bauer 1985) will also generate different contrast for diverse phases. Another example is the Si (0 0 1), (2×1) to (1×2) dimer reconstruction, where on the surface going across the step edges the reconstruction changes to/from (2×1) $\leftrightarrow$ (1×2). When observed through dark field (1/2, 0), the (2×1) terraces appear bright, while the (1×2) terraces appear dark (Tromp, Hamers and Demuth 1985). Finally, in the surface reconstruction of Pb (1 1 0), where c (2×4) $\leftrightarrow$ (1×1) (Altman, Chiang, et al. 1994) is also a phase transition which could occur in the clean Pb surface, the discrete surface reconstructions are clearly distinct in contrast.

Surface adsorbates will also generate different contrast in LEEM due to divergent *R(E)*.

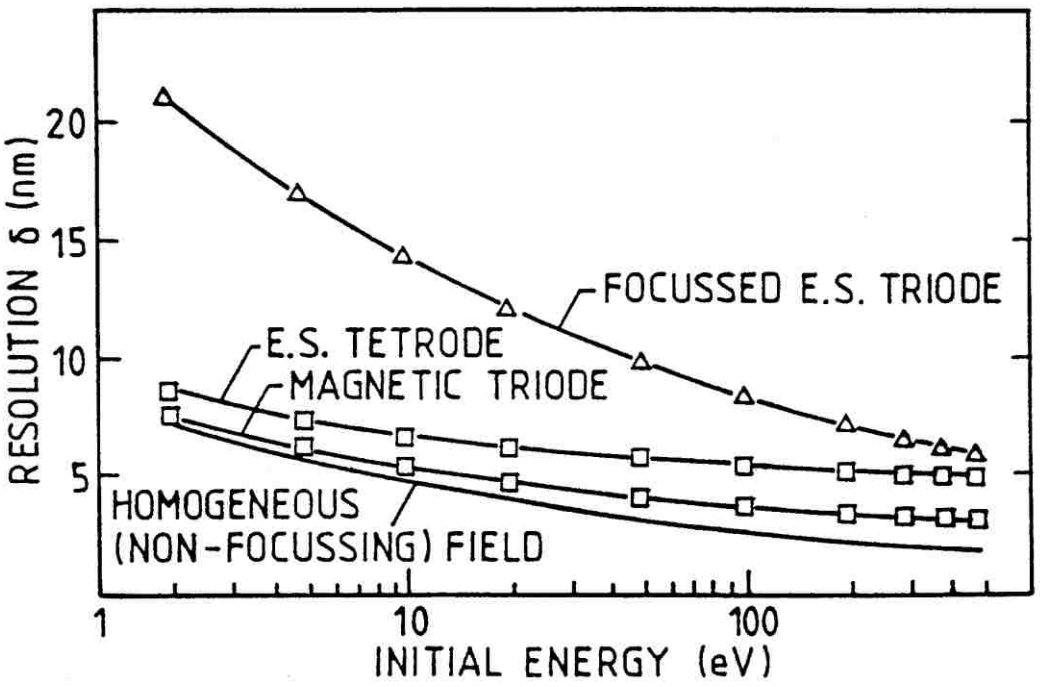

Figure 2.7 Resolution vs. Energy at 0.5eV energy spread for different cathodes, for optimum aperture.

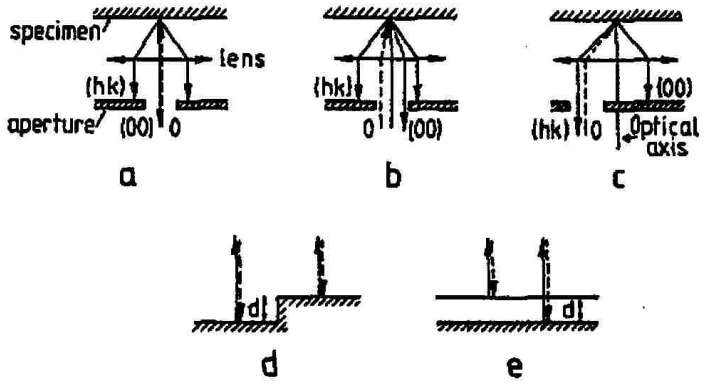

Figure 2.6 A Pictorial representation of different LEEM contrast mechanisms. Diffraction contrast: bright field contrast on a and b, dark field *c*. Interference contrast: geometric phase contrast *d* and quantum size contrast *e*.

In the case of Cu growth on Mo (1 1 0) surface, the variable Cu layers will generate the distinct contrast on the LEEM images that enable the understanding of the rich behavior of the layer growth in the system (Mundschau, et al. 1989). In certain cases, the contrast is attained by the surface compound or alloy formation, as in the case of Cu silicide forming on Si (1 1 1), where the two dimensional (5×5) silicide surface alloying layer and the three dimensional Cu_3Si crystals have divergent contrast, making them readily visible on the image.

In certain cases, as in the case of Si (1 0 0) dimer reconstruction, surface regions differ in the azimuthal orientation on the surface. Therefore, the normal incidence *R(E)* has no variation to differentiate, *i.e.* no bright field diffraction contrast can be observed. Minor slanting in the incident beam, making it better aligned with one domain with respect to the other, will change the contrast between the domains. This is achieved by judicious selection of a diffraction point other than the principal (0, 0) and taking the dark field image of the surface. In the case of R(E) variation zero for a respective surface, contrast can still vary due to the surface faceting and unevenness generating optical path difference (Telieps and Bauer 1985). Mono atomic steps cannot be avoided in the surfaces; they will give rise to the phase differences (Figure 2.7) resulting in constructive/destructive interference. Steps and step bunches have accompanying strain fields that might change the local diffraction conditions. The Si surface step contrast is weak compared to the metal surface step contrast.

The quantum size contrast is generated when the waves reflect from the front and back of the thin film/epitaxial layer. In a crude and simplified approach, this seems like a dielectric coating of antireflection or reflection enhanced light optics system. The *R(E)* will generate maxima and minima as a function of the wavelength (energy) and film thickness. A quantitative approach requires a deeper look into the crystalline periodicity. In order to have contrast variation, adequate reflectivity at the boundaries and a liberal mean free path are necessities.

Increased reflectivity on the substrate-film interface is a product of not having allowed states in the substrate that match to ***E (k)*** of the epitaxial layer or the densities of matching states are lower.

This has been shown true for several different systems (Bauer, Mundschau, et al. 1985). The inelastic mean free path of the electrons having lower energy below the plasmon level (Typically these are above 10eV, but Ag is in the range ~4eV) depends strongly on the band structure above the Fermi level. The probability of inelastic scattering increases with the density of states, because it is possible for an electron to scatter into an available excited state in the band structure. This is clearly seen by the decrease of the electron inelastic mean free path of the transition metals with partially filled *d* states, *i.e.* number of *d* holes (Siegmann 1994). The experimental path difference is twice the thickness of the film, hence the *R(E)* contrast variations decrease rapidly with the thickness of the epitaxial layer.

Typical mean free paths for low energy electrons for transition metals with filled d states are~2–3nm (Cu and Au). In certain cases, contrast variations can be seen for 3nm, as in the case of Co on W(1 1 0) (Altman, Chung and Liu 1998), although with increasing energy the contrast variations decrease as new channels of inelastic scattering are opened. Apart from the contrast variations that could arise from the surface layers, they could also come in to being by variations of height on the surface layer. Therefore the surface of the film has to be atomically flat over lengths of several times that of the lateral resolution.

Contrast is also important in topographical variations on the surface. The application of LEEM generally is used to determine the topographical structures on a surface, but depending on the shape and elevation of protrusions from the surface, the electric field on the surface may be distorted. The primary electron beam couples to this anomalous field and produces distorted and

erroneous images, which are far from identical to the surface structures. The contrast in these cases usually improves at the expense of increased energy of the primary beam, which then is less susceptible to field distortions.

The versatility of LEEM is improved by the ability to combine it with LEED (Low Energy Electron Diffraction). Elucidation of crystal structure, orientation and shape of a small region or an overlayer on a surface is possible by performing LEED on the selected area (Mundschau, et al. 1989). Selected area LEED is done either by placing an aperture on the illumination system, where only the selected area will be illuminated, or on the image system, where the necessary area is selected from the complete image. Positions of the LEED spots in the LEED in LEEM do not change with changing energy, which is advantageous for *I (V)* curves for determining facets of epitaxial over layers (Heringdorf 1998). One of the other advantages is being able to change the LEED energy from 0eV upwards in small steps and record them in real time, preferably in a movie format, giving tremendous amounts of information.

Probe depth of LEEM is an important factor to consider. Probing in the case of the LEEM depends both on elastic and inelastic electron back scattering. In low energies, dynamical LEED theory can be applied readily, as it is well suited for $E \geq 30eV$ (Pendry 1974) (van Hove, Weinberg and Chan 1986). Nevertheless, at even lower energies where the LEEM operates, as the surface barrier become increasingly important, penetration depth calculations are not available. Figure 2.9 shows the attenuation of the electron flux due to scattering for two representative metals, Al and W. It is evident that inelastic scattering makes a clear difference in the attenuation length in both cases. Considering other instances, too, the probing depth of 3 - 10Å can be a fair estimate for LEEM. An exception to this is if the energy of the primary electron is in the range of the band gap in the direction normal to the surface; the evanescent

wave existing in the band gap will determine the how far the electron will travel in to the bulk. In certain cases LEEM will provide the information about buried interfaces and defects, thus going beyond the regular limit to give details about the bulk. In these cases, however, the interfacial details are evident on the surface.

2.2.2 Device

LEEM used for the experiments is a Direct Imaging Ultra High Vacuum surface microscope model LEEM III (Figure 2.8) (GMBH, Elmitech 2007). Achievable imaging modes include bright and dark field LEEM, mirror microscopy, thermionic and Photo Emission Microscopy (PEEM). LEEM resolution is typically better than 8nm with a maximum 4.6nm. Tunable electron energy at the sample is in the range of -5 to 500eV. Field of view is 2 - 80 μm for the LEEM and ≤ 150 μm for PEEM. The range of magnification is 500 - 20000. This is operating at base pressure $p < 2\times10^{-10}$Torr. The possible temperature range variation is from RT to 1800K. The illumination system begins with a thermionic LaB_6 electron gun. Generated e-beam guided by magnetic condenser lenses, magnetic deflection coils, stigmator and an illumination-aperture which have 3 apertures. Illumination and scattered beam splitter is a 60° magnetic. The objective lens is a magnetic lens with deflectors and a stigmator. The sample is mounted on a specimen manipulator while operating the LEEM. The manipulator has freedom of spatial motion with X, Y of ± 5mm and 70mm in Z-axis. Further, it has two eucentric tilts ±3°. It also contains a changeable sample cartridge with e-beam heating. Thermocouples are W5%Re and W26%Re (type C) with maximum measurable temperature of 1873K (Pappas and Arnold 2005) (Germany 1995). The imaging system consists of 5 magnetic lenses, 4 deflectors, 2 stigmators and three contrast apertures coupled to the manipulator. The final image is obtained on a chevron channel plate array with a fluorescent screen. The image on the screen is recorded

by a high resolution CCD piped to a computer integrated with the software for lens controls and data acquisition.

Selected saved files were later ported to a quad core Mac Pro workstation where the image processing took place. The ports surrounding the sample position have various evaporators and a UV short arc lamp in the line of sight of the sample, making it possible to carry out PEEM. The schematic of the LEEM is shown in Figure 2.10, and the sequential lens system is shown in Figure 2.11. Initial beam as expected is relatively convergent, at later stages the beam is held together by the lenses.

Preliminary, sample preparation was done in the prep chamber, followed by sample transfer to the LEEM chamber. LEEM chamber setup is on an aluminum stage that is floating on an air vibration isolation system for better resolution. The microscope is divided to four main moieties: **Illumination column, Imaging column, Beam separator, Magnetic objective**. When looking from the manipulator end (Figure 2.10); the illumination column is on the left, while the beam separator (magnetic prism) is on the center, and the objective is placed in the main LEEM chamber.

In the illumination column, the 20keV electron beam is contrived and focused. A beam separator deflects the oncoming beam that traverses the objective to impinge on the sample. The magnetic objective creates the first intermediate image of the sample surface formed by the elastically back-scattered electrons (the LEEM image of the sample) in the center of the beam separator (Figure 2.11). Lenses in the imaging column then take this as the object, making at least two additional transitional images before making the final image at the image converter, which consists of two micro channel plates (Wiza 1979) (Galileo Co) with a phosphor screen.

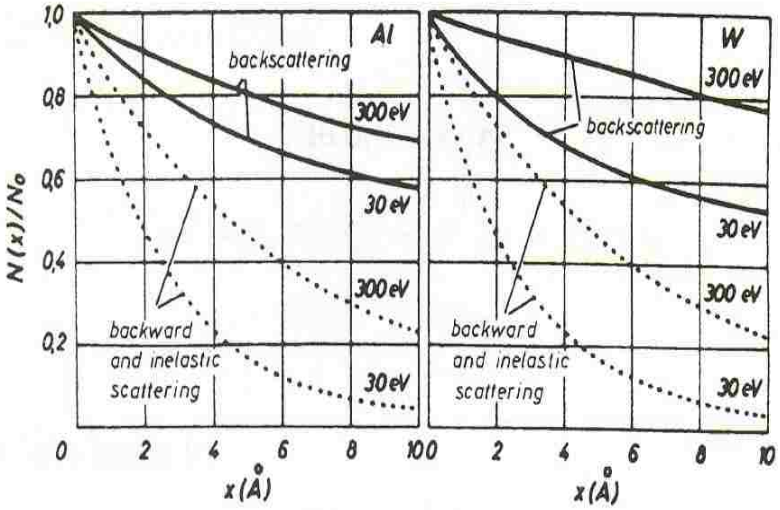

Figure 2.8 Attenuation of the electron flux in to the bulk due to elastic and inelastic backscattering in Al and W. Solid lines: elastic backscattering only, dotted lines: elastic and inelastic back scattering combined.

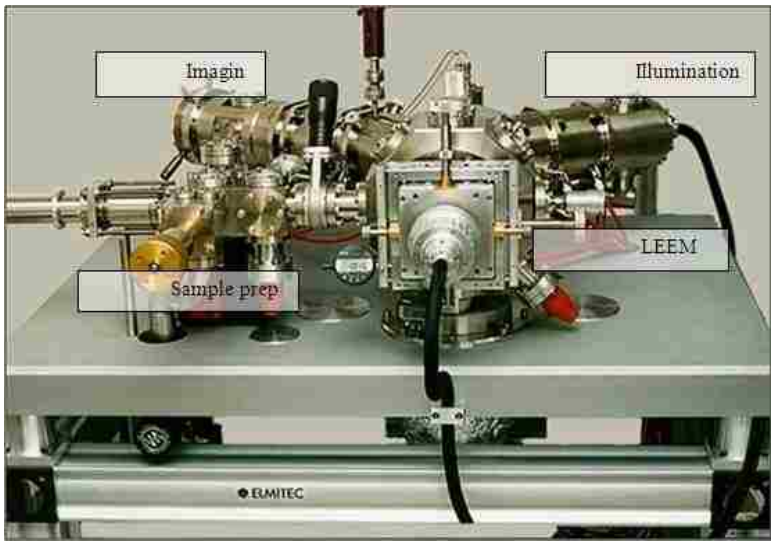

Figure 2.9 ELMITECH - direct imaging Ultra High Vacuum Surface Microscope LEEM III

Having 3 different apertures, the illumination aperture assembly is placed on the beam separator and has 400µm, 100µm and 30µm apertures. This is used to limit the beam size in the separator, which helps in minimizing the beam crossover in the objective back focal plane. In the mirror microscopy and LEED mode, the typical aperture setting is 400µm. In high resolution LEEM, the typical aperture setting is 100µm, while small area LEED requires the 30µm aperture.

The diffraction (contrast) aperture assembly, has three apertures (100µm, 30µm and 10µm), is placed in the center of the field lens. As the name implies, it improves the contrast in LEEM images. The largest aperture is used in the alignment of centering the aperture rod to the lenses. Although both 30µm and 10µm are used with LEEM, the smaller aperture gives better contrast. On the negative side, the 10µm is difficult to center and sensitive to small shifts of the electron trajectories, sample tilt, and stray magnetic fields. In LEED the aperture assembly is removed from the beam path. Due to the requirement of the harmonious behavior of all the lenses, stigmators, apertures, and the beam splitter for the operation of the LEEM, a novice user has to spend considerable time learning all the details and techniques.

A brief description of LEEM alignment follows. LEEM alignment begins with the illumination column. This requires alignment of the LaB_6 cathode.

Initial settings should start with zero values for coils, deflectors, and stigmators in the illumination column, and low emission current. Then the calibration is done by aligning the condenser lenses CL1 - CL3, while observing the emission of the electron gun on the YAG (Yttrium Aluminum Garnet- YAG, $Y_3Al_5O_{12}$) screen. At this point the beam separator is switched off. This is followed by the sample tilt alignment. This is done in the PEEM mode. In this instance, the electron gun is shut off and the sample is only illuminated by UV light from the Hg lamp. Further, the micro channel plates and the screen should be powered up, as the image is

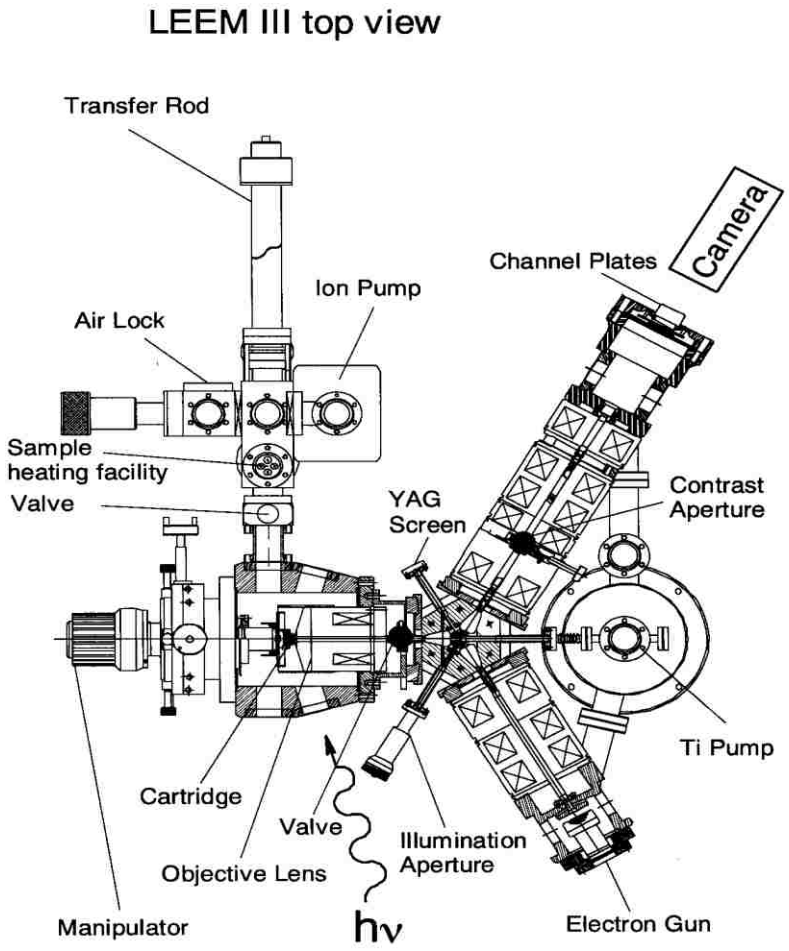

Figure 2.10 ELMITECH LEEM III schematic, UV radiation is by Hg discharge Lamp. LMITEC LEEM III. Beam direction is shown with arrows.

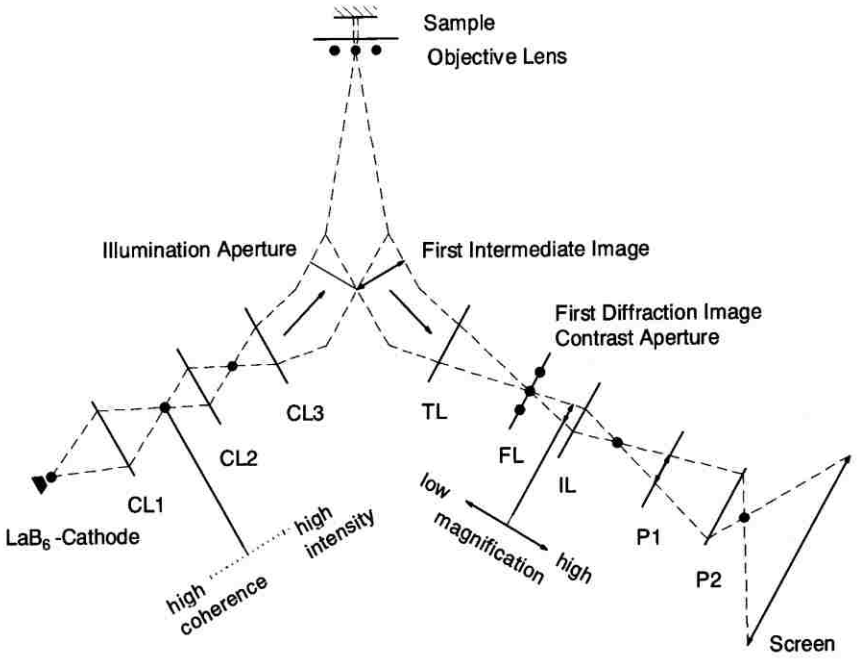

Figure 2.11 Lens system of the ELMITEC LEEM III. Beam direction is shown with arrows.

observed in real time on the computer screen for the alignment. The procedure uses the tuning of TL (Transfer Lens), FL (Field Lens), IL (Intermediate Lens), Projector (P1), and Projector (P2) (Figure 2.11). One of the frequent techniques used in tuning is “breathing the image”. A focused, image view centered, surface structure will behave like breathing when the object current is varied about the proper focus current. When considering another structure in the neighborhood of the first centered structure, it will move away from the center when the current becomes lower and towards the center when the current becomes higher. At points of the alignment procedure, breathing is used to ensure that the respective lenses are suitably aligned. If breathing is not properly observed, corresponding deflectors are used to adjust the lens appropriately.

Once the sample tilt is aligned, the imaging column has to be aligned. In the process, lenses P1 (Projector 1), P2 (Projector 2), and TL (Transfer Lens) (Figure 2.11) are mainly used. “Breathing” is also extensively used in getting a focused electron beam to the micro channel plates. In the later stages, special care has to be taken not to put an intense beam of electrons on the micro channel plates, as immediate degradation will result. Two other alignments are necessary for the operation of LEEM. They are, in order, of the electron beam alignment and the objective alignment. Once these are achieved, LEEM is ready for analysis.

It is possible to record images individually or as a sequence (movie). LEED patterns could be recorded individually and as a sequence with varying energy.

2.3 Scanning Tunneling Microscopy (STM)

2.3.1 Principles

This technique is one of the most powerful and versatile techniques in surface and interface science. Device development and the first successful experiments were carried out by Gerd Binnig, Heinrich Rohrer and their coworkers in March 1981, (Binnig, Rohrer and Gerber,

et al. 1982) (Binnig and Rohrer 1987) in the Zurich IBM Research Laboratory. The application of STM (Scanning Tunneling Microscopy) in both academia and industry has grown rapidly, as Binnig and Rohrer with Ernst Ruska, who had made major contributions towards the development of the electron microscope, were awarded the Nobel Prize in Physics in 1986. The time between discovery of the STM and awarding the Nobel Prize was very short compared to such discoveries in the history of physics, which exemplifies the significance and the impact STM has on physics.

STM belongs to the group of microscopy techniques now considered as Scanning Probe Microscopy (SPM), although it was the STM which introduced the concept. Following the introduction of the STM, Binning *et. al.* also introduced the atomic force microscope (AFM) (Binning, Quate and Gerber. 1986). There are numerous SPM devices with accompanying techniques available for a variety of investigations that are used for, but are not limited to, surface and interface investigations. The quintessential feature of SPM is the physical probe that raster scans the specimen, followed by the output via a probe-surface/interface interaction plotted as function of position (x, y). Interaction is a measure of a physical property that is location dependant.

Usually SPM can measure several properties (modes) simultaneously. In the case of AFM, a micro cantilever (probe) measures tip-sample forces (mechanical contact, chemical, electrostatic, etc.) that deflect the cantilever under Hooke's Law. In the case of the STM, the sharp conductive tip (probe) measures the tunneling current (Figure 2.12) (Fowler and Nordheim 1928) between the tip and the sample as a function of position. Depending on the mode of operation, there can be various other measurements that are also location dependent. Particle tunneling is a quantum - mechanical phenomenon that was introduced in the beginning of the twentieth century. Wave functions of electrons overlap through the classically forbidden

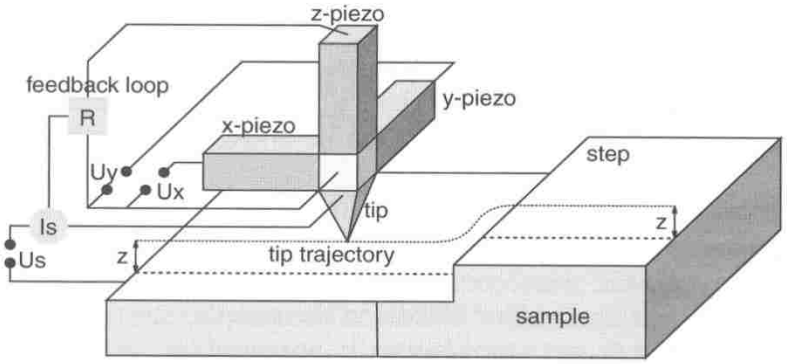

Figure 2.12 Typical schematics of an STM. Here ***Is*** is tip/tunnel current, ***Us*** is the bias between the tip and the sample facilitating ***Is***. ***Ux*** is the applied voltage of x piezo, ***Uy*** is the applied voltage of ***y*** piezo, ***Z*** is the vertical height from the surface.

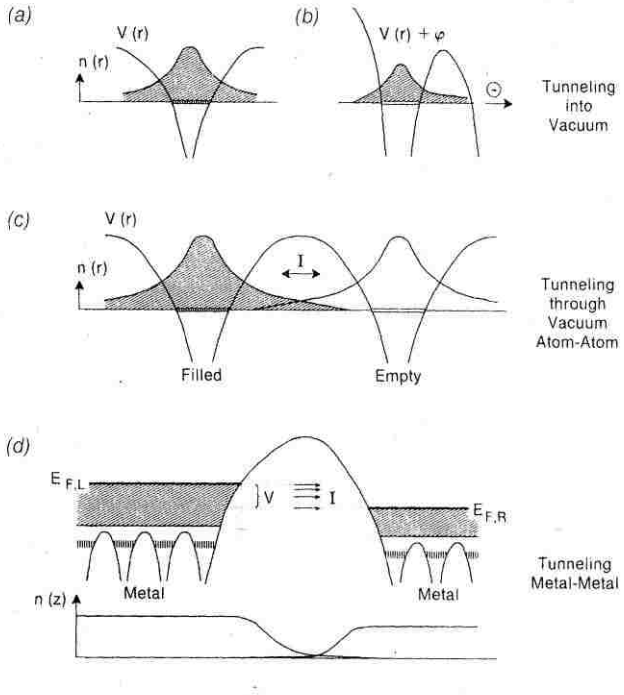

Figure 2.13 Electron tunneling through a coulomb potential barrier and in-between metal/conductive electrodes.

potential barrier, which in this case is the vacuum separating the tip and the sample, resulting in electrons tunneling from one conductor to the other.

In Figure 2.13 (Binnig and Rohrer 1987) (a) the valence electron wave function under the Coulomb potential well of the atom core leaks out – *i.e.* tunnels into the vacuum. (b) By applying an external potential, an electron can be made to tunnel through the barrier and leave the atom. (c) If two atoms are sufficiently close, then an electron can tunnel back and forth through a potential barrier. (d) As the individual potential barriers due to core atoms in a metal are quenched, giving rise to band structure, electrons can move freely in a band. However, on the surface there is a potential rise due to the vacuum that makes a barrier. An electron can tunnel through this barrier to a surface atom of a nearby metal. The Fermi energy of the starting metal is lower than the height of the barrier, making theprocess classically impossible. By applying a potential (V) between the metal surfaces,the Fermi level of the left metal ($E_{F,L}$) is raised with respect to the Fermi level of the right metal ($E_{F,R}$), thus facilitating empty states on the metal on right for the electron to move into. Due to Fowler and Nordheim (H. M. Michaelson 1977) (Fowler and Nordheim 1928) a first approximation for the tunnel current is,

$$I_T \propto \frac{V}{d} \exp\left(-Kd\sqrt{<\phi>}\right), \quad -(2.4)$$

where $\boldsymbol{V}$ is the voltage applied between the tip and the sample, $<\phi>$ is the average work function, $\boldsymbol{K}$ is a constant which has a value equivalent to $\boldsymbol{1.025 Å^{-1}/\sqrt{(eV)}}$ for the vacuum between the tip and the sample, $\boldsymbol{I_T}$ is the tunnel current, and $\boldsymbol{d}$ is the separation between the tip and the sample. The typical range of magnitudes for the work function is 1.5 - 6 eV. Work functions rise with the Z (atomic weight) of the element and compactness of the lattice, which give typically higher values for transition metals like Ag, Cu, and Co, and also depend on the facet or the orientation of the crystal (Stroscio, Feenstra and Fein. 1986). Observing the equation (2.4) for

small variations of the $\boldsymbol{d}$, it is possible to expect major variations in $\boldsymbol{I_T}$, therefore $\boldsymbol{d}$ should be measurable with a precision of 0.05 - 0.1Åto get tangible information about the surface. Such precision along with the x-y motion precision (1 - 2Å) required is attained by the piezoelectric mechanisms. Exponential coupling between I_T and d also indicates that I_T passes through the atom at the edge of the tip, giving local corrugation of the surface. In case the local work function needs to be found, $< \phi >$ is obtained by,

$$< \phi > \cong \left(\frac{\partial \ln I_T}{\partial z}\right)^2 , \quad -(2.5)$$

where $\boldsymbol{z}$ is the tip sample separation measured dynamically via $\boldsymbol{I_T}$. Dependence on electrons limits the versatility of the STM, as it restricts the application of the technique to conductive or semi conductive surfaces. In certain cases this can be achieved by a few monolayers of insulating material on a conducting surface.

A typical STM tip is made up of Ir, Pt-Ir, or W. Different modes in which STM can operate include Scanning Tunneling Spectroscope (STS) (Feenstra, Thompson and Fein 1986) for surface density of state determination, surface state determination as in the case of Si(1 1 1) (2×1) π-bonded surface (Bode 2003), spin-polarized scanning tunneling microscopy (SP-STM), and atom and molecule manipulation including surface modification, as in the case of nano indentation and Xe atom displacement (Lüth 2001).

2.3.2 Aarhus (Scideco I/S) Scanning Tunneling Microscope

The STM used for the experiments in this thesis was designed and built by the Aarhus Scanning Probe microscopy group (SPM) at Aarhus University in Denmark. Figure 2.14 shows the STM on a holding cradle. The same STM was used in three of the previous dissertations from our group (D. Hite 2001) (Kizilkaya 2003) (Zhao 2005) (Aarhus University 1996). The STM is

housed in an ultra high vacuum compatible Al block which weighs 0.6Kg. The Al block, due to its mass and heat capacity, is able to sustain a constant temperature for an increased duration of time. This enables one to carry out STM at low temperatures without being connected to a continuous low temperature cooling source like liquid N_2. The inertial mass of the Al block also decouples the low frequency vibrations from the STM. The Al block is connected to two stainless steel rods via three springs that decouple vibrations from the environment to the STM. The steel rods are rigidly connected to an 8 inch Conflat flange, and the flange is directly connected to the UHV chamber.

A movable contact base, which is connected to a stainless steel tubing system that circulates liquid N_2, is on the flange side of the Al block. This is made in order to contact firmly with the Al block when low temperature operation is desired. Once the required temperature is attained, the base is moved back and the Al block is suspended from the three springs freely. The range of temperatures within which the STM operates is -160°C to 100°C.

Temperatures above room temperature are attained by heating via two Zener diodes (Type BZY93C75) attached to opposite ends of the Al block. All electrical feed-throughs are integrated to the 8 inch flange.

Thermocouples used are Type K – Chromel (Nickel-Chromium Alloy)/Alumel (Nickel-Aluminum) (NIST, National Institute of Standards and Technology (NIST) NIST ITS-90 Thermocouple Database 2007). The wires connecting the various parts of the STM setup within the chamber are UHV compatible Kapton coated thin wires. Tunnel current wire is shielded with a conductive braid to minimize the pickup within the chamber. A schematic of the STM structure is shown in Figure 2.15. Sample holders, which were shown in Figure 2.1, are loaded on top as seen in Figure 2.15–1.

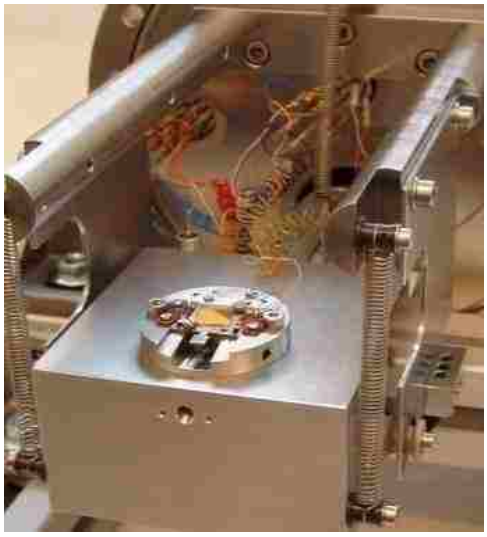

Figure 2.14 Aarhus STM. STM is on the Aluminum block which is suspended by the three springs.

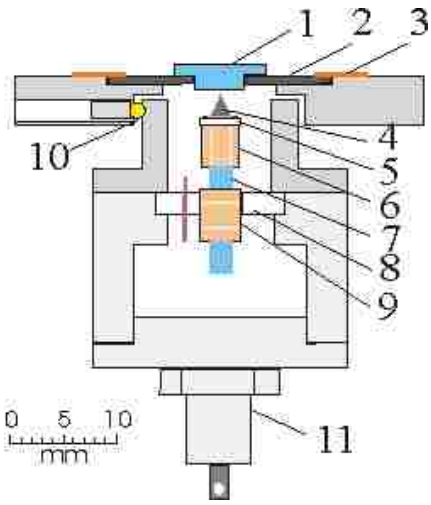

Figure 2.15 Schematics of Aarhus STM [2.4]: 1 Substrate crystal, 2. Ta sample holder, 3. Spring, 4.Tip, 5. Tip holder, 6. Scanner tube, 7. Rod, 8. Macor ring, 9. Linear motion tube, 10.Quartz ball, 11. Zener diode.

The sample is held down firmly by two strips of $Cu_{98}Be_2$ alloy that mimic springs. The top plate is attached to the Al block. It is thermally and electrically isolated from the STM body by three quartz balls. The tip, which in our case is made of Tungsten (W), is held by the tip holder, which is glued to a Macor holder. This is glued to the top of the scanner tube. The scanner tube is 4mm long and has an inner/outer diameter of 2.67/3.18mm. It is made of EBL#2 (Staveley Sensors, Inc.) with Ni electrodes.

The tube is glued to the top (Figure 2.15–7) of the meticulously polished, ceramic (SiC) rod having a diameter of 3mm. When considering the tunneling due to sample - tip separation, tip morphology is an important factor. Tips were prepared from tungsten wires etched in a KOH solution. The coarse approach mechanism is a small inchworm micro motor. The bottom piezo tube is divided into three rings. Two soft solder (10% Ag: Sn: Cu) bearings attached to the ceramic rod are set in between the bottom piezo (Figure 2.15 – 9) tube and the rod. They are placed under the upper and the lower electrode with an extremely good fit, having nearly the same radius as the ($\Delta R < 0.1\mu m$) rod. When a positive voltage is applied on an electrode, it clamps onto the rod, and when a negative voltage is applied, the electrode de-clamps from the rod. Depending on the voltage applied to the center electrode, it will elongate or contract. With the right sequence of applied voltages, three electrodes will make the rod move up or down, because the piezo tube is fixed to the STM body by the Macor ring (Figure 2.15 – 8). The center electrode moves the tip at a speed of 0.8nm/V when the bottom electrode clamps the center rod. (Figure 2.16) Three 16 bit DACs that modulate the voltage to the electrodes are fully computer controlled. This inchworm motor in the lowest speed works in 2Å per step and at the highest speed moves ~ 2 mm/min.

Under the piezo tube at the bottom of the body of the STM, another Zener diode (Type BZY93C75) is connected to heat the body during STM block cooling via liquid N_2. Operating at

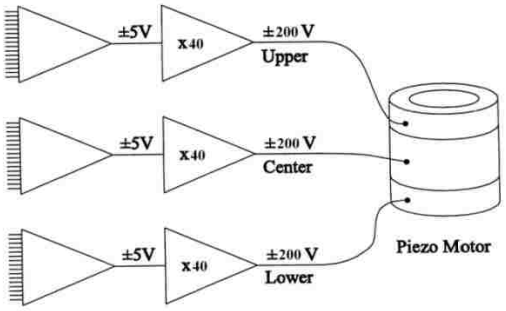

Figure 2.16 Z-Coarse approach mechanism schematics. DACs used are 16bit.

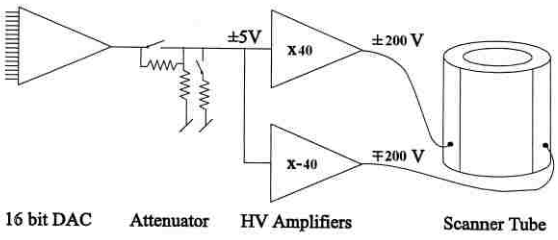

Figure 2.17 X-Y Raster scan:

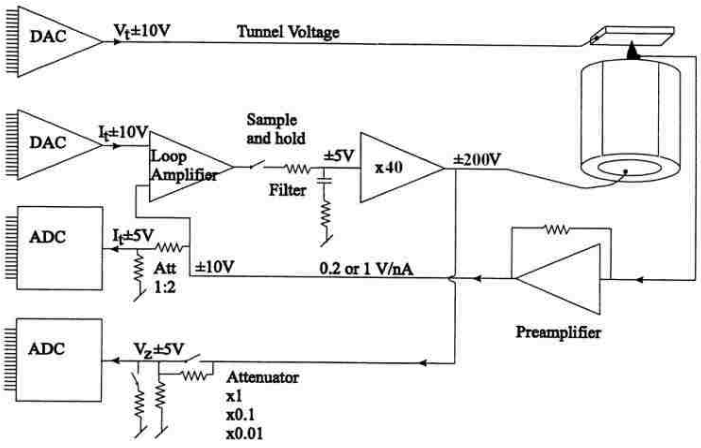

Figure 2.18 Feedback loop with the scan tube.

2–4 mA and ~76 V, this avoids low temperature seizing of the inchworm mechanism. The STM has a maximum scan size of15000Å, with a maximum frame size of 512 × 512 pixels, coupled with a scan speed of 10000 pixel/sec. It has a vertical resolution ≥ 0.1Å and on clean metal surfaces attainable lateral resolution ≥ 1Å.

The small size of the STM aims to produce only high resonance frequencies of the structure. Transverse damping is comparatively weaker than the longitudinal damping. The measured transverse resonance frequency is on the order of 8KHz, and resonance frequency of the STM platform is ~2Hz.

Two versions of software were used for the STM operation. The earlier version was an MS DOS based system that was written in PASCAL (Borland). The second version, which is an upgrade to the first, is fully MS Windows compatible with a GUI (Graphical User Interface). Both were developed by the Aarhus SPM group. Coarse approach is carried out automatically, where the inch worm is moving the center rod and the tip assembly while the monitored tunnel current reaches a preset limit. This avoids crashing the tip onto the sample.

A raster scan is obtained by applying anti-symmetric voltages to the opposite electrodes of the scanner tube while keeping the other two electrodes at a constant voltage (Figure 2.17). Therefore X–Y raster requires two identical channels consisting of 16 bit DACs. Each channel has a three way attenuator with two switches (Figure 2.18).

When the upper switch is closed, the voltage range is ± 400V, which gives a deflection of 6μm;with both switches open, the voltage range is ± 40V, giving a deflection of 5000Å; and when the lower switch is closed, the voltage range is ± 8V, which gives a deflection of 1000Å. The attenuator control is real time with the software, with three settings 0, 1 and 2. The linear deflection (X) response with respect to voltage (V) is given by,

$$\frac{dX}{dV} = \frac{4\sqrt{2}(D+d)l^2 P_c}{\pi(D^2+d^2)(D-d)}. \qquad -(2.6)$$

D/d is outer/inner diameter of the scanner tube, *l* is the tube length P_c is the piezoelectric constant of the piezo material EBL#2. Equation (2.6) gives the deflection sensitivity at the top of the tube; deflection at the top of the tip is given by,

$$\frac{dX_{tip}}{dV} = \frac{dX}{dV}\left(1 + 2\frac{l_{tip}}{l}\right). \quad -(2.7)$$

l/l*$_{tip}$** is length of the tube/length of the tip. It is evident that varying the tube length to tip length ratio will increase the tip deflection sensitivity. In the experiments described in the dissertation, ***l = 6mm and ***l*$_{tip}$** = 3mm were used, giving rise to a tip deflection of2 times the tube deflection. Although the equations are linear, this is not the case in scanning large areas due to hysteresis and creep. In this case, the drive voltage is set nonlinear with an empirical polynomial to correct for the deviation.

After stable tunneling is established, it is necessary to measure and control the Z voltage to keep the tunnel condition stable. While managing the Z voltage raster in X-Y can progress with tunnel condition intact. In constant current mode, the feedback loop is shown in Figure 2.18.

The loop starts with the point of tunneling (tip) followed by the preamplifier, which converts the tunnel current signal to a voltage signal (1V/nA). This is taken in by the loop amplifier, which has a range of gain of 0.1 to 100 with three step (1, 10 and 100) variation. Fine variation of the gain is attained by slider bars in the software as a percentage of the coarse gain. Loop AMP compares the signal from the preamplifier with the tunnel current set dynamically in the program. If it is lower than the set value, then output voltage is increased, which is again increased by the high voltage amplifier (×40) and fed in to the bottom inside of the scanner tube

(this is the Z voltage applied to the tube), which will displace (13Å /V) the tip towards the sample as it extends, increasing the tunnel current between the sample and the tip. This cycle occurs inversely in the case of the tunnel current being higher than the set value. Feedback from the loop continuously keeps the tunnel current constant to the set value in the program, hence keeping the tip sample separation fixed, assuming the surface work function is the same (in most clean metallic samples this is the case). Under the conditions, surface corrugation is a direct function of the applied *Z* piezo voltage and mapped in the XY grid, thus resulting in the surface topography.

2.4 Auger Electron Spectroscopy (AES)

2.4.1 Principles

This technique is generally used to check the cleanliness of a freshly prepared sample surface under UHV conditions, be it by sputter-anneal cycles or cleaving. It is also used in thin film growth studies where a simple growth mode in an epitaxial over-layer can be determined. It can be used for surface chemical (elemental) composition analysis. It is also used for studies of sub surface migration and depth profiling of the concentration of a particular species. (Davis, et al. 1976) (Fuggle and Inglesfield 1992)

The basis of the analysis was found and reported first by Lise Meitner (Sime 1996) (Rife 1999) in 1923, and then independently in 1925 by Pierre Victor Auger, although the process was named after Auger. AES is an electron core-level analysis technique where excitation is induced by a primary electron beam form a gun. Emission is due to secondary electrons which are of narrow energy width, energy differentiated and detected by a standard electron analyzer, usually a Cylindrical Mirror Analyzer (CMA). The principle of the Auger process is as follows: The impinging primary electron beam makes a hole in the core level (K or L shell) by removing the

electron. Due to the complexity of the nature of the scattering process, the ejected electron and primary electron have no viability for the analysis. In order to minimize the energy, electrons rearrange by displacing an electron from a energetically higher lying shell to the core hole. In order to counter balance the resulting energy change, two things can occur. Either a characteristic X-ray photon is emitted or a radiation-less Auger transfer occurs, where an electron from the same or a different shell absorbs the energy released by the falling electron and ejects from the atom with a characteristic Auger energy, while leaving the atom doubly ionized due to two vacant holes.

The ejected X-ray photon or the Auger electron carry well defined energy that directly couples to the core-level energy differences. Accurate measurement of these energies will identify the particular atom, *i.e.* the elemental information. This emitted X-ray analysis giving the chemical concentration is the basis of Energy Dispersive X-ray Spectroscopy (EDX or EDS).

Analysis of the emitted X ray is less surface sensitive compared to the Auger electron due to the lower mean free paths of electrons in solids (Agarwal 1991). Depending on the energy of the primary beam, it is possible to determine that the probe depth in typical AES is in the range of 10Å-30Å. This also depends on the respective surface (Zangwill 1988) (Figure 2.19).

Several mechanisms are at work for the Auger processes. Some of them are shown in Figure 2.10. In Figure 2.20 (a), the primary beam removes an electron from the K shell (dashed arrow), followed by an electron from L_1 moving to the vacant K hole. To offset the energy, an electron from L_2 is ejected as the Auger electron. In accordance with the associated shells, the mechanism is called KLL. In Figure 2.20 (b), primary electrons knock an electron from L_1, and to compensate the energy offset an electron from M_1 moves to L_1, followed by an ejection of an electron from M_1, which is the Auger electron. This is an LMM mechanism. Figure 2.20 (c)

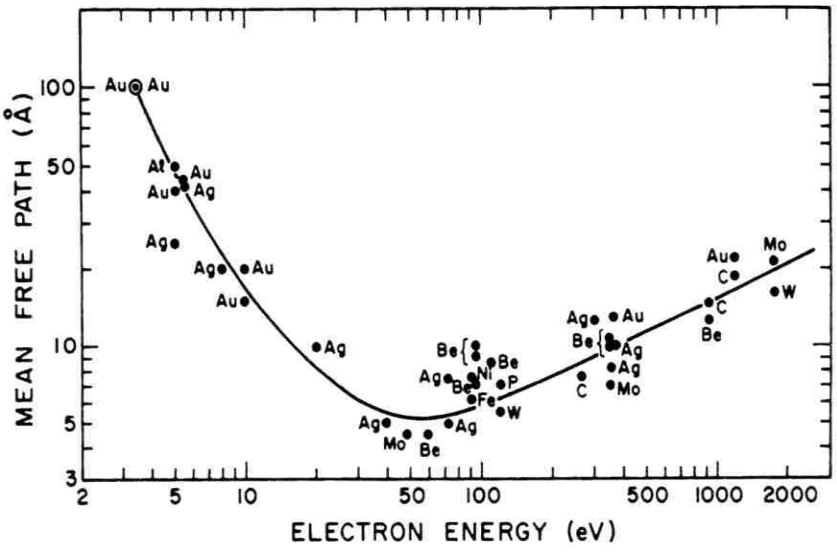

Figure 2.19 Mean free path of electrons as a function of kinetic energy for various elements. (Luth 2001)

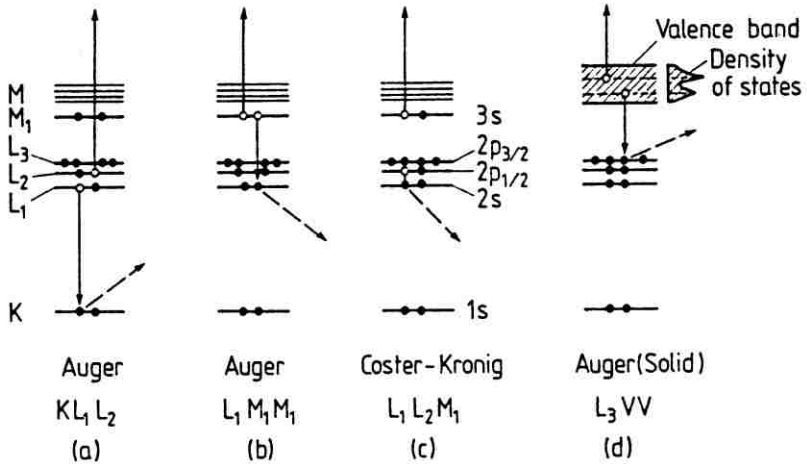

Figure 2.20A selected group of Auger electron emission processes. (Lüth 2001)

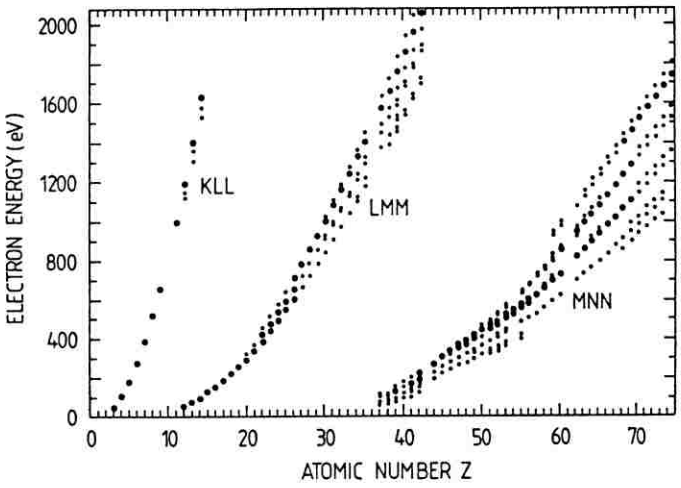

Figure 2.21 Electron energy versus atomic number (Z) variation for different Auger mechanisms. (Lüth 2001)

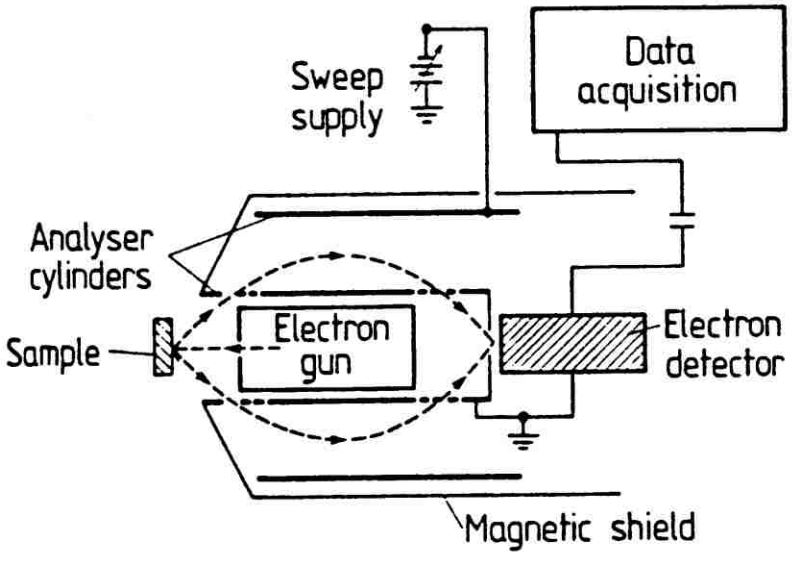

Figure 2.22 Schematics of the CMA Auger setup. (Lüth 2001)

shows a different case where primary electrons remove an electron from 2S, followed by an electron moving from 2p to 2s (same shell). The energy offset is compensated by an ejection of an electron from 3s as the Auger electron. Finally, there is an Auger process associated with an atom in a solid where electronic bands are involved. The primary electron knocks off an electron from L_3, where the energy offset is compensated with an electron moving from valence band (V) to the L_3, followed by an electron ejecting as the Auger electron. The mechanism therefore is LVV. Principal Auger electron energies with the atomic number variation with different processes are shown on the Figure 2.21. As it is evident with incremental Z, electron exchanges of Z Auger transitions move to higher shells from the core. Looking at the energy transfer of the Auger process in the simplest case (KLL), we get,

$$E_{kin} = E_K - E_{L_1} - E_{L_2} \; . \; -(2.8)$$

It is possible to obtain these energies from XPS (X ray Photoelectron Spectroscopy) but they differ because of the extra core hole generated in the Auger process. A correction term is needed to offset the effect. Once the correction term is added, it is possible to determine the atomic element responsible for the respective kinetic energy, enabling us to find the elemental composition on the surface.

2.4.2 CMA (Cylindrical Mirror Analyzer) type AES

An electron gun at the center of the assembly produces the primary beam and it is integrated to the CMA. The primary beam hits the surface, and the secondary electrons enter through the left of the CMA. They get focused by the two concentric electrodes onto an image point where the channeltron is positioned. The cylindrical electrodes are housed in cylindrical magnetic shielding to minimize residual magnetic fields interfering with the beam inside. The pass energy is determined by the radial field between the two concentric electrodes. The inner

cylinder has slits, making reflected electrons go between the electrodes. The slits are made in such a way that electrons entering near a cone with an apex angle 42°±3° are taken in. The pass energy E_o and pass voltage V_o are related by,

$$E_o = \frac{eV_o}{0.77\ln\left(\frac{b}{a}\right)} \qquad -(2.9)$$

where ***a*** and ***b*** are the inner and outer radii of the electrodes, respectively. Due to Auger signals being smaller compared to the background and systematic identification being difficult, the signal was obtained in the derivative mode. Derivative mode (dN/dE) can be attained either by latter stage numerical differentiation or electronic differentiation via a lock– in amp and sinusoidal voltage coupled to the outer electrode while monitoring the detector current. In the literature (Davis, et al. 1976), the reference energy for an element is given at the minimum of the derivative of the respective Auger signal.

2.5 Electron Energy Loss Spectroscopy (EELS)

2.5.1 Principles

High resolution EELS is a powerful surface science technique which can be used for determination of adsorbate vibrational frequencies, the molecular structure of any adsorbates, their surface orientation and bond strengths, surface chemistry, and the investigation of surface acoustic and optical phonons and plasmons.

In this technique, broadly speaking, inelastic scattering of low energy electrons is used to investigate excitations of surfaces and thin solid films. Surface excitations can be studied by low narrow – energy beams of electrons.

The interaction of the low energy electrons and the excitations are mediated via two mechanisms: Dipolar Scattering and Impact Scattering.

2.5.2 Dipolar Scattering

This is a result of the interactions between impinging electron and the dipole field of the surface. Two conditions apply in these interactions. First, only dynamic dipole moments interact, therefore contribute to the scattering. Second, their long range interactions make it irrelevant to consider the detailed surface excitations. Surface excitations can be given by an electrostatic potential of the form:

$$\emptyset(x) = \emptyset_0 e^{(i\bar{q}_{||}\cdot\bar{x} - q_{||}|z|)} . \qquad -(2.10)$$

This potential has 2D wave behavior parallel to the surface while decaying exponentially in the z (normal to the surface) direction. When compared with the long range dipole field, which extends far into the vacuum, thus having long time scale interactions with the oncoming electrons, it is evident that there is strong interaction. This also results in dipolar scattering occurring far into the vacuum and intensity peaks with small angles *i.e.*

$$\Delta\theta = \frac{h}{2\pi}\frac{\omega}{2E_i} \qquad -(2.11)$$

where $h\omega/2\pi$ is the energy corresponding to the excitation, while E_i is the energy of the impinging electron.

There are several theories describing the dipole scattering ranging from classical (Lucas and Sunjic 1971)to semi classical (Lucas and Vigneron 1984) to quantum mechanical (Evans and Mills 1973). Under the Born approximation, quantum mechanical dipole scattering theory gives the differential cross section for elastic scattering for electrons from a flat surface considering that the probability amplitude of the specular ($\boldsymbol{\theta_I = \theta_s}$) reflection and scattering are equivalent ($\mathbf{R_i = R_S}$) :

$$\frac{d\sigma}{d\Omega d\omega} = \frac{2m^2e^2}{\pi^2\left(\frac{h}{2\pi}\right)^4\cos\theta_I}\left(\frac{k_S}{k_I}\right)|R_I|^2\left[\frac{q_{||}}{\left\{q_{||}^2+\left(k_{S,z}-k_{I,z}\right)^2\right\}^2}\right]\frac{P(q_{||},\omega)}{q_{||}} \qquad -(2.12)$$

Here k_S and k_I are the wave vectors corresponding to scattered and incident waves. $P(q_{||},\omega)$ is proportional to the surface response function $\sim q_{||}$ Im $[1/(\varepsilon(q_{||},\omega) + 1)]$. The quantity in the square brackets (kinematic factor) will govern the cross section under the condition that loss is weakly dependent on q. In such a case, the cross section gives rise to an intensity curve peaked in line with the specular direction (dipole lobe).

When the substrate is metallic, metal surface selection rule will give the vibrational modes: **Only the dynamic dipole modes perpendicular to the surface will be observed in the EELS specularly reflected beam**.

2.5.3 Impact Scattering

As seen in the previous section, at large angles from the specular, scattering is no longer determined by the dipolar regime. Then the impact scattering regime dominates. Here the low energy electrons interact with the atomic potential of the substrate. As we have seen, it is evidently short range and requires addressing both crystal structure and multiple scattering.

The selection rule for dipolar scattering does not hold in the impact scattering regime. This gives the versatility to study the surface parallel dipole modes. In contrast to dipolar scattering, the intensity distributions coming out of impact scattering are broad.

Two selection rules pertinent to the experiments performed for the impact scattering regime will be stated without proof here for brevity.

1. **If the scattering plane is a mirror plane of the surface, the intensity will vanish for all modes which are odd with respect to the mirror plane.**

2. **If the scattering plane is perpendicular to the mirror plane of the surface, all modes which are odd with respect to this mirror plane have zero intensity in the specular direction.**

The second selection rule holds under the condition that the energies of the incident and scattered electrons are comparable, in order to fulfill time reversal symmetry. These selection rules enable the determination of various EELS spectra in the experiments (Ibach and Mills 1982).

Considering the surface translational symmetry the momentum component parallel to the surface is conserved in the inelastic scattering (modulo of the surface reciprocal wave vector) process.

The wave vector of an excited plasmon can be obtained from the observed energy loss ($h\omega_s/2\pi$) and scattering geometry (θ_i and θ_s) using the kinematic relation based on the energy and the momentum conservations:

$$q_{||} = \frac{\sqrt{2m}}{\left(\frac{h}{2\pi}\right)}\left(\sqrt{E_i}\sin\theta_i - \sqrt{E_s}\sin\theta_s\right) \quad \text{- (2.13)}$$

Where E_i and $E_s = E_i - (h\omega_s/2\pi)$ are the energies of the incident and the scattered electrons respectively. Fixed angle EELS spectrometer had 128˚ between the incident and scattered ray (θ_i= 62˚ and θ_s = 62˚) at specular geometry. Both incident (θ_i) and scattering (θ_s) angles are varied when the sample is rotated by φ (θ_i= 62˚+ φ and θ_s = 62˚- φ). This facilitates the variation of $q_{||}$. All the data are measured at room (~300K) temperature.

2.5.4 Instrumentation

Two monochromators and the analyzer are crucial for electron energy analysis in EELS (Figure 2.23). The analyzer is the Electrostatic Cylinder Sector Energy Analyzer type (Figure 2.24), with well defined pass energy $\mathbf{E_0}$ for electrons travelling along the center circular path between the electrodes. This path is determined by the balance between the centrifugal force and electrostatic force of the field $\boldsymbol{\varepsilon}$ given by the V_p potential drop across the electrodes. This is given by the equation:

$$E_0 = \frac{eV_p}{2\ln(b/a)} \qquad -(2.14)$$

where *b* is the inner radius of the outer electrode and *a* is the outer radius of the inner electrode.

A cathode setup with accompanying lens system produces a beam of electrons via a hot filament with a Maxwell distribution of energies ranging 0.3 – 0.5eV of half width. The monochromators will filter the electrons in an energy window of a width 1 – 10meV from the distribution.

This primary beam is focused to the sample via a lens system. The primary energy of the e beam is determined by the potential difference between the lens and the sample. The scattered electrons coming from the sample will move to the focusing lens system and then be guided to the analyzer. Here the pass energy and resolution area held constant, but the acceleration voltage between the sample and the analyzer is varied. This is to keep the resolution constant.

If the pass energy is varied, then the resolution also changes, and this is usually not desirable. The lens system coming after the analyzer focuses the e-beam to the detector, which in the LK2000 device is a channeltron working in ~2900V. Here the count rates are measured and taken in as data.

2.5.5 Device

The instrument used is the HREELS LK 2000 DAC by LK technologies, shown in Figure 3.01. It has a maximum resolution of 3meV (*FWHM*). The monochromator has a double pass filter, with the ability to vary the beam energy in the range 0– 240eV. Sample bias can be varied in the range ± 15V. The analyzer comes with fixed geometry, *i.e.* the momentum transfer (q||) is achieved by sample rotation. Sample rotation will vary θ_i and simultaneously θ_r (fixed $\theta_i + \theta_r =$ **128°**) because they are coupled together. The sample is confined to a grounded Faraday cage in order to reduce the effects of stray fields.

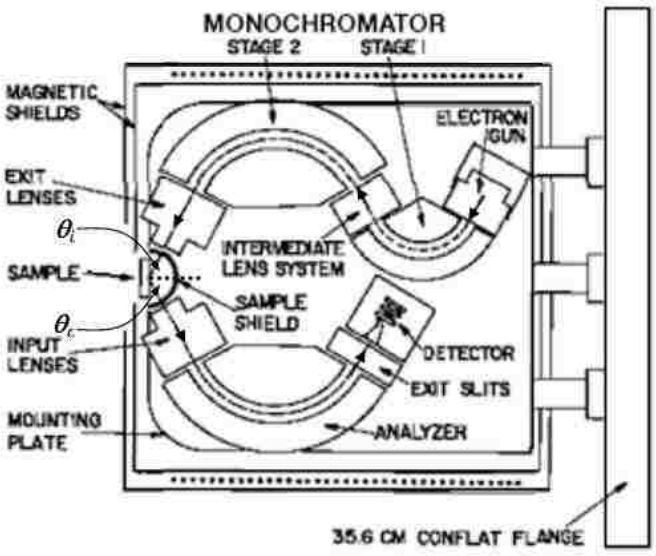

Figure 2.23 Schematic cross section of the LK 2000 HREELS. The incdent electron angle is θ_I and scattered electron angle is θ_r.

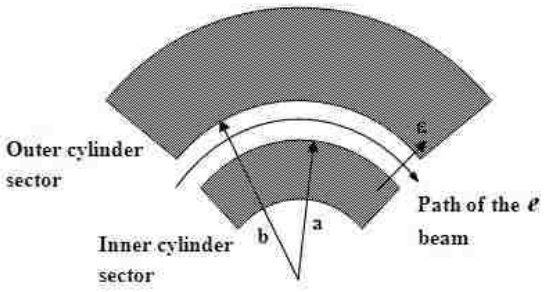

Figure 2.24 Cylindrical Sector Energy analyzer cross – section.

The whole unit is magnetically isolated by Mu-metal shielding. In order to achieve UHV conditions, the unit can be baked up to 200°C. The system is mounted by a 14" OD flange to the vacuum chamber. Sample current routinely observed at 150– 400pA. Background / signal intensity ratio at 25meV is ~ 10^{-5} or lower. The analyzer has a low noise - ripple ratio (> 250μV Peak to Peak) and long time stability, with lens voltage drift less than 1mV/week. The instrument panel gives ready accessibility to controls, with the computer software providing manual and auto-optimization of the lens voltages. Data acquisition and elastic peak fitting can be done by the associated software. Lens settings can be saved on the computer for recalibration when needed.

3 Dynamical Evolution of Ag Nanowires on Clean Cu(1 1 0)

3.1 Introduction

With the invention of SEM (Scanning Electron Microscope), TEM (Transmission Electron Microscope), STM and a multitude of other instrumentation and analysis techniques, elucidating the structure and morphology of nano-scale materials has become increasingly apparent. Although thermodynamics govern the stability of these, kinetics plays an equally important role. In order to obtain a clear picture of the process it is important to understand both facets. Of the two methods ("*bottom up design"* and "*top down design"*) of fabricating nano materials, each has its own merits. However, especially in the case of *bottom up design*, understanding growth dynamics is paramount. It is in this sense the LEEM analysis enable us to model the dynamical growth of the Ag nanowires.

Self-assembly of nanostructures is a *bottom up approach*, where thermodynamical laws and kinetics govern the resulting structure/morphology of a given system. Yet it is by no means restricted to microscopic systems as is evident by a vast number of examples in the macroscopic world of nature (structure formation in astrophysics, micelle formation in soap, crystallization, etc) (Whitesides and Grzybowski 2002). The *bottom-up* concept describes a set of phenomena which can be readily categorized as a subset of self organization. It is possible to classify self-organizing systems into several different kinds. In certain such systems, inherent processes take place in the proximity of thermodynamic equilibrium among the species involved, so called *Static Systems,* which include typical phase transitions and spontaneous symmetry breaking processes like crystallization. Some other such systems are far from thermodynamic equilibrium. Examples are diffusion limited aggregation and reaction diffusion systems such as Belousov -

Zhabotinsky Oscillator (Winfree 1984). These are coined as *Dissipative Structures* and theorized by Nobel Laureate, Ilya Prigogine (Prigogine 1977).

Another set of self-organizing systems are dynamical systems which consists of smaller sub-units interacting with each other. In observing systems exhibiting self-assembly in nano scale, often it is possible to see the systems near thermodynamic equilibrium and far from thermodynamic equilibrium and in certain cases in a mixture of the two kinds. Structure and morphology of the different nano structures and island formation on surfaces have been studied intensely due to the multitude of technological applications (Shchukin and Bimberg 1999). In hetero-epitaxial growth, the ensuing structure is typically determined by the strain due to lattice mismatch competing with the surface and interfacial free energy of the species involved. Heterostructures in semiconductor industry have already seen tremendous growth due to their unparalleled contributions in technological applications (Kroemer 2000) (Alferov 2000).

Self-assembled hetero-epitaxial structures/islands typically can be nanodots or nanorods. Depending on the band structure along and across, nanorods can be conductive (nanowires) or insulating. But, as in the case of carbon nanotubes, the properties can be are tunable. Direction of growth and orientation also differ. For example, Ag nanowires grown on Cu(1 1 0), detailed here, are oriented parallel to the substrate, whereas Si nanowires grown with Au catalysis on Si(1 1 1) are oriented normal to the substrate (Hannon, et al. 2006).

More recently, nanodots, specifically in semiconductor hetero-epitaxial systems, are increasingly being investigated due to their possible applications in the optoelectronic (Pearsall, et al. 1987) industry. In the Ge/Si(0 0 1) system where the thin film to nanodots/island transition can be tuned with a surfactant (As/Sb) (R. M. Tromp 2000), the mediated growth has been explained via dimer exchange mechanism (Tromp and Reuter 1992). Further the Ge nanodots

found to have a regular "hat" structure of four sided pyramids having equivalent facets of {105} (Mo, et al. 1990). Likewise, $Si_{1-x}Ge_x$ nanodots grown on Si (0 0 1) surface resemble a pre-pyramidal structure but with incremental size change to a pyramidal structure (Rastelli, et al. 2003). InAs nanodots on the GaAs substrate which is strongly coupled to the InAs coverage, is another semiconductor nanodot system that has been identified (Leonard, Pond and Petroff 1994). In addition, metal nanodot/island growth has also been observed. For example, Co nanodots that can grow into wires on patterned Ru (0 0 1 1), as well as Fe nanodots/islands growth on flat Ru (0 0 $\bar{1}$ $\bar{1}$) (Cheng, et al. 2004). In certain cases, systems of metallic nanodots are grown on insulating surfaces: Fe (1 1 0) nanodots on Al_2O_3(1 1 $\bar{2}$ 0)/Mo(1 1 0) (Jubert, Fruchart and Meyer 2001).

In the case of self-assembly of nanowires, there also has been keen interest on various quasi-one-dimensional systems. Ag nanowires on Si (0 0 1) substrate are one of the first few systems studied (Tersoff and Tromp 1993). $DySi_x$ and $HoSi_x$ nanowires grown on Si (0 0 1) substrate (Nogami, et al. 2001) and $ErSi_x$ nanowires on Si (0 0 1) (Chen, et al. 2000) are rare-earth silicide nanowire systems. NiSi nanowires were grown on SiO_2 buffer layer supported by Si substrate (Kim, et al. 2005). There are also cases of semiconductor nanowires: Ge nanowires on Si (1 1 3) substrate, which is also a semiconductor (Sumitomo, Omi, et al. 2003). Interestingly oxidation of Cu (0 0 1) has also shown to reflect hetero - epitaxy and growth of CuO_2 quasi-one-dimensional nanowires on Cu (0 0 1) has been observed (Zhou and Yang 2002).

This chapter focuses on the Ag thin film and nanowire growth dynamics on a clean Cu(1 1 0) substrate. Previous studies by our group on Ag/Cu(1 1 0) system has shown several phases (Zhao 2005) of Ag on the substrate. Initial deposition at ~100°C is an epitaxial pseudo hexagonal Ag(1 1 1) layer up to coverage of ~1.2 substrate monolayers (ML) on Cu(1 1 0). Beyond this

saturation, Ag will give rise to self-assembled, uniformly spaced, yet randomly distributed, quasi-one-dimensional nanowires having prismatic or trapezoid cross section. They are aligned to Cu [1 $\bar{1}$ 0] direction and perpendicular to Cu [0 0 1]. Substrate mediated strain fields due to the asymmetry of the Cu(1 1 0) surface and lattice mismatch between Ag and Cu dictates the 1-D growth structure. The ensuing Ag(1 1 0) nanowires have common high symmetry directions [1 $\bar{1}$ 0] and [0 0 1] with the underlying Cu(1 1 0) lattice. Ag nanowire width along the [0 0 1] direction is limited to 100 - 300Å while the length extends to microns and has no discernible limit. Aspect ratios were seen beyond 20:1. Nanowire height ranges 5 - 20ML (~23Å) with respect to Ag(1 1 1) over layer. The overall angle between faceted faces of the Ag nanowires and the surface plane is ~25° as seen on Figure 3.1. As shown in the STM image, the nanowires grow continuously across steps and terraces of the Cu surface while maintaining a coherent structure and a uniform alignment. In the previous study (Zhao 2005), it was observed the nanowires have a narrow distribution of widths taken together with their high aspect ratios as indications of lattice across the nanowires being heavily strained in the [0 0 1] direction. This strain hinders the growth of the structures in [0 0 1] direction.

A pictorial representation of feasible strain fields and growth pattern is shown in the Figure 3.1. The strain field generated by the pseudomorphic collection of atoms in the [0 0 1] direction gives rise to a uniaxial strain energy which extends beyond the interface to near surface region of the Cu(1 1 0) substrate resulting in an ultimate lack of coalescence in the [0 0 1] direction.

An STM image of the Ag nanowires going across a terrace steps is shown on the Figure 3.2. The dynamical growth and structure and evolution of Ag nanowires have been further

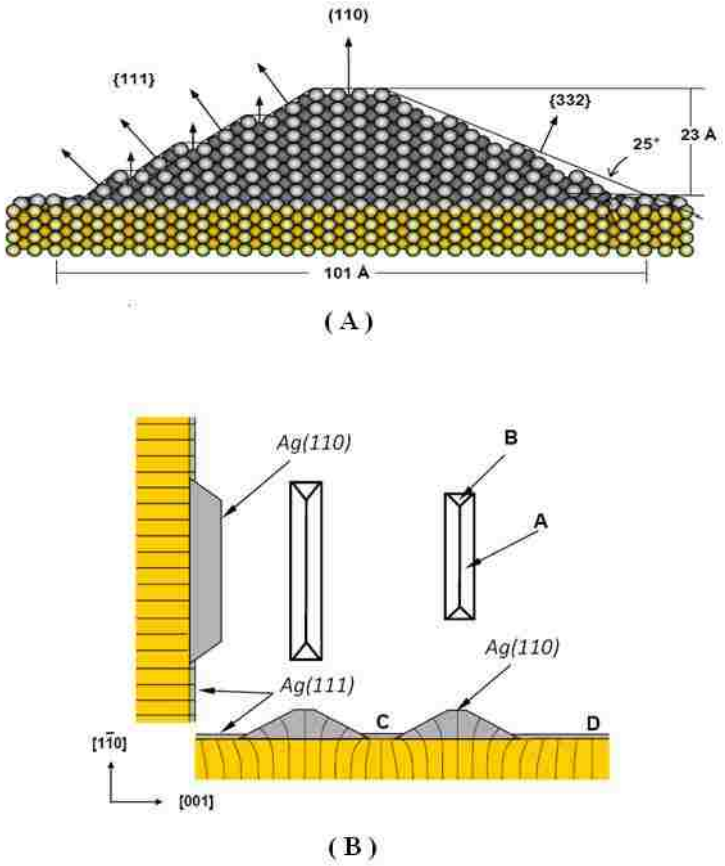

Figure 3.1 In (A) cross section of the Ag nanowire. Note: at the interface the wire and the substrate is commensurate, therefore strained. The strain is relaxed upwards. Facets are shown with the net angle (right side) and atomistic view of the flat and angled sections making the side (left side). (B) Lines show possible strain fields on the interface going both ways in to the substrate and the wire. A, and B are facets of the nanowire and C, and D are Ag (1 1 1) layer (Zhao 2005).

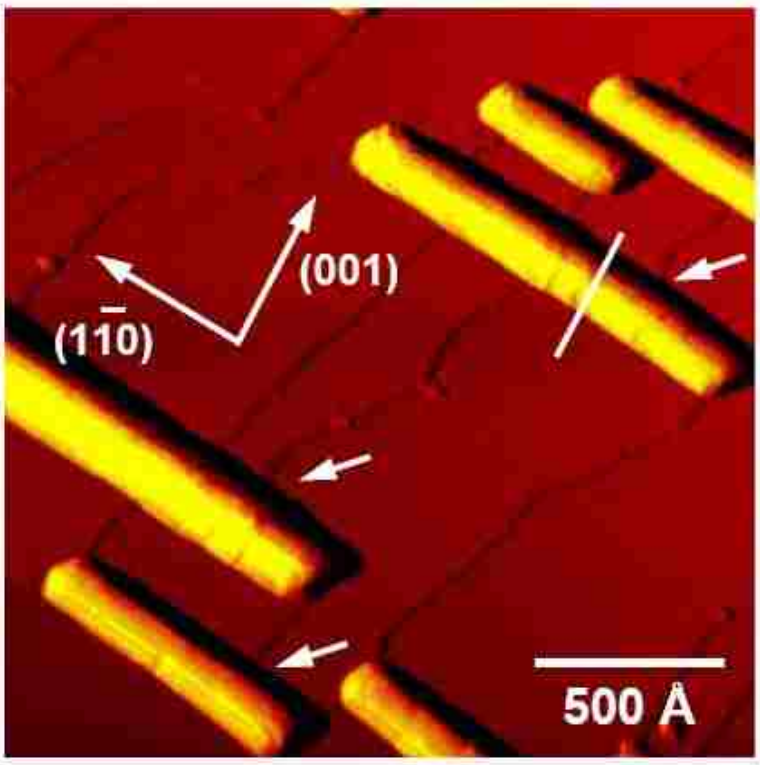

Figure 3.2 STM images of Ag nanowires growth across the terraces on Cu(1 1 0) surface while keeping the coherence (Zhao 2005).

probed in this study. We will show the sudden change in the surface reflectivity of electrons will signal the saturation of the Ag (1 1 1) layer at 1.2ML coverage.

We will also show that the growth of the nanowires is highly dependent on the surface diffusion of Ag atoms on the Ag (1 1 1) layer and, finally will give a model of the growth dynamics of the system. We will extend beyond the earlier study by revealing details of the thermodynamically stable, high temperature phase of giant micron sized Ag clusters.

3.2 Experimental Procedure

Experiments were carried out in the ELMITEC - LEEM (Low Energy Electron Microscope) III in Dr. Gary Kellogg's Surface Imaging Lab, Sandia National Laboratory, New Mexico. Device is completely setup within an inter-connected UHV chamber which achieves a base pressure of $P < 2 \times 10^{-10}$ Torr. Sample holder has W5%Re and W26%Re thermo couples to read sample temperature. The system is connected to 3 ion getter pumps, single turbo-molecular pump, oil-free foreline pump, two Ti-sublimation pumps. Sample preparation chamber is separated by an airlock and connected via a 24-inch magnetic transfer system which is used to transfer the sample from load lock to preparation chamber and then to LEEM chamber. Sample is transferred to the sputter holder to be sputter cleaned by the ion gun (Gun and Controller – *Perkin Elmer*). This holder is equipped with a filament with the possibility of applying a high voltage enabling *e beam* heating while sputtering (therefore it is possible to sputter at considerably high temperatures).

Real time sample temperature was measured by a pyrometer while sputtering and annealing. Sputtering is by ultra clean continuous flow Ne gas. In PEEM mode and by LEEM itself it was possible to observe the surface cleanliness (impurity centers exhibit different contrast); therefore, AES was used sparingly to establish the surface integrity. In the instances of cathode arcing through the sample, extensive sputtering was carried out followed by establishing

surface integrity). In the beginning of each experiment, sample cleaning cycle consist of sputter at 1.5kV for 30 min at sample temperature 300°C - 400°C followed by another sputter cycle at 1.5kV for 30 min at sample temperature 700°C - 800°C. The Ne pressure while sputtering is 5×10^{-10} Torr. Preparation of the samples required high temperature (700°C -800°C) 30 min sputter cycles in order to increase across lengths of the terraces and improve the flatness of the Cu(1 1 0) substrate surface. An Ag thermal evaporator was attached to the LEEM chamber, where evaporated Ag beam focused in line to the sample surface. This enabled the deposition of Ag on Cu(1 1 0) *in situ* while running the LEEM. Ag evaporator had a uniform flux. While on the LEEM, it was possible to e beam heat the samples and the temperature was measured by the attached thermocouples. Initial investigation of the sample was always done by the PEEM. Growth of Ag nanowires was achieved by keeping the sample at elevated temperatures (25°C-200°C) while depositing Ag. Formation and transformation of the nanowires were dynamically recorded. In certain instances, the LEED pattern was also taken. Various fields of views (FOV) were used in the observation depending on the requirement. All the data was collected at either room temperature (RT) or in elevated temperatures (27°C < T < 500°C).

3.3 Data and Observations

3.3.1 Preliminary Features

Cu is an FCC (Face Centered Cubic) (space group: fm3m) crystal and has a lattice constant of 3.615Å (Emsley 1998) compared with Ag, which is also a FCC structure with a lattice constant of 4.086Å. It is immediately clear there is a lattice mismatch of 11.54%. The difference in the lattice parameters is mirrored by the island formation in A growth on Cu(1 1 0) after the first layer; further, the first layer not being anisotropic continuation of the Cu(1 1 0) substrate surface but a (1 1 1) Ag layer. This also indicates that the initial Ag(1 1 1) layer is

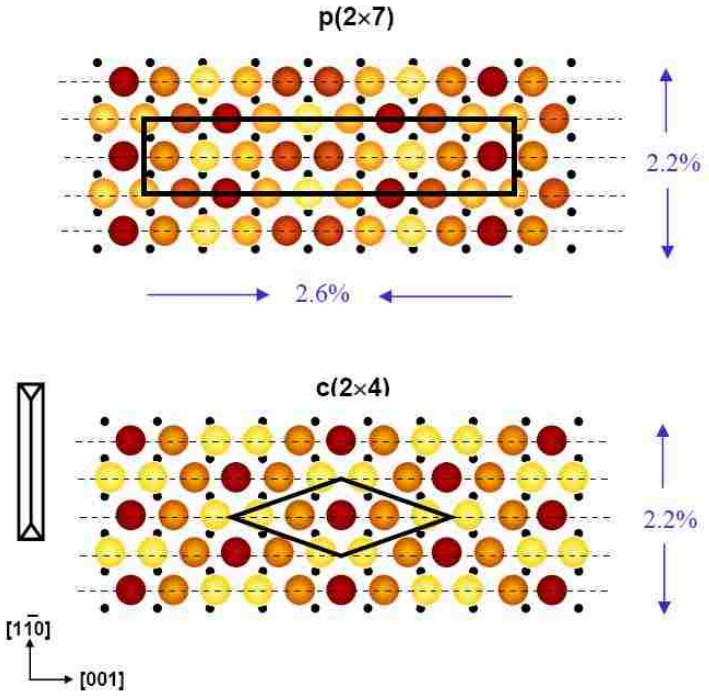

Figure 3.3 Atomic ball model of the Ag(1 1 1) overlayer. Structure is a c(2×4) with a modulation of p(7×2). The dark red is the lowest lying, light yellow highest lying Ag atoms with the small dots being the Cu substrate atoms (Zhao 2005).

energetically more favorable than a coherent Ag(1 1 0) layer on the Cu(1 1 0) substrate surface. Initial Ag(1 1 1) hexagonal layer is buckled *i.e.* pseudo hexagonal; this is seen in Figure 3.3. It has a c(2×4) structure with a modulation of p(7×2).

The primitive modulation domain is compressed by 2.6% in [0 0 1] and expanded by 2.2% in [1 $\bar{1}$ 0] to lattice match to the Cu(1 1 0) surface (Zhao 2005). Since the expansion and compression is nearly equivalent, net strain in the modulation is zero. This is not the case in the c(2×4) structure has 2.2% strain due which to lattice matching expansion in [1 $\bar{1}$ 0] direction. The expansion enables (1 1 1) layer to cover completely the (1 1 0) surface but in expense of a strain field. The strain introduced on the surface builds up, eventually giving rise to Ag nanowire growth process in Stranski-Krastanov (SK) *i.e.* islands initiated by layer mode. The c(2×4) structure with the p(2×7) modulation is also a hexagonal structure with a different periodicity.

It generates a shape of an elongated (in [0 0 1] direction) hexagon. This shape is important in surface diffusion considerations of surface atoms. By observing the nearest neighbour distance in [1 $\bar{1}$ 0] in Figure 3.4 on the Cu(1 1 0): 2.556Å and comparing with pseudo hexagonal Ag(1 1 1) layer, the distance between the rows going in the [1 $\bar{1}$ 0] direction on the hexagon is: 2.519Å which is remarkably small. As seen in Figure 3.2, the lowest-lying (dark red in color/darkest in monochrome) Ag atoms are on the [1 $\bar{1}$ 0] troughs and, as can be seen, the steric hindrance is minimum in the [1 $\bar{1}$ 0] direction whereas in the [0 0 1] direction higher hindrance is evident.

Therefore, it is possible to hypothesize that the Ag(1 1 1) layer is free to move in the [0 0 1] direction and is free floating but locked in the [1 $\bar{1}$ 0] direction. The near free floating Ag(1 1 1) layer has been observed and studied in Ag on Cu(1 0 0) . This is observed by the substrate interaction with delocalized 5s Ag states and 4d Ag states showing only 2D dispersion

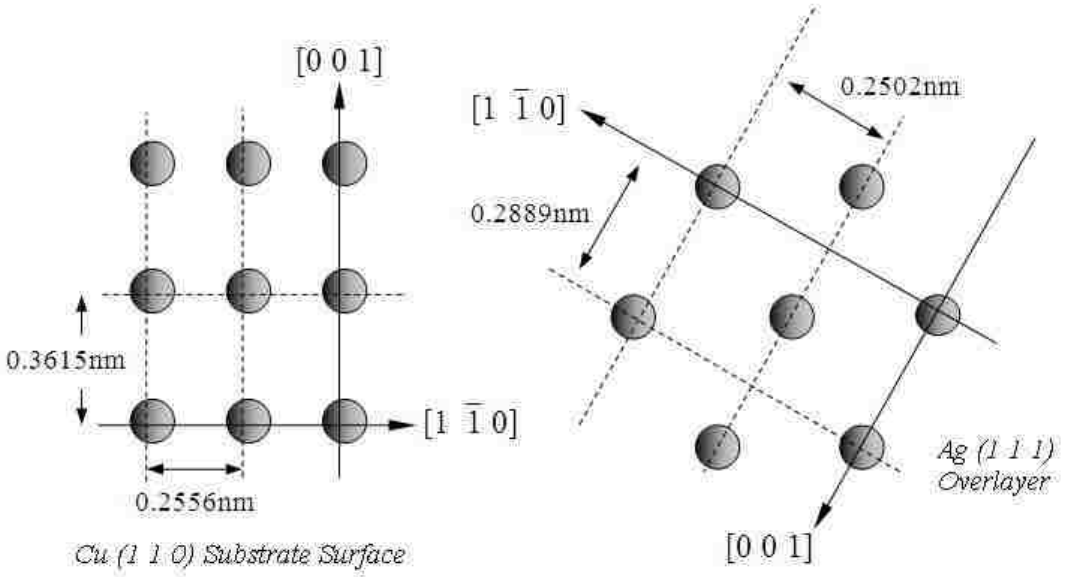

Figure 3.4 Atomic ball model of the separate surface over layer: Ag(1 1 1) and the substrate surface: Cu(1 1 0).

(Tobin, Robey and Shirley 1986) (Tobin, Robey and Klebanoff, et al. 1987). This is especially important considering in the Ag on Cu(0 0 1) system where there exists a pseudo stable alloying phase which de alloys beyond 0.13ML of Ag coverage (Sprunger, Laegsgaard and Besenbacher 1996), indicating improved interactions between Ag and Cu(0 0 1) substrate surface. This is because in Ag on Cu(1 1 0) there is no indication of alloying, implying on Cu(1 1 0) surface, substrate Ag interaction are weaker than in the case of Ag on Cu(0 0 1) surface. This has major implication on the anisotropic diffusion rates of Ag atoms on the surface. The proceeding sections are divided depending on Ag coverage on the substrate. It is possible to observe three distinct phases in Ag growth on LEEM. Staring with *observations in the initial stage*: the low coverage at 0ML < θ < ~1.2ML where the Ag(1 1 1) layer saturates to the maximum followed by *observations in the intermediate stage* with the coverage ranging ~1.2ML < θ < ~25ML where the nanowire growth predominates and finally *observations in the final stage* where heating the system to ~400°C while cutting of the Ag flux resulting in the formation of Ag micro clusters on the Cu(1 1 0) surface.

3.3.2 Observations in the Initial Stage

Clean Cu(1 1 0) substrate is heated to ~100°C to ~120°C prior to the deposition. Once the substrate temperature was stable and Ag evaporation was initiated, the LEEM data recording was started *in situ*. Terraces on the Cu(1 1 0) substrate with increasing overlayer coverage of the Ag(1 1 1) were clearly seen as flat circular areas (Figure 3.6). Ag deposition temperature was kept at ~105°C while LEEM objective at 1.617kV and start voltage at 1.5V. Widths of the terraces range from Angstrom scales to 2.5μm. This is specifically due to the repeated high temperature sputtering and annealing treatment on the surface. The step edge flow with random wobble was observed at the recorded temperature of ~107°C. Although the wobble is random in

direction, the net flow was along the [1 $\bar{1}$ 0] (Y axis as seen on the Figure 3.6) at rate of 0.2μm/s perpendicular motion (X axis) rates 0.1μm/s to 0.4μm/s. Change in coordinates with time for the step bunching point at P in Figure 3.6, is recorded on Table 3.1, where clear net displacement (0.09μm) was recorded along [1 $\bar{1}$ 0] direction while random displacements along the perpendicular [0 0 1] were recorded.

Similar behaviors of surface flow were observed in other instances of observing the *initial stage* of the Ag deposition on Cu(1 1 0). Step shapes (curvature of the oval shapes) changed little but observed changes were random. General shapes of the terraces of Ag(1 1 1) do not change observed initial moments. This is evident in Figure 3.6. The five slides (A - E) of the LEEM images were taken in 0.233s intervals. As seen in Figure 3.6, the shape of the major step edge stays constant, certain sub steps in the middle of the main step edge gradually loose and gain definition.

The Ag deposition rate was at constant about 1ML/s. The field of view (FOV) was 5μm for these images. Taken together, images span deposition duration of almost one second in time length. Similar observations were obtained for other instances as well. Although in some cases the terrace widths were not as large as in Figure 3.6 which were typical for cleaner surfaces and which went through sputter/anneal cycles multiple times.

Steps were always oval on the substrate plane. Apart from observed random step flow, some surface corrugations were starting normal to the edge of the terraces. Step edges show slight random shape variations in the initial observations but, do not show major disparities on the surface until the Ag coverage reach ~1ML. A second set of data (Figure 3.09) was analyzed to observe the comparability of the data and clustered growth of neighboring nanowires compared to relatively uncluttered nanowires (Data set 01).

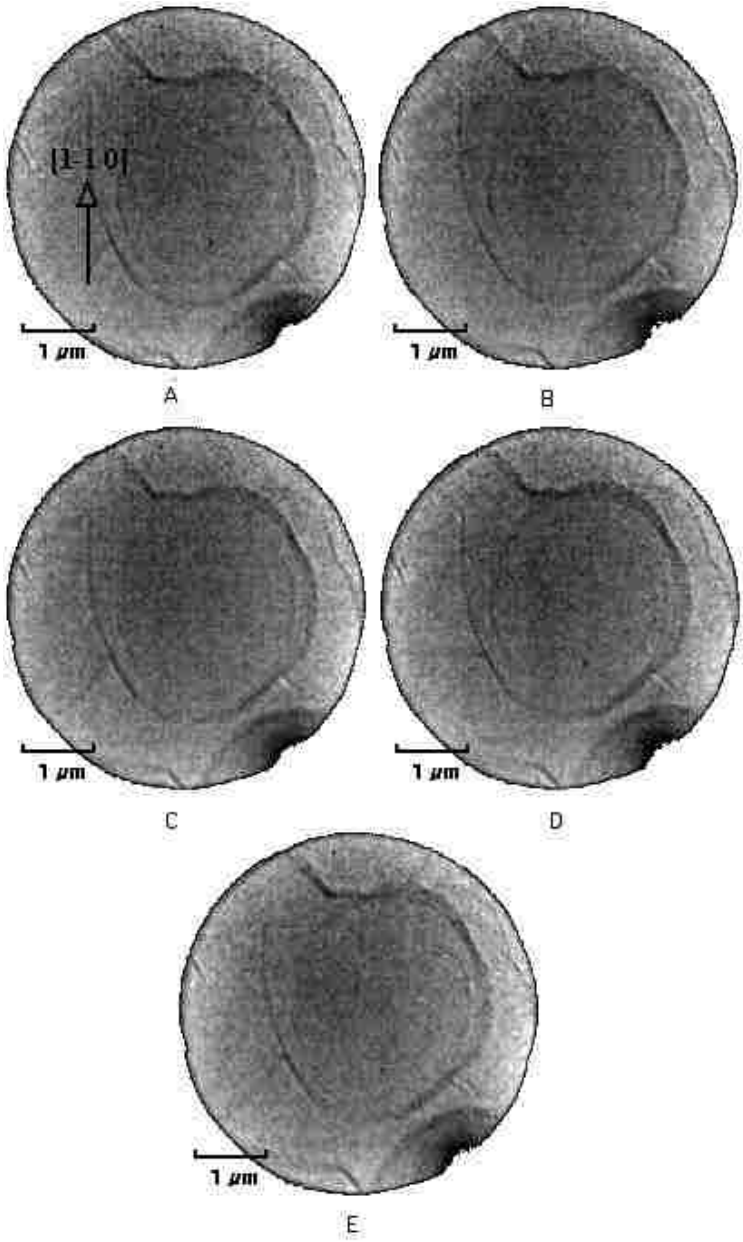

Figure 3.5 LEEM images of gradual saturation of Ag(1 1 1) over layer on the substrate. The terraces can be seen on images.

Table 3.1 Change in coordinates of the step-bunching point P with time.

Time (s)	X (μm)	Y (μm)
0.000	2.12	4.02
0.233	2.14	4.02
0.466	2.15	4.03
0.699	2.19	4.09
0.932	2.15	4.11

Starting at ~1ML, the changes on the surface become apparent. At Ag(1 1 1) saturation (coverage at 1.2ML) on the Cu(1 1 0) substrate and just before the formation of Ag nanowires the surface looses definition drastically. The step edges and terraces almost disappear. The process is illustrated in the sequence of LEEM slides taken in the Figure 3.7. Images were taken at 119°C constant temperature with a FOV 8μm with the objective at 1.622kV. The *in situ* Ag deposition rate is 0.54ML/s. Total time length observed is ~0.9s. The sequence progress is from top to bottom and left to right. One other important observation is the increase in the intensity of the image as the coverage growth initiates at 1.2ML, the increase.

This is observed in all sets of data obtained. As previously mentioned, incremental surface coverage variations were observed up to the initiation of the nanowire growth. First nanowires appeared just after the bottom most image in Figure 3.6.

First two images were taken at 0.867s (Ag coverage 0.73ML) and 0.533s (Ag coverage 0.91ML) respectively and no observable change in the resolution was detected. But beyond this point major changes in the resolution and definition of the surface corrugation and morphology were detected. Therefore it is clear the resolution deteriorates beyond 1ML coverage, about 0.2s before the saturation (coverage becomes 1.2ML and t = 0) of the Ag(1 1 1). Afterwards, surface contrast gets monotonically worse and eventually no surface corrugation: steps and terraces are visible (at 1.2ML and t = 0). The change has a small time constant (0.2s) and occurs within a Ag coverage variation of 0.2ML. Following the initial growth of the Ag nanowires, (in the next

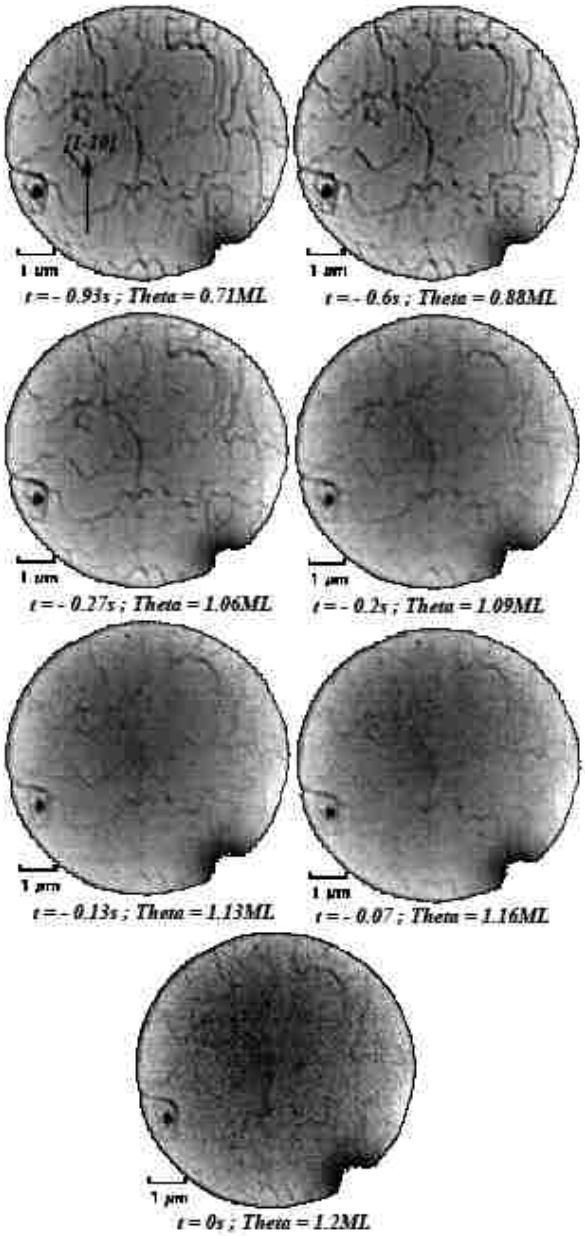

Figure 3.6 Incremental saturation of the Ag(1 1 1) layer with time. Top to bottom and left to right gives the positive time evolution and increasing coverage up to saturation.

section) it is observed the surface contrast improves again, yet does not recover fully.

3.3.3 Observations in the Intermediate Stage

As explained before, the nanowires grow parallel to the [1 $\bar{1}$ 0] direction. At this point, the surface is already covered with Ag at $\theta \approx 1.2$ML and the nanowire formation initiates. The substrate temperature is set to 100°C - 130°C and kept constant throughout this stage. Observations from the Ag coverage of ≈ 1.2ML on substrate, until there is considerable Ag coverage and onset of annealing at high temperature, are included here. The surface resolution loss occurs after the saturation of the Ag layer does not completely recover in higher coverage. Initial growth is shown in Figure 3.8. FOV is 8μm and sample temperature is steady at 119°C (393K). The LEEM objective was kept at 1.6kV.

Time separation between two images in the sequence is 0.0333s. Ag flux on the surface is stable at 0.53ML/s. Observed nucleation centers do not show island/cluster growth right from the beginning. Therefore initial formation of Ag nucleation centers on the Ag (1 1 1)/Cu gives the critical size to grow linearly in [1 $\bar{1}$ 0] direction. Generally uniform formation of nucleation centers was observed on the surface, with some clustering. This clustering has a ringed pattern. In some cases, bunching of nanowires in close proximity was observed. Yet the growth has no preferred areas where the nanowire growth occurs. Both nucleation and linear growth continue with deposition of Ag. For the Figure 3.8 variation of Ag nanowire number density with varying time and coverage is shown above on the table. As stated earlier, the temperature was kept constant at 119°C (393K). The contrast between the nanowires and the Ag(1 1 1) layer is different and this changes in certain cases as the deposition progresses. Typically (in this case 0.53ML), the deposition rate is kept a constant. It is observed that, when the objective potential of the LEEM is changed, resolution of the nanowires changes.

Table 3.2 Initial nucleation number density variation with time and coverage.

Number of Nanowires	Time (s)	Number of New Nucleations	Rate of Nucleation (/s)	~ Coverage (ML)
0	0	0	0	1.20
29	0.0333	29	870.87	1.22
42	0.0666	13	390.39	1.24
51	0.0999	9	270.27	1.25
59	0.1332	8	240.24	1.27
64	0.1665	5	150.15	1.29
70	0.1998	6	180.18	1.31
72	0.2331	2	60.06	1.32
75	0.2664	3	90.09	1.34
80	0.2997	5	150.15	1.36
82	0.333	2	60.06	1.38

In order to see the relationship with the terraces/pining centers and the nucleation; overlap between the surface LEEM image at 0.88ML coverage and images at coverage of 1.2ML, 1.35ML, 2.17ML and 2.96ML were taken. The combined sequence of images is shown in Figure 3.9. They clearly show at nucleation centers are closely associated with the step edges. Although the nanowires can grow across the steps as time progresses with the sequence of images, initiating positions are in the close vicinity of the step edges.

Other pinning centers are of importance too as the impurity point on the surface at the bottom left (A) gives rise to numerous nanowires. With evolving time, the cluster of nanowires associated with the impurity center is elongating but with slower rate. This is seen through the sequence of slides. This phenomenon of low rate of growth is seen also in step bunching/small terrace in points B and C, where again the number of associated nanowires are high with respect to the surroundings and consequently the growth rate is low.

Contrastingly wide terraces are associated with few wires (nucleation centers) and the rate of growth is higher as seen by the elongation of the wires. This is clearly observed in the middle of the images. With the overlap of underlying terrace structure, the ringed patterns of the

nanowires are clearly seen. In order to get a better understanding of the growth of the wires, anabasis of nanowires studied with a sequence of images starting at coverage of 1.39ML to 3.49ML.

Substrate temperature kept at 121°C (394K), a constant throughout the sequence of images. The start voltage is kept at 9.57V and LEEM objective was kept at 1.632kV. In the Figure 3.08 length variation of 21 nanowires was measured and tabulated (Table 3.3). In each instance the Ag coverage was also recorded. Deposition rate was at 0.53ML/s. FOV of the images are 8µm. The corresponding measurements were started at 1.39ML and continued until the coverage is at 3.51ML. At medium coverage as shown, do not obscure the loop structure of the nanowire growth.

This can be seen in the progression of the loop L in Figure 3.08. With time, the nanowires elongate thus gradually come to the middle of the terrace but initial nucleation pin the wire to a fixed position. Therefore the loop stays intact over time.

These looped formations can be seen over the entire FOV. On the figure, nanowires are oriented along [1 $\bar{1}$ 0] direction as expected. The time separation between two images extended to a separation of ~1.7s. The FOV for the images is 3µm and the start voltage kept at 9.98V. LEEM objective fixed at 1.634kV. The Cu substrate temperature kept a constant at 121°C (394K). In the series of images it is seen middle part of the certain nanowires give rise to nucleation centers for other nanowires. Each cluster assigned a number and the letters assigned for constituent nanowires of the cluster. Ag deposition rate is at 0.18ML/s fixed. Bunching of the nanowires is easily observable due to the low FOV.

Yet due to the resolution limit of the LEEM the walls between the wires which are extremely close seems to merge and the boundaries between wires are blurred. Table 3.4 gives the set of data which were obtained from Figure 3.09 and used for the analysis.

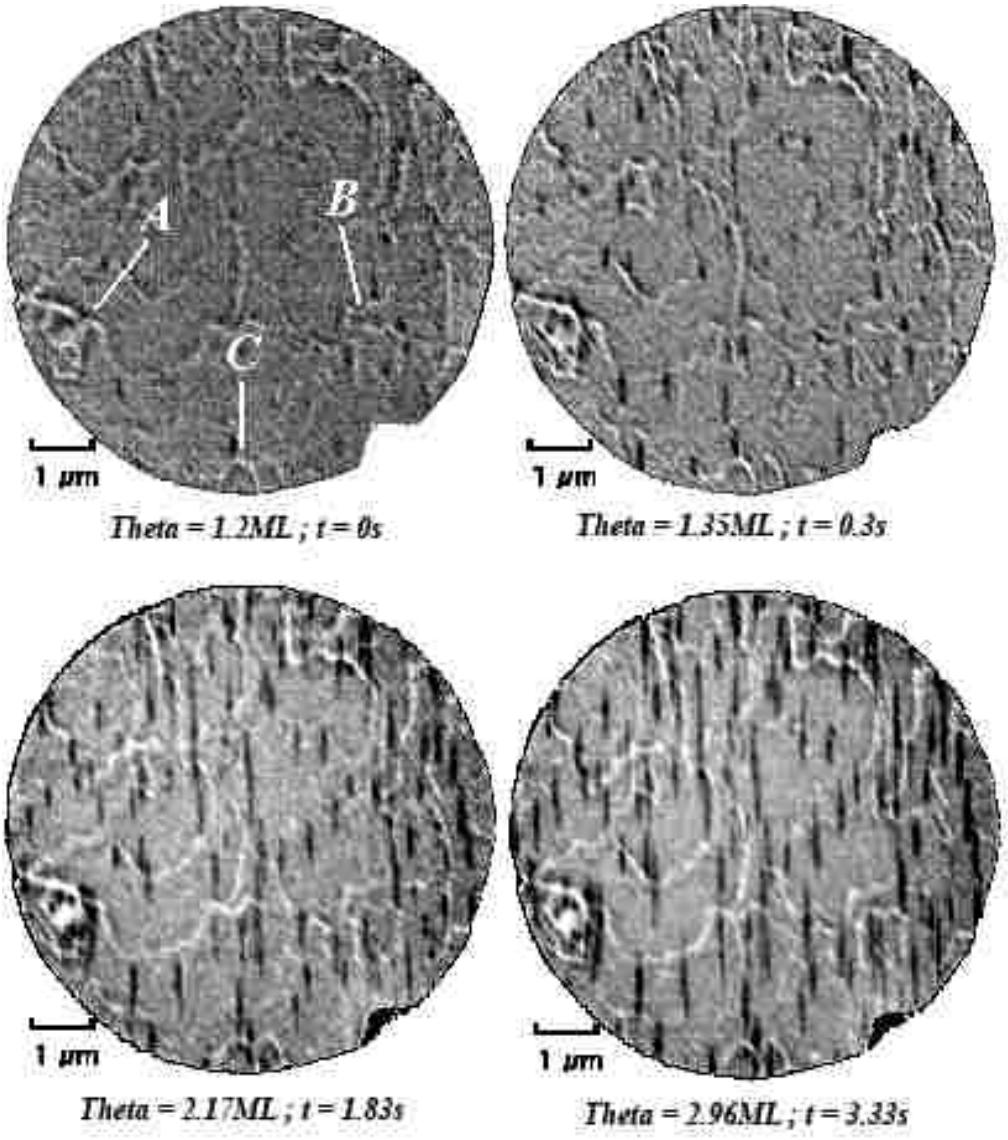

Figure 3.7 Overlap of images at pre-nanowire coverage of 0.88ML and post- nanowire coverage of 1.2ML, 1.35ML, 2.17ML and 2.96ML. Overlap results in the step structure of the bare surface with that of the surface with nanowires, which is otherwise unseen.

Table 3.3 Data Set 01 nanowire length variation with time. Ag coverage is also included at the bottom row.

Time (s)	***2.56***	***3.04***	***3.52***	***4.00***	***4.48***	***4.96***	***5.44***	***5.92***	***6.40***
1(μm)	0.34	0.64	0.64	0.56	0.66	0.64	0.71	0.69	0.81
2(μm)	0.32	0.52	0.58	0.56	0.63	0.66	0.66	0.74	0.84
3(μm)	0.03	0.03	0.19	0.22	0.30	0.32	0.57	0.68	0.79
4(μm)	0.32	0.44	0.42	0.44	0.57	0.74	0.79	0.90	0.84
5(μm)	0.51	0.54	0.54	0.51	0.57	0.63	0.64	0.78	0.91
6(μm)	0.17	0.34	0.22	0.34	0.42	0.57	0.91	0.93	0.98
7(μm)	0.23	0.35	0.39	0.54	0.71	0.74	0.76	0.90	0.98
8(μm)	0.17	0.42	0.46	0.49	0.56	0.64	0.68	0.69	0.86
9(μm)	0.20	0.36	0.42	0.37	0.39	0.59	0.90	0.93	1.08
10(μm)	0.05	0.27	0.29	0.59	0.78	0.89	0.86	1.11	1.20
11(μm)	0.49	0.57	0.47	0.56	0.56	0.63	0.93	0.95	1.18
12(μm)	0.22	0.37	0.56	0.57	0.69	0.79	0.79	0.88	0.91
13(μm)	0.36	0.46	0.49	0.51	0.54	0.56	0.66	0.68	0.73
14(μm)	0.10	0.32	0.35	0.51	0.49	0.59	0.74	0.83	0.86
15(μm)	0.37	0.57	0.54	0.59	0.83	0.98	1.25	1.40	1.43
16(μm)	0.20	0.22	0.46	0.54	1.03	1.38	1.50	1.62	1.69
17(μm)	0.42	0.51	0.49	0.59	0.61	0.74	0.79	0.83	0.91
18(μm)	0.10	0.19	0.56	0.66	0.63	0.84	1.00	0.98	1.05
19(μm)	0.54	0.61	0.63	0.81	0.83	1.03	1.37	1.55	1.44
20(μm)	0.49	0.68	0.62	0.81	0.96	1.08	1.13	1.18	1.27
21(μm)	0.08	0.37	0.37	0.54	0.47	0.66	0.64	0.80	0.73
Theta(ML)	***1.39***	***1.65***	***1.92***	***2.18***	***2.45***	***2.71***	***2.98***	***3.24***	***3.51***

In order to further analyze the separation between nanowire edges with time progression, edge coordinates were recorded for nanowires on Figure 3.09. From here on the nanowire edges are referred to as edge points. Due to the asymmetry of the distribution of edge points on a LEEM image, (on the circular image the circumference is an artificially introduced discontinuity to the surface distribution of the nanowires) displacement values to other edge points are distributed asymmetrically (inside the circle you have edge points, while outside contains none).

Continuous generation of nanowires increased the number of data points with time. *Appendix 01* includes the set of data retrieved from nanowires depicted in Figure 3.09.

Associated IGOR procedures are attached with the *Appendix 02*. Details of the code and a description of the algorithm follow.

3.3.4 Observations in the Final Stage

In this stage the after having considerable number of nanowires on the surface the substrate temperature was increased from to 100°C ~ 130°C to a temperature in the range of 350°C ~ 450°C. Prior to the temperature increase, Ag flux was stopped. Therefore no deposition occurred during the annealing period. A qualitative picture of decay of nanowires is seen in Figure 3.10, where time evolution of four groups of nanowires: **P**, **Q**, **R** and **S** are observed. FOV for the images are 5μm and start voltage of 9.87V with the objective at 1.623kV.

Time separation between the images and the respective temperature is given in Table 3.5. Due to the thermal flow, although the LEEM objective was set at a constant the groups tend to move on the surface. Groups **P**, **Q**, **R** and **R** consist of 4, 3, 2 and 6 wires respectively.

In certain cases as mentioned before the separation between adjacent nanowires is resolution limited by the LEEM. The protrusions and width variation along the nanowire indicate if there are multiple nanowires involved. On the left of the group **S** the change in width indicates the existence of a shorter wire next to the longer wire.

This is clearly seen on the slide C on the Figure 3.12. Similar features are seen in the bottom two wires in group P. Most notable feature of the onset of decay is the length reduction as indicated by along the length contraction of nanowires with increasing temperature. This is not uniform to all the wires. In a group of wires smaller wires tend to contract in length with a higher rate while long wires initially seems to stay constant against increasing temperature. Variation of length in wires in the initial stages show interesting features. On the groups **S** and **R**, as the temperature increased, the loss of length for adjacent but separate nanowires is different.

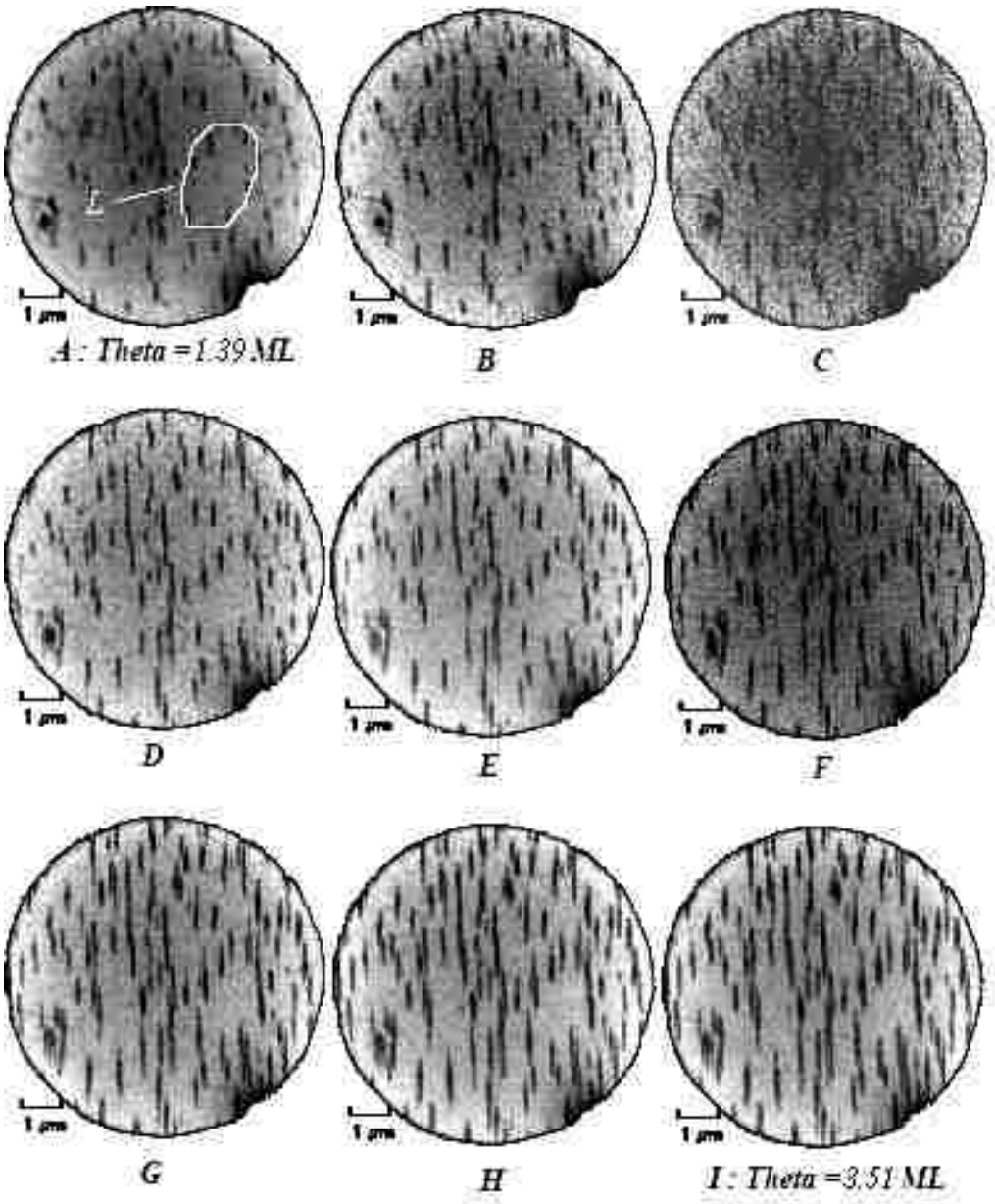

Figure 3.8 Time progression of the nanowire growth, in intermediate coverage. FOV is 8μm. The loop formations of nanowires are seen over the surface. An example of which is given as L.

Table 3.4 Data Set 02 nanowire length variations with time. Ag coverage is also included at the bottom for comparison Part A.

Time (s)	**7.26**	**8.94**	**10.63**	**12.31**	**13.99**	**15.68**	**17.36**	**19.04**	**20.72**
01a(µm)	0.13	0.60	0.59	0.73	0.80	0.83	0.98	1.04	1.02
01b(µm)	0.07	0.20	0.28	0.27	0.22	0.25	0.26	0.22	0.37
02a(µm)	0.44	0.52	0.54	0.49	0.54	0.60	0.53	0.56	0.73
02b(µm)	0.15	0.40	0.61	0.59	0.53	0.55	0.55	0.52	0.55
02c(µm)	0.10	0.27	0.25	0.24	0.22	0.26	0.27	0.18	0.25
03a(µm)	0.42	0.71	0.72	0.74	0.76	0.85	0.90	0.88	0.89
03b(µm)	0.09	0.24	0.58	0.78	0.83	0.86	0.84	0.80	0.84
03c(µm)	0.25	0.41	0.47	0.59	0.63	0.69	0.68	0.74	0.81
04a(µm)	0.00	0.41	0.40	0.62	0.62	0.79	0.76	0.79	0.78
04b(µm)	0.50	1.01	1.04	1.13	1.15	1.17	1.12	1.23	1.25
04c(µm)	0.00	0.17	0.18	0.39	0.40	0.42	0.65	0.75	0.83
05a(µm)	0.03	0.41	0.59	0.73	0.92	0.97	1.07	0.96	0.95
05b(µm)	0.30	0.45	0.58	0.61	0.70	0.62	0.63	0.61	0.62
05c(µm)	0.16	0.37	0.44	0.38	0.48	0.43	0.48	0.46	0.43
06a(µm)	0.20	0.28	0.28	0.31	0.38	0.32	0.31	0.44	0.48
06b(µm)	0.64	0.96	1.07	1.35	1.52	1.44	1.72	1.80	1.82
06c(µm)	0.12	0.17	0.17	0.18	0.28	0.46	0.36	0.32	0.37
07a(µm)	0.39	0.46	0.37	0.72	0.78	0.84	0.89	0.93	0.93
07b(µm)	0.11	0.94	1.55	1.71	1.67	2.03	2.01	2.21	2.33
08a(µm)	0.20	0.20	0.20	0.22	0.21	0.22	0.21	0.66	0.67
08b(µm)	0.33	0.37	0.44	0.77	0.77	0.81	0.86	0.92	0.95
09a(µm)	0.36	0.89	1.06	1.34	1.61	1.59	1.61	1.74	1.82
09b(µm)	0.08	0.08	0.12	0.24	0.29	0.36	0.41	0.42	0.42
Theta(ML)	1.29	1.60	1.90	2.21	2.51	2.82	3.12	3.43	3.74
10b(µm)	0.14	0.21	0.31	0.42	0.48	0.54	0.61	0.65	0.58
10c(µm)	0.55	0.66	0.66	0.73	0.75	0.71	0.79	0.82	0.72
10d(µm)	0.21	0.53	0.55	0.69	0.92	0.62	0.76	0.78	0.75
11a(µm)	0.20	0.43	0.59	0.46	0.56	0.52	0.71	0.81	0.84
11b(µm)	0.07	0.14	0.16	0.47	0.63	0.48	0.52	0.63	0.68
Theta(ML)	**1.29**	**1.60**	**1.90**	**2.21**	**2.51**	**2.82**	**3.12**	**3.43**	**3.74**

Some wires retain Ag atoms longer than the other wires; in doing so their decay rates are lowered. Initial decay rates are randomly set. In the **S** group**,** of the two long wires one on the right decrease its length faster as seen by the progress of the slides. Similar pattern is seen for the **R**, where left–most shorter wire lose its length rapidly compared to the right longer ones.

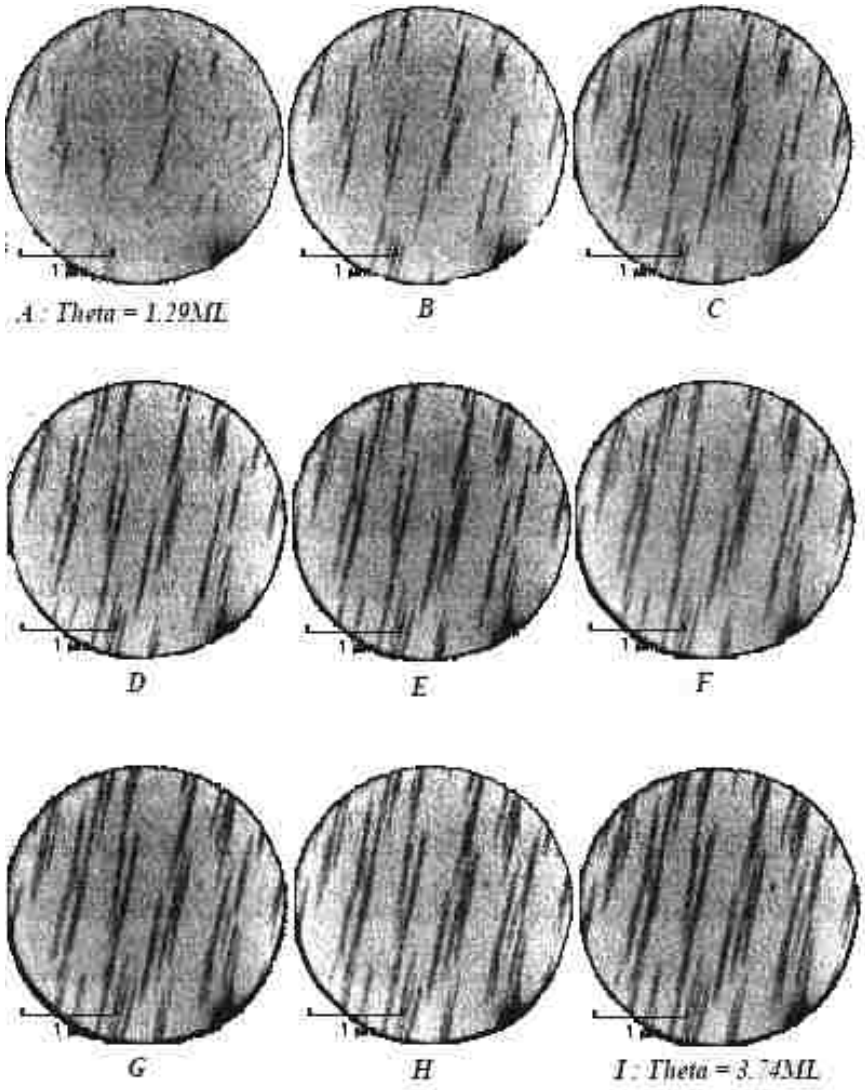

Figure 3.9 Time evolution growth of the nanowires. Nanowires are aligned in [1 -1 0] direction. FOV is 3μm.

Table 3.5 Data Set 02 nanowire length variations with time. Ag coverage is also included at the bottom for comparison Part B.

Time (s)	***0.12***	***0.28***	***0.45***	***0.42***	***0.45***	***0.58***	***0.55***	***0.62***	***0.59***
12a(µm)	0.17	0.28	0.44	0.54	0.42	0.51	0.49	0.64	0.59
12b(µm)	0.11	0.36	0.38	0.48	0.55	0.59	0.61	0.73	0.69
13a(µm)	0.05	0.46	0.61	0.92	0.95	0.97	1.04	1.03	1.11
13b(µm)	0.15	0.79	1.13	1.22	1.31	1.39	1.48	1.51	1.54
14(µm)	0.21	0.42	0.56	0.59	0.61	0.65	0.73	0.79	0.83
15(µm)	0.29	0.65	0.72	0.71	0.67	0.81	0.86	0.82	0.97
16a(µm)	0.10	0.43	0.64	0.63	0.68	0.73	0.80	0.93	0.94
16b(µm)	0.40	0.48	0.51	0.55	0.56	0.55	0.65	0.71	0.75
16c(µm)	0.23	0.40	0.41	0.47	0.47	0.64	0.57	0.59	0.69
17(µm)	0.32	0.42	0.66	0.73	0.81	0.92	0.95	1.01	1.00
18a(µm)	0.00	0.20	0.56	0.53	0.54	0.64	0.67	0.71	1.10
18b(µm)	0.11	0.44	0.54	0.74	0.76	0.83	0.85	1.08	1.02
Theta(ML)	***1.29***	***1.60***	***1.90***	***2.21***	***2.51***	***2.82***	***3.12***	***3.43***	***3.74***

It has been observed qualitatively for wire separated by separation lengths markedly less (*nanowire width >> separation*) than the width of a typical nanowire and if one/few wire/wires are longer and the other/others are shorter by comparison then the shorter wires tend to have higher decay rates than the longer wires. This is seen in the groups **R** and **S** as explained above. The separation length is important as when observing group **P** from slides **H** to **I**, the loss of length is greatest for the longer left wire compared to the shorter right wire. The separation length scale in this example is larger, therefore the condition *nanowire width >> separation* is not satisfied. Width of a nanowire increases with temperature, irrespective to position or the association to another wire. This is a general observation and the effect increases with increasing temperature. Decay process is therefore associated with clear lowering of aspect ratio. The increment is prevalent in higher temperatures as observed on the decaying nanowire groups **P**, **Q**, **R** and **S** at slides **H** to **L** showing marked increase in width. This can be thought to associate with the higher thermal scattering with the increasing temperature, hence virtual, but in close inspection we see no loss in resolution and no drop in sharpness along wire and the boundary,

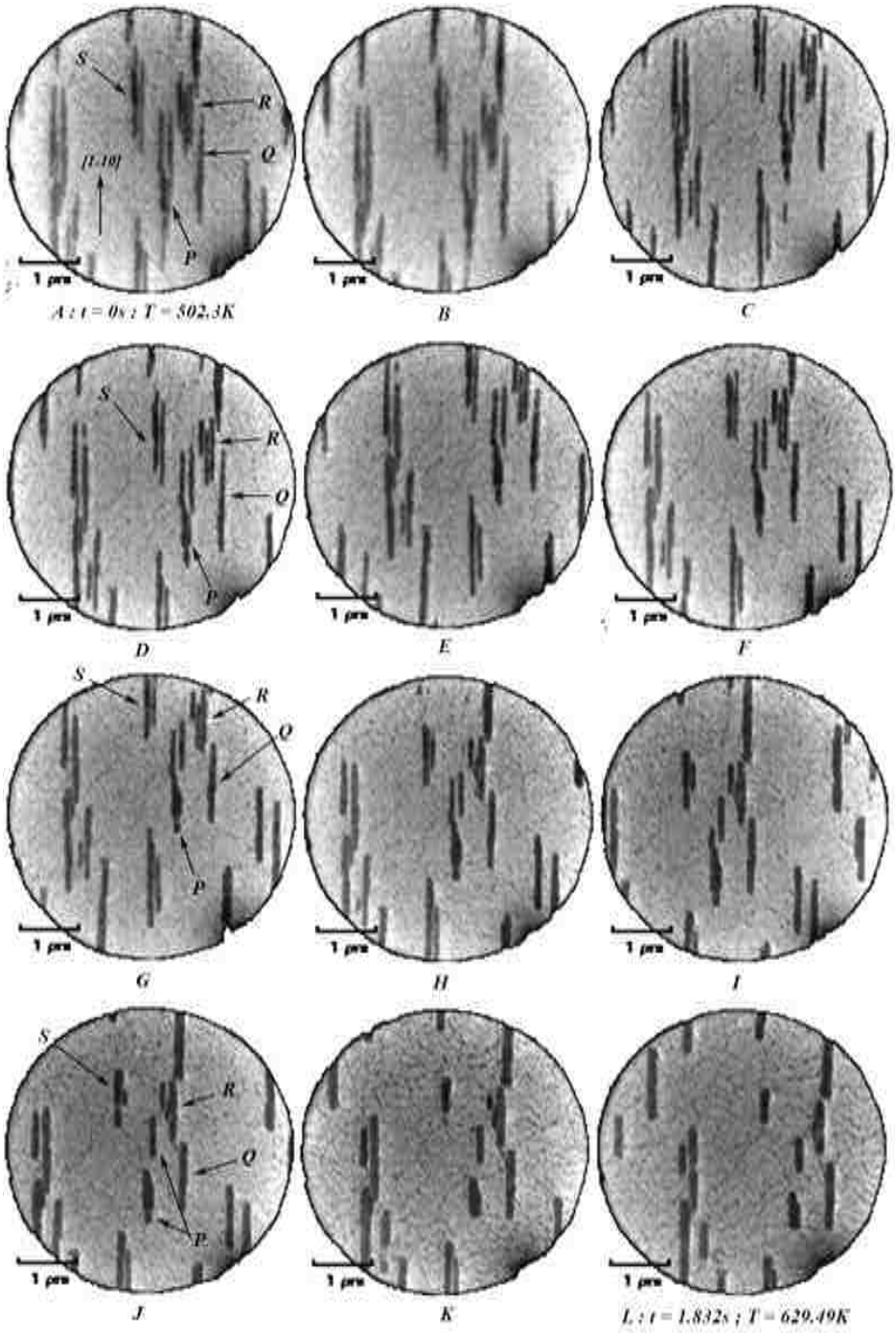

Figure 3.10 Progress of the nanowire decaying process. Each image is separated by 0.17s. Four groups (P, Q, R and S) of nanowires are examined while decaying. Scale on the images is 1μm.

revealing this in fact is real. Decay of wires also mediated in some cases by splitting along the length of the wire. This can be seen in group of nanowires at the bottom of the group **P**. The longer complete wire at the bottom side (seen on slide **C** to **B**) is fragmented at bottom forming low aspect ratio island/wire on south of the group **P**.

Table 3.6 Areas of nanowires with time and corresponding temperature.

Time/s	Temp/K	Nanowire–1 area (μm^2)	Nanowire –2 area (μm^2)	Nanowire –3 area (μm^2)
1.000	502.3	0.0765	0.0462	0.093
1.166	516.33	0.078	0.0616	0.1116
1.333	540.42	0.0564	0.0596	0.108
1.499	559.84	0.0556	0.0576	0.126
1.666	568.89	0.0816	0.0655	0.105
1.832	584.44	0.107	0.0565	0.0959
1.999	597.44	0.0945	0.042	0.1112
2.165	604.44	0.0816	0.0621	0.1197
2.332	615.37	0.0882	0.0329	0.1188
2.498	624.05	0.0882	0.0198	0.174
2.665	631.25	0.0885	0	0.1666
2.832	629.49	0.066	0	0.1526

Further on group **S** in slide **J** the bottom of the long wire fragments and the small wire already almost completely decayed as seen in slide **K** as a black spec under the long wire. Tabulated area with time for decaying nanowires is given in Table 3.5. Area is calculated for a rectangular geometry. Measuring area as a morphological change is a necessity because of the wire width varies with annealing time. Merging between the nanowires was also observed. This is typically observed at higher temperatures. Merging is distinctly different from adjacent nanowire shrinking in length and disappearing. Shrinking is seen in slide **J** for nanowire groups **S**and **R**, the small nanowire on the right side of the long nanowire on **S** group is shrinking in length and is about to get extinct, whereas in **R** the middle nanowire of the three nanowire group has merged with the long wire on the right. Consequently the width is abnormally high in the merging region. As time progress it is seen as in slide **L** the small wire almost completely merged with the long wire in group **R**. Merging is partially responsible for the increase in width

as substrate temperature is raised.

Although not shown on the sequence of images in Figure 3.12, some wires get longer with the time evolution and temperature increment they grow into ***Ag micro-clusters***, which have width scales near microns therefore no longer can be categorized as nano structures.

Table 3.7 Temperature and time variation in Figure 3.10.

Slide Letter	time (s)	Temp. (°C)	Temp. (K)
A	0.00	229.14	502.30
B	0.17	243.17	516.33
C	0.33	267.26	540.42
D	0.50	286.68	559.84
E	0.67	295.73	568.89
F	0.83	311.28	584.44
G	1.00	324.28	597.44
H	1.17	331.28	604.44
I	1.33	342.21	615.37
J	1.50	350.89	624.05
K	1.67	358.09	631.25
L	1.83	356.33	629.49

Extinction of nanowires as the temperature is increased is also measured. This process is seen in the sequence of images in Figure 3.13. FOV for the sequence of LEEM images is 20μm. Start voltage 6.92V and the objective voltage is 1.636kV, in the later stages objective was varied slightly in order to keep the surface and the nano structures focused as the temperature was increased. Focusing is hard due to the increment in the surface thermal flow with the rise in temperature. Temperature variation starts at 120°C (722K) and ends at 449°C (723K). Not all the images analyzed are shown on the figure due to space restrictions. Going through slide letter progression, **A** to **G**, going from left to right and top to bottom the number density of surface nanowires change drastically. Qualitatively the annealing process exhibits a dramatic shift in Nanowire number density reduction at 680K~700K where the reduction before and after going through this temperature range is ~70-80%. This is shown in slide **D** to **E**. Progress of the decay can be explained as gradual shrinking until the wire become a point and then disappear from

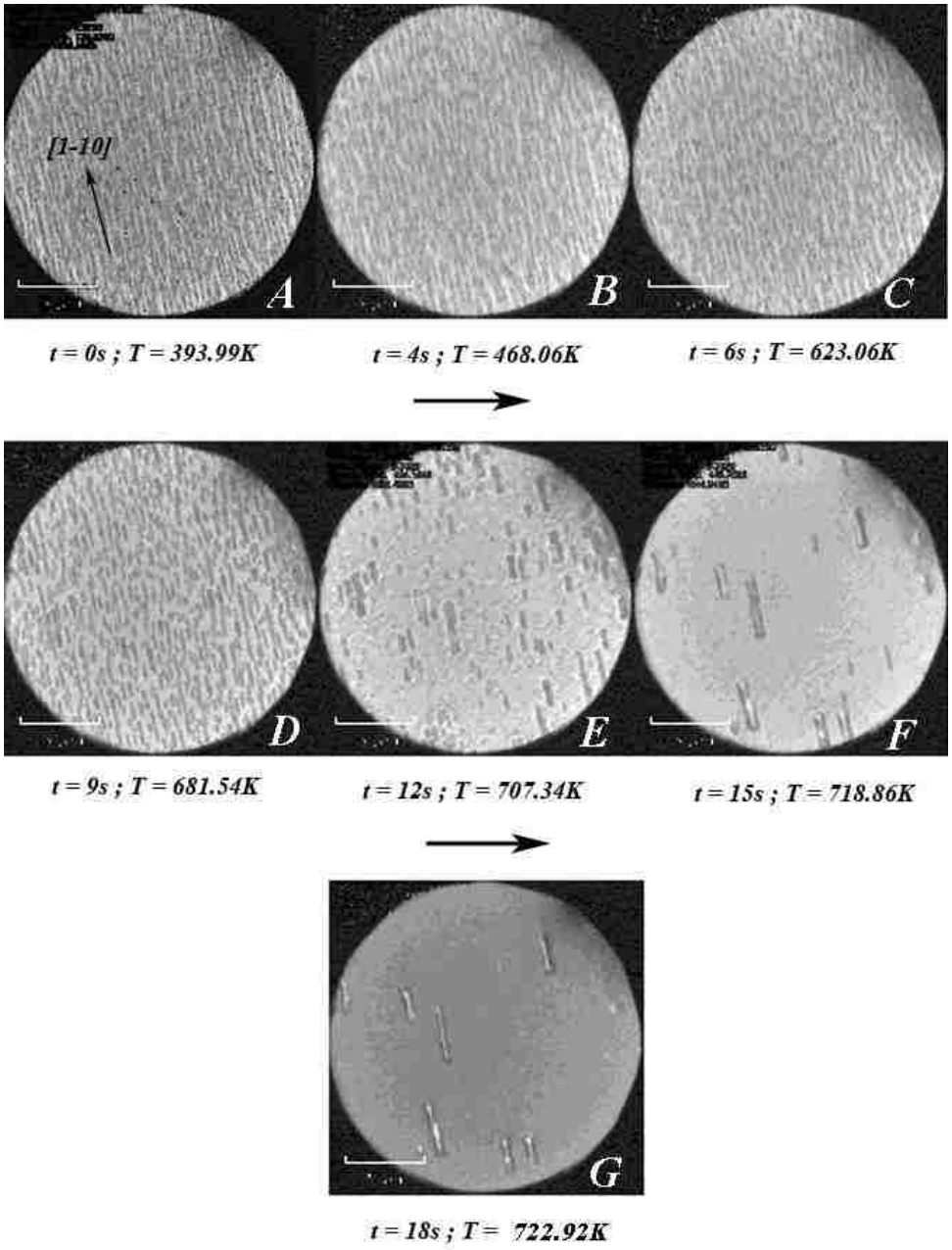

Figure 3.11 Extinction of nanowires on the surface. Left to tight and top to bottom give the progress through time and increasing temperature. FOV is 20µm.Scale on images is 5µm.

Cu(1 1 0) surface. But following sections will explain the point of extinction is left on the surface as dot and can be seen until much later times. Initial decay process associated observations were stated earlier. Now we see more *global* view of the process. Locally (*length scales << width of a nanowire*) we have seen coupling between neighboring wires but globally the extinction is random as we don't see a clear pattern or set of criteria to which wires get extinct at a given time. When selected a random area it is observed there are few wires which stays intact or very few growing while most are rapidly decaying.

At the later stages, it can be seen the formation of Ag micro-clusters initiate early in the process. A striking difference between the wires and clusters is the low aspect ratio and increased width. The difference between these two kinds of structures is seen when compared the slides **B** and **D**. I will denote these initial Ag clusters seen in slide **D**, as *pre-clusters* due to reasons that will be explained shortly. All though initial clusters do show the low aspect ratio and increased width, they are decaying. Therefore they are highly unstable against the temperature. Scarcely few will grow in to micro-clusters while most will decay. And quite interestingly a pre-cluster that grow in a particular time interval might decay in the next interval. This dynamical growth instability was observed up until the highest temperature the substrate was annealed to.

Net extinction of wires was counted by measuring the surface number density of nanowires. In the tabulated form data is shown on the Table 3.6 below. In between the clusters it is possible to observe doted structure due to the contrast variations. They are seen in slide **E** onwards in Figure 3.11. These dots have a diameter approximately equal to ~50nm to ~100nm. With continuous annealing these dots on the surface tend to disappear. Possible relationship between these dots and decaying wires was examined in the Figure 3.12. The data obtained is for rapidly decaying Ag pre-cluster system with FOV 20μm. Where start-voltage is 6.92V and LEEM objective is at 1.636kV. Time between two consecutive slides is 0.133s. Rapidly

decaying and close to extinction three (**N1**, **N2** and **N3**) Ag pre-clusters are shown in slide **A** in Figure 3.12. Observing progress of these it is possible to observe the complete extinction of these at slide **C** but as seen there remains a spot of on the surface which can be identified by the contrast difference with the surface (as seen in slide **D**). The contrast of these dots is different from those of the nanowires or pre-clusters. The dots remain long after the decay of pre-clusters. Qualitatively this is not observed for every decay process of pre-clusters. Yet this happens in the decay of substantial fraction of pre-clusters and as seen on the surface, there are numerous dots. Another important observation is the etching like process that occurs around rapidly forming micro-clusters. It is clearly seen in the formation many bigger micro-clusters, but it is seen in all microclusters, especially when they grow beyond pre-cluster limit *i.e.* when they start growing instead of decaying.

The process is counter intuitive as it seems like the surrounding of the cluster is dissolving. This region when observed dynamically is evolving and spreading out ward while the micro-cluster is growing. This region of a microcluster is also extremely active as continuous motion was observed while the corresponding Ag cluster kept on growing. These etch-like regions are shown on the Figure 3.12 and Figure 3.13.Intriguingly when the LEEM objective voltage is changed while keeping the start voltage a constant, this dotted residue-like structure and etch-like region surrounding the micro-clusters is no longer visible. This is illustrated in Figure 3.13. Therefore by changing focus contrast difference is lost making it not possible to identify it.

Micro-clusters are oriented in the [1 $\bar{1}$ 0] and the shape is that of nanowires but with widths of ~0.3μm and lengths of ~0.5μm, which makes them about 30 - 50 bigger in width scales. These clusters therefore have distinct length scales and width scales that are much larger than the nanowires initially observed. Distribution of micro-cluster width and length is given in

the Tables 3.7 and 3.8 respectively. Following micro-cluster formation surface roughness has depreciated markedly.

Table 3.8 Nanowire number density variation with temperature.

Time (s)	Temperature (°C)	Temperature (K)	Number of nanowires / square μm
0	120.83	393.99	2.66
1	127.88	401.04	3.73
2	194.90	468.06	3.09
3	249.52	522.68	3.23
4	290.96	564.12	3.02
5	324.28	597.44	2.63
6	349.90	623.06	2.97
7	372.37	645.53	2.69
8	390.77	663.93	2.57
9	408.38	681.54	1.77
10	418.51	691.67	1.83
11	427.44	700.60	0.90
12	434.18	707.34	0.38
13	438.99	712.15	0.12
14	442.59	715.75	0.07
15	445.70	718.86	0.04
16	445.70	718.86	0.05

Some accumulation of Ag micro-clusters is seen but it is not uniform. Surface terrace structure or any other corrugations but the Ag micro-clusters are not visible on the images. Figure 3.14 shows the pinning of the Ag micro-wires at the defect sites. Due to the thermal motion on the surface associated with the annealing process, defects and pinning points are not stationary, but quite mobile. This makes it quite hard to observe the relationship between the defect sites and formation of Ag microclusters. In the slides the dark patches in the first few slides are basically surface defect centers. In this case the crystal is in fact not really clean as seen by number of impurity centers on the surface. As time progress in the following slides in Figure 3.14 we see these impurity centers

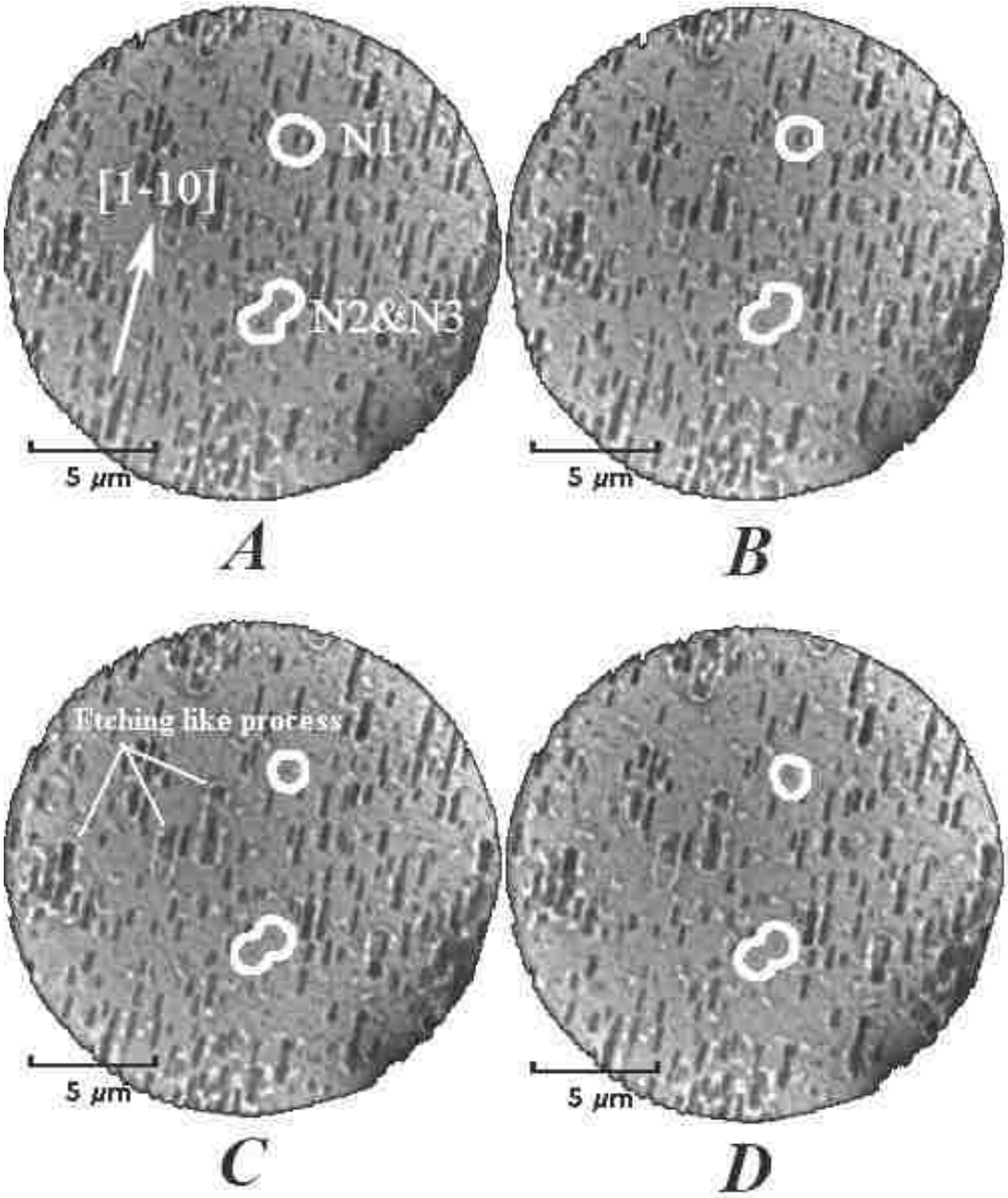

Figure 3.12 Dotted structure which is left after the extinction of the respective nanowire visibly similar to a residue, is seen in the images. And the etch – like regions of the forming microclusters are also shown in the images. FOV 20μm.

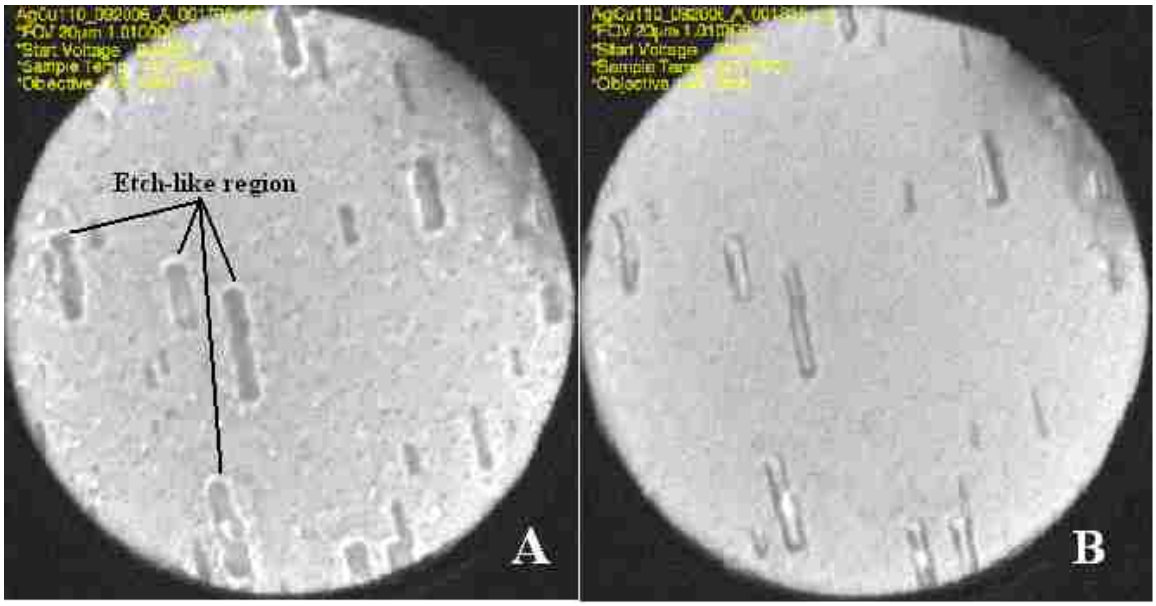

Figure 3.13 Visible etch-like region and dotted surface when observed with LEEM objective at 1.636kV and invisible when observed at LEEM objective at 1.640kV. FOV 20µm. Start voltage (9.302V) is kept a constant.

Table 3.9 Measured Ag micro-cluster width. Data include final cluster widths through multiple experiments.

Number	Width (μm)	Number	Width (μm)	Number	Width (μm)
1	0.06	**21**	0.32	**41**	0.65
2	0.07	**22**	0.44	**42**	0.31
3	0.05	**23**	0.40	**43**	0.31
4	0.07	**24**	0.49	**44**	0.50
5	0.06	**25**	0.25	**45**	0.26
6	0.09	**26**	0.53	**46**	0.21
7	0.05	**27**	0.35	**47**	0.38
8	0.07	**28**	0.17	**48**	0.40
9	0.07	**29**	0.21	**49**	0.32
10	0.05	**30**	0.19	**50**	0.40
11	0.09	**31**	0.27	**51**	0.51
12	0.06	**32**	0.21	**52**	0.38
13	0.05	**33**	0.13	**53**	0.38
14	0.42	**34**	0.34	**54**	0.44
15	0.34	**35**	0.31	**55**	0.34
16	0.21	**36**	0.31	**56**	0.71
17	0.39	**37**	0.28	**57**	0.57
18	0.44	**38**	0.41	**58**	0.31
19	0.30	**39**	0.44	**59**	0.23
20	0.28	**40**	0.31		

are the nucleation centers for the bigger Ag microclusters. Initially the surface is covered by nanowires as observed previously observed in slide t = 0s. As we have shown earlier higher accumulation of nanowires occur at defect points and steps, this happens near and on the impurity centers where the nanowire density is high and concentrated. When the annealing takes place and nanowires decay the ones at the defect centers grow continuously. Eventually these defect center concentrated wires become microclusters.

There is a competition between these, where one of the wires concentrated on the defect point wins over by depleting all the other wires and growing ever larger. Slides on the Figure 3.14 at t = 18s, 19s and 20s gives the transformation of impurity center gradually turning into microcluster. Due to FOV being 20μm for the images the individual nanowires are not resolved, hence not sharp.

Table 3.10 Measured Ag micro-cluster length. Data include final cluster lengths through multiple experiments.

Width (μm)	Length (μm)	Area(μm^2)
0.51	2.64	1.3464
0.49	1.29	0.6321
0.42	0.74	0.3108
0.56	3.08	1.7248
0.41	1.27	0.5207
0.38	1.6	0.608
0.34	0.68	0.2312
0.36	1.81	0.6516
0.41	0.96	0.3936
0.57	2.47	1.4079
0.44	1.16	0.5104
0.41	0.85	0.3485
0.49	3.73	1.8277
0.55	2.08	1.144
0.47	2.62	1.2314
0.78	3.46	2.6988
0.78	2.99	2.3322
0.79	3.52	2.7808
0.75	2.23	1.6725
0.88	3.69	3.2472
0.77	3.26	2.5102
0.45	1.38	0.621

But it is possible to see clearly the formation of microclusters at this defect points on the surface. These microclusters then gradually get bigger or smaller, with time and the rise in temperature. One other important feature throughout this decaying process is the alignment of the structures; nanowires to microclusters they are aliened towards [1 $\bar{1}$ 0] direction. This has not changed while the system is heated. One short coming on the part of data was exact temperature was not possible to state explicitly on the system because there was no thermocouple on the sample. Thermocouple was on the sample holder right next to the sample. Typically temperature of the sample was observed about 50 - 80K more than the holder. We are taking the holder temperature as the sample temperature since it is the recorded value and assume the discrepancy has no bearing on the rational explanations given to the physical evolution of the

system due to the small deviation.

3.4 Analysis and Discussion

3.4.1 Initial Stage

At the *initial stage* for increasing Ag deposition we see no change in surface morphology. Surface thermal motion at ~100°C (which corresponds to about ~34eV) is not prominent due to the low temperature regime. This was seen in the motion of the steps, pinning points like impurity centers and step bunching points. The observations of wide terraces and no pinning points indicate low surface contamination and better long range order on the surface. When the surface motion/flow is not high, this implies diffusion rate is not high. Possible metal on metal epitaxy, prevalent mechanisms of surface diffusion of Ag on Cu(1 1 0) include particle hopping, exchange or tunneling (Tsong 2001).

Of these mechanisms, particle tunneling is a low temperature process where possible atomic vibrations are quenched. Thus tunneling dominates at lower temperatures. At ~100°C condition are better suited for rapid and high flux diffusion mechanisms: hopping and exchange, making it the least probable mechanism of the system. The exchange mechanism a will result Ag getting covered by Cu.

At coverages of 0ML < θ < 0.4ML it has been observed in STM and Photo – emission studies Ag forming a surface substitution alloying phase by exchange (Hite, Kizilkaya and Sprunger 2002). Considering at this low range of coverage the exchange diffusion is a plausible mechanism. At little higher coverage, 0.4ML < θ < 0.6ML it has been observed a compressive strain driven de – alloying phase where Ag makes dimer and trimer chains on the Cu(1 1 0) surface (Zhao 2005). Hence the long range diffusion of Ag atoms on the virgin Cu(1 1 0) surface is clearly mediated via a non mixing mechanism: most probably by hopping mechanism.

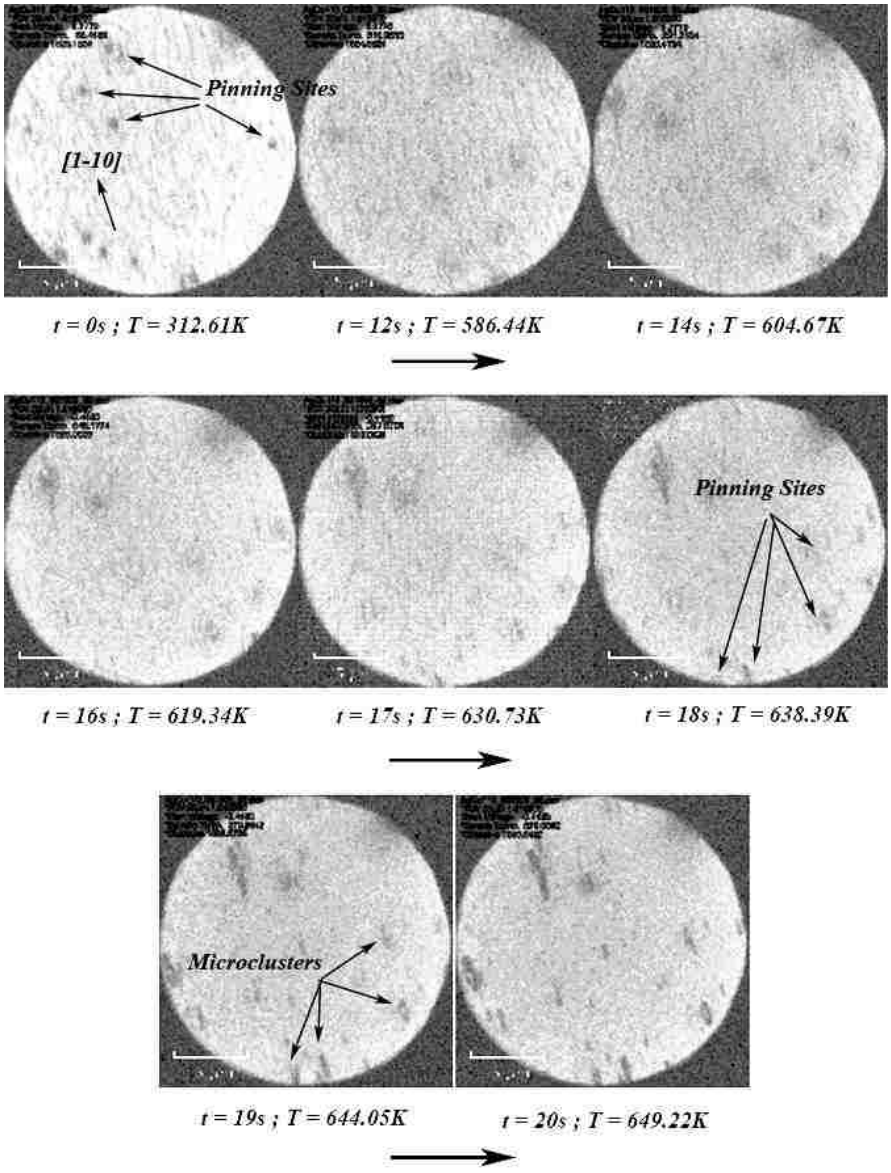

Figure 3.14 Ag microcluster growth via defect pinning. Initial defect sites are shown in slide t = 0s and the surface thermal flow of these defects are seen through the subsequent slides (t = 12s, 14s, 16s etc…), as the points move on the surface. Ag nanowires are seen on the back ground on the first few slides with large pinning centers as black specs.

Surpassing of diffusion activation directly depends on the thermal energy of the system. Once Ag(1 1 1) ad layer saturates other available channels of diffusion will open for Ag diffusion, Ag atoms now can diffuse on Ag(1 1 1) layer. If the ad atom Ag has enough thermal energy to overcome energy barrier then it will hop to a neighboring state, assuming it will dissipate acquired energy soon enough.

Depending on the temperature of the surrounding the dissipation can be fast or slow. If the energy dissipation is slow then the diffusing atom can migrate further. Although with LEEM resolution it is not possible to observe individual atoms, short range random motion of the surface structures and slow drift indicates the rate of diffusion is fast. The motion of the step bunching point P indicates there is a net flow along [1 $\bar{1}$ 0] direction, where as in the perpendicular direction [0 0 1] it is random. This indicates thermal motion on the surface is directional and confined in [1 $\bar{1}$ 0], even at moderate temperatures. Surface thermal flow in elevated temperatures shows this clearly as we will see a very high directional thermal drift restricted only on [0 0 1] direction but free flowing in [1 $\bar{1}$ 0] direction.

In the Arrhenius form of the diffusion equation the activation energy (E_{act}) and the pre exponential factor (D_0) of clean metal surfaces, (1 1 0) surface has a lower E_{act} and D_0 than of the (1 0 0) surface and higher than of (1 1 1) surface (For Ag on Ag, E_{act} on (1 1 0) on [1 $\bar{1}$ 0] direction is 0.59eV while on (1 1 1) it is 0.1eV). But the distinct difference is the diffusion along the channels of the (1 1 0) surface, where relatively the activation energy and pre exponential factor along the [1 $\bar{1}$ 0] is much lower than those along [0 0 1] (Agrawal, Rice and Thompson 2002). This enables the activation of the diffusion channels along [1 $\bar{1}$ 0] much earlier when annealing initiates. When both channels are open and diffusion is bi directional the rate of diffusion along [1 $\bar{1}$ 0] is always higher and therefore predominates over the [0 0 1] direction. This atomistic diffusion probably has given rise to the surface flow in the mesoscopic scale that

is observed on LEEM. Directionality is due to the surface corrugation where Ag atoms going along [0 0 1] has to move across corrugation resulting in a reduction in coordination numbers which requires higher activation energy. This is the opposite of the Ag atoms moving along [1 $\bar{1}$ 0] direction. Low variation of coordination number has given them lower activation energy to surpass the activation barrier and hop into a stable site. Moreover diffusion is a stochastic process, but once initiated the local maximum of the decreasing chemical potential will determine the direction of motion of the diffusing atoms. Disregarding the effect of impurities, (in this case) this is generally dependant on the surface channel structure.

At coverage range 0.6ML < θ < 0.9ML, Ag dimer and trimer chains merge and make the Ag(1 1 1) overlayer on Cu. Saturated pseudo hexagonal Ag(1 1 1) surface shown to have accumulated strain on [1 $\bar{1}$ 0] direction as seen by the domain boundary generation along the [0 0 1] direction (Zhao 2005). It is considered to be a surface stress relieving mechanism as it is evident by the buckling lines of atoms. These domain boundaries are less than 10 Å (< 50Å = resolution limit) in width, therefore beyond the sensitivity threshold of the LEEM and are not visible in LEEM images. Therefore the saturation process introduces an incremental strain on the Ag overlayer.

Loss of surface contrast with the saturation of the Ag (1 1 1) (Figure 3.7) has been observed with variation in other systems: Ge growth of Si(1 0 0) with As terminating surface it has been shown the resolution loss due to 2D islanding nucleation process that gives rise to distributed islanding on the terrace surfaces with island size below the threshold of the LEEM giving away to loss of contrast at Ge coverage of every 0.5n ML; $n \in \mathbf{Z}$ (Tromp and Reuter 1992). This is different to what has been observed for Ag(1 1 1) overlayer saturation, where the contrast never recovers. STM images (Zhao 2005) have shown the step structure intact before and after the growth of nanowires.

Therefore the step contour disappearance observed with LEEM should be due to the variation of work function on the surface, in other words a change in electron beam focus. Substrate surface undergoes structural and elemental transitions in the sense (1 1 0) surface changes to (1 1 1) surface while Cu changes to Ag. It has been generally observed, is when the surface become more closed the work function (W) decrease and surface free energy increase: $W_{(1\,1\,1)} < W_{(1\,0\,0)} < W_{(1\,1\,0)}$.

Considering the work function measurements of Ag(1 1 0) and Ag(1 1 1) surfaces, they have been shown to have values of 4.52eV and 3.86eV respectively (Prutton 1998) (H. B. Michaelson 1978). In the case of surface transformations: (1 1 0) to (1 1 1) there is a net loss of 0.66eV in case of Ag. Moreover mean work functions for Cu and Ag respectively is 4.5eV and 4.26eV that is net loss of 0.24eV (Farral and Lafferty 1980) (Bennette, Swanson and Charbonnier 1967).

Loss in surface work function translate as a direct gain in reflected low energy electron beam from the surface, *i.e*. there should be an increase in the observable intensity at the point of saturation, which was in fact observed in all data sets related to saturation point and initial growth of nanowires. This intensity is electronically controlled by the CCD camera this results in the reduction of the step contrast, which leads to major loss of surface structure.

Uniform intensity increment/ loss of contrast over the surface, indicate Ag(1 1 1) overlayer growth on the surface is uniform and spontaneous. Ag (1 1 1) overlayer should have a patched growth extending randomly but uniformly over the surface. Close to saturation STM images have shown random but areas of Ag(1 1 0) overlayer on the substrate surface (Zhao 2005) implying randomly spread anomalies on the pseudo hexagonal Ag (1 1 1) layer. This also favor Ag(1 1 1) growth proceed through partly randomly distributed nucleation centers and step edges spread over the entire surface.

3.4.2 Intermediate Stage

Resolution loss occurred in the initial stage is observed not to recover during and after the intermediate stage (step contours are lost). This can be explained with the even after the formation of nanowires the surface in between the wires stays as Ag(1 1 1), hence the reflected beam intensity that has increased stays increased and the LEEM focus shift stays through to the end.

The number of nanowires formed is equivalent to the critical nucleation centers. This is because all the observable nucleation centers grow into nanowires and none of them observed to decay in the intermediate stage. Number of nucleations with increasing time is shown on Figure 3.15. This show the nucleations are gradually decreasing. In Figure 3.16 nucleation rate vs. Ag coverage and time are shown. Using the curve fit formula alone it is possible to estimate the nucleation rate at t = 0 (initial moment of nucleation at a coverage 1.2ML) which gives an approximate value of $\sim 1.77\times10^{3} s^{-1}$. This gives the maximum possible nucleation rate at a given temperature and at a given deposition rate. Figure 3.16, rate of nucleation decreases rapidly with a time constant of 4.12×10^{-2}s. Similar association is also seen for the coverage and rate of nucleation, on the scale of coverage the time constant is 3.2×10^{-2}ML. These time constants are obvious functions of the absolute temperature of the system. There small scales imply the quick pace of the rate change.

Using the Bauer's capillary theory of nanostructure formation and ignoring strain effects on the process it is possible to state the nanowire nucleation rate with the following equation (Luth 2001),

$$\mathbf{J_N = Ke^{\left[-\frac{\Delta G(j_{cr})}{kT}\right]}} \qquad \text{- (3.1)}$$

Where J_N is the nucleation rate (rate at which the critical nuclei are being formed),

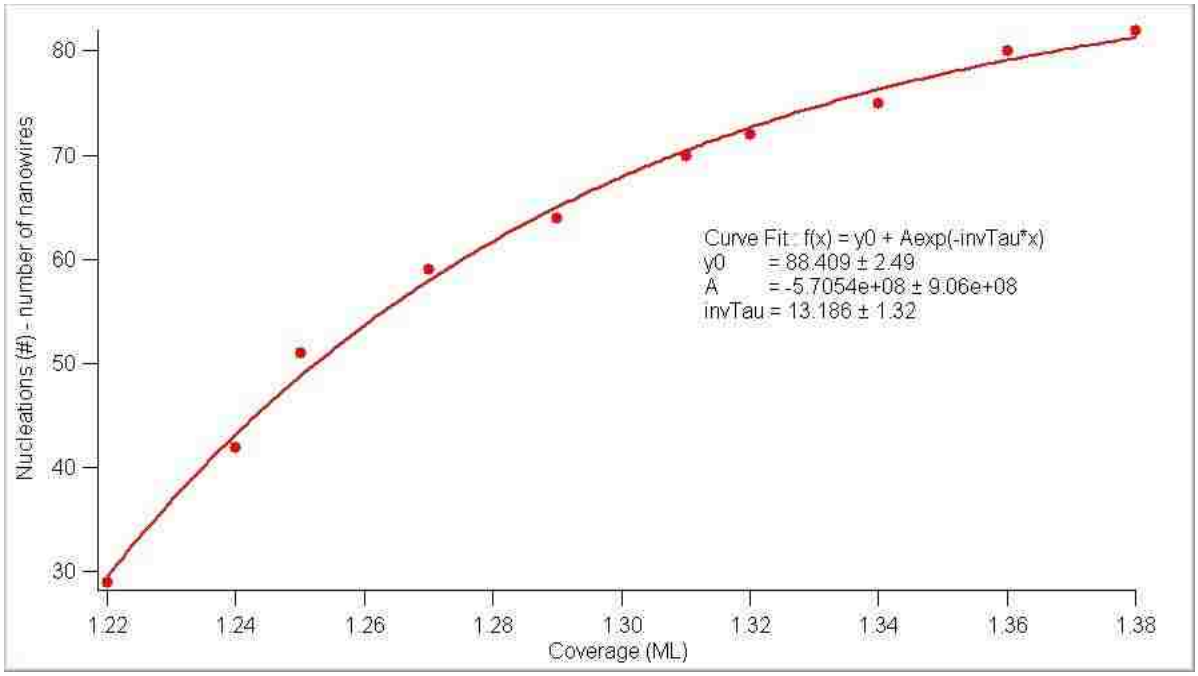

Figure 3.15 Number of Nanowire Nucleation vs. Ag coverage in ML.

$\Delta G(j_{cr})$ is the Gibbs free energy of formation of a nucleation center, K is a constant, k is Boltzmann constant and T is the absolute temperature. Combining the Equation 3.1 with curve fit formula of Figure 3.15 it is possible to obtain the relation (Appendix 3) (T is kept a constant),

$$\frac{\partial \Delta G}{\partial t} = \left(1 - \frac{y_0}{J_N}\right)\left(\frac{kT}{Tau}\right) \qquad \text{- (3.2)}$$

Here *Tau* is the curve fit parameter obtained from Figure 3.15. Here we have considered the nanowires we observe are already past the critical dimensions of an island. This is justified by the continuous growth of the observed wires.

Therefore each new wire we see is a new nucleation *i.e.* matured critical nuclei. By counting the new wires we count the new nucleation centers. Equation 3.2 shows when the maximum rate of nucleation (J_N) is present (at t = 0) the *variation of $\Delta G(j_{cr})$ with time* is at its highest, and it is decreasing and gradually flatten out due to J_N eventually becoming a constant.

This indicates $\Delta G(j_{cr})$ depends on the J_N, which depends on the coverage making $\Delta G(j_{cr})$ slowly go up with coverage. This makes nanowire nucleation less probable as Ag atoms tend to join existing nanowires, making them longer. Growth of existing wires and new nucleations are two processes in the system, at any given time, which are constantly at competition with each other.

The nanowires are attached to defect sites on the surface. This is clearly seen in the Figure 3.7. These points or regions on the surface there is clear discontinuity of surface diffusion flux. When observed closely we see nanowires forming at points where there is an obstruction to the diffusion. Comparative to the non saturated Cu(1 1 0) surface a new diffusion pathway opens at Ag(1 1 1) layer saturation. Both the atomic exchange mechanism and the hopping mechanism,

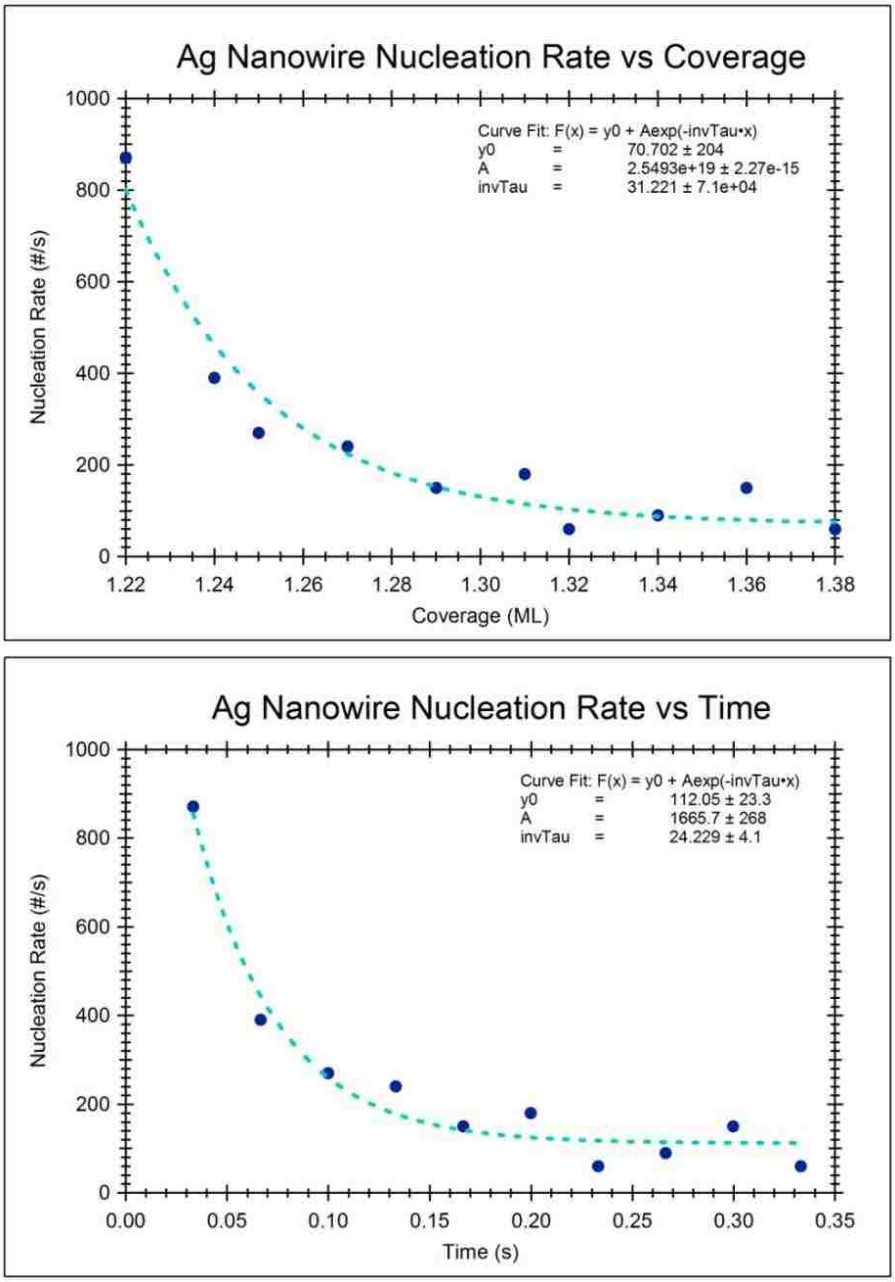

Figure 3.16 Ag nanowire nucleation rate - drop with Ag coverage and Time. Data fit with an exponential curve. Fit parameters are given on the graph.

become available for Ag surface atoms on the Ag(1 1 1) layer. Exchange diffusion of Ag between the ad atom and Ag on the (1 1 1) layer does not alter the Ag(1 1 1) layer. Although the Ag(1 1 1) layer is strained/buckled the on Cu(1 1 0), on Ag(1 1 1) the surface diffusion is omni-directional with no significant directional anisotropies like a (1 1 0) surface. Further the activation energy and pre exponential factor are much lower than (1 1 0) surface.

When the diffusing Ag atoms get pinned on defect points/sites, local concentration of Ag atoms go up, leading to a 2D condensation which gives rise to nucleation of the islands. The initial 2D condensation or nucleation centers are (1 1 0) surface structured Ag islands which have been observed in STM to grow on either Ag(1 1 1) domain boundaries or step edges (Zhao 2005). As we have pointed out it is not possible to observe Ag(1 1 1) domain boundaries in LEEM as it is beyond the resolution limit of the instrument. These nucleation centers grow into nanowires while they are strained due to mismatch between the Ag and Cu. The reasoning behind Ag and Cu interactions are considered, while not considering Ag on Ag(1 1 1) is because the nucleation centers of Ag(1 1 0)/Ag(1 1 1) domain boundaries are on Cu(1 1 0).

Question of the directionality of the nanowires are explained by the strain fields rising due to the lattice mismatch (Zhao 2005). There are several systems that have similar behavior under the strain relaxation. For example Ge nanowires grown on Si(1 1 3) have shown by MEIS studies, there exist clear evidence of strain relaxation giving rise to a nanowire width of 200Å (Sumitomo, Omi, et al. 2003). In many aspects Ge nanowire / Si (1 1 3) system exhibits similarity to Ag on Cu(1 1 0) system, although former is clearly a semi conductive elemental system. Strain effects on the growth have been exhaustively explained by Zhao (Zhao 2005) we'll focus on the kinetic picture of the growth. Although the strain fields undoubtedly play a crucial role, especially in confining the nanowire width, local kinetics also plays an important role in the growth process.

On Ag(1 1 0) surface, activation energy for Ag atomic diffusion along [1 $\bar{1}$ 0] channel is 0.59eV and the pre exponential coefficient is 0.0026cm^{2}s^{-1}, which are lower than for the channel on [0 0 1] direction. It is expected these values will deviate slightly when considered the Ag on Cu, as oppose to Ag on Ag(1 1 0). When compared this to Ag on Ag(1 1 1): activation energy 0.10eV (Agrawal, Rice and Thompson 2002) and pre-exponential coefficient 0.00014cm^{2}s^{-1*}. Even with this lowering of threshold for the surface diffusion, pinning sites such as step edges and dirt points appear to obstruct the diffusion, as these are the most probable places where the nanowire formation initiates. Diffusion damping associated with the moderate temperatures is a natural consequence to the islanding on substrate epitaxy (Schindler and Wolf 2000).

On the newly formed Ag(1 1 0) nucleation centers there exist a clear diffusion anisotropy due to [1 $\bar{1}$ 0] direction having lower activation energy (E_a) and pre-exponential coefficient (D_0) compared to [0 0 1]. This implies the growth being propagated at the ends of the nanowire by continuous flow of Ag ad – atoms towards the ends. Ad atoms can reach a terrace due to the impinging flux or migrate via steps up wards of each layer of the nanowire. It has shown the side facets of the nanowire are made in a stepped morphology by alternating {1 1 0} facets of the horizontal surface and {1 1 1} facets. This implies the at the minimum, on the {1 1 1} surface the diffusion is as dominant as the Ag(1 1 1) wetting surface. If considered the hopping diffusion the {1 1 1} layer has no preferred direction, but the {1 1 0} does have a preferred direction. This is pointed to the nanowire ends. Nanowire side facets {1 1 1} are at an angle to the surface wetting (1 1 1) layer changing facets requires extra energy (so called step – facet barrier) and this is common to both exchange and hopping mechanisms (Huang and Wang 2003). At the experimental temperature ~100°C this is easily overcome by Ag ad atoms. Another important

[*] All these are for the Arrhenius form of the surface diffusion equation: $D = D_0 \exp(E_{act}/kT)$ where E_{act} is the activation energy and D_0 is the pre exponential coefficient.

factor is the Ehrlich–Schwoebel barrier (Ehrlich and Hudda 1966) (Schwoebel and Shipsey 1966) associated with step edges of the layered nanowire. ES barrier prevents the step up/down migration of the Ag atoms on the bottom/top of the nanowire. Near the step edge of the nanowire there is continuous attachment and detachment. Ag flux will increase the number density of Ag atoms on the surface. These atoms diffuse towards the local energy minima where Ag nanowires will behave like sinks. Long range minima are not available at this temperature. When the temperature is increased these will be available for Ag atoms as we will see in the final annealing of the system.

Observation of asymmetrical growth up step and down step across the terrace edge is very interesting. It is evident the growth is not symmetrical, terrace up step and step down does not grow at the same time. Further when they do start growing on to the opposite side of the terrace edge the wires visually not as dark as the initially grown half. This indicates the difference in maturity of the step up and step down parts. On the LEEM image, unlike the STM it is not possible to explicitly distinguish which is up step and which is down step across a step contour. In thermodynamical sense it is possible to distinguish tentative upper terrace by considering it to be the concave side of the oval terrace edge. This is because if the cohesive energy of the atoms makes them agglomerate in order to maximize the coordination number of all the atoms on the terrace, thereby minimizing total energy. Although there are instances of lower terrace being inside of a completed oval shape[†], this is atypical. Following through this line of reasoning we see nanowires typically initiate at the bottom of the terrace pinned to the terrace edge but growing only on the bottom terrace in the beginning. In Figure 3.7 it is possible to observe in certain instances that they continue to grow on the upper terrace, eventually but in others they never do, during the observed duration of time. Step contours observed on the LEEM

[†] So called *Inverted Droplet Phase* of Pb self assembling on Cu(1 1 1) at a coverage of 0.48ML (Plass, et al. 2001).

images quite possibly be of multiple steps.

When the ad atoms get attached to the ledge typically they diffuse along the ledge because the activation energy of the ledge diffusion is lower than that to climb the step[‡]. But the nanowire growth is on the [1 $\bar{1}$ 0] direction and diffusion on the layers of the wire is directed along [1 $\bar{1}$ 0] direction because of the step edge barrier (ES barrier) Ag migration to the opposite direction to the step edge, along the wire is facilitated while the diffusion towards the step edge, along the wire is inhibited.

Thus the wire growth occurs on the lower terrace. When layer growth of the wire has progressed to some extent, there will be an instance where wire height is nearly equivalent to the step edge. Es barriers are important because they obstruct the Ag diffusion across the step edge thereby quenching the wire growth across the step.

But as the wire matures and increases height, energy barrier become surmountable by Ag ad atoms. Then the nanowire continues to grow across the step edge and on the top terrace. Strain field confinement of the width has no bearing to the fact the nanowire continues to grow on the top terrace, because the surface structure is the same.

We propose nanowire bridging the step up and down terraces opens low energy path ways between up and down terraces for the diffusion of Ag ad atoms. This is via the side facet {1 1 1} of the nanowire upward Ag diffusion. When they reach a horizontal layer {Ag(1 1 0) surface of the wire} they can migrate preferentially on [1 $\bar{1}$ 0] direction to the top side of the step. This facilitates the opening of low energy diffusion pathways between up and down the multiple or single steps, in the thermodynamic equilibrium (No Ag deposition and at constant temperature). Wire growth can be mediated via both Ag flux coming to both up and down the

[‡] For Ir/Ir(1 1 1) in hopping mechanism, Ledge Atom Diffusion has an activation energy (E_a) of ~0.76eV compared to Up – Step Atom Diffusion has an activation energy (E_a) of ~1.50eV (Tsong 2003).

steps. Length of nanowires is a direct consequence of available Ag atoms. This can be clearly seen in Figure 3.7 point ***A***. Where to the dirt pinning of the nucleation centers for the nanowire increase the number of nanowire forming but none of them grown to be elongated natural shape of the wire. There is substantial competition between nanowires for the Ag in their neighborhood.

In nanowires growing comparatively apart, we see a higher growth rate and better elongation, clearly because they have higher area around them meaning more Ag (= flux × area) to feed from. Although this is readily seen on the LEEM images, this so far is a qualitative observation. Measured length variations in Data Set 01 over time for all the nanowires are graphed in Figure 3.17 while length variations of Data Set 02 are shown in Figure 3.19.

In top graph of each Figure 3.17 and Figure 3.19 shows the time evolution in color and the arrow on the top left with the box inset gives the color variation with time. In both cases it is possible to see the length variations do not show monotonic increments or monotonic depreciations.

Initial increments are typically large followed by several instances where the nanowire length is increased moderately. Finally the rate length increase gradually slows but in some cases respective nanowires shrink (negative increase). This seen in the black data points of the dropping below colored data points. This indicates a shortening of length. This is seen in the graphs on the top of both Figure 3.17 and Figure 3.19.

The sequence of LEEM images shown in Figure 3.8 and Figure 3.9 correspond to these graphs. In Figure 3.8 loop L shows the nanowire pinned around (oval shape) a terrace and further amplifies our explanation of the nanowires at step edge pinning sites. In data Set 01, the nanowires were selected to be isolating with minimum interaction where as in Data set 02 they were selected belonging to a group. Data Set 01 gives a global perspective of the system with

FOV of 8μm while Data Set 02 gives a local view with a FOV of 3μm. Each member of a group where identified with a letter. Each group member has a separation between them less than 3 nanowire widths between them in [0 0 1] (across the wire) direction.

The groups are formed due to the local kinetics compared to global kinetics of the diffusion of Ag ad atoms. It is possible to see the new nanowires forming closer to the existing nanowires in the Figure 3.9.

This is also seen in the nanowire group members 6 band 6 c, in Figure 3.19 bottom graph. Local coupling is evident by the coupled length variations (one gets shorter while the other elongates), shown. This is observed in several groups (not shown) where the local interactions dominate over global interactions.

In order to understand the inter-wire Ag transport we look at the atomic picture. Consider the buckled Ag(1 1 0) hexagonal layer depicted in Figure 3.18. On Ag(1 1 1) pseudo hexagonal layer the hopping diffusions is not exactly symmetric in three possible directions (these direction are at an angle of 30˚ with [0 0 1] substrate direction and vertically upward in $[1\ \bar{1}\ 0]$ direction) assuming it being mediated via hopping mechanism.

Of the possible sites on the surface for a Ag ad - atom on Ag(1 1 1) surface, the sites A and B have different energies due to the vertical positioning of the surrounding atoms. Site A has lower energy compared to site B. Therefore chemical potential gradient is lower for a jump/hop to site A.

The site vertically up respect to both A and B is energetically equivalent to site B, therefore has the same chemical potential gradient. Probability of these migrations may be not equivalent as these atoms are buckled, but they do not lie in different planes. Therefore their height variations in the vertical direction are comparatively small making the energy variations between them are also small.

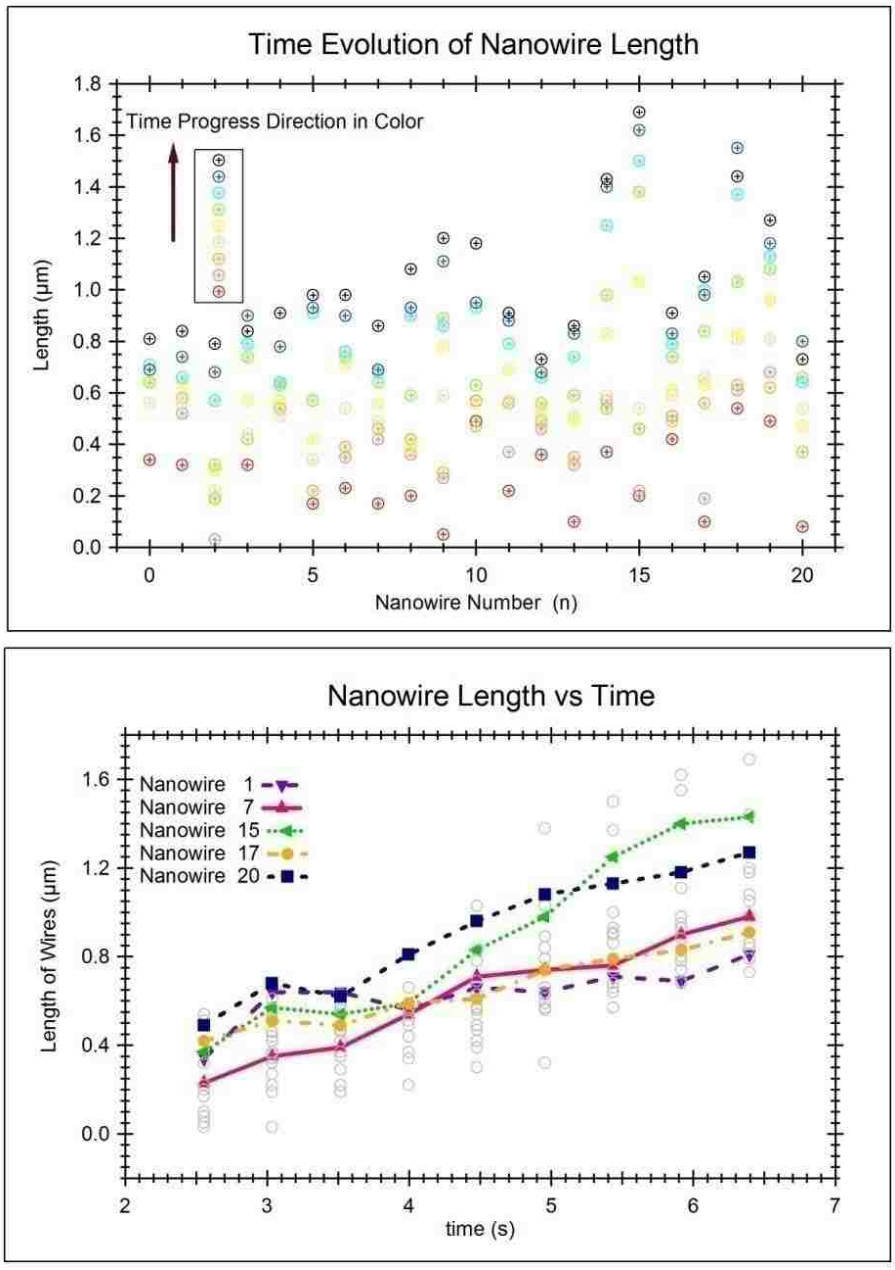

Figure 3.17 Nanowire length variations of Data Set 01 with time. On the bottom graph length variation of only 5 nanowires are shown continuously for clarity. Each group of vertical data points shows a time instance measurements of the length of the nanowires. Numbers of the wires measured is shown in the inset of the bottom image.

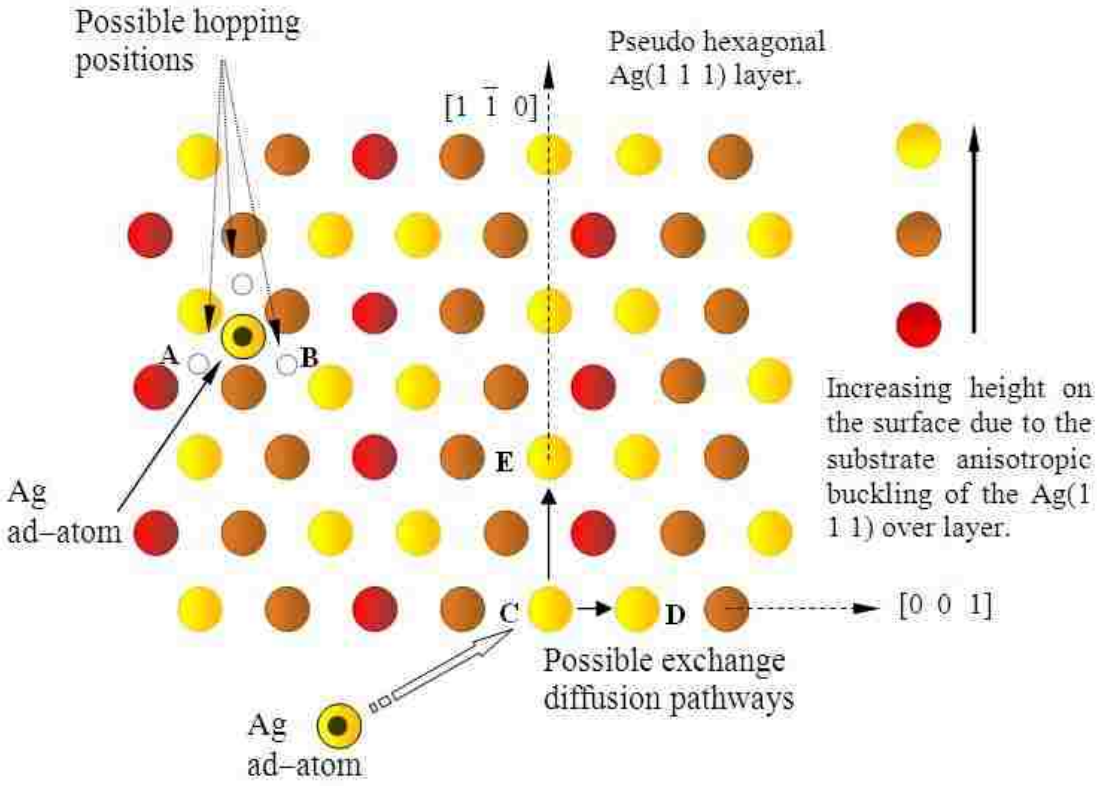

Figure 3.18 Possible surface diffusion pathways of Ag(1 1 1) overlayer on Cu(1 1 0). Both Hopping Mechanism and Exchange Mechanism are considered. Possible pathways are determined by local surface corrugation resulting local chemical potential variations.

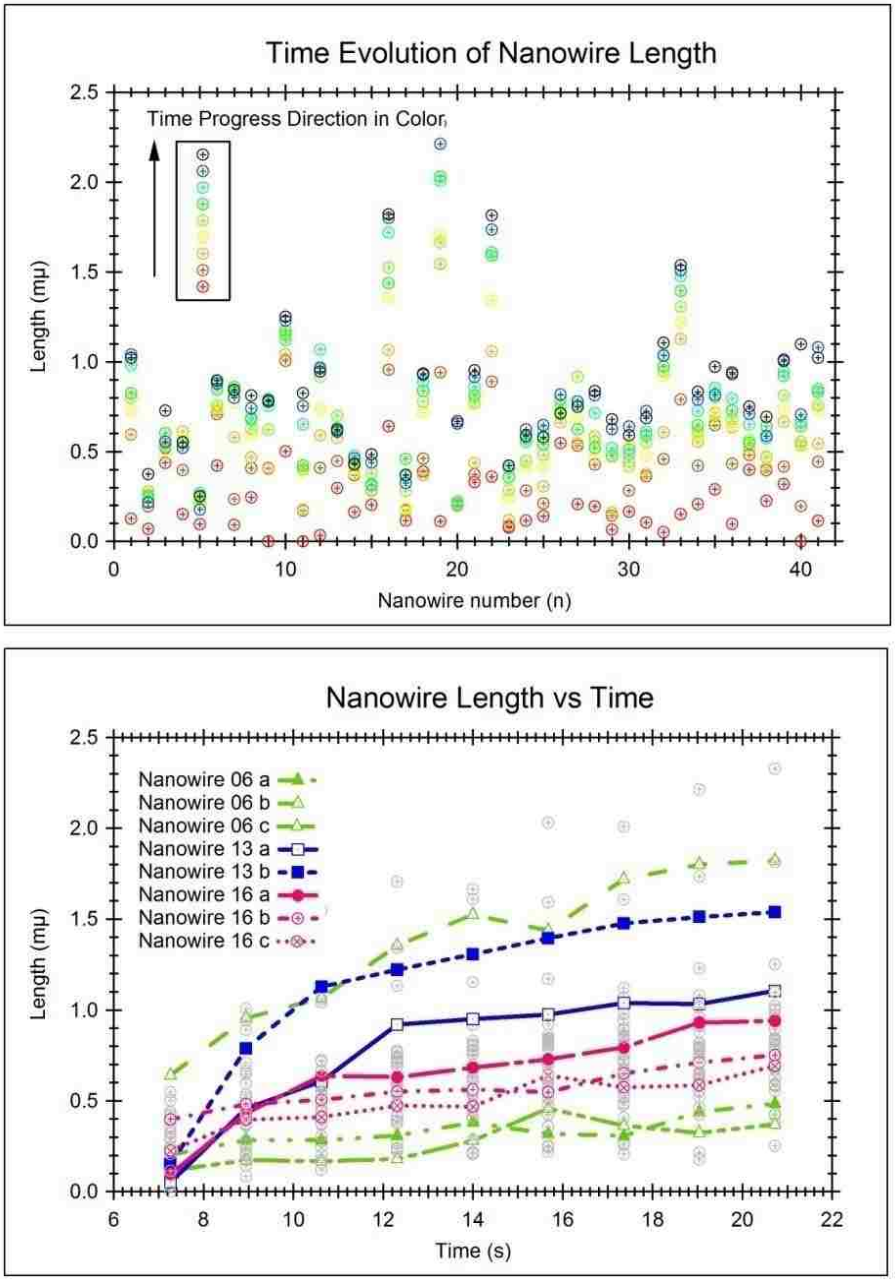

Figure 3.19 Nanowire length variations of Data Set 02 with time. On the bottom graph length variation of only 3 nanowire groups (members of a groups are denoted a, b, c) are shown continuously for clarity. Each group of vertical data points shows a time instance measurements of the length values of the nanowires. Numbers of the wires measured is shown in the inset of the bottom image.

If we assume the transport of Ag ad atoms via exchange mechanism lowest possible activation energy pathways are for [1 $\bar{1}$ 0] direction and [0 0 1] direction. As seen in the Figure 3.18, the yellow atoms have the least coordination making them energetically better suited for the creation of the intermediate state. In contrast lower lying atoms have higher coordination making them energetically less suited for the intermediate state in exchange mechanism. As in the case of hopping mechanism we have to consider the relative variations due to buckling of the atoms that make the Ag(1 1 1) are not as drastic as in the case of atoms lying in different plans.

Taken all these reasons we propose in the low temperature regime these exchange diffusion paths become favorable above other possible diffusion pathways. Therefore surface diffusion in the [0 0 1] direction can be achieved via hopping and exchange mechanisms readily. When we consider the elongations are fluctuating: this implies a Ag transport between the wires. This is readily seen for the group 6 in Figure 3.19. At *t =16s* we see a dip in the length of **6b** while the length of **6c** grows in near correlation. Growth of the nanowires 6b and 6c show correlation throughout their growth. Another example is in group 16 between **16a** and **16b** wires at the same t=16 time, where we observe drop in length for **b** while **c** increase in length at the same time. It should be emphasized the in both Data Set 01 and 02, nanowire length measurements the new nucleations are ignored.

Only the nanowires which are distinct on the surface length increments are measured. Therefore when it is observed the increasing length of nanowires gradually drops, or as in some cases wires gradually shrink the deposited Ag is being absorbed by new wires that are being nucleated on the surface. It is observed new nanowire nucleation in the vicinity of a group member is usually begins close to the middles of an existing wire.

Possible explanation to this may lie in increased ad atom concentrations on the Ag(1 1 1)

overlayer surrounding the middle of the wire due to the growing nanowire edges being at a considerable distance away from the wire center. Requirement of increased Ag concentration is necessary but not the only requirement as the growth requires a nucleation center with a Ag(1 1 0) patch or domain boundary which works as a template for the wire. At this point we don't have an explanation to what gives rise to this Ag(1 1 0) template near the middle of an existing wire. Strain field anomalies between the wire and the Ag(1 1 1) layer may locally favor the formation of Ag(1 1 0) patches, which acts as templates for the nanowires.

We have plotted the nanowire growth rate variations with time and the length in Figure 3.20 and Figure 3.21. These rate variations also give indications to the dynamic nature of the growth. The wires cannot be considered just as sinks as they sometimes become sources. There exists a high level of dynamic interaction between the wires: in the atomic scale there is continuous attachment – detachment processes takes place. Local chemical potential variations will effect whether the there is a gain or a loss of atoms at a particular time. The length variation a very good measurement of this underlying kinetics because of the narrow near fixed width (~100Å) distribution of the nanowires. They will yield direct measurements of the mass transport between the wires. Both length variations and rate of length variations are not monotonic functions. The increased kinetic energy in higher temperatures will result in rapid decay in the nanowire state. This implies the local short range interactions dominate in these ~373K temperatures, while at higher temperatures long range kinetics dominates.

We have proposed the mass transport in nanowire growth along [1 $\bar{1}$ 0] direction possibly occur along the Ag(1 1 1) side facets and almost certainly along the horizontal Ag(1 1 0) layers. This should indicate a higher rate of growth for longer wires, due to the fact longer wires mean longer facets and longer facets attract more Ag ad atoms due to attachment. In Data Set 01 (Figure 3.20) the observations were carried out in the initial moments of the system while

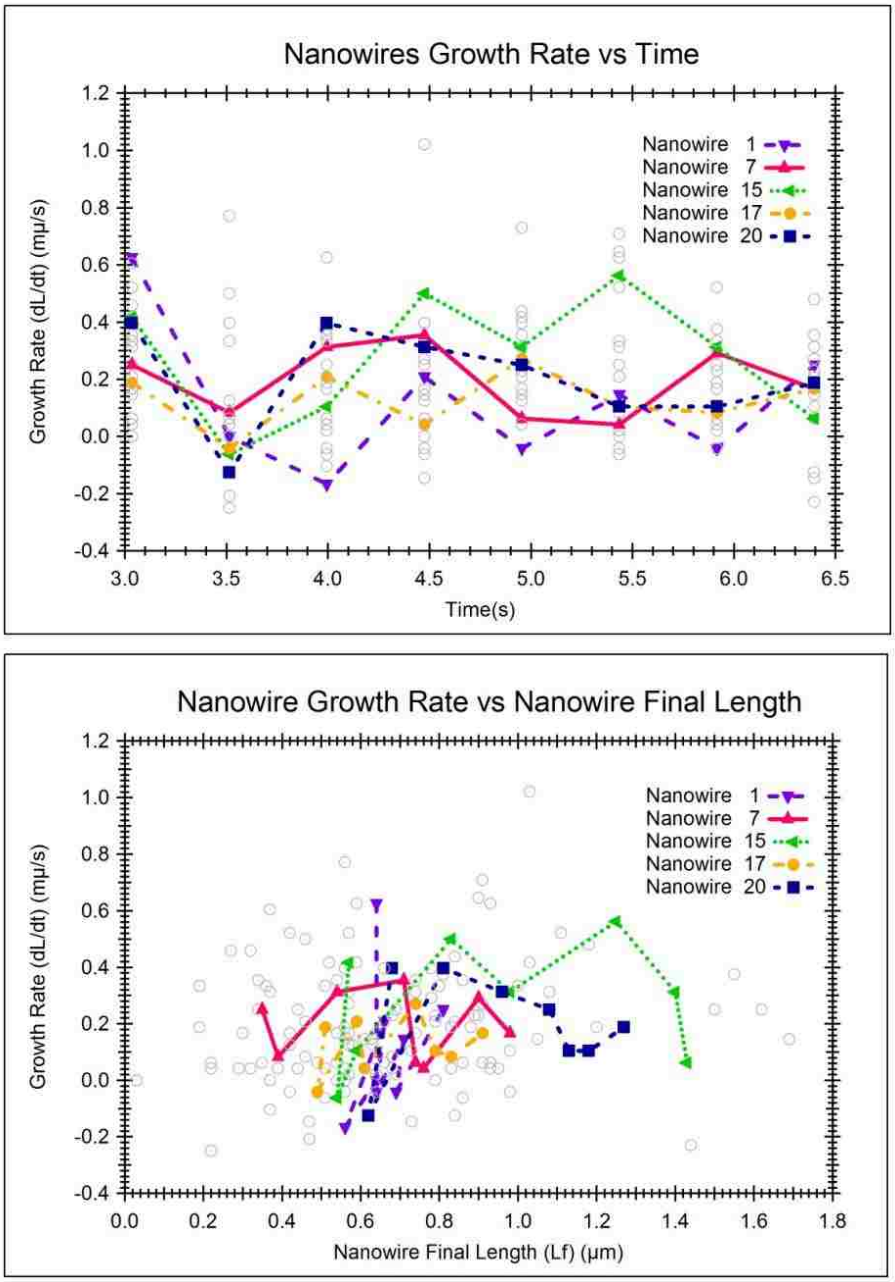

Figure 3.20 Growth rate variations of nanowires for Data Set 01, with time and real time length of the wire. For clarity only five nanowires were shown.

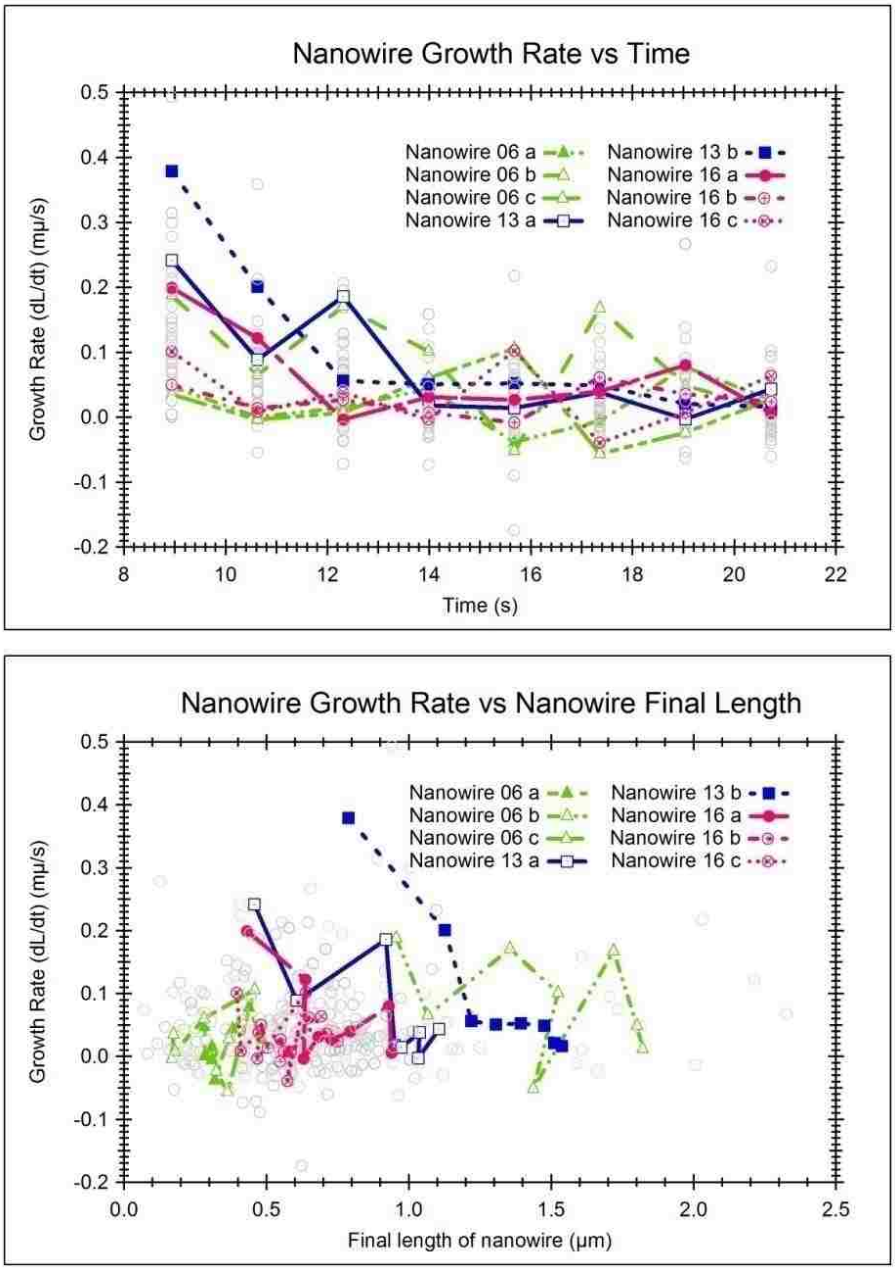

Figure 3.21 Growth rate variations of nanowires for Data Set 02, with time and real time length of the wire. For clarity only three nanowires groups were shown. Each member of a group is denoted by a letter.

in Data Set 02 (Figure 3.21) the observations are carried out in latter stages. As it can be seen clearly in the Figure 3.20 and Figure 3.21 the growth rates doesn't show a direct linear proportionality to the nanowire length.

The growth rates have high oscillatory behavior in time. Careful examination of the growth rate tracks for nanowires in Figure 3.20 reveals with oscillations the growth rates drop slowly with length and time. This is more prominently seen in nanowire growth rate tracks on Figure 3.21. This can be thought of as a linear drop coupled with oscillations. This oscillatory behavior is shown by the repetitive structure "***m***" of the wire growth rates vs. length and wire growth rates vs. time. With increasing length we see nanowire growth rates going through a cycle. This "***m***" structure is prominent especially for growth rates vs. length. Rates start low and gradually increase and then go through a maximum and then come to a step minimum. At that point, cycle starts over. To observe the group growth rates of nanowires growing in clusters we grouped the nanowires according to the criterion no member of a group should be separated by more than ~300Å (~3 nanowire widths). Physical basis behind this characterization is nanowires separated by small length scales will facilitate better diffusion between them. Under this condition the group behaves more like a single long nanowire. This also helps to isolate and remove the inter member mass transport.

We have added the lengths all the members belonging to a group. Then the rate of growth of total length of a group was plotted against time and total length of the groups in Figure 3.22. In Figure 3.22 we have only plotted seven groups for clarity. This behavior is typical in all the groups. The same "***m***" like structure is present in almost all the curves we observed. In some cases this is at different stages. In other words some curves (growth rate tracks) start at the growth rate maximum and then go through a minimum followed by a maximum and so forth. This indicates there are particular values of a length total length of a nanowire and nanowire

group where the growth rate becomes a minimum and these minima change from group to group. Length of a nanowire is representative of the volume of the Ag in a nanowire as the width of a wire is a constant.

This indicates a local total free energy variation of the system where energy minima and maxima are a function of Ag nanowire Ag volume and for a group of nanowires the Ag volume collectively of a group. Depending on this local free energy condition, growth or decay can occur. Principle of Detailed Balance will govern system dynamics in equilibrium conditions, where attachment and detachment processes occur in equal frequency.

In other words there could be no growth or decay for nanowires. But far from equilibrium systems have shown to oscillate in whatever physical parameter representative of the equilibrium conditions (Alberty 2004) (Klein 1955). Such as the case in nanowire growth under continuous deposition of Ag on the Cu(1 1 0) substrate.

When a nanowire or a group of nanowires attain a length corresponding to minimum growth, this is seen by the growth rate being minimum but as the Ag keeps coming due to the continuous deposition, this extra Ag will move the system Gibbs Free Energy of the system beyond the minima. The system strives to attain local minima by moving Ag to nanowires by growing them. This will increase the growth rate of the respective nanowires. Once this growth consumes the Ag in the local environment the growth rate drops down. This is the re-attaining the minimum growth rate. This cycle repeats continuously. System strives to attain the minimum Gibbs Free Energy at all times. This is the driving force of the dynamics of system.

When cycles complete it can be seen the amplitudes of the of these oscillations decrease. This is as explained before a linear decrease in growth coupled to the oscillations. Time to achieve energy minima is proportional to the diffusion and transport of Ag, as the nanowires nucleate and grow even closer with progressing time, diffusion lengths decrease and therefore

time takes to readjust the system also decrease. This we attribute to the decrease in amplitude. These observations give direct evidence to the atomistic and highly dynamical growth of nanowires.

In order to investigate the effect nanowire end attachment of Ag atoms on growth of wires, we tabulated the nanowire ends on Appendix 1. Corresponding displacement distributions are shown in Figure 3.23. The mean of the displacements and standard deviations (= width) of the displacement distributions are plotted with time (top) and Ag coverage (bottom) in Figure 3.24. In the figure mean displacement between the nanowire ends stays almost constant and has a range 1.19μm < mean < 1.27μm. The spread of nanowire end distribution (standard deviation = width) although get higher does not grow fast. The range of this quantity is 1.01μm < STD (= width) < 1.10μm for the growth duration. If nanowire growth predominantly facilitates via attachment of Ag atoms at wire ends, wires with more separation between neighboring ends will grow faster due to better Ag availability by virtue of less competition by other wire ends. This will tend to make these select wires grow faster. This will intern will make ends come closer. Conversely wires with edge having less separation will grow slower. With time this will increase the standard deviation (= width) of the displacements and mean of the displacements should drop down gradually as the wires come close. Figure 3.24 shows mean of the displacement to be increasing gradually and standard deviation of the displacement increasing slowly. These two observations rule out predominant wire growth by means of Ag attachment at the nanowire edges. It is simply not possible to mediate the nanowire growth by dominant edge attachment process of Ag.

Finally the depending on all these observations we have shown. The nanowire kinetic growth depends on the local Gibbs free energy of the system. System tries to minimize the free energy by modulating the growth in line with the free energy.

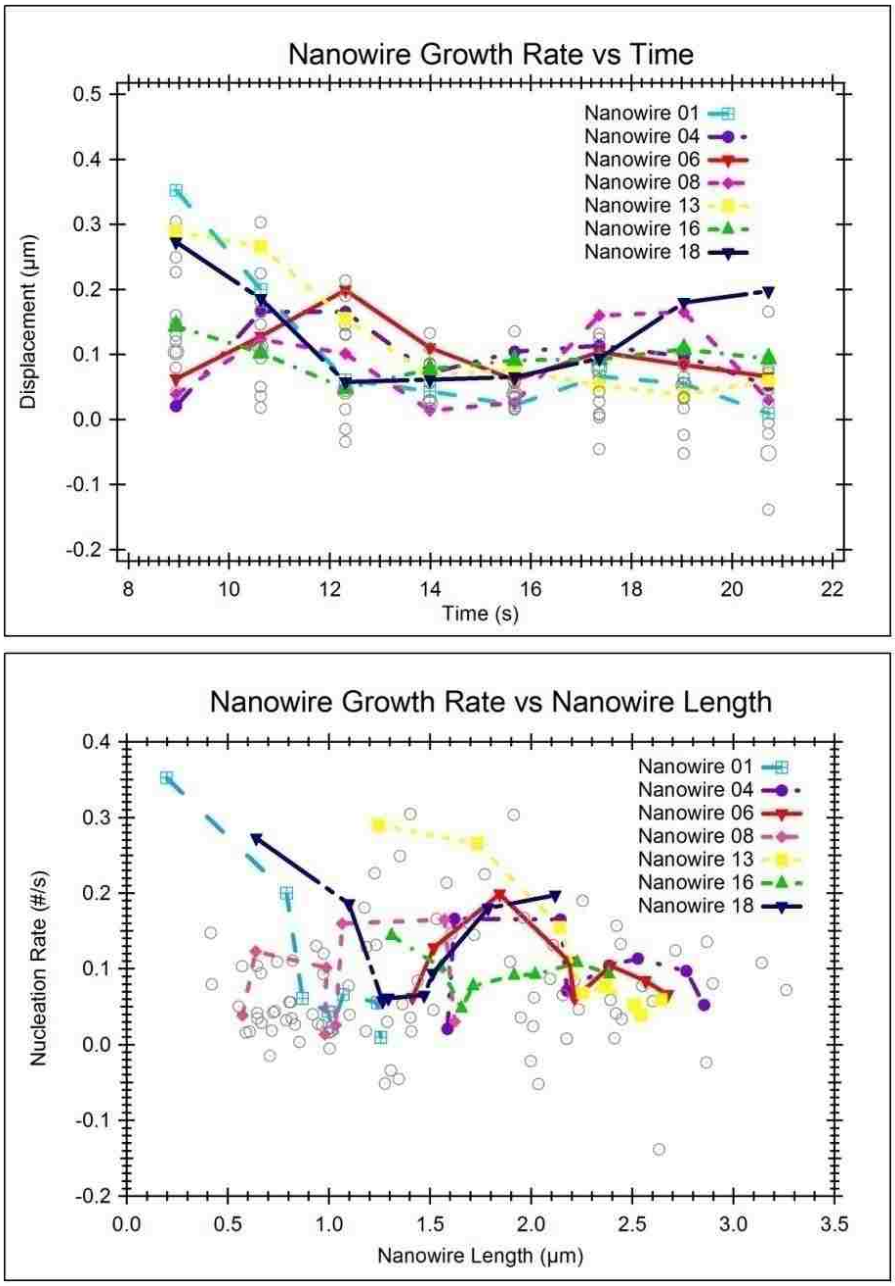

Figure 3.22 Growth rate variations of nanowire GROUPS for Data Set 02, with time and length of the wire. Here we have summed up the lengths of all the nanowire members in a group and this is identified by the group number given. For clarity only seven nanowires groups are shown.

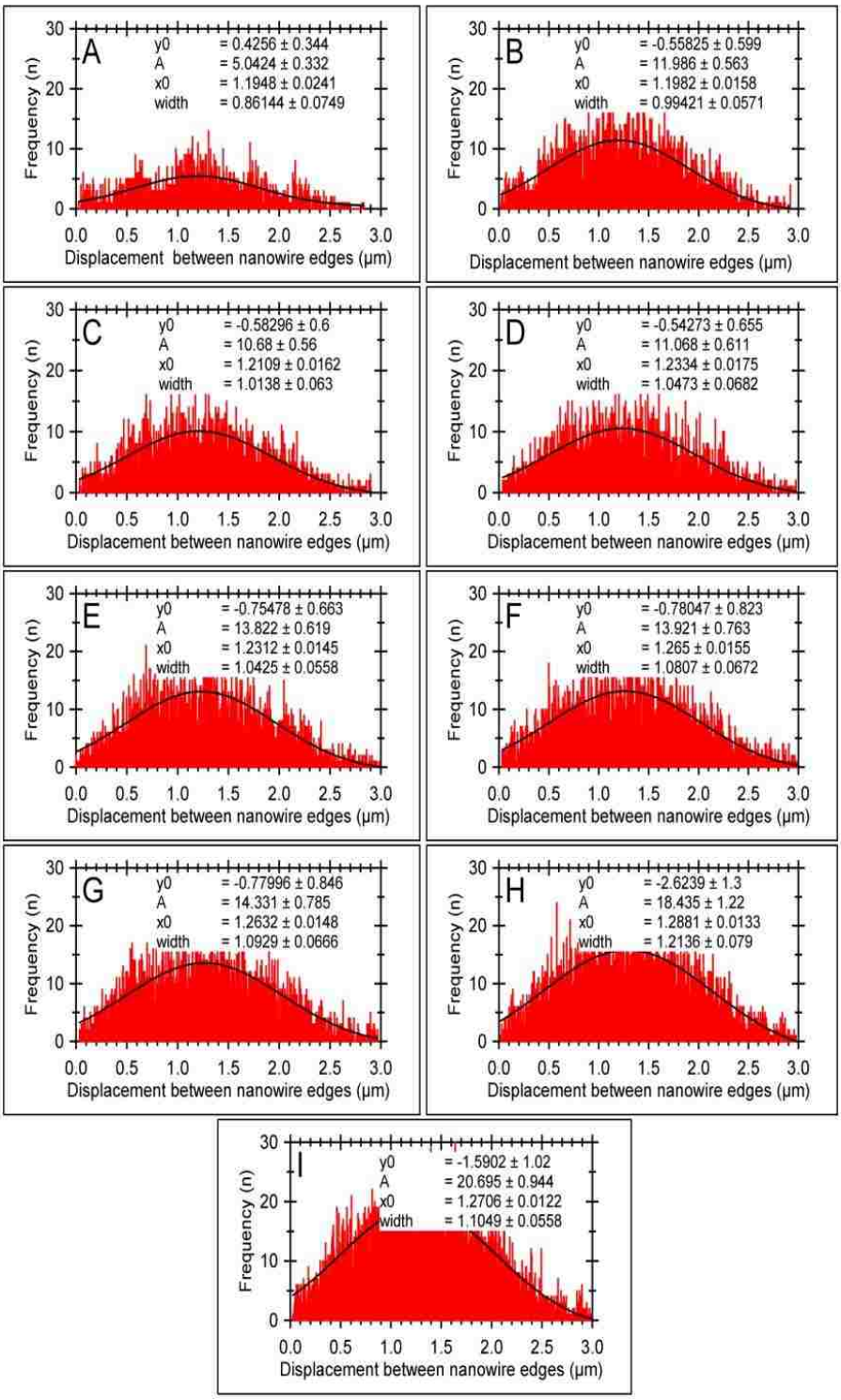

Figure 3.23 Evolution of displacement between nanowire edges with increasing Ag coverage/time. Each distribution is fitted with a Gaussian: $y = y0 + A \exp -\{(x-x0)^2/width^2\}$ and the fit parameters are shown in the inset.

When Ag accumulates locally on the surface they increase the growth of the nanowires in the neighborhood. And when no Ag is present on the surface the growth rate drops down. This gives the oscillatory growth of wires. This indicates highly dynamic nature of the growth. There is no explicit coupling to length of the wires or edge of the wire. Rather wire growth is mediated by Ag concentration on the neighborhood and diffusion among wires. Diffusion among the wire can be readily facilitated by the Ag(1 1 1) overlayer as we have shown considering the atomic structure. Once Ag attaches to the wire, possibly the atoms are carried to the edges by anisotropic diffusion of the wire favoring diffusion along the [1 $\bar{1}$ 0] direction.

3.4.3 Final Stage

Nanowires start decaying at around 300°C – 400°C into microclusters. This is seen clearly by Figure 3.10 as the structure of nanowires visibly changes during the variation of temperature. In between 503K – 630K aspect ratio gets gradually lowered. The data given in Table 3.5 is shown graphically in Figure 3.25. Figure show the complexity and the dynamic growth of the system. Nanowires shown are respectively are groups **S** and **Q**. It is possible to see nanowire 2 getting completely extinct while nanowire 1 the area (= volume) staying the same. Contrastingly the nanowire 3 increases its area (increases volume).

These are clear indications of the diffusion assisted Ostwald ripening process (Ostwald 1900). Ostwald Ripening, where growth of large islands progress via the dissolution of small islands mediated by Gibbs – Thompson effect which describes the concentration at the surface of the island (Zinke - Allmang, Feldman and Nakahara 1987). In the initial phase of the ripening process there is clear indication of high degree of competition among wires to dominate and grow. This completion at its earliest instance is seen by the Figure 3.10 and 4.25. A more global picture is seen in Figure 3.11. Numerous wires get extinct and few ripen to be microclusters.

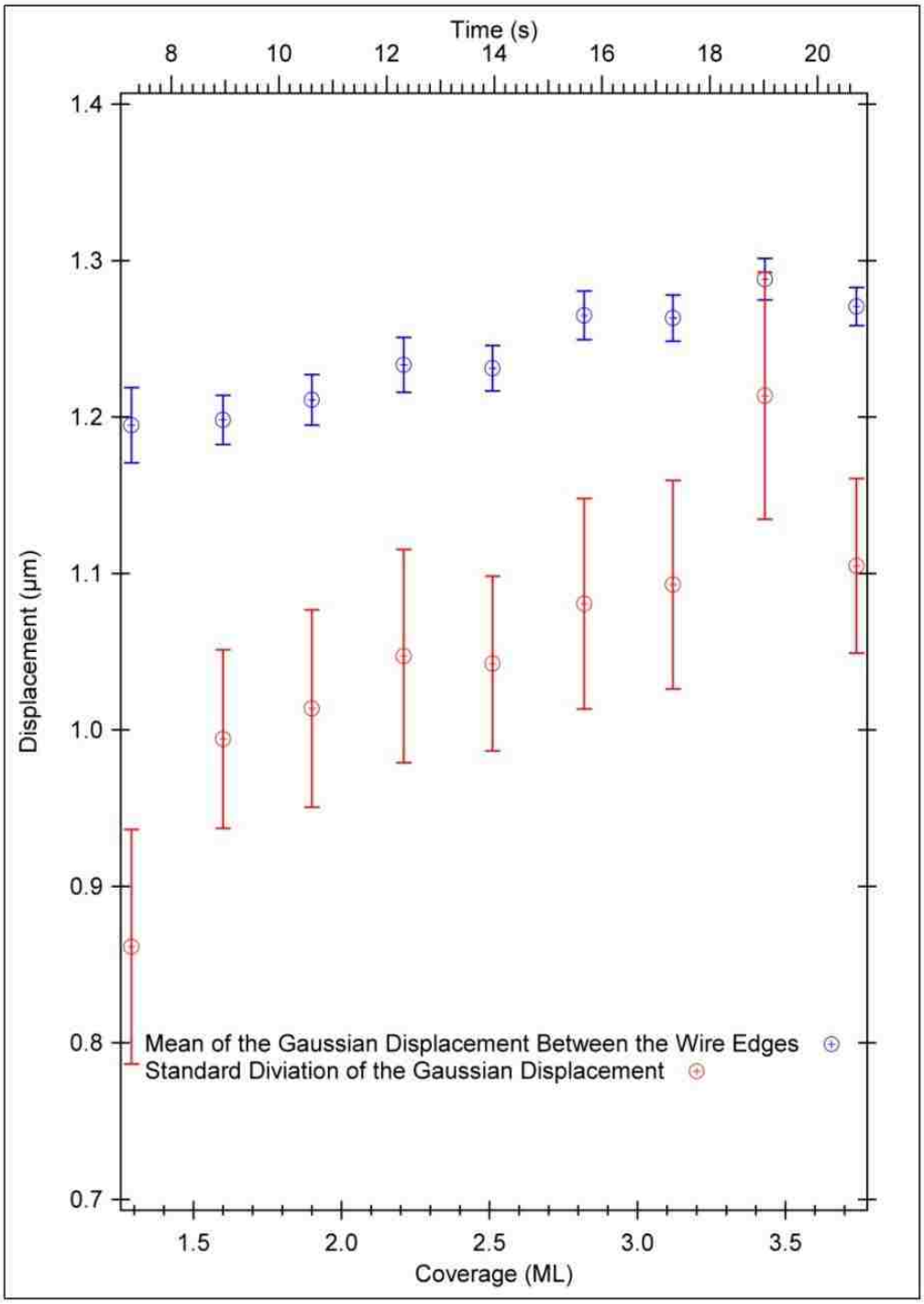

Figure 3.24 Variation of the mean displacement between the nanowire edges with increasing coverage (bottom scale) and time (top scale) with the standard deviation of the distribution of displacements.

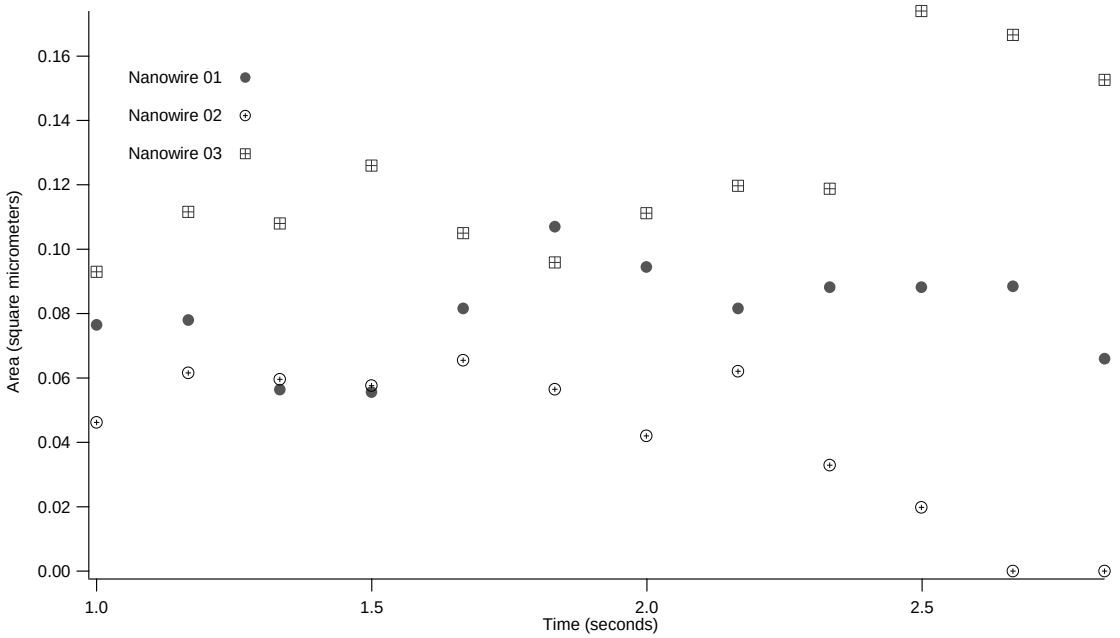

Figure 3.25 Nanowire area variations with time for three nanowires. System temperature is increased while being observed.

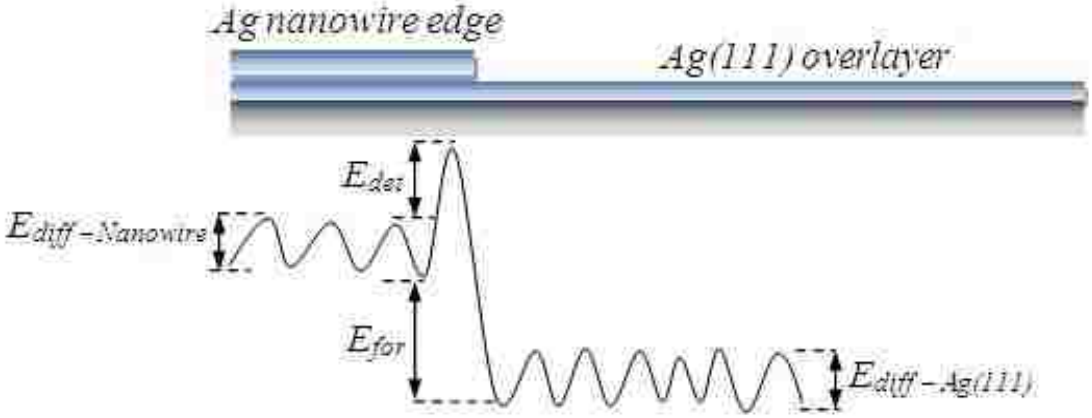

Figure 3.26 Energy Schematics of the Ostwald's ripening process. E_{det} is the detachment energy and E_{for} is the energy of formation. Schwoebel - Ehrlich barriers due to step edges associated with the nanowire height are ignored for simplicity. Modified from (Fitting, et al. 2003).

Atoms detach from smaller islands and move by means of surface diffusion through the adatom sea of the Ag(1 1 1) overlayer and attach to bigger clusters. The growth behavior of a typical island is governed by three factors:

1. Chemical potential of the surrounding.
2. Chemical potential of the island.
3. Attachment – detachment barrier.

Process can be kinetically limited in the simplest sense due to two factors: if the exchange of Ag atoms between the nanowire edge and Ag(1 1 1) overlayer is sufficiently high owing to increasing temperature, then the flux of atoms to and from a nanowire is limited by the rate of Ag diffusion on the Ag(1 1 1) overlayer which is given the respective chemical potential gradient.

On the other hand if the rate of surface diffusion of Ag on Ag(1 1 1) overlayer is substantially rapid then the flux of Ag atoms to and from the nanowire depends on the attachment – detachment barrier at the nanowire. Whichever that is the slowest will govern the rate of ripening of the nanowires to Ag microclusters.

In the attachment – detachment limited regime the activation energy $E_a \sim E_{det} + E_{for} + n \times E_{ES}$. Here E_{det} and E_{for} respectively are for detachment energy barrier and formation energy barrier. And E_{ES} is the Schwoebel–Ehrlich (Ehrlich and Hudda 1966) barriers due to step edges associated with the nanowire height (n depending on atomic steps). Conversely for the diffusion limited regime activation energy $E_a \sim E_{diff\ on Ag(1\ 1\ 1)}$. As we have stated before surface diffusion on Ag(1 1 1) is uniform on all directions and highest compared to Ag(0 0 1) and Ag(1 1 0) surfaces. Schematic picture of the energy barriers associated with process is shown in Figure 3.26. Liftshitz and Sloyozov (Lifshitz and Slyozov 1961) explained the Ostwald's ripening in bulk

for 3D clusters. This is particularly important in the case of sold solutions and alloying. Their work focused on diffusion limited regime. In the case of adatom attachment – detachment limited regime preliminary work was by Wagner (Wagner 1961). Surface agglomerated clusters for the 2D and 3D cases was studied by Wynblatt (Wynblatt and Gjostein 1975) initially and McLean *et. al.* (McLean, et al. 1997). Experimentally Ga and Sn clusters on Si(0 0 1) and Si(1 1 1) surfaces was shown to be ripen in diffusion limited regime (Zinke - Allmang, Feldman and Nakahara 1987) while attachment and detachment limited ripening was observed for ErSi wires on Si(0 0 1) (Fitting, et al. 2003).

Generally it is possible to state the ripening process by: $\mathbf{A} \propto \mathbf{(t)^n}$ where **A** is the area of the nanostructure/cluster and **t** is the time elapsed. The exponent **n** gives the limiting mechanism in the ripening process. If $\mathbf{n \sim 2/3}$ then the ripening is diffusion limited and $\mathbf{n \geq 1}$ gives the attachment - detachment limited ripening (McLean, et al. 1997) (Wynblatt and Gjostein 1975). In our system temperature and time both changed concurrently. Therefore relationship changed the form to: $\mathbf{A \propto (t/T)^n}$. This is owing to the fact for both cases: $\mathbf{A = (C/T)^k \times (t)^k}$ where C is the constant of proportionality which is different for each limiting case (McLean, et al. 1997).

We have measured the evolution of areas for three microclusters shown in Figure 3.11. The corresponding data is given at Table 3.10.

Table 3.10 Microcluster evolution with time and temperature.

Time/s	Temp/K	Area1(μm^2)	Area2(μm^2)	Area3(μm^2)
5.084	679.5	0.714	0.359	0.217
6.062	691.7	0.907	0.475	0.313
7.04	700.6	1.658	1.292	0.892
8.018	707.3	2.839	1.888	1.241

We have plotted the data from the Table 3.10 for the two microclusters increasing with the annealing (time/Temperature) in Figure 3.27. We see clearly the $\mathbf{n \geq 1}$ with slopes giving 3.39 ± 0.54, 4.29 ± 0.76 and 4.52 ± 0.74. This conclusively proves the ripening process is not

mediated by surface diffusion limited mechanism. Attachment - detachment limited mechanism is given by $n \geq 1$ making the process dependent on attachment – detachment mechanism. Ag microcluster formation at annealing of the system is limited by attachment and detachment from the initiating nanowires edges with the barrier $E_a \sim E_{det} + E_{for} + n \times E_{ES}$. This includes an interesting feature: when nanowires decay the rate accelerate because with every layer decaying off the nanowire, the E_a gets reduced because one E_{ES} factor gets taken off from the activation energy E_a. Deviations from the ideal **n ~ 1** corresponds to having other possible significant mechanisms such as evaporation, surface alloying, effect of terrace edge barriers on surface diffusion, etc... .

At a temperature of ~100°C the nanowire growth proceeds due to having favorable conditions towards diffusion but unfavorable, lower energy to overcome detachment barrier. When deposited Ag atoms overcome the diffusion barrier, diffuse through the surface and join the nearest nucleated nanowires, elongating them.

At temperatures ~400°C the detachment barrier is overcome and Ag nanowires exiting on the most favorable (energetically) accumulates Ag owing to their favorable chemical potential gradient via Ostwald's ripening while smaller wires decay.

Nanowire number density variations given in Table 3.7 are shown on the Figure 3.28. Initial decrease is slower but the slope increase drastically. This clearly indicates there is a temperature (~ 670K) at which an acceleration of ripening occurs. This may possibly be the energy corresponding to the surpassing the detachment barrier.

Figure 3.29 gives the distribution of microcluster width and length. The system was annealed to ~700K before taking this data. Therefore system has changed completely to the microcluster surface phase. The distributions are clearly different for nanowire in the intermediate state. They have longer mean length of ~2μm as oppose to ~0.5μm of nanowires.

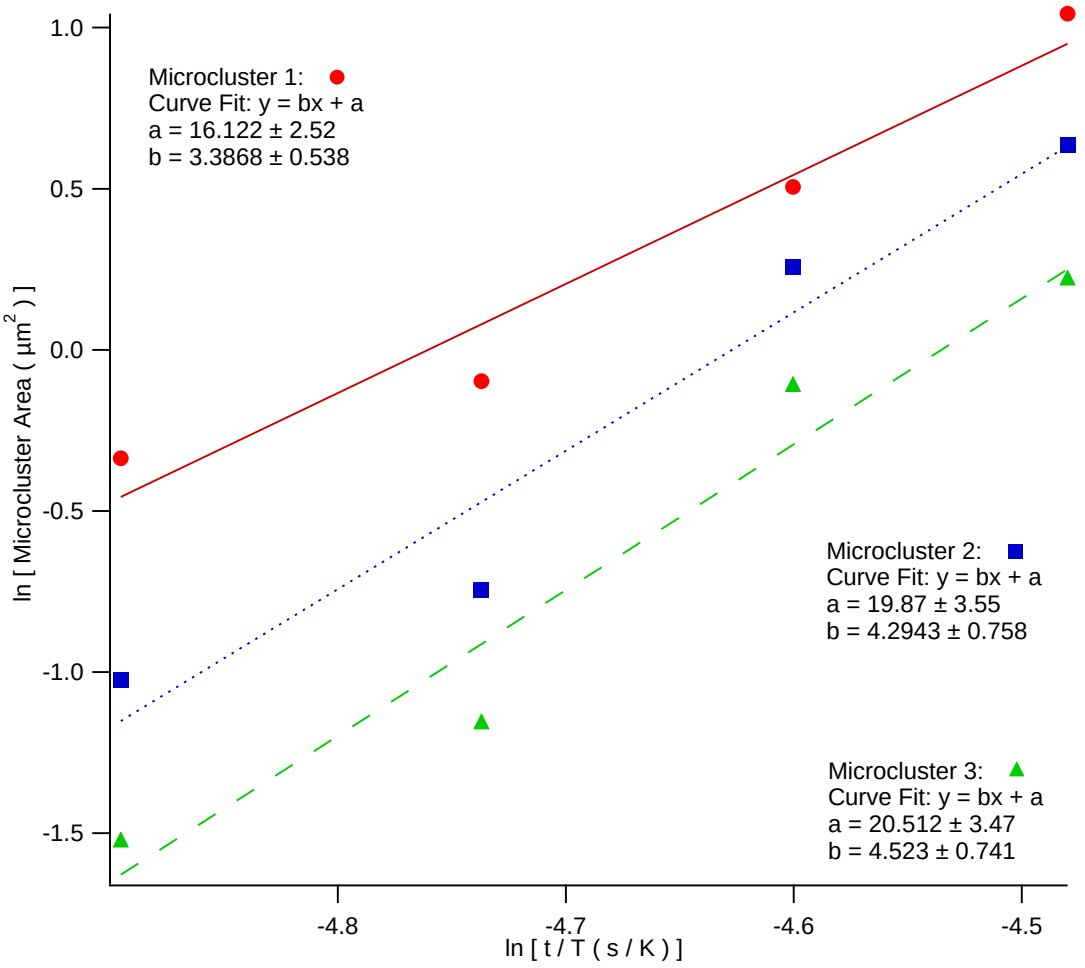

Figure 3.27 Natural Logarithmic curves of microcluster area vs. time/Temperature, for three microclusters.

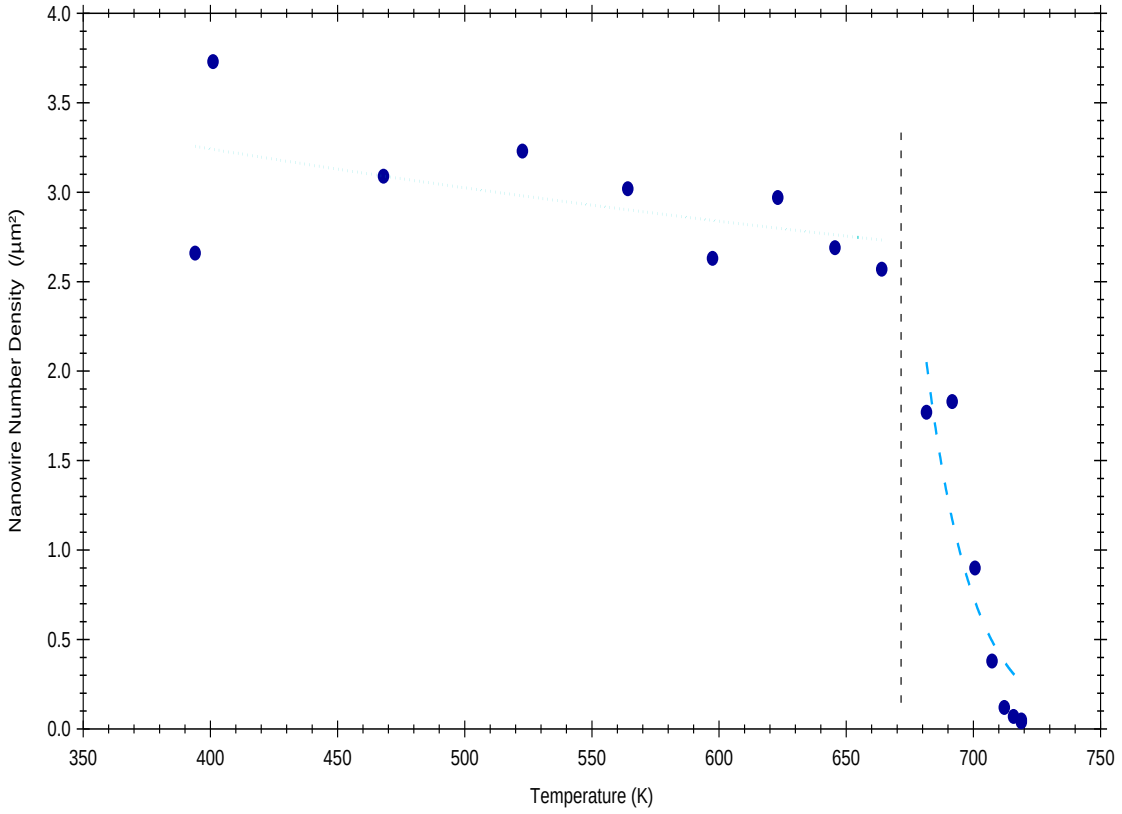

Figure 3.28 Microcluster surface number density change with temperature.

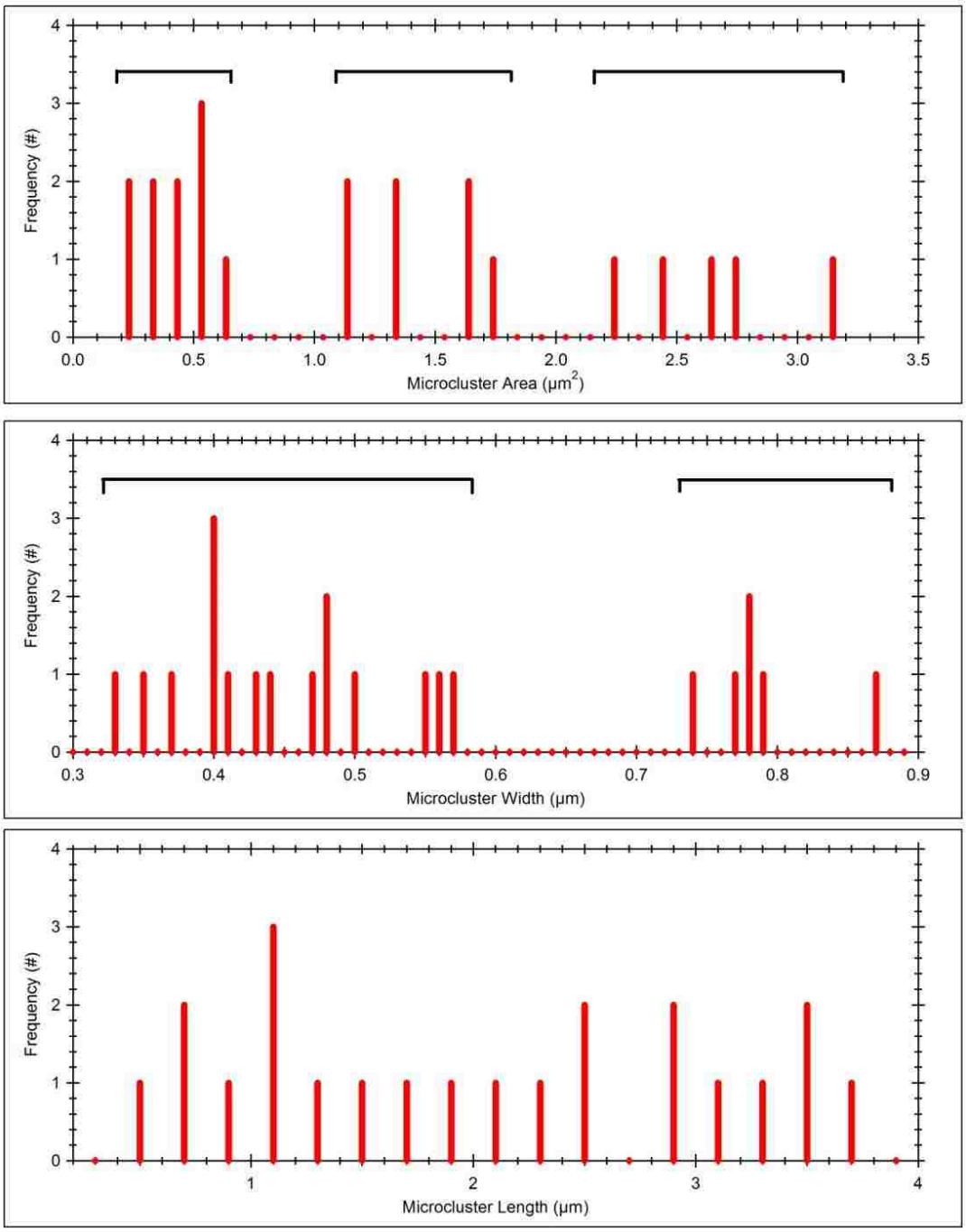

Figure 3.29 Distribution of microcluster area, width and length through multiple experiments.

Similarly widths are much higher ~0.3µm, compared to ~0.03µm for nanowires (Zhao 2005). Indicating the microcluster phase is distinctly different surface phase as opposed to nanowires of Ag on Cu(1 1 0) substrate.

It is possible to observe three (3) distinct groups of microclusters when considering their surface area on the Cu(1 1 1) substrate. They are shown on the Figure 3.29. Similarly but more prominently we see two (2) distinct groups in the microcluster width distribution, this is clearly shown on the Figure 3.29. The microcluster area having there different distributions may be coming out of the confined width of the clusters. Like the Ag nanowires the microclusters also clearly show width being confined, this is because of the strain effects due to lattice mismatch still having considerable control of growth properties of the clusters. This is also shown by their clear elongated morphology. Ag microclusters still grow along [1 $\bar{1}$ 0] direction, and confined in [0 0 1] direction. Strain effects are reduced but far from being removed.

If the nanowire phase of Ag is dominated by the surface strain confinement which is shown by their uniform widths the microcluster state exhibits the surface free energy dominance by reducing the area to volume ratio owing to reduced aspect ratio. One other factor in this is the reduction of strain energy by promoting misfit dislocations. Misfit dislocations are accelerated by elevated temperatures (Khantha and Vitek 1997) (LeGoues, et al. 1994). Ag nanowires which ripen to microclusters will possibly have increased the dislocation density leading to strain relaxation. This reduces the confinement of the widths thus increase the width to ~0.4µm and the aspect ratio is thereby reduced. The observed clusters have considerably less aspect ratio as expected.

Spread of the widths and lengths are also an indication of the attachment – detachment limited growth. Narrower the dimensional (length and width) distribution of the respective clusters more the indication towards a diffusion limited growth (ripening) corresponding to the

mean field theories of Ostwald ripening (Bartelt, Theis and Tromp 1996). Since our distributions are clearly divergent from this behavior, it is also an indication towards the attachment – detachment limited growth.

The small patches left by the decayed wires as seen in the Figure 3.12 is possibly surface alloying centers. Since they show contrast differences in LEEM hence their surface electronic structure have to be distinct from Ag(1 1 1) overlayer.

Microcluster etching at the edges is possibly due to increasing attachment – detachment initiated surface alloying/mixing process. This description fits with increased etching seen around the bigger/matured clusters. We cannot give definitive description without knowing the morphology at a better resolution with a corresponding chemical picture.

3.4.4 Summary

Our study has revealed the following about the Ag on Cu(1 1 0) system.

1. Motion of step contours indicates considerable surface diffusion on Ag(1 1 1)/Cu(1 1 0) even at ~100°C initial temperature.

2. Strain build up beyond saturation coverage of Ag 1.2ML {Ag(1 1 1) overlayer} leads to immediate nucleation/self assembly of Ag nanowires.

3. Nanowires originate at impurity defect sites and step edges where surface diffusion damping gives rise to nucleation centers.

4. Nanowires at a terrace edge grow down - step and then eventually grow up - step keeping the same morphology, alignment and direction.

5. Nanowire growth along [1 $\bar{1}$ 0] direction is highly dependent to the facet structure due to their anisotropic transport of Ag ad atoms along the [1 $\bar{1}$ 0].

6. Growth process of nanowires show high level of interaction among the close neighbors (separation << width) in their growth indicating significant inteρ− wire adatom exchange.

7. Rate of new nanowire nucleations drop with time indicating decreased free energy loss.

8. Rate of nanowire elongation decrease with time indicating saturation of total wire strain and free energy equilibrium with the adatom sea.

9. Growth rate versus length and time indicate oscillatory growth. Similar behavior has been observed in other far from equilibrium systems. This indicate high dynamical response towards growth of wires to the ad atom concentration in the Ag(1 1 1) overlayer.

10. Inter – wire atom transport is mediated by the high surface diffusion among nanowires mediated by Ag(1 1 1) overlayer.

11. Ag nanowire state converts to Ag microcluster state when the system temperature surpasses ~700K.

12. Nanowire decay occurs via Ostwald Ripening. Ripening process is NOT diffusion limited but attachment detachment limited with other limiting steps playing a considerable role.

13. There exists a transition temperature: ~670K where a drastic reduction of nanowires (extinction) is observed.

14. Reduced aspect ratios indicate a lowered but still existing strain effects due to the micro cluster geometry.

15. Ag microclusters show two distinct widths.

16. Microcluster edges exhibits a mixing/surface alloying process which needs to be further explained.

In future studies, it is important to get better temperature measurements as we were handicapped with reading sample holder temperature instead of the sample. Residues left after the extinct nanowires / decayed smaller clusters can be investigated by an STM study. Possible future study should involve *in situ* AES of real time decaying /ripening surface giving measurements of $N(t)/N(0) = I(t)/I(0)$ which will provide us better estimates of parameters associated with ripening and surface diffusion. Further LEEM studies on the system should focus on getting wires under low coverage to reduce inter – wire interactions and to isolate long range interactions.

4 Study of Co Nanodots on Clean Single Crystal Ag(1 1 0) Surface

4.1 Introduction

Epitaxial thin film growth is a vital branch in surface studies. This is not only for the scientific and intellectual curiosity but also of its immense practical and technological implications. Range of epitaxial growth extends from the domain of electro chemistry where there are numerous examples of heterogeneous catalysis to the epitaxial nanophase materials which are used for wide array of technological applications. Specifically metal on metal thin films are of particular importance to the electronics industry as many new technological breakthroughs depend on them. Structure and morphology of magnetic thin films on non magnetic substrate are of greater significance due to their impact on phenomena such as surface magnetic anisotropy and interlayer exchange coupling (Bruno 1995).

Ferromagnetic/nonmagnetic/ferromagnetic layered films are particularly important in Giant Magneto-Resistance (GMR) which was found in 1988 independently by 2007 Physics Nobel Laureates Albert Fert*et. al.* (Baibich, et al. 1988) and Peter Grünberg *et. al.* (Binasch, et al. 1986)is one of the novel phenomena in physics which have already been used in electronic devices. Although the initial discovery of GMR was with the Multilayer, of the three types of GMR: Multilayer, Spin-valve and Granular, the most application oriented is the Spin-valve GMR. In next generation spintronic and spin dependant devices, Spin-valve GMR will play a dominant role.

It is important to obtain high GMR while decreasing the size of the resulting residual magnetic field. It also depends on the relative orientations of the layered films as shown for oriented Co-Pt films grown on GaAs substrate (Lee, et al. 1990). Films with high long-

wavelength surface roughness (Orange peel coupling in Neel's model) (Nẽel 1962)are not desirable as it increases the residual fields by giving rise to magneto static coupling on the surface (Egelhoff Jr., et al. 1996). Further there is evidence that the film thickness also plays a crucial role in determining the coercivity of the film (Camarero, et al. 2000) (Kief, Mankey and Willis 1991) which will affect the GMR. Therefore study and elucidation of controlled epitaxial growth, mechanism and structure of layer by layer, ferromagnetic thin films/non magnetic films is hugely important even if taken purely by the application oriented standpoint.

Our system is Co deposited by means of MBE (Molecular Beam Epitaxy) on clean single crystal Ag(1 1 0). Here we approach to elucidate the structure, morphology and possible subsurface migration of Co on clean Ag (1 1 0) substrate. Co being ferromagnetic with a Curie point of 1388 K (1114°C) on Ag (being diamagnetic) multi-layers has shown GMR (Pratt Jr., et al. 1991) as expected. As expected, GMR effect was observed in Fe or Co films layered with alternate films of non magnetic metals like Ru, Pt, Ag, Au or Cr (Egelhoff Jr., et al. 1996) (Gijs, Lenczowski and Giesbers 1993).

Previous studies of Co growth on different surfaces have shown multiple growth structures and mechanisms. In some semiconductor surfaces like GaAs (1 1 0) it has been shown to facilitate preferential migration of Ga against As atoms, progressively altering the stoichiometry of the substrate (Xu, et al. 1987). On Au (1 1 1) (nearest neighbor distance 2.88Å) non pseudomorphic growth of Co (film on the substrate is Co(0001) with nearest neighbor distance of 2.51Å) films have been observed and it is been argued that is due to the ~14% lattice mismatch giving rise to strain fie (Marsot, et al. 1993).

Richer behavior has been observed on Co on Cu surfaces. Strong evidence of Frank-van der Merwe (FM),layer by layer coverage growth (90% surface coverage at ~3 to ~4ML) of Co on Cu (1 0 0), Cu (1 1 0) and Cu (1 1 1) at low temperature (~80K) has been stated (Kief and

Egelhoff Jr. 1993). It is suggested this is due to low mobility at low temperatures. Furthermore it has been observed at RT (~300K) growth mode deviate from FM. At RT growth of Co on Cu (1 0 0) it is been theorized of Cu segregation to the top of Co layer from the substrate by a mechanism of fast inter-diffusion via formation of microscopic pin holes on the Co layer. It was also shown Co segregates under the bulk Cu substrate (Schmid, et al. 1993).

Most of these mechanisms are attributed to the surface free energy, interface free energy and strain energy where minimizing system total free energy is the driving thermodynamics of the mechanism. Equally crucial is the growth kinetics which will also determine the state of the system at each stage of varying temperature and coverage. These observations in different systems involving Co are important in providing insights to the behavior of Co under hetero epitaxy. In the Co on Cu system the surface free energies of the components are σ_{Co} = 2.78 Jm^{-2}, σ_{Cu} = 1.93 $Jm^{-2}$and the interface free energy $\sigma_{CoCu\ (1\ 1\ 1)}$ = 0.2 Jm^{-2} (Kief and Egelhoff Jr. 1993) (Schmid, et al. 1993) (Vitos, et al. 1998). These with the kinetic limitation of Cu having higher mobility over Co on the Cu substrate enable the formation of the subsurface Co layer. In contrast $\sigma_{Ag(1\ 1\ 0)}$= 1.24 Jm^{-2} [21] which is evidently lower than σ_{Cu} of any facet of Cu, and interface energy is σ_{CoAg}= 0.6 Jm^{-2}, (Mezey and Giber 1982) when considered the lattice mismatch between Co and Ag gives ~13%, converse to Co and Cu have a very low lattice mismatch ~2%.These factors illustrate the difficulty of having high area of interface between Co and Ag.

One approach to the problem is using surfactants. This helps to lower the surface free energy, of the substrate layer and some cases introduce the novel kinetic pathways to the system. Drop of surface free energy will enable the surface wetting by the absorbate (Egelhoff Jr. and Steigerwald 1989). Further the surface strain energy and anisotropy may be altered by a particular surfactant as in the formation of (3x1) reconstruction on Co (1 1 0) layer when grown on Cu (1 1 0) with O (Tolkes, Struck, et al. 1998). Type of surfactant typically chosen to

establish the necessities of the desired surface and the growth dynamics as layered Co on Cu can be achieved with O or In as the surfactant (Egelhoff Jr., et al. 1996) (Tolkes, Struck, et al. 1998) (Tolkes, Struck, et al. 1998). Kinetic alterations to the process is seen though Ag on Ag (1 1 1) system with Sb the surfactant (Rosenfeld, et al. 1993) (van der Vegt, et al. 1992). As it can be seen it is extremely versatile to find a surfactant that gives optimum growth conditions for a system on the application standpoint.

In this chapter it will be shown at high coverage Co self assembles into spherical 3D nanodots on the substrate possibly driven by minimization of surface and interface free energy which at higher coverage seems to be stable and do not coalesce and keeps distinct boundaries even when stacked next to each other. Upon annealing successively at high temperatures Ag segregates to the surface by exchange transaction of Co to the bulk selvage. In the bulk Co possibly forming a phase of spherical clusters under the substrate surface to minimize the interface free energy, $\sigma_{Co\text{-}Ag}$.

Experimentally STM has been carried out on low and high Co coverage on Ag (1 1 0) surface. These surfaces were examined after annealing to investigate the surface in order to investigate the Co cluster morphology and possible subsurface migration against temperature increments. LEED (Low Energy Electron Diffraction) was done on clean Cu(1 1 0) to establish the surface structural integrity and order, then at low and high Co coverage to determine the crystal structure of both Co islands and post annealed, segregation exposed Ag surface. LEED is also done sequentially, while annealing the system to higher temperatures. Auger Electron Spectroscopy at initial stages to establish the surface integrity against contaminants and after sputtering cleanness. It was also used on low and high Co coverage on Ag(1 1 0) and following successive annealing at higher temperatures of the system to see Co migration/segregation in to the Ag bulk.

4.2 Experimental Procedure

Experiment was carried out in the ultra high vacuum chamber (UHV), (base pressure ~2 x 10^{-10} Torr) in the Surface Science Lab in the Department of Physics and Astronomy at LSU. Ag (1 1 0) substrate is 5mm in diameter and 3mm thickness. Sample mount and the picture of the Ag crystal with the Tantalum sample holder is shown in chapter 1. Thermocouples connected to the sample enabled direct real time *insitu* measurements of substrate temperature.

Ag (1 1 0) crystal was prepped by ultra clean - static Ne sputtering at ~5 x 10^{-5} Torr at RT for 30 min followed by annealing to 823K for 10 min. Cold trap was kept filled with liquid N_2 to keep the vacuum conditions better. To get the optimum surface we repeated this procedure, twice for each step and some time more where and when we needed a clean Ag (1 1 0) surface.

Temperature variation during the deposition was also mediated by a sample holder where it's possible to change the temperature in the range 123K-1200K. Thermal heating was obtained by both filament (radiative) and e-beam heating. While annealing, the holder was air cooled by sucking air through the integrated tubing system. Same system was used when needed a low temperature measurement of the sample through liquid N circulation.

Co was evaporated on Ag (1 1 0) by a Co evaporation source (MBE) where both thermal and an e – beam were used to sublimate Cobalt and deposit on Ag(1 1 0). Base pressure of ~8 x 10^{-10} Torr was maintained during Co deposition.

In-situ Auger and LEED analysis on the Co deposited Ag (1 1 0) substrate were carried out by the respective equipment which were as mentioned directly connected to the main chamber. erLEED used for LEED analysis was by SPECS instruments and the Auger was CMA type. STM used for the analysis was as mentioned in detail in chapter 2 is a variable temperature Arhus STM, where substrate temperature could be varied within the range 123K-373K. Temperature regulation was obtained by the Zener Diode (heating) directly attached to the

bottom of the STM and the liquid N (cooling) circulation heat transfer from the STM block. Chromel-Alumel thermocouple wires were attached to the STM thus giving a very accurate temperature of the substrate when on the STM. For each part of the experiment substrate cleanness is established after two sputter anneal cycles followed by taking an Auger spectra to determine the surface impurity concentration and a Low Energy Electron Diffraction (LEED) to verify the proper crystalline Ag (1 1 0) surface. The coverage of Co on the Ag(1 1 0) surface was calibrated by STM, LEED and AES measurements.

4.3 Data and Observations

4.3.1 Preliminary Features

Co is a transition metal element existing in two different allotropic forms under normal pressure. At RT Co has a hexagonal closed packed (HCP) crystalline structure with a = 2.507Å and c = 4.07Å (space group $P6_3/mmc$). This is stable below 690K. At elevated temperatures Co has a face centered cubic (FCC) structure (space group Fm3m) with a = 3.544Å. (Emsley 1998).It is a ferromagnetic metal with highest known Curie point of 1394K (Encyclopædia Britannica. 2008). Calculated surface energies for varying facets assuming HCP lattice, give (0001) = 2.775Jm^{-2} and (10 $\bar{1}$0) = 3.413Jm^{-2}[(we have taken the mean surface energy for the two surface layers of (1 0 $\bar{1}$ 0)[§]] (Vitos, et al. 1998).Ag is also a transition metal with FCC structure (with space group Fm3m) where a = 4.086Å. Calculated surface energy for varying facets give (1 1 1) = 1.172Jm^{-2}, (1 0 0) = 1.200Jm^{-2}, (1 1 0) = 1.238Jm^{-2} (Vitos, et al. 1998) (Jiang, Lu and Zhao 2004). Comparing Co and Ag heat of mixing between the species; it is evident the value is significantly high [ΔH = +28$kJmol^{-1}$ (Miedema 1978)]. When considered the binary alloy phase diagram of the two-component Co and Ag system, Co solubility in Ag bulk is between 0.0002

[§] A typical HCP structure has two (1 0 $\bar{1}$ 0) surfaces which depend on the first interlayer distance $d = (\sqrt{3}/6)\cdot a$ and $d = 2\cdot(\sqrt{3}/6)\cdot a$. In full charge density (FCD) calculations they give differing surface energy values (Vitos, et al. 1998).

and 0.009 atomic percentage Co in the temperature range 873C˚ to 1213 ˚C (1146.16˚K to 1486.16˚K) (ASM International 1995). These factors make system practically immiscible at temperatures less than ~700˚C (~934K).

4.3.2 LEED Investigation of Co on Ag(1 1 0)

LEED was taken on the Co deposited Ag(1 1 0) surface for two different coverage at ~1ML and ~8ML at different instances. This is to investigate possible surface crystalline structure and surface modification coupled with annealing. Initial LEED images were taken for the bare clean Ag(1 1 0) at RT. Subsequently LEED images were taken, immediately after Co deposition. Finally LEED images were taken with the system annealed incrementally from 300K (deposition temperature) at incremental 100K intervals for 5 min at each instance. Subsequent to the annealing, system was allowed to cool down to RT prior to the LEED was taken. This is meant to minimize the Debye-Waller factor[**] on the surface structure that is reflected on the LEED images.

Figure 4.1 shows LEED images taken with the sequential annealing of system with Co deposition ~ 0.5ML (relatively low coverage). In figure 5.1, A shows the LEED after deposition. From B to F gives the annealing steps 400K, 500K, 600K, 700K and 800K. In both figure 5.1 and 5.2 post annealed visible Ag(1 1 0) LEED images do not have (0, 0) spot as it was covered with screen holder. Spots which are clearly visible include (0, $\bar{1}$), ($\bar{1}$, 0) , (0, 1) and (1, 0).

Figure 4.2 shows LEED images taken with the sequential annealing of system with Co deposition ~ 4ML (relatively high coverage). In figure 4.2, A shows the LEED after deposition. From B to G gives the annealing steps 400K, 500K, 600K, 700K, 800K and 900K. For both

[**] Scattered intensity due to vibrating lattice is: $I_g = I_o \exp(-\alpha\langle u^2\rangle|g^2|)$ thermal mean square amplitude of simple harmonic motion of the centers is $\langle u^2\rangle$, the reciprocal vector associated with the respective oscillation is $|g|$ and I_o is the scattered intensity of the rigid lattice. α is a constant associated with the dimensionality of the motion. *Debye - Waller factor* is the exponential.

figures 4.1 and 4.2 we have LEED taken at beam energy ~50eV.

As seen in figure 4.1 at coverage LEED just after deposition had considerable amount of background with no coherent LEED pattern indicating either surface structure is covered with diffuse Co or have a completely random distribution of structures destroying any periodicity. Depending on the coverage reemergence of the Ag(1 1 0) surface LEED pattern vary with annealed temperature.

At low coverage condition did not improve until the system is annealed to ~400K. At ~400K only one or two diffuse spots were observed with lot of background. Annealing at higher temperatures made the LEED pattern successively better. At 800K LEED gave the sharpest images after deposition. After annealing we see no change in surface compared to Ag(1 1 0) clean surface, apart from the apparent increase in back ground. Therefore LEED shows no superstructure different form the substrate surface Ag(1 1 0).

When considered ~4ML coverage the similar results were seen. Initial deposition gave the diffused back ground and no structure. When annealed the spots appeared comparatively later after being annealed at 600K. Surface gave best images after the highest annealing. As in the low coverage case, the post annealed surface does not show any reconstruction. Interestingly we have not seen the surface completely restored after even annealed at 800K-900K. Spots are little diffused with slight back ground present.

Annealed surface show no reconstruction by the LEED at the end of the annealing; Ag(1 1 0) surface is exposed at the end. This being said it is interesting to see some streaking on the emerging LEED pattern that runs [0 0 1] direction on the surface. This streaking pattern starts at LEED image E and can be seen F through G in figure 4.2. But not present on the LEED images of the sub monolayer coverage (figure 4.1). Apart from this there are clear indications of surface being restored at the end of the annealing process further implying deposited Co has been

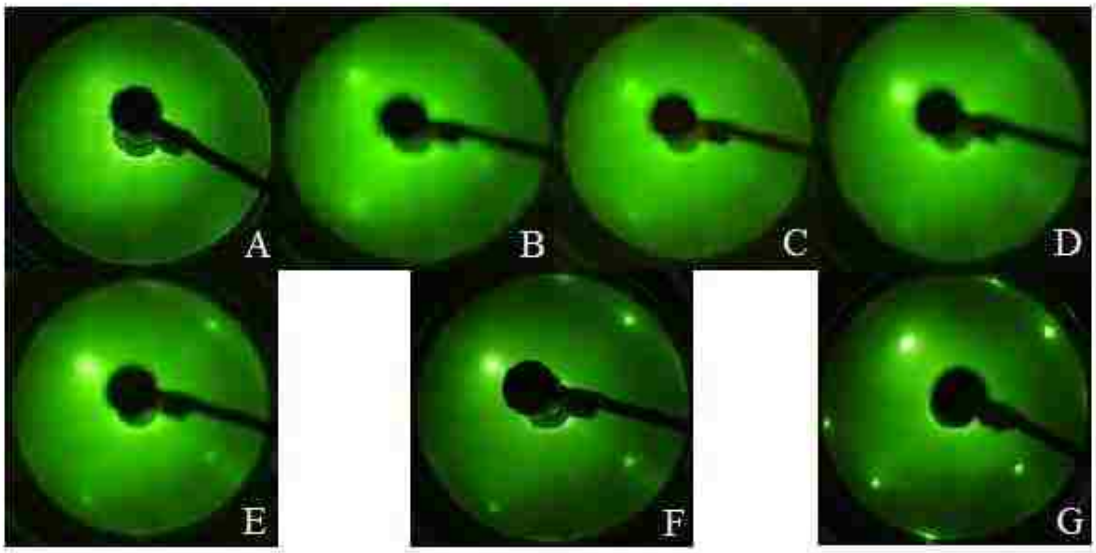

Figure 4.1 LEED images at coverage of ~0.5ML of Co on Ag(1 1 0). Images were taken at LEED energy ~50eV. Image A is taken just after deposition. Images, from B to F show in incremental annealing for a time interval of 5 minutes, at 400K, 500K, 600K, 700K and 800K. G is taken for clean Ag(1 1 0). [0,0] is not seen as it is covered by the screen holder in the middle.

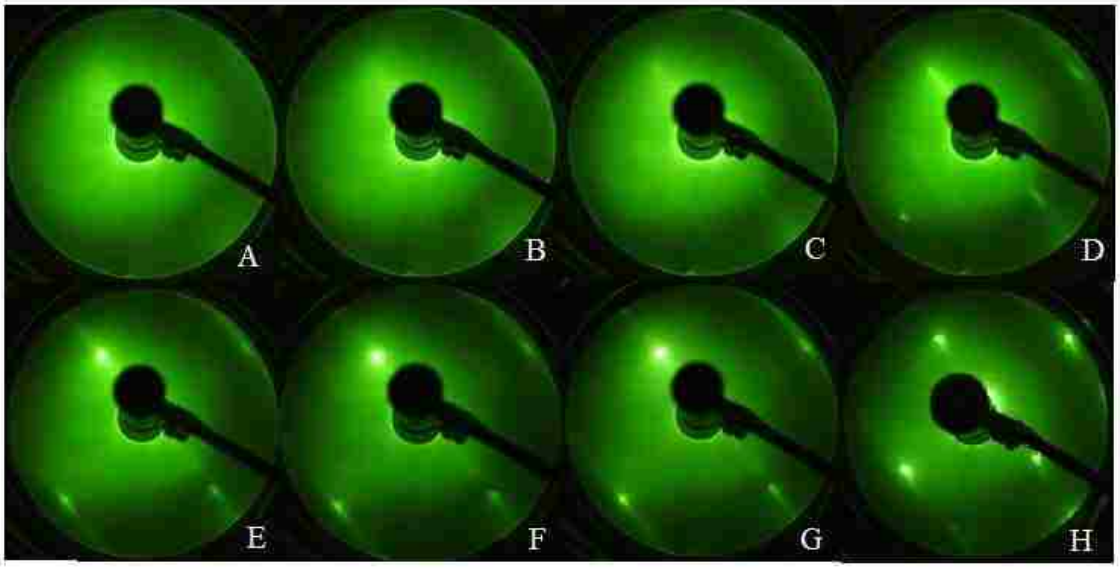

Figure 4.2 LEED images at coverage of ~4ML of Co on Ag(1 1 0). Images were taken at LEED energy ~50eV. Image A is taken just after deposition. Images, from B to G show in incremental annealing for a time interval of 5 minutes, at 400K, 500K, 600K, 700K, 800K and 900K. H is taken for clean Ag(1 1 0). Here too [0,0] is not seen as it is covered by the LEED screen holder in the middle.

removed from the surface without Ag(1 1 0) surface being changed.

We propose a possible sub surface segregation process to account the displacement of deposited Co on Ag(1 1 0). Further it is possible to observe the onset of the LEED pattern at the end of annealing depends on the initial Co coverage. Implying higher the Co coverage on the surface longer and hotter it needs to be annealed in order to drive Co into the Ag selvage.

4.3.3 Auger Electron Spectra for the Co on Ag(1 1 0)

Surface deposition of metal on metal systems gives characteristic AES curves for deposition intensities dependant on coverage (Luth 2001). To observe this behavior of the AES intensities on deposition, Co and Ag AES intensity were measured with incremental Co deposition on the Ag(1 1 0) surface. Peaks selected for the Auger analysis were Ag [356eV] (Childs and Hedberg 1995)(corresponding to MNN transition) and Co [775eV] (corresponding to LMM transition). Peak to peak (pp) intensities of Ag [356eV] and Co [775eV] was recorded at RT (~300K). This is shown on Figure 4.3. The graph is a typical AES deposition curve of straight island: VW (Vollmer–Weber) mode. We see a sudden drop (Point A to B) in the Ag[356eV] intensity, possibly a surface goes through a mode where the total Ag cross section undergoes a pronounced change resulting marked intensity drop. Further during the same instance we see no marked alterations in Co [775eV] increase.

This implies the process is comparatively surface oriented[††]. We have measured the intensities in 4ML steps due to the respective deposition rate and time. We infer the drop of Ag intensity has occurred at much earlier Co coverage and it was not possible to observe the instance of the drop as we have measured the intensity past the point. We propose a drop point (C on the Figure 4.3) which occurs at much earlier coverage.

[††] Ag [356eV] signal corresponds to ~6Å (2-3 atomic layers) in electron mean free path while Co [775eV] correspond to ~12Å (4-5 atomic layers) in mean free path.

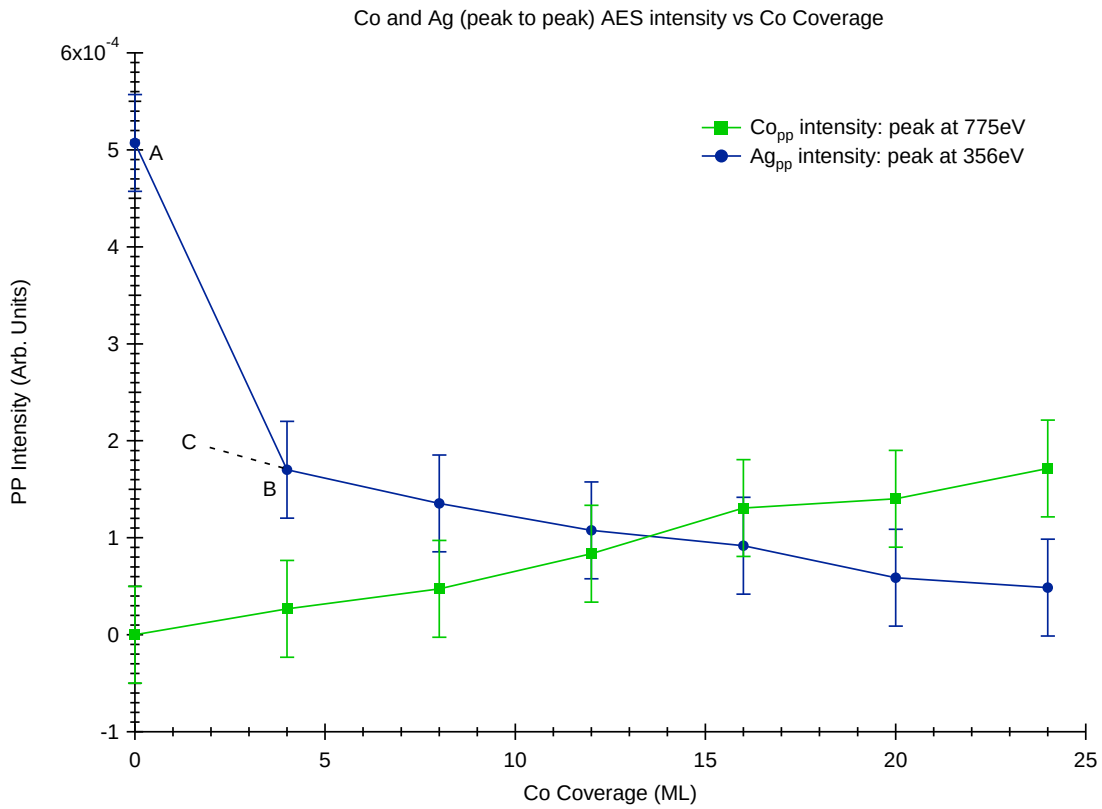

Figure 4.3 Ag and Co AES intensity variation with increasing Co coverage. Measurements were at RT (~300K)

In overall the intensity curves behave like VW mode of island growth as the slopes are less steep. This is verified by our STM observations at initial stages of Co coverage where we only see islanding with finite size islands saturating the surface with increasing Co coverage. At long range high coverage (~5ML < θ_{Co}< ~20ML) overall intensity curves of Figure 4.3 resembles layered FM mode. This is clearly evident by the STM analysis where at high coverage (θ > 8ML) we see saturated surface covered with finite uniform sized Co clusters giving a layered outlook in the large length scales. This is readily shown on the STM images with high coverage (Figure 4.13).

In order to gain better understanding of the annealing triggered segregation process of Co into the Ag bulk, AES analysis was carried out at each instance after the annealing of Co deposited surface. Auger spectra of Ag (1 1 0) surface before and after Co evaporation were taken, in order to measure the coverage achieved. Co and Ag AES spectra give a direct measurement of elemental concentration because the peak to peak elemental signal is coupled to the respective concentration of the elements. Primary Auger e-beam energy was set at 3kV. Data was collected for three instances of Co coverage on Ag(1 1 0): ~0.5ML, ~2ML and ~8ML. Peaks selected for the Auger analysis were Ag [356eV] (Childs and Hedberg 1995)(corresponding to MNN transition), Co [53eV] (corresponding to MNN transition) and Co [775eV] (corresponding to LMM transition). Peak to peak (pp) intensities of Ag [356eV], Co [53eV], and Co [775eV] was recorded at RT (~300K). After annealing for 5 min at 400K, 500K, 600k, 700K, 800K and 900K consecutively pp intensities were again measured. At each instance Auger was taken after cooling down to the RT. For each temperature minimum of 2 spectra were taken and then the mean of the 2 peak to peak values were taken for the analysis.

These data are then normalized by taking Co [53eV] pp/ Ag [356eV] pp and Co [775eV] pp/ Ag [356eV] pp (Thompson and Vaughan 2001), thereby making each spectrum, Auger

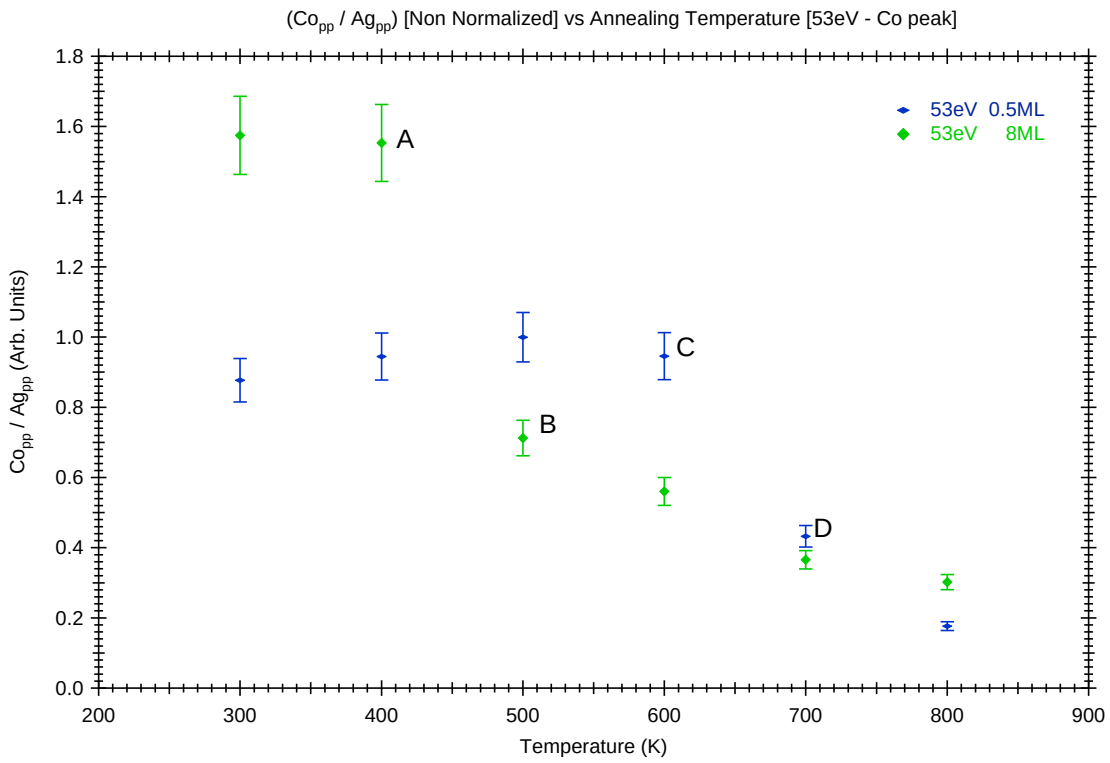

Figure 4.4 Auger intensity ratios of {Co [53eV] / Ag [356eV]} for Co coverage of ~0.5ML and ~8ML annealed at different temperatures for 5 min at each instance.

spectrometer setting independent. Respective AES spectra are shown on Figure 4.4 and Figure 4.5.Considering the mean free paths of the electrons in Ag at the energies of 53eV and 775eV, corresponding probe depths of ~6 Å and ~12 Å (Thompson and Vaughan 2001) (Penn 1987) were obtained. Figure 4.4 shows a distinct point (A) of onset for the reduction of Co surface concentration is due to annealing at high coverage (~8ML). Similar observations for the low coverage (~0.5ML) were also taken the point denoted B. In the case of ~8ML coverage point is after annealing at ~500K. When considered the low coverage (~0.5ML) it is possible the corresponding point of onset but the point B is at much higher temperature (~700K).

These points imply at low coverage the initiation Co reduction has a higher activation energy compared to the high coverage ($T_B > T_A$). Important factor to consider is the electron mean free path of ~6Å in Ag which correspond to 53eV Co signal. Data in the Figure 4.5, by the same reasoning corresponds to a mean free path of ~12Å (higher electron energy at 775eV). In the case of Co high coverage (~8ML) we see the previously observed trend of Co reduction onset points. These points are shown on figure as A(at ~500K), B (at ~570K) and C (at ~700K) for decreasing initial Co coverage. When compared the Co reduction activation at each coverage it is possible to observe the same trend of lower the coverage higher the activation temperature ($T_C > T_B > T_A$).

In order to observe the data without the dependence of the coverage these ratios were again divided by the ratios taken just after the Co evaporation (t = 0). Therefore the plotted data in Figure 4.6 and Figure 4.7 consecutively obtained for different coverages of the intensity variation of {Co [53eV]/Ag [356eV]}/ {Co [53eV]/Ag [356eV] at t=0} and {Co [775eV]/Ag [356eV]}/ {Co [775eV]/Ag [356eV] at t=0} versus variable annealing temperatures. Similar to the case of non normalized intensity ratios it is possible to observe the onset point of the Co reduction in Figure 4.6.It is possible to observe the onset points A and B as in the

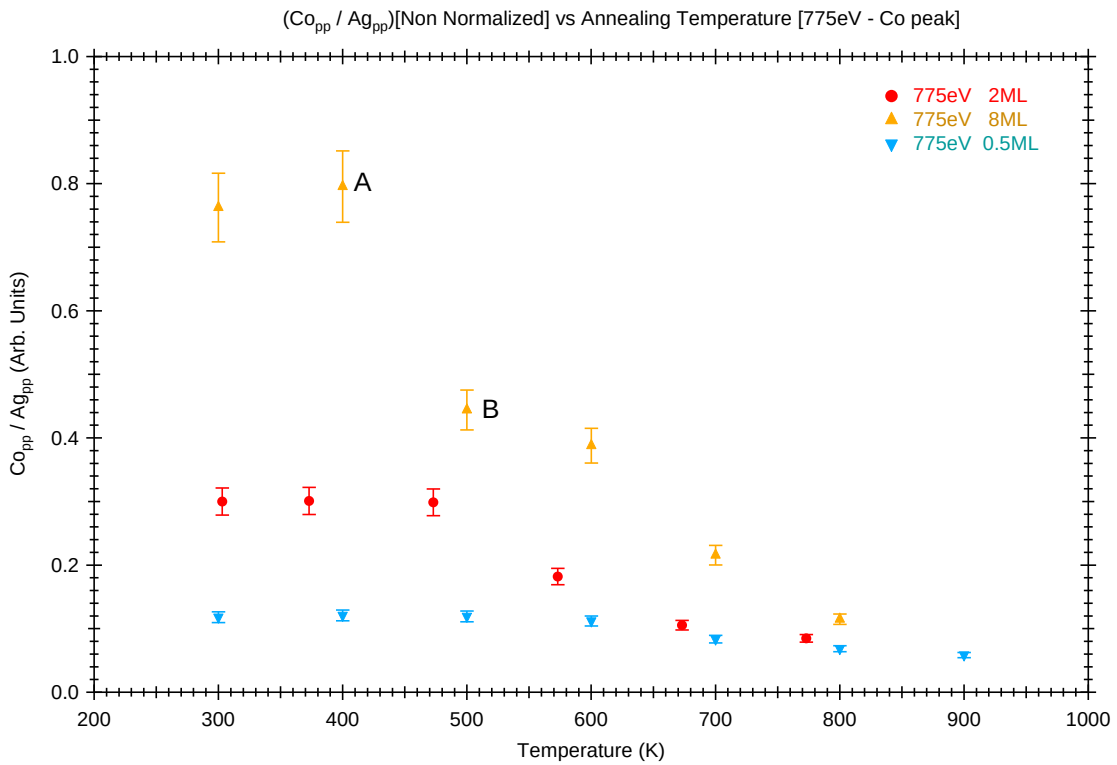

Figure 4.5. Auger intensity ratios of {Co [775eV] / Ag [356eV]} for Co coverage of ~0.5ML, 2ML and ~8ML annealed at different temperatures for 5 min at each instance.

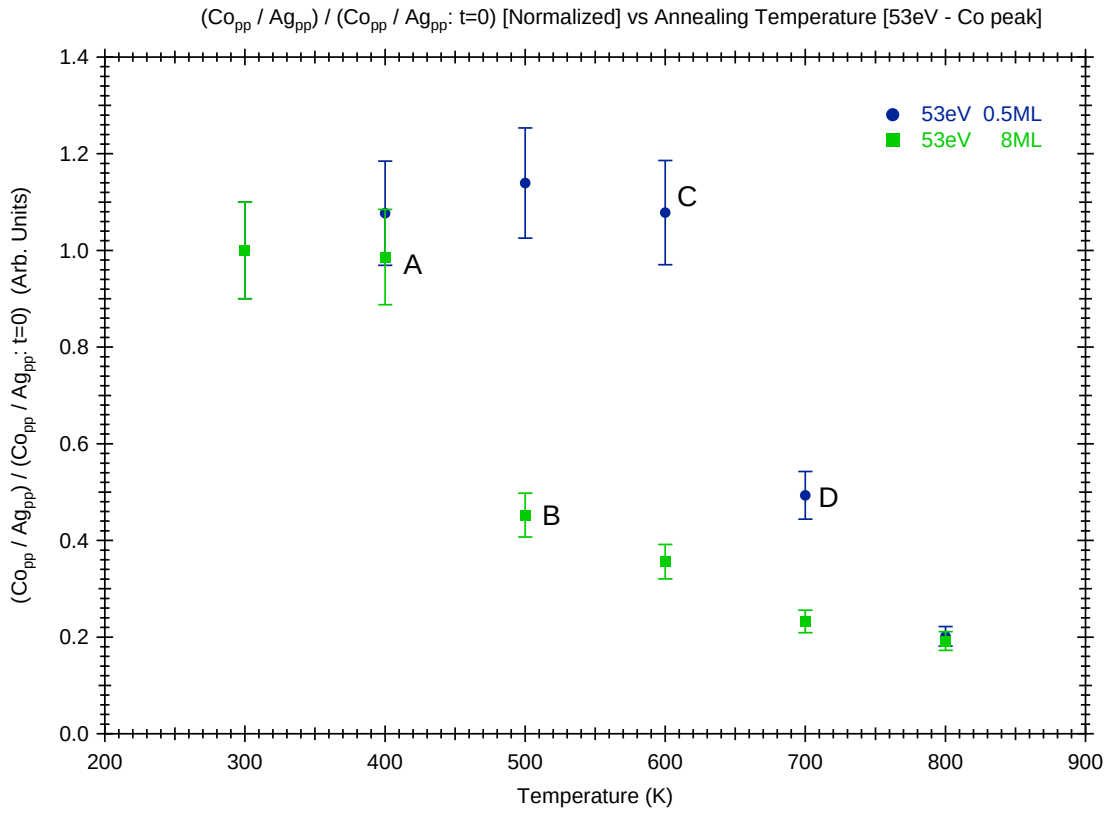

Figure 4.6 Auger intensity ratios of{Co [53eV]/ Ag [356eV]}/{Co [53eV]/ Ag [356eV] at t=0} for Co coverage of ~0.5ML and ~8ML annealed at different temperatures for 5 min at each instance.

previous case and with the same on set temperatures. The identical observations can be said about the figure 4.7 which correspond to a mean free path of ~12Å. Here too it is possible to observe the onset points A, B and C. Considering the AES plots it is possible to say the onset temperature is directly coupled to the deposited Co coverage. Surface concentration of Co depletion initiation falls at the onset point range 500K to 700K depending on the coverage. Interestingly the onsets of this is seen in both energies of 53eV and 775eV having different mean free paths of ~6Å and ~12Å. From Figure 4.4 and 4.7, it is also evident after successive annealing Co concentration tends to zero, both at ~6 Å (53eV) and ~12 Å (775eV) given the annealing time is increased or the temperature is increased. It is possible to estimate of Co concentration after the finite sequence of annealing events using sensitivity factors of Ag (0.95 for MNN 356eV peak) and Co (0.29 for LMM 775eV peak) with the intensities measured through the Auger spectra (Thompson and Vaughan 2001).

These calculations show reduction of Co concentration is 40-60%after annealing. Depending on coverage, reduction varies, as for ~8ML coverage, reduction is ~61% and for ~0.5ML coverage, it is ~42%. The obtained data trends indicate this fraction of initial reduction will go up with higher coverage.

This Co concentration reduction pertains to an electron mean free path of ~12 Å (about 4 Mono Layers) from the surface. Although it is interesting to see how the concentration varies at ~ 6 Å (about 2 mono-layers) depths under the surface, an accurate sensitivity factor for Co 53eV is not available as the Auger peaks at energies below 100eV are less accurate due to distortion by local magnetic anomalies and local surface charge buildup. According to the calculations, after the annealing the Co concentration has not changed considerably which means surface segregation is not particularly a fast process relative to temperature. Data shown on Figure 4.4, 4.5, 4.6 and 4.7 the clearly indicate Co reduction.

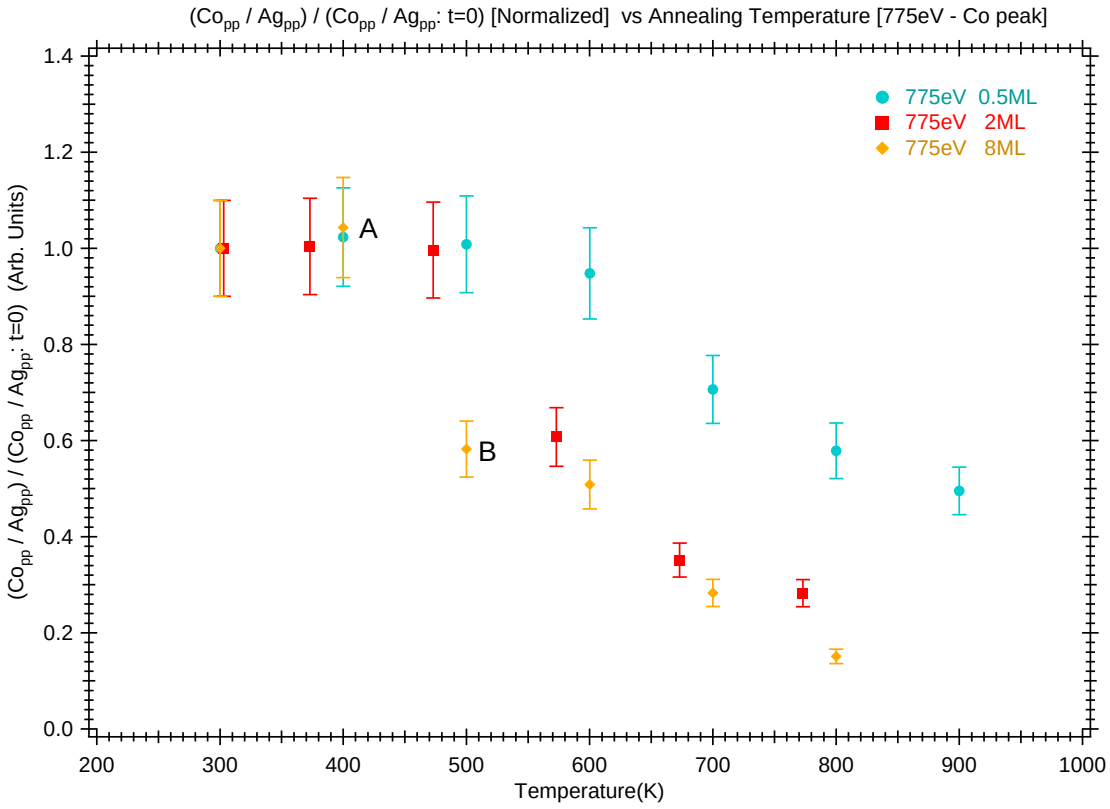

Figure 4.7 Auger intensity ratios of {Co [775eV] / Ag [356eV]} / {Co [775eV]/ Ag [356eV] at t=0} for Co coverage of ~0.5ML and ~8ML annealed at different temperatures for 5 min at each instance.

There are several possible mechanisms by which the Co concentration can deplete on the surface due to thermal energy increment: diffusion assisted agglomeration in generating bigger clusters, Ag capping of the Co and Co subsurface segregation. While it is not possible to conclusively prove, from AES data it is highly likely considering the kinetics and thermodynamics of the system. This is a common route taken in many heteroepitaxial systems to reduce surface free energy. Similar behavior has been observed in Ni on Ag(1 1 1) and Ag(1 0 0) (Rolland and Aufray 1985) (Aufreyl 1994). Further there are studies of Co epitaxially grown on Cu(1 0 0) showing similar Cu capping Co behavior upon annealing (Schmid, et al. 1993) (Li and Tonner 1990). These observations coupled with the free energy arguments we consider later make it a very plausible mechanism.

Scenario most consistent with our data is a possible agglomeration due to surface diffusion as a mechanism which is responsible for the depletion of Co. This is clear in STM images; as we see indications of agglomeration in higher/lower coverage. This is better suited to occur in low temperatures as surface diffusion mediated reactions do not need to be excited with higher energy[‡‡]. For Cu surface diffusion activation energy is 0.57eV (Prutton 1998), this indicate a possible Ag surface activation energy of ~1eV. Factors that have to be considered: typically (1 1 0) surfaces have higher activation energies for FCC metals compared to (1 0 0) and (1 1 1) surfaces (Agrawal, Rice and Thompson 2002). Still the surface diffusion energies comparative to subsurface diffusion is lower. Another important reason for the agglomeration to be realistic is, at lower coverage this mode is effectively shut off due to Co nanodots being wide apart and having lower number density. This indeed shows on Auger spectra as lower the coverage, higher the energy needed to see a drop in concentration by the initial mechanism. Subsurface migration of Co should activate at a comparatively high temperature. We will

[‡‡] Room temperature corresponds to ~1/40eV.

Figure 4.8 Distributed Co islands on Ag(1 1 0) surface. Uniformity of the islanding on the surface is evident. Co coverage is 0.7ML at RT. FOV 200nm × 200nm.

observe this in the following STM images.

In some cases we see an initial increase of the Co/Ag signal with annealing (Figure 4.4 to 4.7) is believed to be due to a slight error in data as all the graphs are consistent with the description provided.

4.3.4 STM Analysis of Co on Ag(1 1 0)

Further light on Co structure on the surface and segregation due to annealing is revealed by the surface morphology and structure examination by STM (Scanning Tunneling Microscopy). As previously explained the substrate was sputter cleaned and annealed prior to the Co deposition Surface integrity was verified by LEED. Co coverage was calibrated initially by STM and then Auger spectroscopy (AES).

At sub monolayer Co coverage at low temperature (150K) alloying mechanism between Ag and Co has been observed (Kizilkaya and Sprunger, Unpublished transactions. n.d.). This is mediated by Co atomic segregation in to the Ag surface layer by squeezing out Ag atoms by Co. Ag act as a surfactant arranging on the Ag lattice epitaxy, in single to bi-atomic heights. These Ag structures are aliened to [1 $\bar{1}$0] direction.

This is shown in especially at low Co coverage. When the surface is exposed to oxygen, O atoms preferentially bind to Co which is in the depressions of the surface; because of the large sticking probability of Co to O compared to that of Ag. This enables the determination of Co sites on the surface. Although our data concentrated on higher coverage and on or above RT temperatures, previous observations are consistent with our STM analysis (Figure 4.9) were we see clear retention of orientation for few structures low Co coverage with Co clusters with aspect rations larger than one. When the temperature increased to RT there surface alloying phase is no longer thermodynamically and kinetically a viable state.

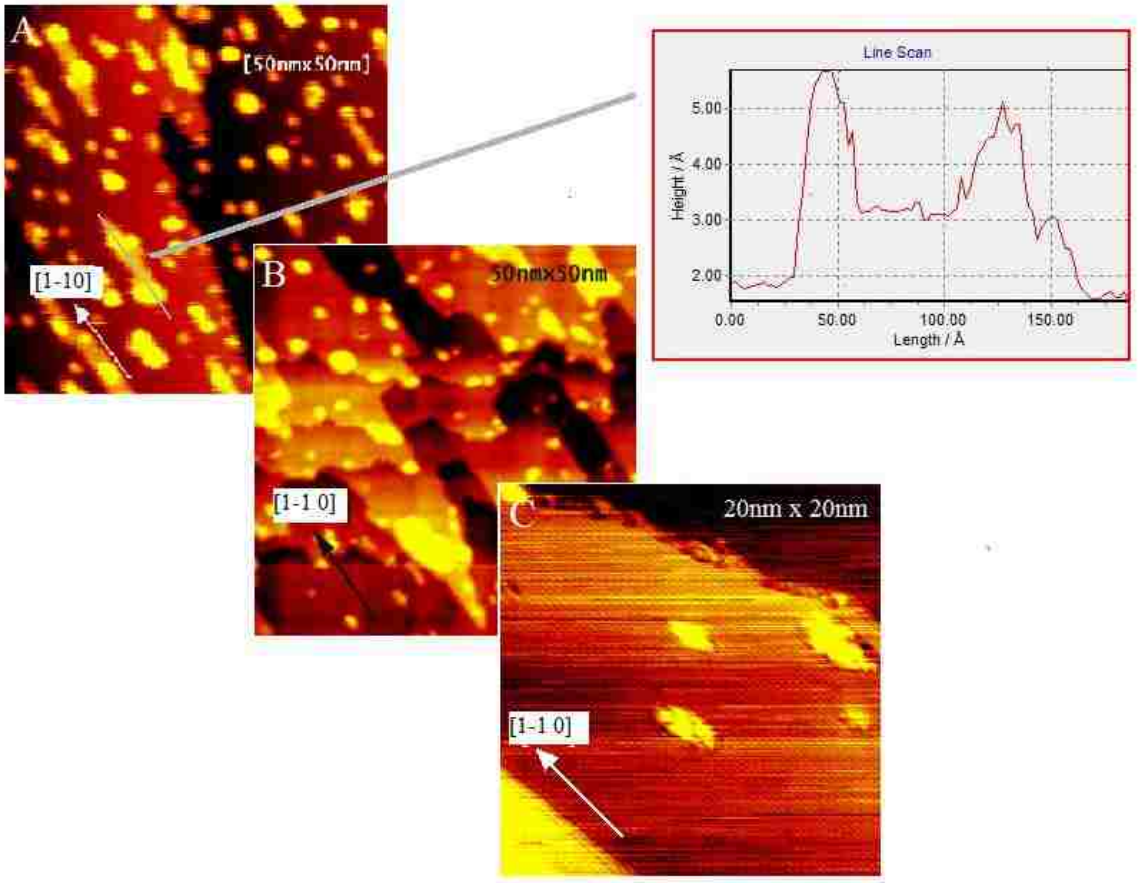

Figure 4.9 Low coverage (0.7ML) Co on Ag. Figure A is just after deposition, figure B is after annealing at 200˚C for 5 min and figure C is after annealing at 400˚C for 5 min. Inset shows an island oriented [0 0 1] and with edges growing Co on the second layer (bi-layer islanding).

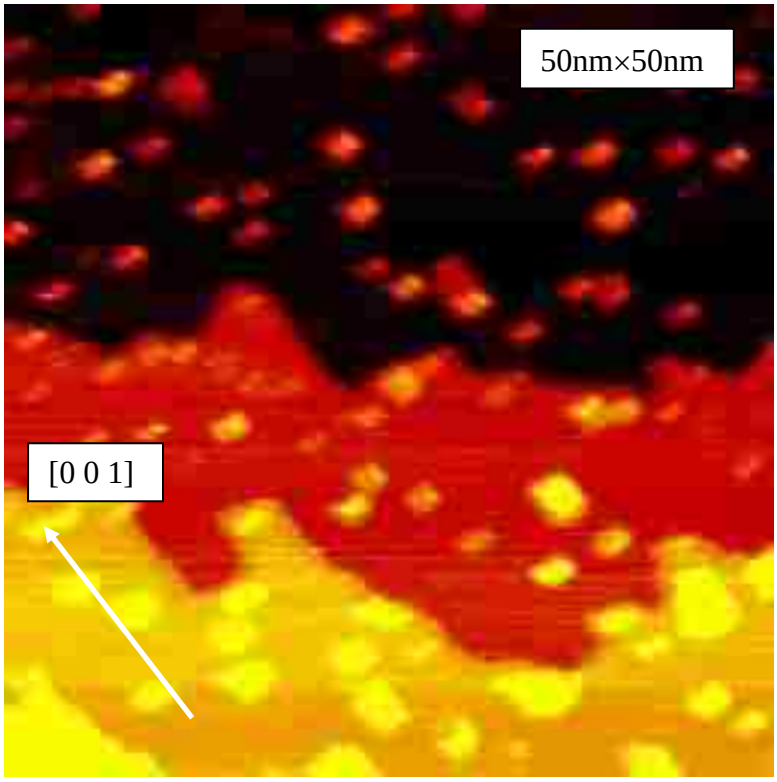

Figure 4.10 Co ~1ML deposited on Ag(1 1 0) at RT. Co Nanodots nucleating near the surfaces can be readily seen.

Therefore, Co ends up making clusters on the surface. These Co nanodots are possibly covered with Ag. The longer dimension of the Co clusters at this low coverage is oriented towards Ag[1 $\bar{1}$ 0].

But this linearity is neither uniform nor dominant among clusters (Figure 4.9). Most of these clusters never elongate upon further deposition of Co, their geometrical shape is more to the circular form but never a perfect spherical dome, more of an oval shape. This is possibly due to the anisotropic strain on the Ag(1 1 0) surface. Further the surface anisotropy will give rise to divergent diffusion rates along [0 0 1] and [1 $\bar{1}$ 0]. Both these effects will tend to change the isotropy of the Co cluster. They will be competing with the minimization of free energy as the minimum surface for a given volume is always a spherical surface and that is tended by the thermodynamics of the system. By observing the cluster geometry it is safe to state the minimization of free energy seems to weigh over the strain effects. Of the clusters those elongate, the edges of the clusters we see islanding. In the low coverage regime (0.5ML < θ < 1ML) we observe more of a rectangular/square shape for the Co clusters.

Distribution of clusters is almost uniform on terraces, but close inspection reveals a rise in number density of the clusters near the step edges (Figure 4.10). When compared clusters near the step edges are not regular to Co clusters seen on the terrace sites, rather they seem to be nucleation centers for the cluster formation. Within experimental limits Co flux on the surface is uniform. Except the step edges everywhere on the terrace diffusion has symmetric (except the anisotropy due to the [0 0 1] and [1 $\bar{1}$ 0] directions) the freedom under the influence of anisotropic surface strain. But at a step edge the symmetry is broken hence diffused and impinged Co accumulates. This is due to the Ehrlich-Schwoebel (ES) barrier (Ehrlich and Hudda 1966) (Schwoebel and Shipsey 1966) which necessitates extra energy for a Co ad atom to move

from one terrace to another (Amirthapandian, et al. 2002). Resulting higher local Co concentration near step edges gives rise to increased nucleation of Co clusters.

Two other possibilities may give rise to the accumulation and nucleation of nanodots near step edge as observed in Figure 4.10. Pinning of Co on an edge at the down step will start growing once it passes the critical size the growth will tend to accumulate the Ag around the cluster to minimize the surface free energy making these clusters embedded in the surrounding Ag. On the other hand the Co nanodots might evaporate the Ag from the step edges to account the strain increase. Yet they tend to cover the dots due to the drive to minimize the free energy. Widths of the clusters are in the range ~5Å to ~55Å.

The distribution of the width for Co clusters is given in the table 4.1. The corresponding histogram is shown on the figure 4.11. From the Gaussian fit the mean for a typical Co cluster is 23Å and there is a quite a wide range values [~5Å to ~55Å] are possible to observe from the graph. Distribution also has a standard deviation of ~0.38Å. The annealing depletion of the Co islands on the surface is shown on figure 4.9. Initial deposition at RT (27˚C) is shown on A, followed by 200˚C (for 5 min) annealed surface by B and finally in C, the surface after being annealed at 400˚C for 5 min. We see sequential depletion of the number of Co islands. Comparing STM images we see the relative depletion after annealing at 400˚C is considerable compared to RT to 200˚C annealing. This is consistent with AES and LEED data.

We have calculated the volume of the individual Co nanodots fitting them with half an ellipsoid. This was then used to find the net Co volume on Ag (1 1 0) surface. Same process was repeated after annealing at 673K for 5 min. Surface reduction of islands when annealed is qualitatively evident when STM images are observed. Initially at 2ML Co coverage surface agglomerated Co volume is 2.44×10^{-2} nm^3 per unit Ag surface area. After annealing at 673K for 5min, this decreased in to a Co volume of 1.07×10^{-2} nm^3 per unit Ag surface area.

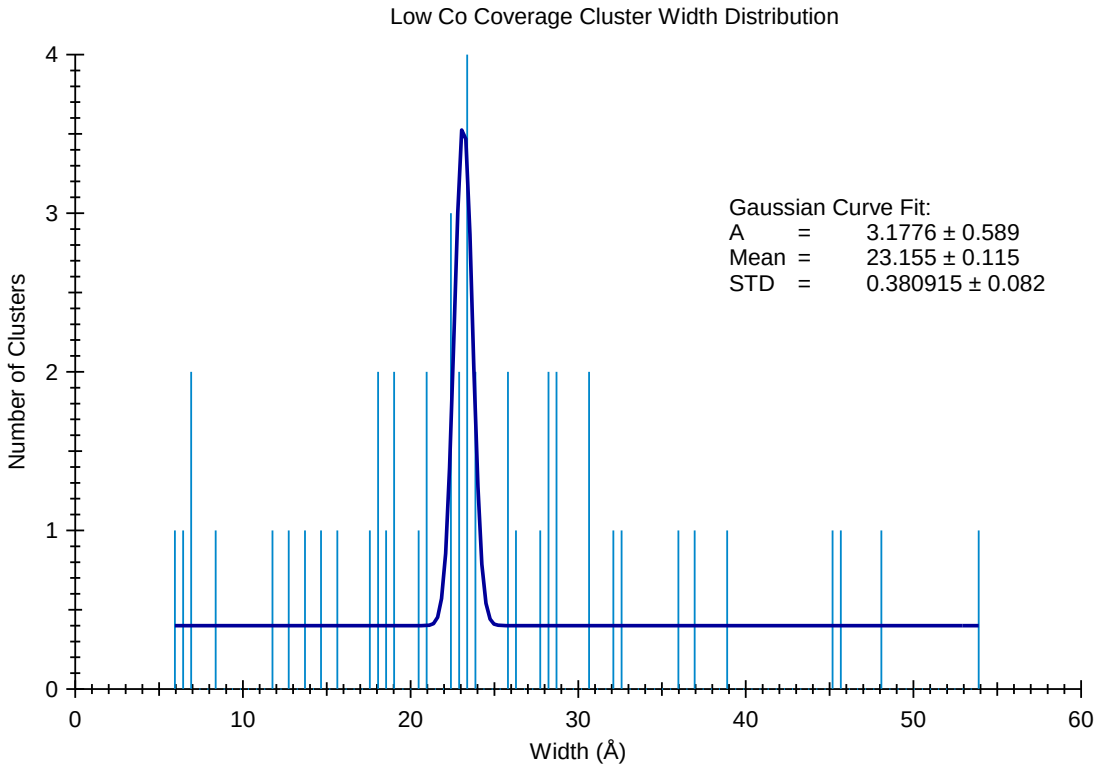

Figure 4.11 Distribution of width for Co clusters at low Co coverage.

Table 4.1 Sorted list of Co cluster widths for low coverage regime.

Co Cluster Number	Co Cluster Width (Angstrom)	Co Cluster Number	Co Cluster Width (Angstrom)	Co Cluster Number	Co Cluster Width (Angstrom)	Co Cluster Number	Co Cluster Width (Angstrom)	Co Cluster Number	Co Cluster Width (Angstrom)
1	5.95	11	17.21	21	22.76	31	24.21	41	31.07
2	6.82	12	17.81	22	22.84	32	25.98	42	32.39
3	7.05	13	18.06	23	22.89	33	26.14	43	33.01
4	7.27	14	18.51	24	23.12	34	26.61	44	36.15
5	8.81	15	18.95	25	23.32	35	27.82	45	37
6	12.07	16	19.17	26	23.57	36	28.42	46	38.93
7	13	17	19.51	27	23.58	37	28.54	47	45.58
8	13.88	18	20.59	28	23.6	38	28.78	48	46.13
9	15.04	19	21.32	29	23.83	39	28.92	49	48.12
10	15.64	20	21.44	30	23.93	40	30.91	50	54.38

This is a ~56% decrease of Co volume on Ag(1 1 0) surface upon annealing. Number of Co islands also decrease from 4.24×10^{-2} nm^{-2} to 1.36×10^{-2} nm^{-2} to during the same process. This is a ~68% decrease in number of Co islands on the surface. Correlating these factors will increase Co cluster mean volume from $0.58nm^3$ to $0.79nm^3$ resulting ~36% annealed volume increment for Co nanodots. This verifies that portion of Co leaves the surface while the other portion makes the existing nanodots larger.

Inset shows the Co island oriented [1 $\bar{1}$ 0]. Typical elongated islands show second layer growth at the two edges. This implies a possible increased nucleation at linearly opposite edges of the cluster. This interesting feature is shown on the few elongated islands on the Figure 4.9 inset A. We don't observe these elongated islands at all after annealing at ~400˚C. Implication is these elongated islands are especially unstable against a rise in temperature. This can be understood from the increased diffusion due to higher temperatures and increased availability Co atoms at higher deposition. At low temperatures and limited flux, surface Co diffusion is confined and possibly anisotropic. Therefore the resulting elongated structures are meta-stable

state. Regular clusters seem flat on the top and parallel to the surface. Clusters are typically one to two atomic layers high (~3Å - ~6Å.) At even lower coverage of ~0.2ML when the Co deposited as expected (Figure 4.12) we see less islanding. Interesting features were revealed upon annealing to 400˚C.

The surface roughness has decreased markedly. Importantly we see the randomly distributed induced defects possibly due to strains by subsurface segregated Co. Since Co has a large density of 3*d* electron states near E_F, in contrast to the Ag *sp*-band, it is possible that subsurface clusters of Co can enhance the density of states locally and provide additional charge for tunneling. In figure 5.9 B we see these point defects spread on the surface over randomly.

In line with the STM showing Ag(1 1 0) surface after the annealing, inset shows a tentative process model for low Co coverage annealing. Here the Ag caps Co trapping and driving Co into the bulk. Annealing at ~473K show decrease in number density of Co by ~50%. When annealed at ~673K the number density of islands decreases further by 80% of the initial density. This results in further smoothing-out of the surface.

At high coverage as will be explained shortly the increased cluster density makes the clusters closer and even possibly going over each other; effectively closing the possibility to see the Ag(1 1 0) surface.

When the Co coverage is increased to ~4ML at RT deposition most striking feature is the increase of the number density of Co islands (Figure 4.13). Another observable feature is the arrangement of the clusters: we observe some arrangement of clusters along [0 0 1] direction.

The width and the height of the islands do not change. Length of the islands decrease, making the aspect ratio close to one and islands look circular. None of the islands show any orientation. These islands never observed to coalesce but at this coverage it is not possible to see with STM if there is a layered structure underneath the clusters. Islands cover the entire surface.

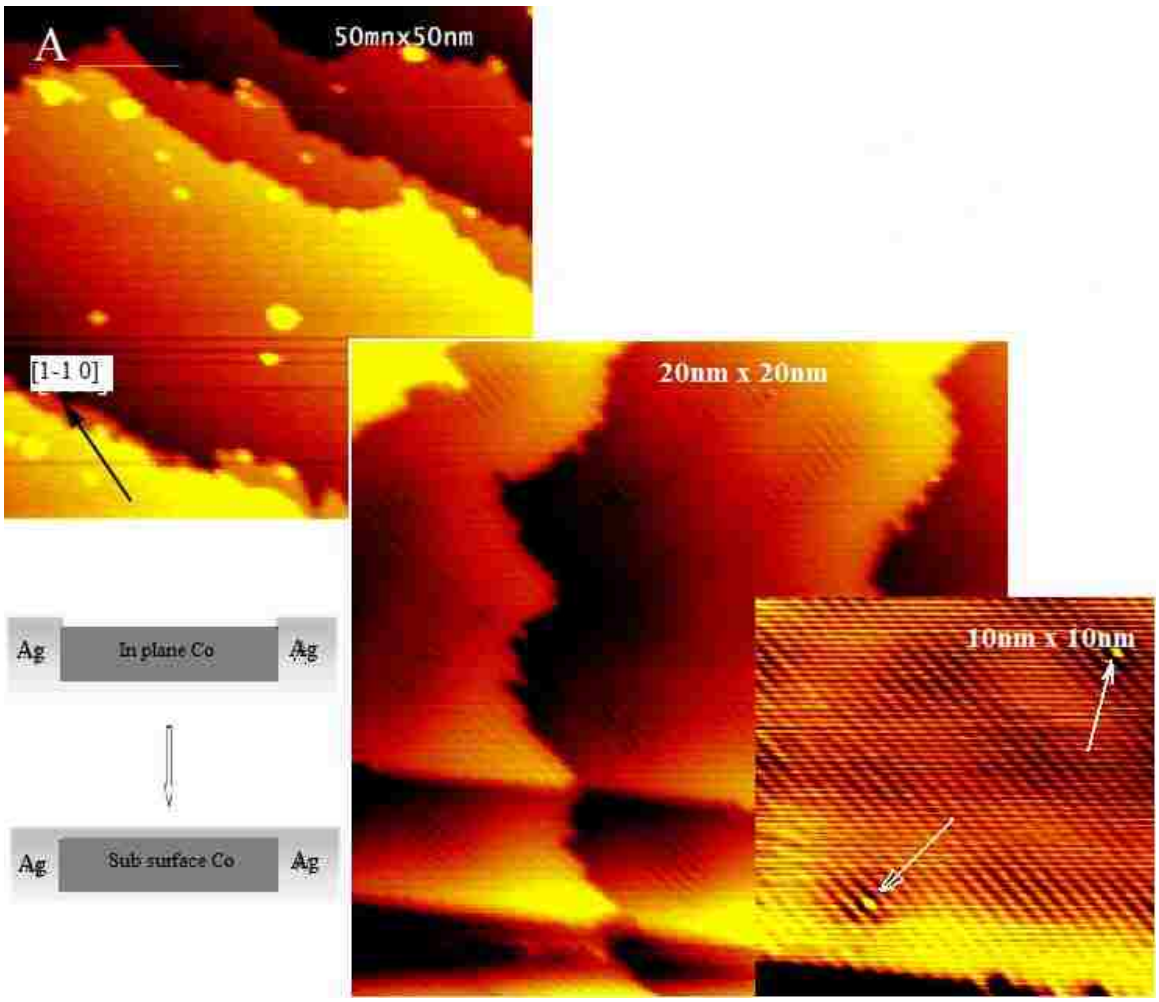

Figure 4.12 Low coverage Co on Ag: annealing effects. Figure A is RT Co 0.2ML deposited surface. Figure B annealed at 400˚C for 5 min. Surface shows strain defects (white arrows) induced by the Co segregation (inset) in to the selvage. The Model exhibits the possible migration of Co into Ag bulk.

The coverage of Co nanodots is stochastic and distinctly uniform in the long range. Stacking is observed and in short range island density, varies on the surface. In the length scales of ~2Å - ~5Å surface roughness has considerably increased as the terraces are impossible to be seen with the islands covering the surface completely. Surface is highly rough with abnormal unevenness. Possible reasoning for this can be explained by considering the nanodots being well embedded in the Ag(1 1 0) surface. The embedding (growth towards the Ag bulk) drives/displaces Ag and this displaced Ag makes the surface abnormally uneven. Still with the higher flux at high coverage Co nanodots nucleate on this Ag making the surface highly uneven at high coverage (Figure 4.13).

When the coverage is further increased to ~6ML the number density of islands increases in lock step. Yet the size of Co islands stays the same. We can expect to see this in any increment of Co coverage on Ag (1 1 0). The distribution of the Co cluster widths at high coverage regime is given in the table 4.2 with the distribution histogram shown on Figure 4.15. Important contrast is of high coverage and low coverage regimes is, the range of widths: in high coverage the variance has increased (2.14Å) but the range of widths (~17Å to ~29Å) have decreased compared to the low coverage. Interestingly the mean width of a cluster has not changed and is ~25Å.

In order to understand the change in structure with annealing, temperature was raised sequentially starting from RT (~300K) to 900K in 200K intervals. STM shows after annealing at 500K for 5 minutes surface roughness decreasing by agglomeration of smaller clusters.

Yet it is observed the islands are distinct and the size has not changed. After annealing at 700K number density decrease by ~30% and the Co islands starting to merge and make bigger circularly ordered stacks of islands.

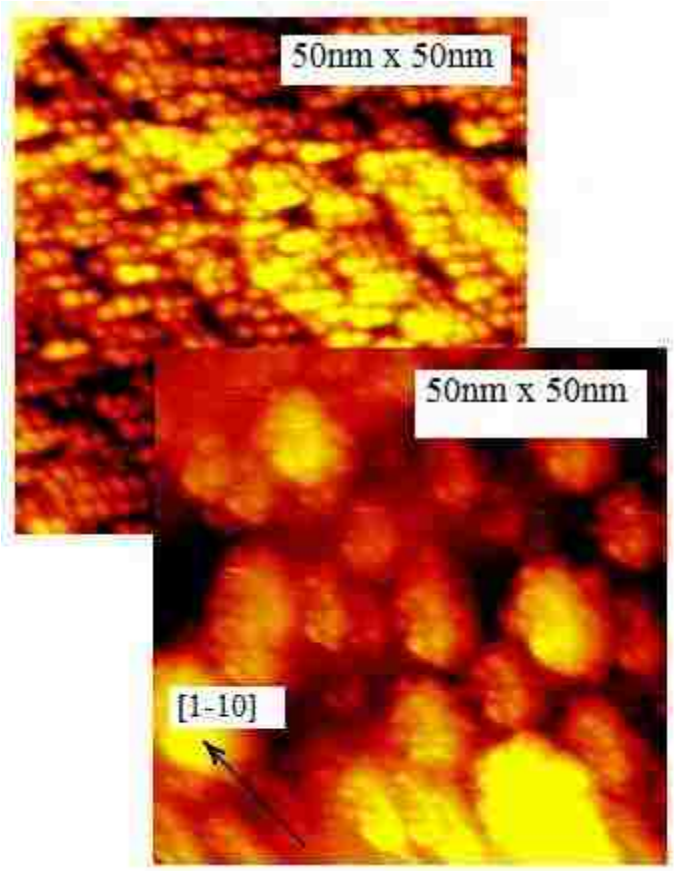

Figure 4.13 Co coverage ~4ML surface A and surface annealed at 900K. Shows clearly the nanodots are coalescing and forming super clusters with wider dimensions and heights. Grains in the super clusters are Co nanodots.

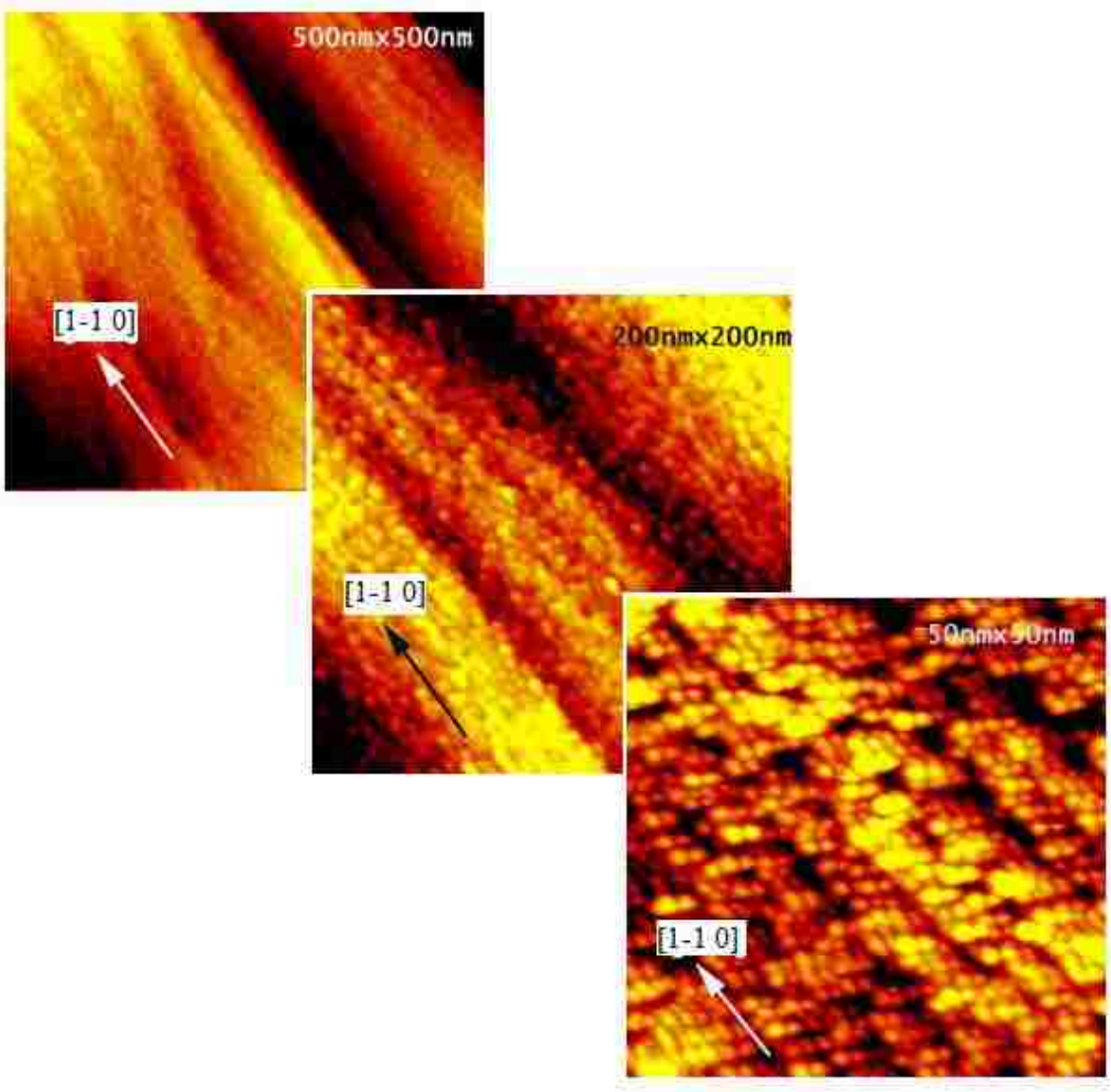

Figure 4.14 Co on Ag at ~4ML coverage. Co clusters do not show coalescence even at high coverage. Islands have distinct grain boundaries and almost identical size distribution.

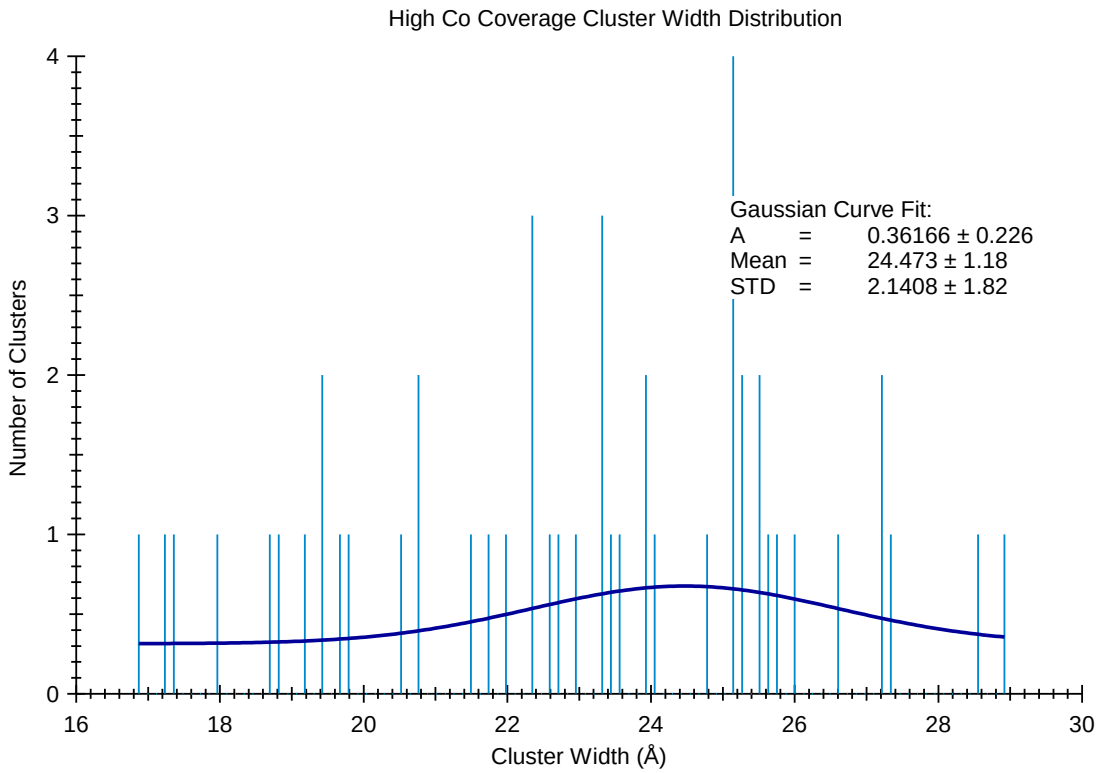

Figure 4.15 Distribution of Co nano cluster width at high Co coverage.

Table 4.2 Sorted list of Co cluster widths for high coverage regime.

Co cluster number	Co Cluster Width (Angstrom)	Co cluster number	Co Cluster Width (Angstrom)	Co cluster number	Co Cluster Width (Angstrom)	Co cluster number	Co Cluster Width (Angstrom)	Co cluster number	Co Cluster Width (Angstrom)
1	16.87	11	19.88	21	22.66	31	24.08	41	25.63
2	17.35	12	20.59	22	22.72	32	24.41	42	25.71
3	17.44	13	20.84	23	23.02	33	24.82	43	25.83
4	18.02	14	20.87	24	23.37	34	25.24	44	26.11
5	18.71	15	21.5	25	23.43	35	25.25	45	26.69
6	18.84	16	21.76	26	23.43	36	25.25	46	27.25
7	19.3	17	22.01	27	23.53	37	25.25	47	27.3
8	19.45	18	22.4	28	23.62	38	25.33	48	27.42
9	19.46	19	22.43	29	23.97	39	25.34	49	28.64
10	19.77	20	22.44	30	23.97	40	25.52	50	29.04

After annealing at 900K the merged super islands can be seen very clearly in Figure 4.13 B. These are made of agglomerations of smaller islands (seen as grains of the bigger islands) yet there is no set number of small islands that can come together to make these super islands as they can have variable width, lengths and heights which are considerably higher than for the small islands. Width is in the range ~70Å to ~120Å and height is in the range of ~10Å to ~25Å of the observed super clusters. They have an aspect ratio close to 1 making them slightly oval shaped rather than circular. They are slightly aligned towards [1 $\bar{1}$ 0]. Distinctive edges of smaller islands are decreasing indicating their heights are decreasing hinting sintering. And the dimensions of the smaller clusters (grains) which make the super-clusters are observed distinctly smaller than their counterparts at before annealing. These observations indicate a long range Oswald's ripening process probably due to increased surface diffusion kinetics and short range sintering process. Since we observe a agglomeration of nanodots this process is also mediated by cluster migration. Once they become closer short range sintering is responsible for the size reduction of smaller clusters. While these processes are happing on the surface subsurface

segregation Co is responsible for driving Co into the Ag bulk. This is evident in the Auger spectra we observed.

We propose two general possible mechanisms for visible depletion of Co islands when annealed, directly on our STM and Auger observations:

1. Co nanodots coalesce to make super islands.

2. Co segregation in to the Ag Bulk indicated by STM and AES data removing surface Co in the Co phase in bulk.

4.4 Analysis and Discussion

Considering the different analysis techniques carried out on the Co on Ag (1 1 0) system it is possible to come up with a consistent structure of the system in different stages of evolution including the annealing.

First studies at Co coverages at ~0.06ML at low temperature (~150K) it has been shown that Co making a surface alloy by substitution displacement of Ag from the surface making Ag mono to bi atomic rows on the surface (Kizilkaya and Sprunger, Unpublished transactions. n.d.). The driving force of the mechanism was proposed to be the tendency to reduce the surface free energy.

Following very low coverage surface alloyed state at switching to a little higher coverage at RT deposition we see a de-surface-alloying transition where Co is released form pits and nucleating on the surface as clusters. This de-alloying transition possibly occurs at a very low Co coverage (~0.1ML) and it is also very much dependant on the temperature. It has been clearly seen that at RT ~0.2 ML Co coverage, clusters are present on the surface. Where it has been observed at ~0.06ML at low temperature Co alloyed on the Ag(1 1 0) surface displacing Ag to make clusters on the surface. It is possible to follow the line of argument that is common in literature (Schmid, et al. 1993) (Egelhoff Jr. and Steigerwald 1989) (Zimmermann, et al. 1999).

Considering surface energy for Ag (1 1 0) surface $\sigma_{Ag\ (1\ 1\ 0)}$ = 1.238Jm^{-2} (Vitos, et al. 1998) (Mezey and Giber 1982)and minimum surface energy facet $\sigma_{Co\ (0001)}$ = 2.775 Jm^{-2} (Vitos, et al. 1998) (Mezey and Giber 1982)and the interface energy $\sigma_{Ag\ -Co}$ = 0.6 Jm^{-2} using average of the high angle grain boundary values between Co/Ag.

When the Co coverage is increased to ~0.1ML at RT the formation of the Co islands on the surface is also driven by surface free energy minimization. At low coverage and low temperature only the first monolayer has substitution-alloyed and near immiscibility of Co in Ag [Co solubility in Ag bulk is between 0.0002 and 0.009 atomic percentage Co in the temperature range 873 to 1213 K (ASM International 1995)] leaves no room for further alloying. Ag and Co have ~13% lattice mismatch (a_{Co}= 3.544 Å and a_{Ag}= 4.086 Å).The electron negativities between Co (Pauling 1.88 and Allered – Rochow 1.70) and Ag (Pauling 1.93 and Allered – Rochow 1.42) are almost the same (Emsley 1998). The high lattice mismatch violates the first Hume–Rothery (Kittle 1996) rule for alloy formation but close electro negativity satisfies the second rule. The severe lattice mismatch with the high heat of mixing [for Co-Ag 28kJ/mol (Amirthapandian, et al. 2002)] hinders the formation of an alloy between the species. Therefore the alloying mechanism between the species is only limited to very low coverage and low temperature and confined only on the surface. Interestingly when the lattice mismatch due to lattice parameters is considered the Co to Ag one to one alignment on the surface is obtained at length of ~19Å and the typical Co nanodots has a width of ~25Å.

When Co deposition on the Ag surface is considered, typically it is possible to consider the three possible modes of surface accumulation and growth: FM (layer by layer), SK (layer plus island) and VW (islanding without layering). This also readily satisfies the thermodynamic arguments given by Bauer (Bauer 1982) on film growth. Co does not wet the Ag surface according to the quasi-equilibrium explanation of surface growth. If Co grows on the thin film

mode even for few atomic layers, the increase in surface energy is forbiddingly high. Ignoring the strain energy (assuming only capillary forces) we have following change in free energy:

$$\Delta\sigma = \sigma_{\mathrm{Co}\,(0001)} + \sigma_{\mathrm{Ag-Co}} - \sigma_{\mathrm{Ag}\,(110)} = 2.137\ \mathrm{Jm}^{-2}$$

This increase in energy makes FM and SK modes inaccessible due to the extremely unfavorable local thermodynamics. Therefore clustering is the preferred direction of growth. Even with clustering the difference in Co and Ag surface free energies is considerably high, the clusters tend to make minimum possible surface area. This requires cluster geometry to be closer to a sphere. We observe elongated Co structure; although ellipsoidal it is close to being spherical on Ag(1 1 0). Further the clusters are possibly about one to two layers embedded in the surface. A parallel observation was, in the annealed case for low coverage where we see pits going around the Co clusters. This is possibly due to the bulk migration reduction in Co of the respective cluster and resulting shrinking of the cluster dimensions. Embedding is thermodynamically feasible as this further reduces the surface energy by removing exposed Co surface by exchanging it with an increase of Co-Ag interface. According to the free energy values involved this is highly energetically favorable. This mechanism has been observed in Co grown on Cu(1 1 1) where it was observed Co making trilayer islands with one layer subsurface (Pedersen, et al. 1997).

At higher coverage we see sharp grain boundary definition between clusters and surface, possible byproduct of near perfect immiscibility of Co and Ag and high lattice mismatch between the species. Even higher coverage the clusters have increased number density and visibly stacking next to each other. Even under these conditions no clear coalescing was observed until the temperature was raised up to ~500K. As the temperature increased cluster agglomeration increase in lockstep. If we apply the same arguments of minimization of surface free energies it is natural to expect coalescing even before system temperature reach ~500K. For

a long range and short range processes diffusion kinetics is the limiting factor that hinders any surface system reaching thermodynamic equilibrium. Oswald's ripening can easily occur given enough diffusion is facilitated and similarly sintering is also favorable but dependant on propinquity of the Co islands as this is a short range process.

Earlier it was argued; local energetics governs the semi spherical morphology of the Ag clusters. We propose Co on Ag surface diffusion rate governs the rate at of Co cluster coalesce on the Ag(1 1 0) surface. For the diffusion references it best consider the typical Arrhenius equation: $D = D_o \exp(-E_{act}/k_BT)$. Surface diffusion activation energy (E_{act}) for Ag (on Ag lattice) for two directions [0 0 1] and [1 $\bar{1}$ 0] are ${}^{Ag}E_{act[0\ 0\ 1]}$=1.10eV, ${}^{Ag}D_{o[0\ 0\ 1]}$= 0.0069eV and ${}^{Ag}E_{act[1\ \bar{1}\ 0]}$=0.59eV, ${}^{Ag}D_{o[1\ \bar{1}\ 0]}$= 0.0026eV. These give mean value of ${}^{Ag}E_{act}$= ~0.84eVand ${}^{Ag}D_o$= ~0.0048eV which we take as isotropic.

Since accurate Co diffusion data is not available, considering Rh[§§] (on Rh FCC lattice) it is possible to obtain the same isotropic parameters: ${}^{Rh}E_{act}$ = ~1.63eV, ${}^{Co}D_o$ = ~0.0027eV (Agrawal, Rice and Thompson 2002). From this we assume (considering the structural and chemical similarity between the elements) the surface diffusion kinetic energy of Co is ${}^{Co}E_{act}$ ~ 1.5eV and ${}^{Co}D_o$ ~ 0.003eV. In this case the most accurate would have been the Co diffusion parameters on Ag, but the data at present is not available. By inspection it is possible to see Co has higher diffusion activation energy (E_{act}) and lower pre exponential coefficient (D_o) compared to Ag. Therefore we state the activation of Co diffusion is later than Ag when temperature was increased. As we have indicated the local nucleation properties have no bearing on these diffusion rates and Co nucleates into clusters. But agglomeration of clusters into Co super-clusters needs thermal energy input where by surface diffusion activation is surpassed and large

[§§] We have ignored the deviations that might occur if Rh (*i.e.* Co) was on the Ag interface instead of being on itself. These Arrhenius coefficients are calculated applying Monte Carlo Variational Transition state theory with Lennard-Jones potential (Agrawal, Rice and Thompson 2002).

scale agglomeration takes place.

One other feature that is evident from the data is the different activation energies in the two high symmetry directions on the Ag surface we see activation energy in the direction [1 $\bar{1}$ 0] is much lower than [0 0 1] direction. Although these data are for Ag diffusion on Ag typically it is common for other elements diffusion on Ag. Implying comparatively higher rate of surface diffusion on a given temperature happens on [1 $\bar{1}$ 0] direction apart from the surface anisotropic strain fields on Ag(1 1 0) this is another factor that enables initial growth of elongated Co islands. At higher temperature the fractional difference between the two directions vanishes and the surface tend to increased but isotropic diffusion rates. Typically diffusion rates are high along the troughs [1 $\bar{1}$ 0] for almost all of the metal (1 1 0) surfaces.

On the Ag(1 1 0) surface three mechanisms in equilibrium give rise to the Co cluster phase: anisotropic surface diffusion, surface free energy minimization and the anisotropic surface strain. We come to the conclusion the surface strain is comparatively has the least affect because the near spherical symmetry of the islands. This is an indication the free energy minimization dominates among the competitive mechanisms. At higher energy however diffusion increasingly plays a pivotal role in the development Co on Ag phase.

Although the orientation is not seen in LEED some orientation is seen in the STM images. Absence of a LEED pattern can be described by the spherical faceted surfaces and stochastic distribution of Co islands on the Ag surface. This will destroy the coherence of the LEED diffracted beam. Coherence length of a typical LEED electron beam is in the order of 100Å. Although at higher coverage it evident these reasons might give a diffuse LEED it is unclear why it gives a diffuse pattern at lower coverage. At low coverage diffuse LEED gives spots when annealed at ~100˚C but still when consider the coverage it should give at least some

spots at that coverage. Possible reason is our coverage when we did LEED analysis is slightly off giving higher coverage than we anticipated.

Annealing the system reveals the depletion of Co from the surface by ~ 50% according to AES and STM data. Apart from the agglomeration processes involved we propose there should be subsurface migration of Co to account the reduction of Co from the surface.

When considering other systems that have been previously studied, there are several mechanisms that has been suggested for the same process of Co moving into the bulk observed for Co/Cu (1 1 0) by Li and Toner (Li and Tonner 1990) where when annealed system makes a sandwich structure of Cu/Co/Cu (1 1 0) rather than surface alloying of Co/Cu (1 1 0) as earlier work by J. de Miguel et al (De Miguel, Cebollada, et al. 1989) (De Miguel, Cebollada, et al. 1991) suggested. But the Auger data contradicts this in our system. This is mainly because the systems are very different from surface energy perspective and as described above the lattice mismatch (Co to Cu lattice mismatch is only ~3%) is huge for the Co and Ag.

In contrast the previous studies we see almost continuous decrease in Co concentration with annealing. Considering the near total immiscibility of Co in Ag the segregation has to be cluster segregation compared a surface alloying process. It is evident this introduces a significant strain on the Ag lattice. It is not possible observe any distributed uniform defects such as holes indicating a possible capillary mechanism of Co migration.

In the absence of alloying and other such methods this is a viable alternative. STM images at ~0.2ML coverage (Figure 4.12) with high annealing showing point defects where surface is buckled at certain distributed points strengthen this argument. As we believe these points are strain centers due to the introduction of Co cluster embedding on the surface and migrating in to the bulk. Ensuing high lattice mismatch points give these buckled defects.

Further we propose in order to compensate for the considerable surface energy disparity the Co

phase imbedded in the Ag lattice should be spherical in structure since as we argued before spherical surfaces have the least surface/volume ratio. By contrast if we assume Co makes a layered sandwich structure, the Auger data should curve and flatten out with increased annealing as seen by Schmid *et. al.* (Schmid, et al. 1993). By embedding a Co phase of spherical volume the loss of surface free energy to the system can be roughly estimated using surface energies of the Co and Co/ Ag interface which gives 78% loss or about 2.175 Jm^{-2} loss of free energy.

But in loosing free energy as we mentioned above a lattice strained is introduced by burying the Co nanodots in to the Ag bulk. Yet it seems when annealed the surface energy reduction dominates.

Although we have not explicitly carried out any preferential adsorption on the surface to differentially identify Co and Ag, here we propose a possible mechanism that is very possible in our system. Energetically capping the Co cluster surface by Ag is extremely preferable because instead of exposed higher free energy Co surface system is end up with an interface of Co-Ag and a Ag overlayer. When considered the free energy values in-cooperating surfaces this is apparent. Further we have argued the surface diffusion rate of the Ag is comparatively higher even at RT, but possibly not of Co. Both these reasons and pointing out that this has been observed previously in many systems involving transition metals and Ag and in Co and Cu (Rolland and Aufray 1985) (Schmid, et al. 1993).

It is evident from Auger annealing will further reduce Co concentration in the top layers, it suggests a migration of phase further in to the bulk. Although we have provided a tentative mechanism a clear mechanism is need to explain all the details of the process. Due to the Co migration in to the bulk and the clustering of Co islands on the surface, Ag (1 1 0) surface is exposed which gives the weak LEED pattern of Ag (1 1 0) lattice after annealing at high temperatures.

4.5 Summary

Finally, following conclusions are reached from the study.

1. At sub monolayer, possibly ~0.2ML Co coverage on Ag(1 1 0) Co initiates the clustering with mono to bi atomic height (~3Å to ~6Å) having widths of ~25Å (about 8 to 9 atoms) 3D nanodots.

2. At higher coverages Co makes 3D islands keeps the same dimension but never coalesce in RT even with the considerably increasing coverage.

3. Annealing above 700K results in agglomeration of Co nanodots into super islands with variable heights and widths, with individual nanodots making up the super islands.

4. Annealing shows reduction of Co concentration on the surface which onsets at ~500K. By considering thermo dynamical arguments we propose subsurface Co cluster migration into the Ag lattice.

5. Growth of thin Co films is hindered on Ag (1 1 0) due to difference in surface free energy and high asymmetry between lattices of the Ag and Co.

This study shows the difficulty of growing thin films when the substrate and evaporant having such divergent surface free energies and lattice constants in the bulk phase. This can be expected of other systems with the same properties.

Further investigation of the Co/Ag (1 1 0) system is necessary to elucidate the composition and characteristics of the surface layer. An important investigation would be an adsorption study possibly of O_2 or CO as this will reveal the capping and other island morphologies associated with Co clusters. CO has already been used to this end in determining Co growth on Cu(0 0 1) (Pedersen, et al. 1997). And Co segregated spherical phase has to be investigated in order to determine its structure. UV core level photo emission study on the system should reveal the binding energy shifts in Co $^2p_{3/2}$and Ag $^3d_{5/2}$ peaks. These shifts should

indicate the possible surface alloying states between the two species in the system (Godowski, et al. 2006). Although there is strong evidence towards the process as described here, it needs further clarification. Possible paths are Extended X-ray Absorption of the Fine Structure (EXAFS) and X-ray Absorption Near Edge Structure (XANES) will help to determine the local structure and composition on the system. A possible extension is to find a proper surfactant in order to minimize the effects of the surface energy difference between Co and Ag. Further ab initio calculation of the system might reveal interesting properties and shed light into Co cluster grain stability and low temperature Co-Ag 2D surface alloy phase.

5 Anisotropic Plasmon Dispersion of Ag Nanowires on Cu(1 1 0)

5.1 Introduction

All matter dynamically interacts with electromagnetic radiation. In the case of insulators it can be lattice absorption and/or color centers in the absence of conduction band electrons. In the case of semiconductors the interactions arise because of energy bands, Urbach tail and excitons. It is prominent in metals due to their higher density of free electrons where interactions arise because of the bound and free electrons, plasma oscillations etc…

In the case conductors the conduction band electrons can undergo coherent collective oscillations: Plasmon oscillations. Interactions in reduced dimensional clusters (micro and nano particles) show wide and interesting range of phenomena due to the changed electronic properties arising from small size effect. Depending on the surrounding and existing geometry they can be characterized as bulk Plasmon: for the collective electron oscillations in bulk (Maier 2007), surface Plasmon (Ritchie 1957) for planar geometry, Mie Plasmon for spherical geometry (Mie 1908) and for varying shapes of reduced dimensional particles, particle Plasmon. The name particle Plasmon is used in literature to distinguish the unique plasmonic properties that are being exhibited by various nano particles (Sonnichsen, et al. 2002).

There is a plethora of applications being implemented from nano/micro particle Plasmon. Optical components coming from long range optical polaritons (surface Plasmon coupled to a photon), nano – micro metal strips and wave guides for surface plasmons, super resolution microscopy by means of surface plasmons and bio – sensing with plasmonic nanoparticles (Shalaev and Kawata 2007).

Apart from this wide array of applications there are other theoretical and fundamental interests as well. Investigation of plasmon modes of nano structure especially resonance shifts and dispersion relations are extremely important in understanding the electronic structure of the respective nano structures and their optical properties. Using electrons (in case of HREELS) to transfer momentum ($\boldsymbol{q}_{\parallel}$) and excite the plasmon modes on/in matter is a direct and a powerful method to investigate the resonance modes and dispersions. Apart from using electrons (as in HREELS) to investigate dispersion relations of nanowires, it is possible to use optical coupling of photons (such as a laser) as well. But direct coupling of light with surface plasmon modes on an unmodified surfaces are not possible due to k mismatch (Raether 1988). But there are two widely applied techniques: Kretschmann and Otto configuration uses intermediate media to match k vectors (using Attenuated Total Reflection) to excite the plasmons on a surface. Another possibility is to use gratings to directly couple plasmons to photons, which have been shown many times in literature (Shalaev and Kawata 2007).

There are numerous studies in literature about surface plasmon dispersion relations on planar metal dielectric interface as in the case of clean Ag(0 0 1), Ag(1 1 0) and Ag(1 1 1) surface (G. Lee 1995) (Raether 1988) but comparatively few nano structured systems have been studied. Many of these systems were studied by the means of optical plasmon –polaritons dispersions or resonances. In plasmon – polaritons dispersion relations measured using optical transmission of Au and Ag nanowires lithographically grown on glass (Schider, et al. 2003) multi polar resonances has been described as standing plasmon waves. Plasmon resonances of Au and Ag nanoparticles of different sizes and shapes have shown to exhibit different extinction spectra. They also show distinct resonance spectra belonging to different wave lengths for same element but different geometry (Orendorff, Sau and Murphy 2006). It is also shown when Ag nanoparticles increase in size the scatter spectra get red shifted. It is also observed to radiation

damp for plasmonic lines for both Ag and Au nano particles (Sonnichsen, et al. 2002). Our system is distinct in comparison to many systems. It is the hetero epitaxial metal on metal Ag nano wires self assembled on clean Cu(1 1 0) surface (same system in Chapter 3). We will show that there exists a plasmon mode unlike bulk or surface therefore unique to the nanowires. The plasmon modes exist only along the nano wire [1 $\bar{1}$ 0] direction but not across the wire.

To the best of author's knowledge this is the first time a Plasmon dispersion relation has been shown for self assembled hetero epitaxial system of nano wires. Due to multitude of reasons this is particularly hard. To obtain a reasonable far field signal one needs an ordered array of nanowires with sufficient number density on the surface. This is readily achieved by our system of Ag nanowires on the Cu(1 1 0) substrate but due to the dynamic and stochastic nature of the growth (as explained by Chapter 2) wires tend to have a high degree of non uniformity. The wires grow on random pinning centers (defect sites and step edges) on Cu(1 1 0). This gives rise to inhomogeneous optical properties and random scattering. These adverse effects have been overcome by increasing the number density of wires to a very high value and keeping the substrate as clean as possible before, during wire growth and while taking data.

5.2 Experimental Procedure

Experiment was carried out in the ultra high vacuum chamber (UHV), (base pressure ~2 x 10^{-10} Torr) and attached EELS chamber (base pressure ~8 x 10^{-12} Torr) in the Surface Science Lab at LSU. Ag nanowires were grown on the Cu(1 1 0) substrate with rectangular geometry having, width ~8mm, length~1.2mm and thickness ~3mm. Sample holder is as shown on the picture of the Ag crystal in chapter 1 (Figure 2.1). Thermocouples connected to the sample enabled direct real time *insitu* measurements of substrate temperature at the preparation step. At the data retrieval step at EELS the sample holder has no thermocouple wires to measure the temperature. This has not impaired our experiment as all samples were studied at RT (~25°C).

Cu(1 1 0) crystal was prepped by ultra clean - static Ne sputtering at ~5 x 10^{-5} Torr at RT for 30 min followed by annealing to 823K for 10 min. Cold trap was kept filled with liquid N_2 to keep the vacuum conditions better. To get the optimum surface we repeated this procedure, twice for each step and some time more where and when we needed a cleaner (flatter) Ag (1 1 0) surface.

Temperature variation during the deposition was also mediated by a sample holder where it's possible to change the temperature in the range 123K–1200K. Thermal heating was obtained by both filament (radiative) and e-beam heating. While annealing, the holder was air cooled by sucking air through the integrated tubing system. Ag was evaporated on Cu(1 1 0) by a Ag evaporation source (MBE) where thermal and an e – beam were used to sublimate Ag and deposit on Cu(1 1 0). Two evaporators were used, where in the e – beam evaporator Tantalum crucible was used to keep the melted Ag and in the thermal evaporator tungsten filament was wound with Ag (99.9999% w/w pure) wire. Base pressure of ~8 x 10^{-10} Torr was maintained during Ag deposition.

In-situ Auger and LEED analysis on the Ag deposited Cu(1 1 0) substrate were carried out by the respective equipment which were as mentioned directly connected to the main chamber. Cleanliness of the Cu(1 1 0) was established by using LEED and Auger. The same techniques was used to calibrate the Ag coverage on the clean Cu(1 1 0) surface. ErLEED used for LEED analysis was by SPECS instruments and the Auger was CMA type.

EELS used for the analysis which is explained in detail in chapter 2 is a LK2000 fixed lens HREELS.

For each part of the experiment substrate cleanness is established after at least two sputter anneal cycles followed by taking an Auger spectra to determine the surface impurity concentration (especially C and S contamination or surface segregation from bulk) and a Low

Energy Electron Diffraction (LEED) to verify the proper crystalline Cu(1 1 0) surface. Further to calibrate the initial Ag(1 1 1) overlayer prior to the formation of Ag nanowires on Cu(1 1 0) Auger and LEED was used. Ag(1 1 1) layer can be clearly identified by LEED. Ag(1 1 1)/Cu(1 1 0) overlayer was initially calibrated using STM too. Using the time as the variable, coverage of Ag on the Cu(1 1 0) surface was calibrated by STM, LEED and AES measurements.

5.3 Data and Observations

5.3.1 Preliminary Features

Ag is an element which has been used in optical application for millennia even without the knowledge of having unique plasmonic properties. Figure 5.1 and Figure 5.2 Top parts shows the dielectric constants for the Ag and Cu (Ehrenreich and Philipp 1962). Drude absorption governs the ε_2 ($\varepsilon = \varepsilon_1 + i\varepsilon_2$) at low $h\omega/2\pi$ and above 2eV both Ag and Cu show the onset of their respective inter band transitions (4d for Ag and 3d for Cu) at ~4eV and ~2eV. This is also seen in Figure 5.3 for Ag and Cu respectively. Collective excitations for the different geometries which correspond to each case (bulk, surface and Mie) are given by the poles of the respective response functions. They are in the non retarding limit ($q \gg \omega/c$);

$$b(\omega) = -1/\varepsilon \qquad -(5.1)$$

$$\sigma(\omega) = \left[\frac{\varepsilon-1}{\varepsilon+1}\right]\frac{1}{2\pi} \qquad -(5.2)$$

$$\alpha(R,\omega) = R^3\left[\frac{\varepsilon-1}{\varepsilon+2}\right] \qquad -(5.3)$$

Respectively the Equations 5.1 – 5.3 are bulk response function, surface response function and Mie response function. The poles of these give the corresponding conditions for collective modes. Therefore $\varepsilon = 0$, $\varepsilon = -1$ and $\varepsilon = -2$ will give bulk, surface and Mie resonance

condition. In scattering experiments the imaginary part of the response function give the scattering cross − section. This is a consequence of **Fluctuation Dissipation Theorem** (Nyquist 1928). Therefore respective cross − sections are **im(1/ε)** (bulk loss function), **im[(ε-1)/(ε+1)]** (surface loss function) and **im[(ε-1)/(ε+2)]** (Mie loss function).

Here the system excitations are of nanowire/nano particle plasmons. Due to the physical geometry and elemental composition of the systems they may have some similarities with plasmons mentioned above. Over system is described exhaustingly in Chapter 3. In order to avoid the repetition we refrain from giving a complete description here.

Ag nanowires of have self assembled on the Cu(1 1 0) single crystal system when the substrate is kept at ~373K while Ag is being deposited on the substrate by MBE. They are highly anisotropic with typical width being ~100Å and height being ~25Å. Wires have side facets of {1 1 1} and {1 1 0}. The growth mode is Stranski − Krastanov where the wetting layer of Ag(1 1 1) is present. Upon saturation of this wetting layer at 1.2ML Ag nanowires self assemble on Cu substrate. At low Ag deposition (Coverage $\theta < 10$ML) there exist pronounced substrate effects due to the low coverage. Here the combined cross section seen by e beam is mainly Ag(1 1 1) layer covering the surface area in between the wires. Therefore the data are for $\theta > 20$ML of Ag on Cu(1 1 0) substrate surface.

5.3.2 Observations

HREELS spectra for clean Cu(1 1 0) and clean Ag(1 1 0) are shown on the Figure 5.3. It is evident that the line shapes of the two excitations clearly different. Cu excitation is broader while Ag is narrower and has higher intensity. These were taken to establish the collective behavior of the system. When the Ag nanowire were grown on the Cu(1 1 0) the narrow Ag

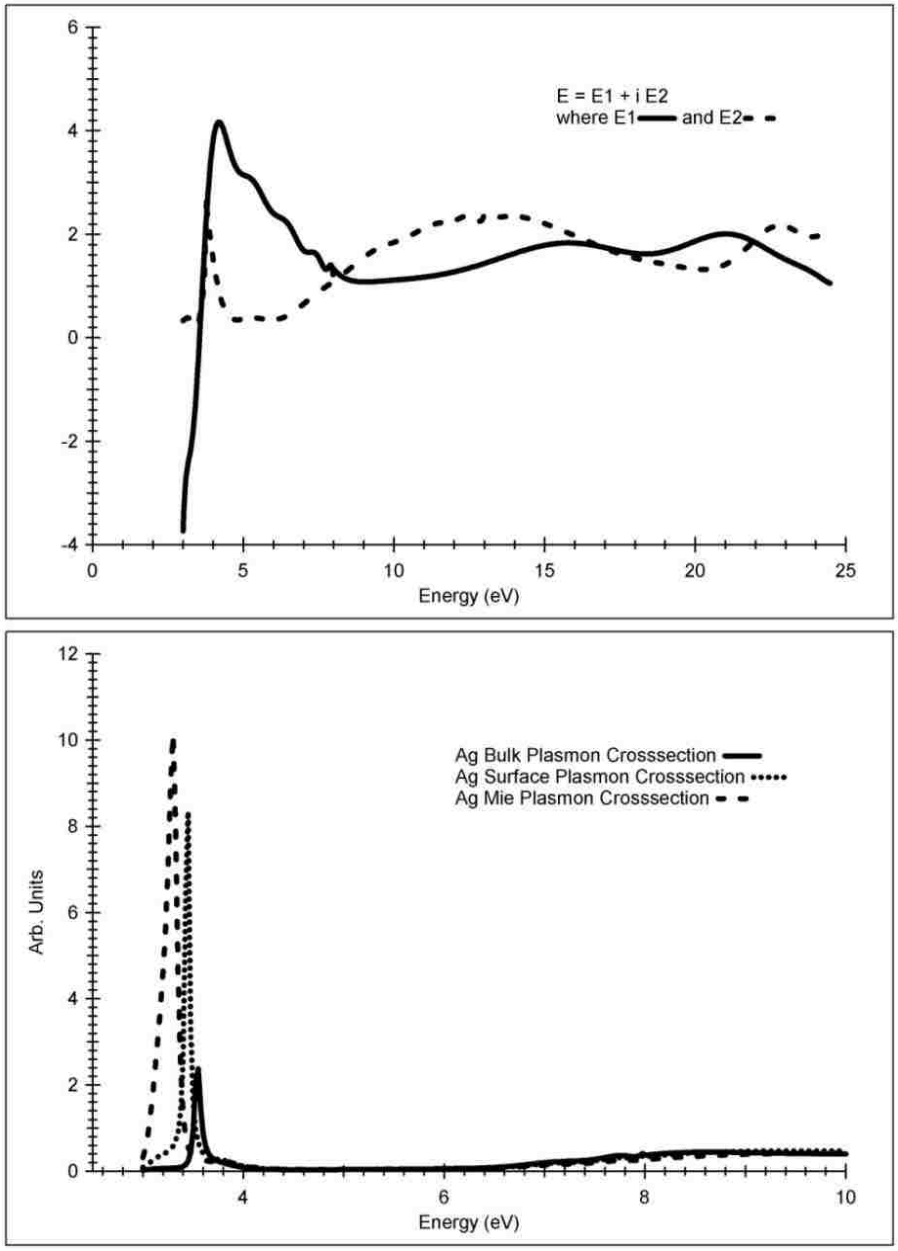

Figure 5.1 TOP: dielectric constant of Ag produced from optical data (Ehrenreich and Philipp 1962). BOTTOM: using data from TOP, scattering cross sections numerically calculated by author for Ag bulk plasmons, surface plasmons and Mie plasmons.

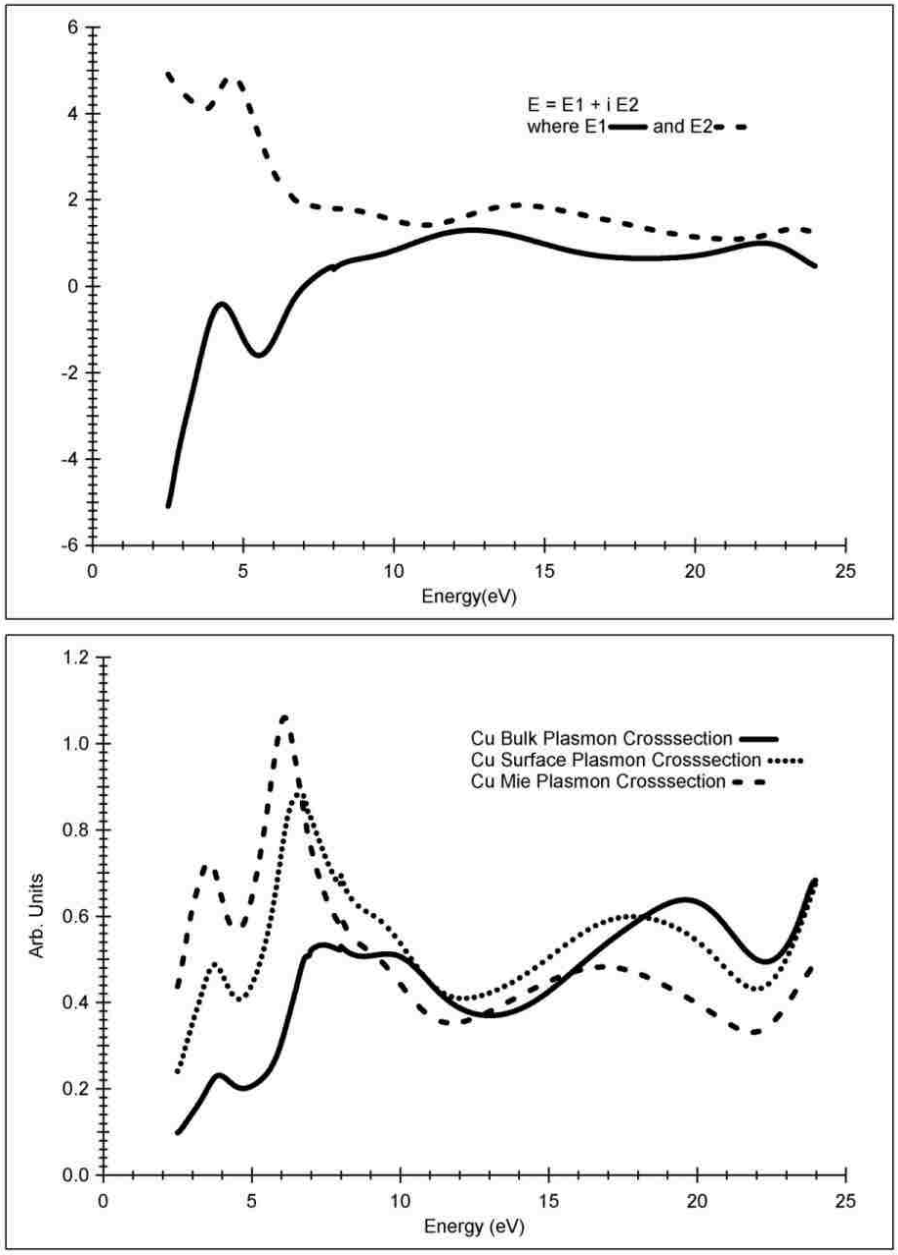

Figure 5.2 TOP: dielectric constant of Cu produced from optical data (Ehrenreich and Philipp 1962). BOTTOM: using data from TOP, scattering cross sections numerically calculated by author for Cu bulk plasmons, surface plasmons and Mie plasmons.

peak sits on top of the broad Cu peak. But they are clearly differentiable due to their distinct energies and shapes. Ag peak comes at 3.7eV while Cu peak come at 2.1eV.As explained, in order to improve the collective cross section of the epitaxial nanowires, spectra for higher coverage are taken. Ag nanowires HREELS spectra of Ag deposited (θ ~ 20ML) Cu(1 1 0) substrate is shown in the Figure 5.4 and Figure 5.5.

These graphs are complementary to each other as they show the spectra along the nanowire [1 $\bar{1}$ 0] (along the ΓX) and across [0 0 1] (along the ΓY) the nanowire. We see clear dispersion along the wire as peaks corresponding to the plasmons excitations are moving with varying q. It is observed for the near specular spectra the width of the spectra is higher. As explained before Ag peak sits on a broad Cu peak, therefore the fit is a line and a Lorentzian function together.

We have increased Ag coverage further to ~30ML. This is to see possible variations due to coverage. Ag nanowires HREELS spectra of Ag deposited (θ ~ 30ML) Cu(1 1 0) substrate is shown in the Figure 5.6.Like above these graphs are also complementary to each other as they show the spectra along the nanowire [1 $\bar{1}$ 0] and across [0 0 1] the nanowire. We see clear dispersion along the wire as peaks corresponding to the plasmons excitations are moving with varying q. Qualitatively, it is possible to state the movement of the peak is comparatively more prominent at ~30ML Ag coverage compared to ~20ML. Here too the fit is a line and a Lorentz together.

5.4 Analysis and Discussion

Considering the cross sections derived by the loss function, it is possible to comment on the loss function and their behavior. By using $\varepsilon = \varepsilon_1 + i\varepsilon_2$, and taking the imaginary parts of the response function Equations 5.1 – 5.3 will give the scattering cross sections,

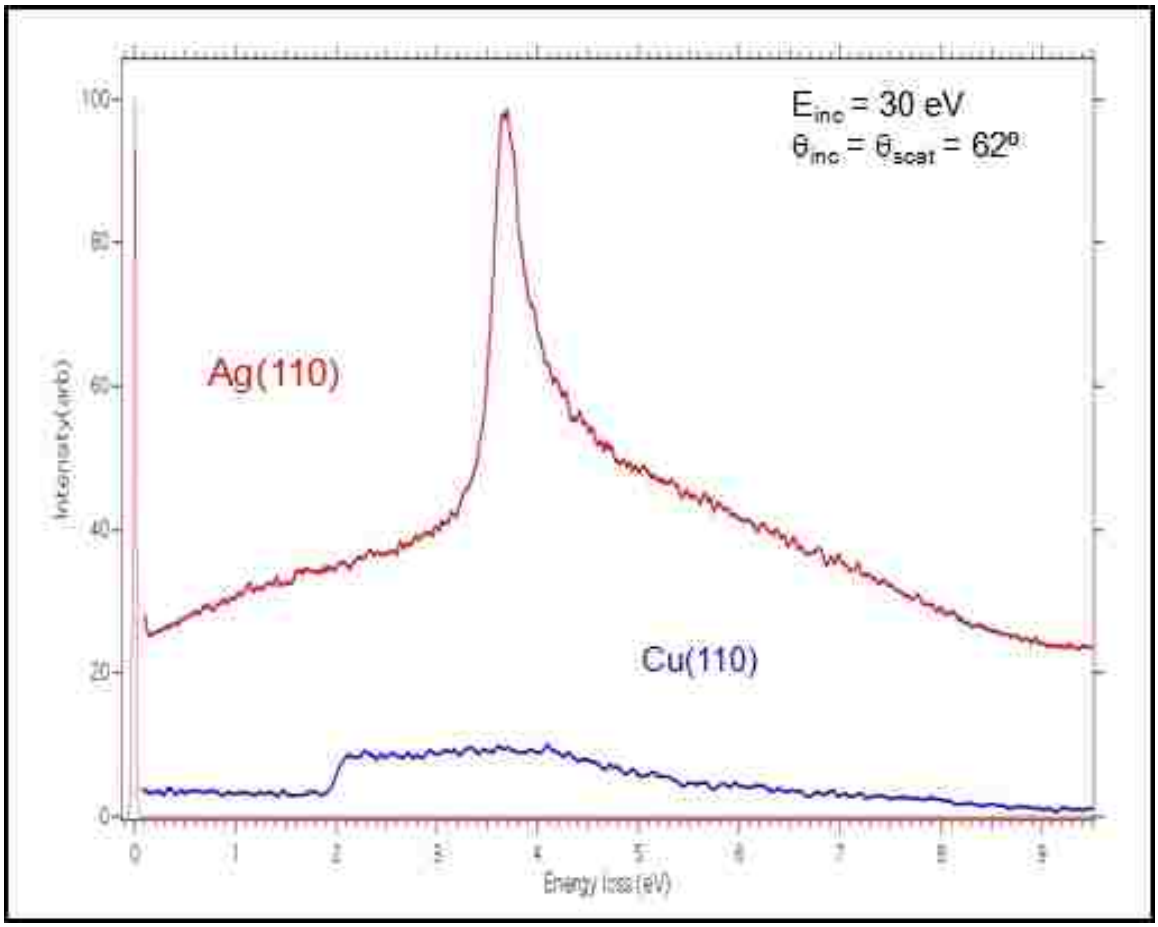

Figure 5.3 Clean Ag and Cu HREELS spectra. These are plasmon resonance peaks for Ag and Cu respectively, and obtained for specular geometry with E = 30eV. Narrow Ag and broad Cu clearly show distinct differences. The lowest red spectrum shows the elastic peak at 0eV.

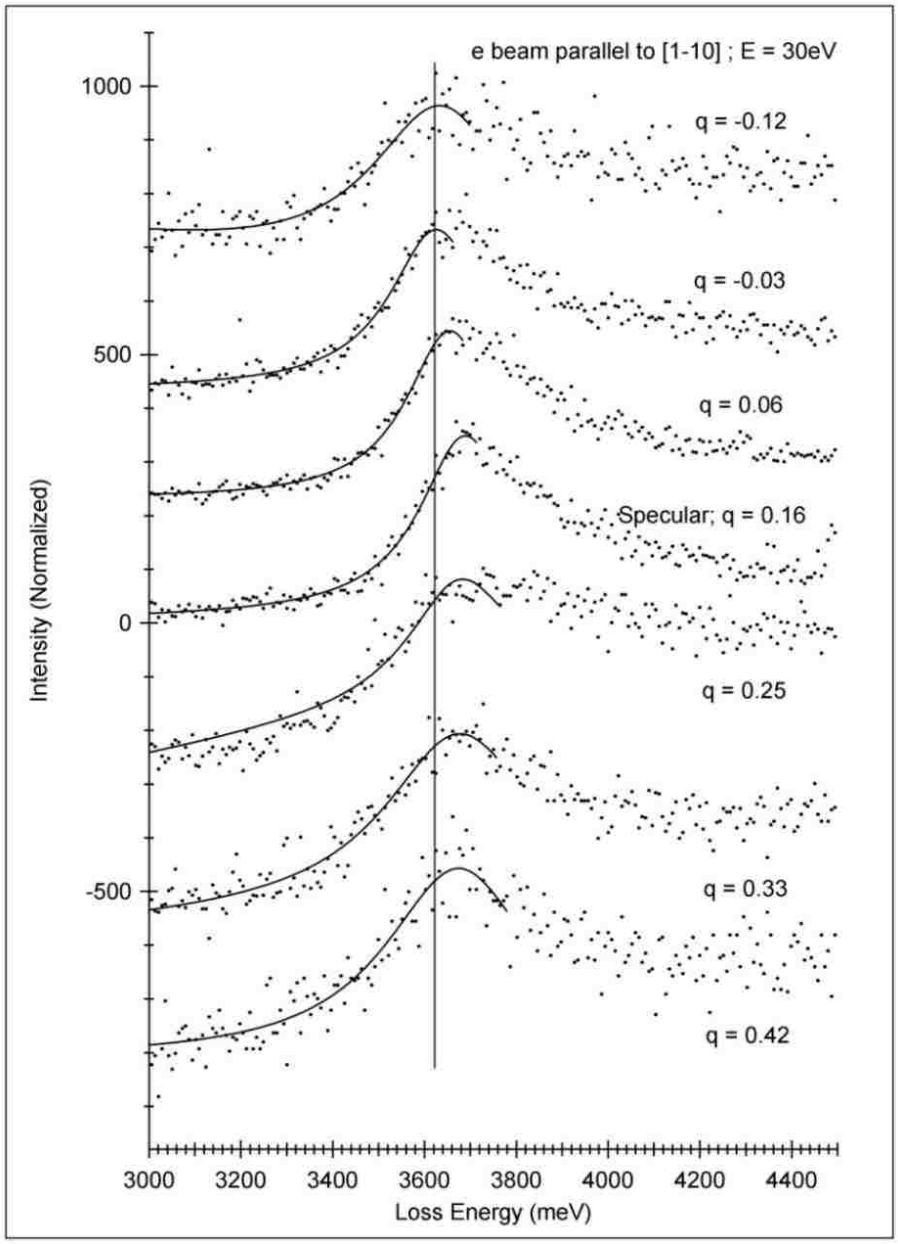

Figure 5.4 Off specular HREELS spectrum of the Ag/Cu(1 1 0) surface for Ag coverage of ~20ML. Dots represent the data and line represents the curve fit with a Lorentzian and a line together. Corresponding angles are 68˚–56˚ (q = 0.42-0.12). These measurements are along the nanowire.

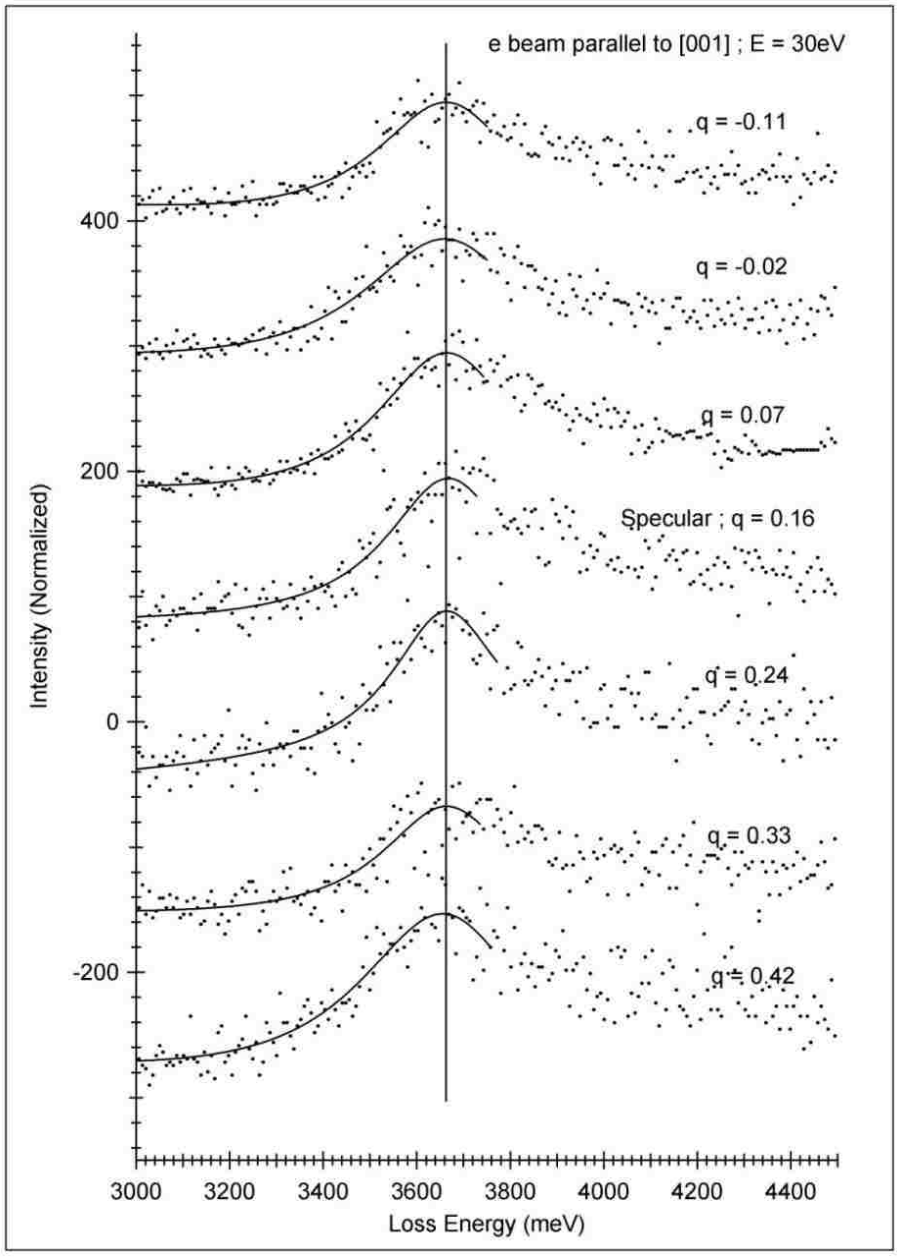

Figure 5.5 Off specular HREELS spectrum of the Ag/Cu(1 1 0) surface for Ag coverage of ~20ML. Dots represent the data and line represents the curve fit with a Lorentzian and a line together. Corresponding angles are 68˚–56˚ (q = 0.42-0.12). These measurements are across the Ag nanowire.

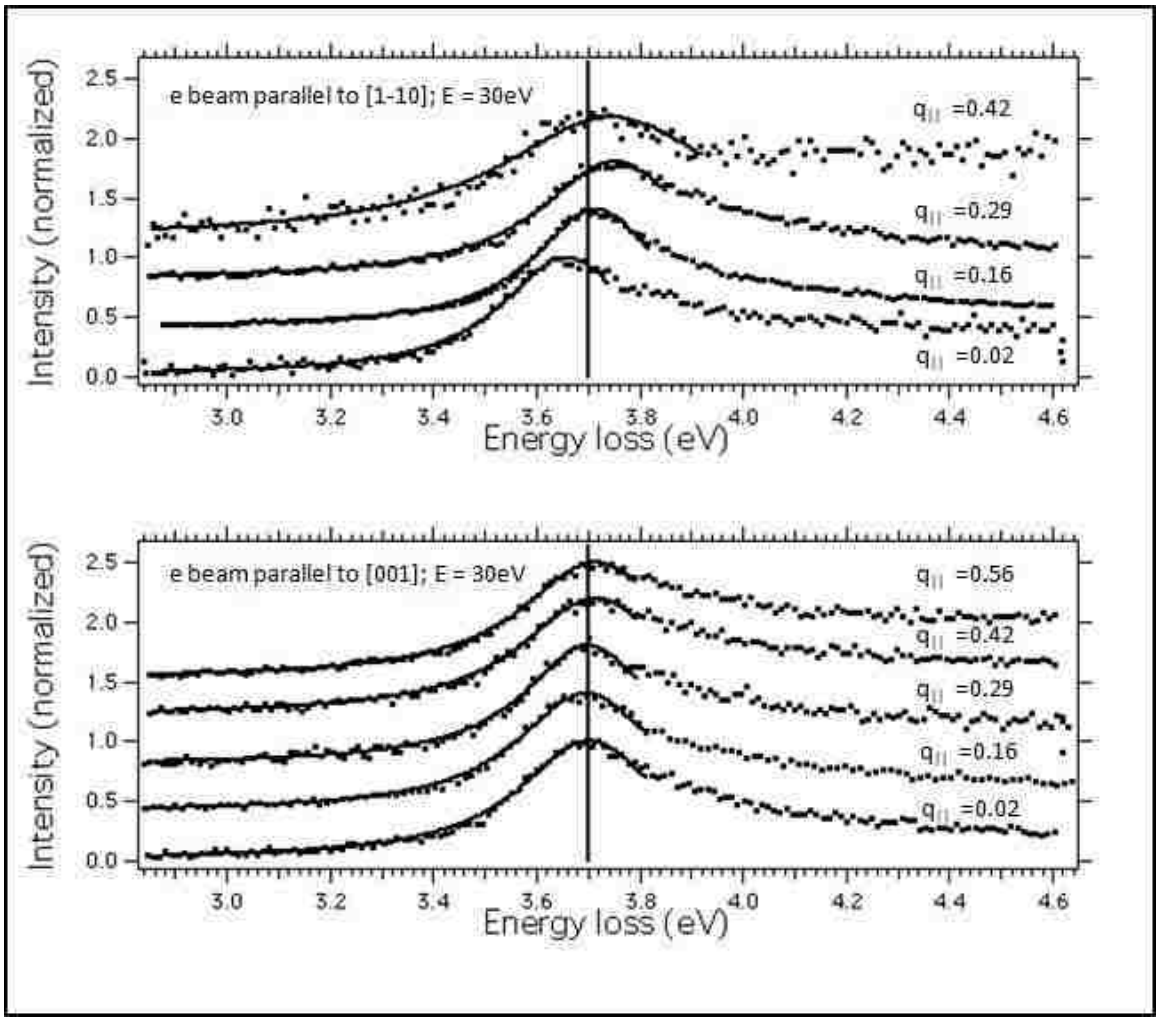

Figure 5.6 Off specular HREELS spectrum of the Ag/Cu(1 1 0) surface for Ag coverage of ~30ML. Dots represent the data and line represents the curve fit with a Lorentzian and a line together. The TOP figure is for along the Ag nanowire. The BOTTOM is for across the nanowire.

$$\text{im}\left(-\frac{1}{\varepsilon}\right) = \varepsilon_2/(\varepsilon_1^2 + \varepsilon_2^2) \qquad -(5.4)$$

$$\text{im}\left[\frac{\varepsilon-1}{\varepsilon+1}\right] = 2\varepsilon_2/(\varepsilon_1^2 + \varepsilon_2^2 + 2\varepsilon_1 + 1) -(5.5)$$

$$\text{im}\left[\frac{\varepsilon-1}{\varepsilon+2}\right] = 3\varepsilon_2/(\varepsilon_1^2 + \varepsilon_2^2 + 4\varepsilon_1 + 4) -(5.6)$$

Equations 5.4 – 5.6 will give scattering cross sections for bulk, surface and Mie plasmon. Using these with the dielectric constant data in Figure 5.1 and 5.2 (TOP parts), numerically calculated plots of cross sections are shown in the Figure 5.1 and 5.2 (BOTTOM parts). We see interesting trends from the figure. In the case of Ag it is shown the bulk plasmon resonance comes at ~3.6eV and this resonance energy down shifts when moving from bulk to surface (surface plasmon resonance from the data is ~3.4eV) plasmon.

The trend continues when moving from surface to Mie resonance where the resonance occurs at ~3.3eV. It is possible to see the intensity also increase by several magnitudes when moving from bulk to Mie plasmons. Similar behavior is observed for Cu where the peaks are shifting when moving from bulk to surface to Mie plasmons. Although less pronounced the Cu resonance peaks also increase in intensity moving from bulk to surface to Mie.

Ag has extremely sharp bulk plasmon resonance as opposed to Cu where there are no plasmon peaks. Without the contribution of from d bands both Ag and Cu will have one electron (from s) per atom. This will yield $h\omega_p/2\pi$ (Ag) = 9.0eV and $h\omega_p/2\pi$ (Cu) = 10.8eVrespectively for their bulk plasmon frequencies, given by the condition $\varepsilon = 0$. In the case of Ag the strong inter – band transition increases the $\varepsilon_1$before ε_2 ($\varepsilon = \varepsilon_{1+} i\varepsilon_2$) increases near 4eV making the plasmon excitation condition satisfied at a new energy (3.78eV).

Contrastingly the onset of same inter band transition for Cu occurs at ~2eV but the ε_2 being a large value while ε_1 is smaller (ε~0) will make the plasmon gets highly damped. This

makes the dielectric contribution from the inter – band transition of Cu weak to make a plasmon condition.

It is possible to explain the surface plasmon condition in the similar lines. The energies for the surface plasmon is given by $\varepsilon_1 = -1$ and ε_2 being small. For Cu this condition is satisfied at ~3.65eV although the free electron energies is at 6.4eV even then the excitation is damped because ε_2 is not particularly small. Similar conditions apply to the Mie resonance of the Cu but the intensity gradually increases and resonance condition is satisfied at $\varepsilon_1 = -2$ and ε_2 being small. From free electron energies this is at5.2eV. This energy gets shifted to ~3.5eV where it is slightly below the interband transition energy.

For Ag on the other hand surface plasmon and Mie plasmon condition gets satisfied extremely close to each other. ($\varepsilon_1 = -1$ and $\varepsilon_1 = -2$ while $\varepsilon_2 \sim 0$) This is seen by the resonance peaks of the cross sections of Figure 5.1, this is because ε_2 stay very small for this region. It also makes Ag resonance particularly intense.

As it is seen clearly by the resonance energies the ratios between the bulk and the surface plasmon, bulk and Mie resonance energies $\omega p/\omega M=\sqrt{2}$ and $\omega p/\omega M=\sqrt{3}$ (this is exact for the Jellium model and closely satisfied for the simple metals) do not hold for Ag. This is one of the reasons that make collective excitations of Ag interesting. One has to keep in mind the dielectric constants used to derive these relations are bulk dielectric constants. In our system the surface contribution dominates over bulk. Therefore excitations of the collective modes become sensitive to the surface properties (e.g. surface band structures of the nanowires). Therefore the comparisons to be taken with care.

Using the dispersion of the plasmon peaks we have calculated energy of the plasmon resonance with respect to the momentum transfer in ~20ML coverage in Figure 5.7 and ~30ML coverage in Figure 5.8. We see essentially the same trend in both cases. There is no dispersion

across the nanowire direction. This is clearly seen in the Figure 5.7 and Figure 5.8 Along the nanowire direction we see dispersion as the increasing momentum transfer the plasmon resonance energy increase. We see no change in the trend when the coverage is increased from 20ML of Ag to 30ML of Ag.

Clearly the resonance peaks observed in the dispersion relationship cannot be that of Cu. This is because the energies are completely different from that of Cu. The Ag nanowires have side facets of {1 1 1} and {1 1 0} as stated before. Therefore dispersion relations could arise due to the surface dispersion of the Ag(1 1 1) overlayer and the side facets of the nanowires. But when consider the published literature by Lee *et. al.* (G. Lee 1995) and Rocca *et. al.* (Rocca, Lazzarino and Valbusa 1992) which among them are in qualitative agreement suggest the dispersion in the case of Ag(1 1 1) and Ag(1 1 0) is linear plus a quadratic term:

$$\frac{\hbar\omega_{sp}}{2\pi} = \frac{\hbar\omega(0)}{2\pi} + Aq_{||} + Bq_{||}^2 \quad -(5.7)$$

Although the constants A and B for the groups are different they both have obtained the quadratic term (B≠0) making our dispersion relation distinctly different from Ag(1 1 0) or Ag(1 1 1).

In the Ag nanowire dispersion we see a linear dispersion relation:

$$\frac{\hbar\omega_{Np}}{2\pi} = \frac{\hbar\omega(0)}{2\pi} + Aq_{||} \quad -(5.8)$$

where $\omega(0) \sim 5.46\times10^{15} eV$ and $A \sim 0.3 eV\text{Å}$ for the both dispersion relations we have obtained data. The values reflect clear linearity and deviation from quadratic form. Further the distinct shape where the linear followed by flat line has not been seen in literature for bulk or surface plasmon dispersion.

When compared the nanowire plasmons to the Mie plasmons, we clearly there could be no dispersion relation if the nanowire plasmons are Mie plasmons. This rules-out any connection

to their behavior to the Mie resonances. Taken all these factors we conclude the dispersion relation we have obtained for the Ag nanowires is unique and has not be seen for any of the involved surfaces or bulk in the system.

Our q|| (relatively high) values make the dispersion relation is (strictly) can be applied to non retarding region where $q_{||} >> \omega/c$. In line with the Ag surfaces our dispersion relation is also positive as oppose with other simple metals having negative dispersion. Another intriguing factor in this is the $q_{||} \sim 0$, loss energies along the nanowire and across the nano wire never seem to be equal to each other. This cannot be explained so far and it is highly unlikely that this be a data error as both dispersion relations show this clearly.

Coupling of the electron wave vector to the nanowire is seen with increasing angle, *i.e.* increase momentum transfer along the wire (e beam along [1 $\bar{1}$ 0] or ΓX direction of the Cu substrate). With increasing transfer vector ($q_{||}$) we see clear increase in Ag plasmon resonance frequency. This is an unambiguous indication of the existence of normal modes of the collective oscillations giving rise to plasmon modes along the Ag nanowire. Contrastingly we don't see any change in resonance energy for the momentum transfer carried out in the across the wire direction (e beam along [0 0 1] direction of the Cu substrate). This leads us to conclude there are no normal modes of collective oscillations give rise to plasmon modes across the wire.

In our system (self assembled Ag nanowires in Cu(1 0 0)) the dispersion curves from photo emission also gives similar results (Zhao 2005). There is clear evidence of anisotropic nanowire band dispersion investigated by ARUPS (Angle Resolved Photo Emission Spectroscopy).

It has been shown by Zhao *et. al.* that there exists non zero dispersion along the nanowire ([1 $\bar{1}$ 0] direction or ΓX direction on Cu(1 1 0)) direction while no dispersion across the nanowire([0 0 1] or ΓY direction on the Cu(1 1 0)) . Ag nanostructures on Cu(1 1 0) substrate is

defined aptly as nanowires due to the existence of these conduction bands along the wire as opposed to across the wire. This indicates the anisotropic plasmon dispersion is a possible manifestation of the anisotropic electronic structure of the wire.

Coupling of photons along the wire via plasmon excitations has been observed for multitude of nanowire systems. Standing wave patterns were observed for the excited plasmons (via a laser) in lithographically patterned, Ag nanowires (Ditlbacher, et al. 2005).

This is shown with SPP (surface plasmon polaritons) for a similar system of Ag and Au nanowires by measuring optical transmissions associated extinction (Schider, et al. 2003). Schider *et. al.* have come up with a simple but elegant way of explaining the standing waves by a standing wave vector and have used it to describe the dispersion relation.

The dispersion relation they have obtained is markedly different from ours. They have obtained a quadratic dispersion. Their dimensions are considerably higher compared to our Ag nanowires system.

As opposed to Ag nanowires in our system having dimensions with height = 2.5nm and width = 10nm their nanowires were height = 75nm and width = 85nm. This is a common contrast with our systems and other Ag nanowire systems described here. Plasmon propagation, redirection and fan out between connected wires is shown for another lithographically patterned Ag nanowire system where the fan out of plasmons is achieved by having fanning wires at closer proximity than the decay length of the plasmons in the wires.

Nanowires used in all these systems were lithographically patterned making them 1. uniform 2. arranged/ patterned on a substrate surface. These factors make it comparatively easy to study these systems by the virtue of increase homogeneity of the optical/electronic and structural properties. Still in our system we have obtained the dispersion relationship comparable to the other systems investigated predominantly by optical spectroscopes.

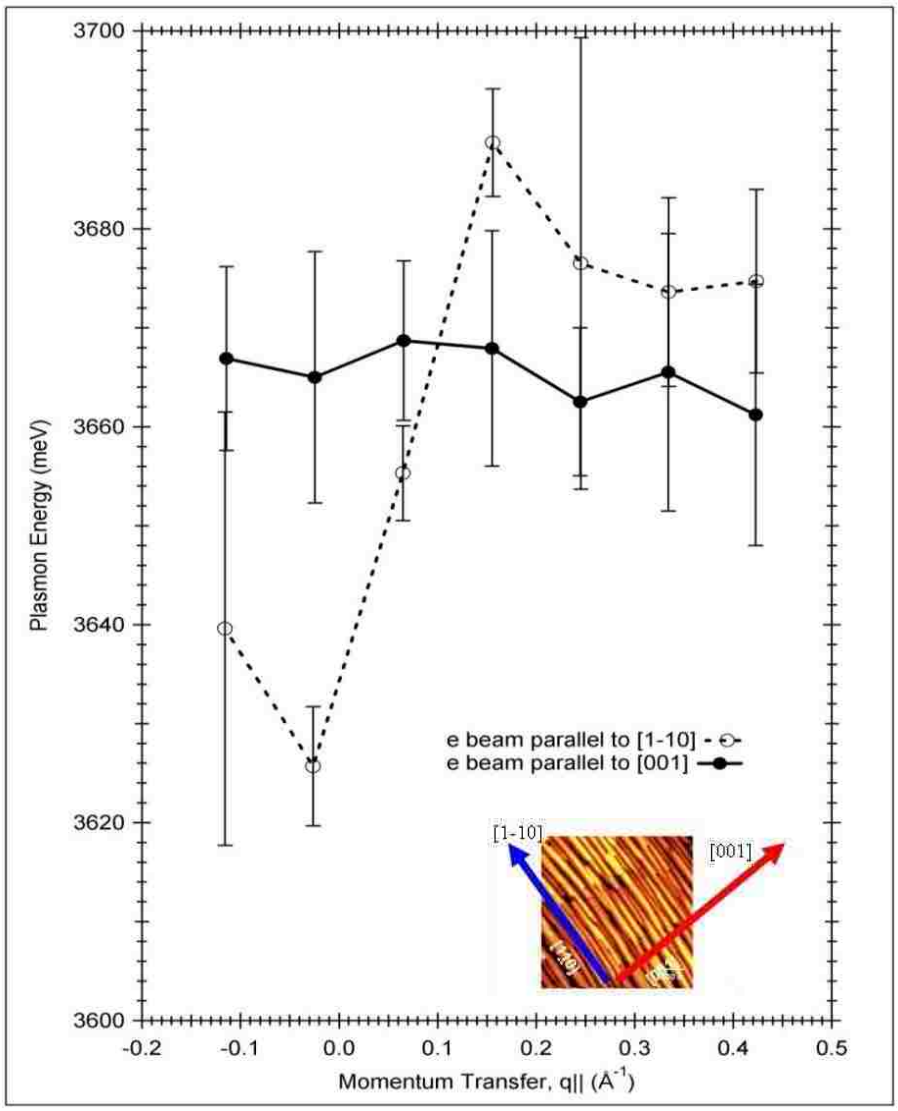

Figure 5.7 Dispersion relation for the Ag nanowires θ ~ 20ML on Cu(1 1 0). Energy vs. momentum (q||) of the plasmon peaks form Figure 5.4 and Figure 5.5 are plotted on this figure. Errors are for the Lorentzian fits used. Inset shows the STM image of the corresponding coverage with the respective directions. Along the wire is [1-10] while across the wire is [0 0 1].

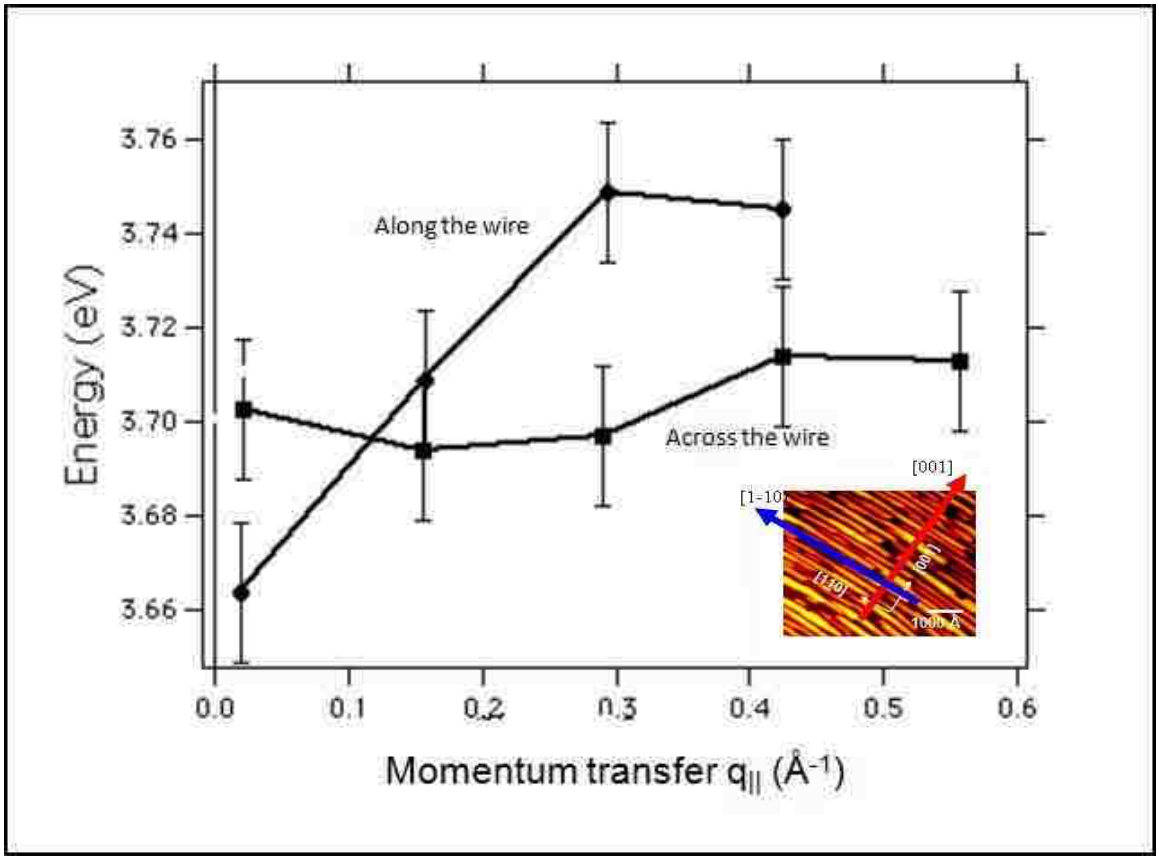

Figure 5.8 Dispersion relation for the Ag nanowires θ ~ 30ML on Cu(1 1 0). Energy vs. momentum (q||) of the plasmon peaks form Figure 5.6 is plotted on this figure. Errors are for the Lorentzian fits used. Inset shows the STM image of the corresponding coverage with the respective directions. Along the wire is [1-10] while across the wire is [0 0 1].

5.5 Summary

For a self assembled, anisotropic, heteroepitaxial Ag (metal) on Cu (metal) nanowire system we have shown:

1. Existence of dispersive normal modes of collective oscillations giving rise to plasmon modes along the wire.

2. Non dispersive normal modes (Mie like) *i.e.* plasmon modes across the wire direction, therefore anisotropic plasmons on the system.

3. Nanowire plasmon dispersion relation is unique to the nanowires. It shows no direct connection to bulk, surface or Mie plasmons.

4. Linear short $q_{||}$ plasmon dispersion along the wire flattens out almost abruptly for increasing $q_{||}$, unlike any other system.

5. Increased nanowire number density shows no change in the dispersion relation making it more of a nanowire property rather than a nanowire population property.

6. These plasmon dispersion relations are possible manifestation of the anisotropic electronic structure of the wires.

Further investigations are necessary to establish a clear picture of the process. This includes the extended HREELS study with varying energies and extended range of momentum transfer. This can be complemented by an in situ optical spectroscopic study of the system. Concurrent theoretical picture is increasingly needed at this point. One other question that has not been answered is the mismatched plasmon energies at $q_{||} = 0$ for the different directions. This needs to be address in a proper theoretical frame work.

6 Summary

In this dissertation we have worked to develop a better understanding of the structure and morphology of metal-on-metal nanostructures, the kinetics and thermodynamics of their self-assembly, their thermodynamic stability under variation of temperature, and excitations of their collective modes. These investigations were focused on two model systems:

1. Ag nanowires on Clean Cu(1 1 0)
2. Co nanodots on clean Ag(1 1 0)

In our first study we investigated the structure, kinetics and thermodynamics of Ag deposited on Cu(1 1 0). We have used LEEM and AES to study this system. For Ag deposited on Cu(1 1 0) at ~400K we found that the there is considerable surface diffusion of Ag, even at this moderate temperature. We have identified the saturation of the wetting Ag(1 1 1) monolayer by the decreased work function exhibited in LEEM, and the nucleation of Ag nanowires at a coverage of 1.2ML. The wetting layer of Ag(1 1 1) exemplifies Ag surface free energy being lower than that of Cu, yet the nucleation of anisotropic nanowires reveals the underlying strain due to the lattice mismatch of the system. The nucleation sites were identified as impurity-atom defects and step edges, which pin initial adatoms in place and restrict diffusion. Following saturation of the Ag(1 1 1) wetting monolayer, additional Ag leads to a dramatic increase in nanowire nucleation, a nucleation rate which drops down exponentially overtime possibly as nanowires elongate rather than nucleate at new sites. Ag adatom transport along the nanowire enables the growth towards [1 $\bar{1}$ 0] direction and the most preferable bonding site is found at the ends of the nanowires. There is a high degree of inter-wire adatom transport between closely spaced nanowires (separation << width). This is indicative of the effect of low diffusion lengths on growth of wires.

Following nucleation, nanowires initially grow along the [1 $\bar{1}$ 0] direction, growing out from the bottom step and, as the nanowire height increases, it eventually grows across the step edge onto the terrace above. This indicates an energy barrier at play for the diffusion across the step edge. Nanowires that spontaneously nucleate at multiple sites across the surface continue to grow with increasing Ag coverage, reaching similar aspect ratios and sizes. Substrate-mediated strain constrains nanowire widths and prevents the coalescence of nanowires that grow parallel to one another.

Nanowire growth rate versus length and time shows fluctuations suggesting that some nanowires will grow at the expense of the elongation of other nanowires. This may be due, in part, to a blocking effect as one nanowire preferentially accommodates new Ag adatoms deposited on the surface.

Upon annealing a surface covered with nanowires to temperatures near ~700K, nanowires ripen to larger Ag nanobars and microclusters. The mechanism governing this transformation is Ostwald ripening in where large clusters grow at the expense of smaller ones. The process is observed to occur at a transition temperature: ~670K where a dramatic reduction in the number of nanowires is observed. The smaller aspect ratios of the microclusters indicate a reduction in the dominance of strain, although the anisotropic shapes suggest that it still exists.

The reduced strain may be due to the promotion of misfit dislocations in the microclusters that are now kinetically available via the elevated temperature. The Ag microclusters have two distinct widths indicating a possible quantum size effect. The microcluster edges exhibit a mixing/surface alloying, which bears further investigation. Bulk alloying of Ag and Cu is not thermodynamically stable therefore this etching mechanism may be a special case of surface alloying. In our second system we studied the structure of thermally-driven subsurface migration and agglomeration of Co nanodots on Ag(1 1 0). Measurements

were carried out using STM, LEED and AES. At sub monolayer Co coverage on Ag(1 1 0), Co forms nanodots of ~3-6Å heights with widths of ~25Å. When Co coverage is increased we see an increased number density of nanodots stacking next to each other, and at different heights. One potential explanation for the height variation involves the displacement of surface Ag, which allows Co to minimize its surface free energy by changing it to an interfacial free energy with Ag. The displaced Ag forms islands in between Co clusters and additional Co may nucleate on these terraces, giving rise to new clusters growing at different heights. When the system is annealed by gradually increasing temperature we find that sintering of clusters leads to super-clusters. Interestingly we do not see Ostwald ripening in this case and it appears that the original clusters migrate and sinter, and these distinct smaller clusters join intact to form the super-clusters. Since they retain their individual nature, it is possible that there may be Ag wetting layers between the smaller clusters, providing a reduction in the Co surface free energy through the creation of a lower interfacial free energy with Ag. There is evidence that a portion of Co segregates in to the Ag bulk. In this form, it appears that Co nanodots have great structural stability against temperature increments and this is quite intriguing. As mentioned, we see no layered growth of Co on Ag(1 1 0) due to its large relative surface free energy and the considerable lattice mismatch with Ag.

In the case of Ag nanowires on Cu(1 1 0), we extended previous work by investigations of the optical properties of quasi-1D materials by investigating their plasmon dispersion relations. Since the nanowires are so anisotropic, the likelihood of exhibiting anisotropic excitations is expected to be high. Using EELS, we find that there are collective oscillations in the nanowires and they are found to differ when we compare their properties for momentum transfer along or perpendicular to the wire. For momentum transfer across the wire, the plasmon modes do not exhibit momentum dependence, so that they are a localized excitation similar to

the Mie resonance exhibited in clusters. For momentum transfer along the nanowire we find that there is a striking difference. For momentum transfer near $q_{||} = 0$ the plasmon dispersion is linear, and it flattens out to a constant value for $q_{||} > 0.3\text{Å}^{-1}$. Increased numbers of nanowires on the surface has little impact on this dispersion relation suggesting that these excitations do not couple between nanowires.

Our studies of these model metal-on-metal systems have revealed quite different outcomes when one considers the competition between kinetic effects and the thermodynamic limit for material stability. In one case, where the surface free energy of the adatom species is lowest, kinetic limitations during growth lead to anisotropic nanowires that have new quasi 1-D collective excitations. In this system, one approaches the thermodynamic equilibrium more closely by heating, and the result is an Ostwald ripening that will ultimately lead to two independent crystalline phases of the starting materials. In the second case, where the adatom surface free energies are much larger than the substrate, we find cluster formation that is driven by free energy considerations – essentially forcing a thermodynamically driven endpoint from the beginning. Upon annealing to further approach equilibrium, we find indications that the materials are still far from equilibrium, and the sintering of clusters indicates that surface-free energy considerations are still dominating material structures.

Bibliography

Aarhus University, Denmark, 1996. "Aarhus STM Manual." Aarhus: Aarhus University, 1996.

Agarwal, B. K. *X-Ray Spectroscopy.* Vol. 15. Berlin, Heidelberg: Springer, 1991.

Agrawal, P. M., B. M. Rice, and D. L. Thompson. *Surface Science* 515 (2002): 21.

Alberty, R. A. "Principle of Detailed Balance in Kinetics." *Journal of Chemical Education* 81 (2004): 1206-1209.

Alferov, Z. I. "The double heterostructure: concept and its applications in physics, electronics and technology. ." *Nobel lecture*, 2000: Stockholm.

Altman, M. S., S. Chiang, P. Statiris, T. Gustafsson, and E. Bauer. "Stress-Induced Microfacetted Reconstructions of the Pb(110) Surface." In *The Structure of Surfaces IV*, by X. Xie, S.Y. Tong and M.A. Van Hove, 183. Singapore: World Scientific Publishing Company, 1994.

Altman, M. S., W. F. Chung, and C. H. Liu. *Surf. Rev. and Lett.* 5 (1998): 1129.

Amirthapandian, S., et al. *Journal of Physics: Condense matter* 14 (2002).

Andersson, S. *Surf. Sci.* 18 (1969): 325.

Archard, G. D., and T. Mulvey. *J. Sci. Instrum.* 35 (1958): 279.

ASM International . *Binary Alloy Phase Diagram (Version 1.0).* Materials Park, OH, 1995.

Aufreyl, B. et al. *Surface Science* 531 (1994): 307.

Baibich, M. N., et al. *Physical Review Letters* 61 (1988): 2472.

Bak, P., C. Tang, and K. Wiesenfeld. *Physical Review Letters* 59 (1987): 381.

Bartelt, N. C., W. Theis, and R. M. Tromp. *Physical Review B* 54 (1996): 11741.

Bauer, E. *Applied Surface Science* 11/12 (1982): 479.

Bauer, E. *Surf. Rev. & Lett.* 5 (1998): 1275.

Bauer, E. *Rep. Prog. Phys.* 57 (1994): 895.

Bauer, E. *Ultramicroscopy* 17 (1985): 51.

Bauer, E. Edited by S. S. Breese. *Electron Microscopy* (Academic Press Inc) 1 (1962): D-11.

Bauer, E. "Interactions on Metal Surfaces." Edited by R. Gomer. (Springer) 1975: 225.

Bauer, E., M. Mundschau, W. Swiech, and W. Telieps. *Ultramicroscopy* 17 (1985): 57.

Bennette, C. J., L. W. Swanson, and F. M. Charbonnier. *Journal of Applied Physics* 28 (1967): 634.

Bensaude-Vincent, B., and A. Hessenbruch. *Nature Materials* 3 (2004): 345.

Berkowitz, A. E., et al. *Phys. Rev. Lett.* 68 (1992): 3745.

Binasch, G., P. Grunberg, F. Saurenbach, and W. Zinn. *Physical Review Letters* 57 (1986): 2442.

Binnig, G., and H. Rohrer. *Rev. Mod. Phys. Nobel Lecture delivered on 8th Dec., 1986.* 59 (1987): 615.

Binnig, G., H. Rohrer, C. Gerber, and E. Weibel. *Phys. Rev. Lett.* 49 (1982): 57.

Binning, G., C. F. Quate, and C. H. Gerber. *Phys. Rev. Lett.* 56 (1986): 930.

Bode, M. *Rep. Prog. Phys.* 66 (2003): 523.

Brink, J. van der. *Nature Nanotechnology* 2 (2007): 199.

Bruno, P. *Physical Review B* 52 (1995): 411.

Camarero, J., J. J. de Miguel, R. Miranda, and A. Hernando. *Journal of Physics Condense Matter* 12 (2000).

Chen, Y., D. A. A. Ohlberg, G. Medeiros-Ribeiro, Y. A. Chang, and R. S. Williams. *Applied Physics Letters* 26 (2000): 4004.

Cheng, R., et al. *Physical Review B* 69 (2004): 184409.

Childs, K. D., and C. L. Hedberg. *Handbook of Auger Electron Spectroscopy.* Eden Prairie, MN:

Physical Electronics Publishing, 1995.

Chmelik, J., L. Veneklasen, and G. Marks. *Optik* 83 (1989): 155.

Davis, L. E., N. C. McDonald, P. W. Palmberg, and R. E. Weber. *Hand Book of Auger Electron Spectroscopy.* Eden Prairie, MN: Physical Electronic Industries, 1976 .

De Miguel, J. J., et al. *Surface Science* 211-212 (1989): 732-739.

De Miguel, J. J., et al. *Journal of Magnetism and Magnetic Materials* 93 (1991): 1-12.

Dietzel, W., G. Meister, and E. Bauer. *Z. Phys. B Condense Matter* 47 (1982): 189.

Ditlbacher, H., et al. *Phys. Rev. Lett.* 95 (2005): 257403.

Egelhoff Jr., F. W., P. J. Chen, C. J. Powell, M. D. Stiles, and R. D. McMichael. *Journal of Applied Physics* 79 (1996).

Egelhoff Jr., W. F., and D. A. Steigerwald. *Journal of Vacuum Science and Technology A* 7 (1989).

Ehrenberg, W. *Philos. Mag.* 18 (1934): 878.

Ehrenreich, H., and H. R. Philipp. *Phys. Rev.* 128 (1962): 1622.

Ehrlich, G., and F. Hudda. *Journal of Chemical Physics* 44 (1966): 1039.

Emsley, J. *The Elements* . Oxford: Clarendon Press , 1998.

Encyclopædia Britannica. *Cobalt (Co) Encyclopædia Britannica Online.* 2008. <http://www.britannica.com/eb/article-9024523>. (accessed 04 23, 2008).

Evans, E., and D. L. Mills. *Phys. Rev. B* 8 (1973): 4004.

Farral, G.A., and J. M. Lafferty. *Vacuum Arcs Theory and Applications.* New York : John Wiley & Sons, 1980.

Feenstra, R. M., W. A. Thompson, and A. P. Fein. *Phys. Rev. Lett.* 56 (1986): 608 .

Fink, M., M. R. Martin, and G. A. Somorjai. *Surf. Sci.* 29: 303 .

Fitting, L., M. C. Zeman, W. -C. Yang, and R. J. Nemanich. *Journal of Applied Physics* 93 (2003): 4180.

Fowler, R. H., and L. W. Nordheim. *Proc. Roy. Soc.* 1928. 173.

Fuggle, J. C., and J. E. Inglesfield. *Unoccupied Electronic States, Topics Appl. Phys.,* (Springer) 69 (1992).

Germany, ELMITEC Elektronenmikroskopie Gmbh –. *Model LEEM III, Low Energy Electron Microscope Manual – Version V1.4* . manual, ELMITEC Elektronenmikroskopie Gmbh – Germany, 1995.

Gijs, M. A. M., S. K. J. Lenczowski, and J. B. Giesbers. *Physics Review Letters* 21 (1993): 3343.

GMBH, Elmitech. *www.Elimitech.com.* 2007. http://www.elmitec-gmbh.com/.

Godowski, P. J., J. Onsgaard, M. Trzebatowska-Gusowska, K. Pater, and Z. S. Li. *Physical Review B* 73 (2006): 193403.

Hannon, J. B., S. Kodambaka, F. S. Ross, and R. M. Tromp. *Nature* 440 (2006): 69.

Heringdorf, F. J. Meyer Zu. *Surf. Rev. Lett.* 5 (1998): 1167.

Herlt, H. J. *Ph.D. Dissertation.* TU Clausthal, 1982.

Herlt, H. J., and E. Bauer. *Surf. Sci.* 175 (1986): 336.

Herlt, H. J., R. Feder, G. Meister, and E. Bauer. *Solid State Commun.* 38 (1981): 973.

Hite, D. Baton Rouge: Louisiana State University, 2001.

Hite, D. A., O. Kizilkaya, and P. T. Sprunger. *Physical Review B* 65 (2002): 113411.

Huang, H., and J. Wang. *Applied Physics Letters* 83 (2003): 4752.

Ibach, H., and D. L. Mills. *Electron Energy Loss Spectroscopy and Surface Vibrations.* New York: Academic Press, 1982.

Jiang, Q., H. M. Lu, and M. Zhao. *Journal of Physics: Condense Matter* 16 (2004): 521.

Jubert, P. O., O. Fruchart, and C. Meyer. *Physical Review B* 64 (2001): 115419.

Khantha, M., and V. Vitek. *Acta Mater.* 45 (1997): 4675.

Kief, M. T., and W. F. Egelhoff Jr. *Physical Review B* 47 (1993): 10785.

Kief, M. T., G. J. Mankey, and R. F. Willis. *Journal of Applied Physics* 69 (1991).

Kim, J., W. A. Anderson, Y. Song, and G. B. Kim. *Applied Physics Letters* 86 (2005): 253101.

Kittle, C. *Introduction to Solid State Physics.* 1996.

Kizilkaya, O. Baton Rouge: Louisiana State University, 2003.

Kizilkaya, O., and P. Sprunger. *Unpublished transactions.*

Klein, M. J. "Princilple of Detailed Balance." *Physical Review* 97 (1955): 1446-1447.

Kolarik, V., M. Mankos, and L. H. Veneklasen. *Optik* 87 (1991): 1.

Kroemer, H. "Quasi-electric fields and band offsets: teaching electrons new tricks." *Nobel Lecture,* 2000: Stockholm.

Lander, J. J., J. Morrison, and F. Unterwald. *Rev. Sci.Instrum* 33 (1962): 784.

Lee, C. H., R. F.C. Farrow, C. J. Lin, E. E. Marinero, and C. J. Chien. *Physical Review B* 42 (1990): 11384.

Lee, G. *Dissertation.* Philadelphia: University of Pennsylvania, 1995.

LeGoues, F. K., M. C. Reuter, J. Tersoff, M. Hammar, and R. M. Tromp. *Phys. Rev. Lett.* 73 (1994): 300.

Leonard, D., K. Pond, and P. M. Petroff. *Physical Review B* 50 (1994): 11687.

Li, H., and B. P. Tonner. *Surface Science* 141 (1990): 237.

Lifshitz, I. M., and V. V. Slyozov. *J. Phys. Chem. Solids* 19 (1961): 35.

Lucas, A. A., and J. P. Vigneron. *Solid State Commun.* 49 (1984): 327.

Lucas, A. A., and M. Sunjic. *Phys. Rev. Lett.* 26 (1971): 229.

Lüth, H. *Solid Surfaces, Interfaces and Thin Films.* 4. Berlin: Springer, 2001.

Luth, H. *Solid Surfaces, Interfaces and Thin Films.* Berlin: Springer-Verlag, 2001.

Maier, S. A. *Plasmonics.* Springer, 2007.

Marsot, N., R. Belkhou, H. Magnan, P. Le Fevre, C. Guillot, and D. Chandesris. *Physical Review B* 59 (1993): 2855.

McLean, J. G., B. Krishnamachari, D. R. Peale, E. Chasen, J. P. Sethna, and B. H. Cooper. *Physical Review B.* 55 (1997): 1811.

Mezey, L. Z., and J. Giber. *Japanese Journal of Applied Physics* 21 (1982).

Michaelson, H. B. *Journal of Applied Physics* 48 (1978): 4729.

Michaelson, H. M. *J. App. Phys.* 48 (1977): 4729.

Mie, G. *Ann. Physik* 25 (1908): 377.

Miedema, A. R. *Phillips Technical Reviews* 36 (1978): 218.

Mo, Y. W., D. E. Savage, B. S. Swartzentruber, and M. G. Lagally. *Physical Review Letters* 65 (1990): 1020.

Mundschau, M., E. Bauer, W. Telieps, and W. Swiech. *Surf. Sci.* 213 (1989): 381 .

Nature Nanotechnology Editorial. *Nature Nanotechnology* 2 (2007): 191.

Nĕel, L. *Comp. Rend. Acad. Sci.* 255 (1962): 1545.

NIST. *National Institute of Standards and Technology (NIST) NIST ITS-90 Thermocouple Database.* 2007. http://srdata.nist.gov/its90/main .

NIST. *NIST Electron Elastic Scattering Cross Section Database - Standard Reference Data Base 64* . Gaithersburg: NIST, 1996.

Nogami, J., B. Z. Liu, M. V. Katkov, C. Ohbuchi, and N. O. Birge. *Physical Review B* 63 (2001): 233305.

Nyquist, H. *Phys. Rev.* 32 (1928): 110.

Orendorff, C. J., T. K. Sau, and C. J. Murphy. *Small* 2 (2006): 636.

Ostwald, W. *Z. Phys. Chem.* 34 (1900): 495.

Pappas, D. P., and C. S. Arnold. *Rev. of Sci. Inst.* 76 (2005): 016104 .

Pearsall, T. P., J. Bevk, L. C. Feldman, J. M. Bonar, J. P. Mannaerts, and A. Ourmazd. *Physical Review Letters* 58 (1987): 729.

Pedersen, M. O., et al. *Surface Science* 387 (1997): 86.

Pendry, J. B. *Low Energy Electron Diffraction.* London: Acedemic, 1974.

Penn, D. R. *Physical Review B* 35 (1987): 482.

Plass, R., J. A. Last, N. C. Bartelt, and G. L. Kellogg. *Nature* 412 (2001): 875-876.

Pratt Jr., W. P., S. F. Lee, J. M. Slaughter, R. Loloee, P. A. Schroeder, and J. Bass. *Physical Review Letters* 66 (1991): 3060.

Prigogine, I. "Time, Structure and Fluctuation"." *Nobel Lecture.* Stockholm, 1977.

Prutton, M. *Intoduction to surface Physics.* New York: Clarendon Press, 1998.

Raether, H. *Surface Plasmons.* Springer, 1988.

Rastelli, A., H. Von Kanel, B. J. Spencer, and J. Tersoff. *Physical Review B* 68 (2003): 115301.

Rife, P. *Lise Meitner and the Dawn of the Nuclear Age.* Birkhäuser, 1999.

Ritchie, R. H. *Phys. Rev.* 106 (1957): 874.

Rocca, M., M. Lazzarino, and U. Valbusa. *Phys. Rev. Lett.* 69 (1992): 2122.

Rolland, A., and B. Aufray. *Surface Science* 530 (1985): 162.

Rosenfeld, G., R. Servaty, C. Teichert, B. Poelsema, and G. Comsa. *Physical Review Letters* 71 (1993).

Scheibner, E. J., L. H. Germer, and C. D. Hartmann. *Rev. Sci. Instrum.* 31 (1960): 112.

Schider, G., et al. *Phys. Rev. B* 68 (2003): 155427.

Schindler, A. C., and D. E. Wolf. "Diffusion and Growth of Stained Surfaces." Edited by P. Entel and D. E. Wolf. *International Symposium on Structure and Dynamics of Heterogeneous Systems.* World Scientific, 2000. 124.

Schmid, A. K., D. Atlan, H. Itoh, B. Heinrich, T. Ichinokawa, and J. Kirschner. *Physical Review B* 48 (1993): 2855.

Schwoebel, R., and E. Shipsey. *Journal of Applied Physics* 37 (1966): 3682.

Shalaev, V. M., and S. Kawata, . *Nanophotonics with Surface Plasmons.* Elsevier, 2007.

Shao, Z., and A. V. Crewe. *Ultramicroscopy* 31 (1989): 199.

Shchukin, V. A., and D. Bimberg. *Reviews of Modern Physics* 71 (1999): 1125.

Siegmann, H. C. *Surf. Sci.* 1076 (1994): 307-309.

Sime, L. *Ruth Lise Meitner: A Life in Physics.* Berkeley, CA: University of California Press, 1996.

Sonnichsen, C., T. Franzi, T. Wilk, G. von Plessen, and J. Feldmann. *New Journal of Physics* 4 (2002): 93.

Sprunger, P. T., E. Laegsgaard, and F. Besenbacher. *Physical Review B* 54 (1996): 8163.

Stroscio, J. A., R. M. Feenstra, and A. P. Fein. *Phys. Rev. Lett.* 57 (1986): 2579.

Sumitomo, K., H. Omi, Z. Zhang, and T. Ogino. *Physical Review B* 67 (2003): 035319.

Sumitomo, K., H. Omi, Z. Zhang, and T. Ogino. *Physical Review B* 67 (2003): 035319.

Taylor, T. N., R. E. Muenchausen, and M. A. Hoffbauer. *Surface Science* 243 (1991): 65 - 82.

Telieps, W. *Appl. Phys.* A44 (1987): 55 .

Telieps, W., and E. Bauer. *Ultramicrosc.* 17 (1985): 57.

Tersoff, J., and R. M. Tromp. *Physical Review Letters* 70 (1993): 2782.

Thompson, A. C., and D. Vaughan. *X-Ray Data Booklet.* Berkeley, California: Center for X-Ray Optics and Advance Light Source, Lawrrence Berkeley National Laboratory, University of California, 2001.

Tobin, J. G., S. W. Robey, and D. A. Shirley. *Physical Review B* 33 (1986): 2270.

Tobin, J. G., S. W. Robey, L. E. Klebanoff, and D. A. Shirley. *Physical Review B* 35 (1987): 9056.

Tolkes, C., R. Struck, R. David, P. Zeppenfeld, and G. Comsa. *Physical Review Letters* 80 (1998).

Tolkes, C., R. Struck, R. David, P. Zeppenfeld, and G. Comsa. *Applied Physical Letters* 8 (1998): 73.

Tromp, R M, and M C Reuter. *Physical Review Letters* 68 (1992): 954.

Tromp, R. M. *IBM Journal of Reasearch and Development* 44 (2000): 503.

Tromp, R. M. *IBM J. Res. Develop.* 4 (2000): 44.

Tromp, R. M., and M. C. Reuter. *Physical Review Letters* 68 (1992): 954.

Tromp, R. M., and M. C. Reuter. *Ultramicrosc.* 50 (1993): 171.

Tromp, R. M., M. Mankos, M. C. Reuter, A. W. Ellis, and M. Copel. *Surf. Rev.Lett.* 5 (1998): 1189.

Tromp, R. M., R. J. Hamers, and J. E. Demuth. *Phys. Rev. Lett.* 55 (1985): 1303.

Tsong, T. T. *Progress in Surface Science* 67 (2001): 235-248.

Tsong, T. T. *Progress in Surface Science* 74 (2003): 69-80.

van der Vegt, H. A., H. M. van Pinxteren, M. Lohmeier, E. Vlieg, and J. M. C. Thornton. *Physical Review Letters* 68 (1992).

van Hove, M. A., W. H. Weinberg, and C. M. Chan. *Low Energy Electron Diffraction* . Berlin: Springer , 1986.

Veneklasen, L. H. *Rev. Sci. Instrum.* 12 (1992): 63.

Veneklasen, L. H. *Ultramicrosc.* 76 (1991): 36.

Vitos, L., A. V. Ruban, H. L. Skriver, and J. Kollar. *Surface Science* 411 (1998): 186.

Wagner, C. *Z. Elektrochem* 65 (1961): 581.

Whitesides, G. M., and B. Grzybowski. *Science* 295 (2002): 2418.

Winfree, A. T. *Journal of Chemistry Education* 61 (1984): 661.

Wiza, J. L. *Nuc. Inst. Meth.* 162 (1979): 587.

Wynblatt, P., and N. A. Gjostein. Edited by J. O. McCaldin and G. Somorjai. *Progress in Solid State Chemistry* (Pergamon) 9 (1975).

Xu, F., et al. *Physical Review B* 35 (1987): 2375.

Zangwill, A. *Physics at Surfaces.* Cambridge: Cambridge University Press, 1988.

Zhao, W. *Ph.D. Dissertation, Louisiana State University.* Baton Rouge: Louisiana State University, 2005.

Zhou, G., and J. C. Yang. *Physical Review Letters* 89 (2002): 106101.

Zimmermann, C. G., et al. *Physical Review Letters* 83 (1999).

Zinke - Allmang, M., L. C. Feldman, and S. Nakahara. *Appl. Phys. Lett.* 51 (1987): 975.

Appendix 1 Measured Nanowire - End Coordinates

Data used in the analysis of Ag nanowire end (Ag-sink) separation measurements. Each point is manually measured on ***Image XSM*** *(Steve Barrett v. 1.84, June 2007)*. The collection of nanowire end coordinates from wires on Figure 4.09. As seen the number of nanowires, therefore number of data points increase with time. Integers under time column represent nanowire–end numbers (indexed).

T=7.26s	X	Y	T=8.94s	X	Y	T=10.62s	X	Y	T=12.3s	X	Y
1	1.06	2.91	1	1.32	2.96	1	1.31	2.98	1	1.35	2.98
2	0.98	2.65	2	1.19	2.4	2	1.2	2.41	2	1.2	2.26
3	1.02	2.62	3	1.28	2.96	3	1.24	2.85	3	1.27	2.88
4	0.98	2.53	4	1.24	2.76	4	1.2	2.62	4	1.21	2.56
5	0.93	2.61	5	1.07	2.92	5	1.05	2.78	5	1.09	2.78
6	0.91	2.52	6	0.93	2.23	6	0.93	2.26	6	0.96	2.28
7	0.66	2.21	7	0.93	2.66	7	1.06	2.93	7	1.09	2.93
8	0.64	2.05	8	0.87	2.28	8	1	2.69	8	1.03	2.71
9	0.38	2.48	9	0.79	1.97	9	0.97	2.88	9	1	2.9
10	0.24	1.87	10	0.57	0.97	10	0.83	2.26	10	0.9	2.34
11	0.66	1.98	11	0.69	1.43	11	0.82	2.19	11	0.86	2.32
12	0.57	1.6	12	0.62	1.09	12	0.53	0.91	12	0.51	0.71
13	0.67	1.88	13	0.69	1.67	13	0.69	1.45	13	0.78	1.66
14	0.6	1.61	14	0.68	1.55	14	0.54	0.85	14	0.62	1.02
15	0.66	1.7	15	0.73	2.36	15	0.69	1.88	15	0.72	1.9
16	0.61	1.54	16	0.57	1.47	16	0.62	1.6	16	0.65	1.6
17	0.52	1.48	17	0.69	1.83	17	0.73	2.38	17	0.76	2.41
18	0.52	1.43	18	0.63	1.58	18	0.53	1.32	18	0.57	1.37
19	0.69	1.55	19	0.53	1.48	19	0.54	1.53	19	0.56	1.53
20	0.6	1.17	20	0.5	1.31	20	0.5	1.35	20	0.47	1.02
21	1.87	2.49	21	0.4	2.07	21	0.4	2.12	21	0.51	2.58
22	1.74	1.95	22	0.36	1.85	22	0.35	1.88	22	0.36	1.8
23	1.18	1.55	23	0.41	2.52	23	0.42	2.52	23	0.46	2.55
24	1.12	1.18	24	0.28	1.83	24	0.28	1.84	24	0.21	1.52
25	1.09	1.58	25	0.29	2.04	25	0.28	2.06	25	0.32	2.09
26	1.05	1.25	26	0.22	1.76	26	0.21	1.65	26	0.25	1.75
27	1.06	1.17	27	1.14	1.83	27	1.15	1.88	27	0.78	0.69
28	1.06	1.08	28	1.09	1.4	28	1.05	1.44	28	0.68	0.34
29	1.86	1.85	29	1.25	1.81	29	1.12	1.65	29	1.21	2.1
30	1.83	1.73	30	1.07	0.96	30	1.08	1.35	30	1.09	1.47
31	1.79	1.83	31	1.1	1.28	31	1.09	1.28	31	1.19	1.86
32	1.66	1.34	32	1.09	1.23	32	1.06	1.15	32	1.12	1.43
33	1.67	1.26	33	1.05	0.76	33	1.28	1.95	33	1.12	1.33

34	1.62	1.1	34	0.9	0.17	34	1.07	0.9	34	1.07	1.1
35	1.74	1.33	35	1.14	0.56	35	1.05	0.87	35	1.32	1.99
36	1.7	1.23	36	1.1	0.29	36	0.9	0.15	36	1.02	0.67
37	1.97	1.62	37	1.21	0.55	37	1.19	0.81	37	1.09	0.8
38	1.96	1.57	38	1.09	0.09	38	1.04	0.19	38	0.92	0.14
39	2.29	2.5	39	1.26	0.44	39	1.21	0.56	39	1.22	0.83
40	2.23	2.22	40	1.18	0.08	40	1.07	0.09	40	1.06	0.17
41	2.45	1.81	41	1.52	1.23	41	1.26	0.47	41	1.24	0.59
42	2.39	1.59	42	1.39	0.52	42	1.16	0.07	42	1.1	0.07
43	2.86	1.62	43	1.81	1.86	43	1.6	1.59	43	1.29	0.52
44	2.79	1.39	44	1.63	1.04	44	1.48	1.02	44	1.18	0.05
45	2.33	1	45	1.88	1.92	45	1.48	0.95	45	1.61	1.61
46	2.28	0.79	46	1.84	1.67	46	1.36	0.47	46	1.46	0.88
47	2.13	0.98	47	1.8	1.66	47	1.95	2.85	47	1.57	1.23
48	2.08	0.78	48	1.71	1.15	48	1.74	1.95	48	1.4	0.5
49	0.99	0.54	49	2.23	1.31	49	1.85	2.28	49	1.98	2.92
50	0.93	0.28	50	2.07	0.6	50	1.8	2.05	50	1.76	1.87
51	1.09	0.38	51	2.38	1.14	51	1.79	2.23	51	1.81	2.26
52	1.07	0.26	52	2.29	0.76	52	1.74	2.03	52	1.73	1.86
53	1.17	0.4	53	2.44	1.78	53	1.83	2	53	1.95	2.63
54	1.09	0.09	54	2.38	1.38	54	1.71	1.34	54	1.83	2.04
55	1.2	0.24	55	1.93	2.73	55	1.88	1.94	55	1.85	1.95
56	1.17	0.07	56	1.83	2.16	56	1.78	1.51	56	1.73	1.32
			57	1.86	2.48	57	1.7	1.43	57	1.71	1.44
			58	1.72	1.83	58	1.6	0.95	58	1.63	0.94
			59	2.36	2.57	59	1.76	1.4	59	1.92	1.96
			60	2.3	2.29	60	1.7	1.05	60	1.81	1.56
			61	2.31	2.55	61	2.38	2.63	61	1.81	1.5
			62	2.24	2.1	62	2.28	2.14	62	1.73	1.06
			63	2.28	2.5	63	2.31	2.5	63	2.36	2.35
			64	2.22	2.21	64	2.2	2	64	2.26	1.95
						65	2.28	2.53	65	2.41	2.68
						66	2.2	2.21	66	2.23	2.02
						67	2.3	1.71	67	2.34	2.62
						68	2.05	0.63	68	2.21	2.16
						69	2.16	0.96	69	2.35	1.84
						70	2.1	0.67	70	2.12	0.66
						71	2.51	2.03	71	2.21	1.26
						72	2.39	1.37	72	2.01	0.39
						73	2.45	1.84	73	2.57	2.14
						74	2.42	1.66	74	2.45	1.68
						75	2.37	1.19	75	2.53	1.88
						76	2.26	0.64	76	2.41	1.41
									77	2.42	1.22
									78	2.28	0.6

T=13.98s	X	Y	T=15.66s	X	Y	T=17.34s	X	Y	T=19.02s	X	Y
1	1.37	2.98	1	1.38	2.99	1	1.4	2.98	1	1.4	2.98
2	1.21	2.21	2	1.19	2	2	1.21	1.94	2	1.19	1.99

3	1.33	2.98	3	1.33	2.99	3	1.34	2.98	3	1.31	2.87
4	1.22	2.49	4	1.24	2.6	4	1.27	2.6	4	1.26	2.62
5	1.09	2.76	5	1.12	2.83	5	1.27	2.13	5	1.26	2.13
6	0.94	2.18	6	0.94	2.12	6	1.09	1.26	6	1.1	1.35
7	1.09	2.93	7	1.12	2.95	7	1.21	1.71	7	1.22	1.81
8	1.04	2.73	8	1.05	2.69	8	1.17	1.5	8	1.16	1.52
9	1	2.9	9	1.04	2.93	9	1.17	1.39	9	1.17	1.47
10	0.9	2.38	10	0.91	2.37	10	1.1	1.09	10	1.1	1.07
11	0.87	2.35	11	0.57	2.69	11	1.43	2.28	11	1.43	2.23
12	0.52	0.71	12	0.4	1.86	12	1.06	0.72	12	1.04	0.59
13	0.8	1.81	13	0.48	2.63	13	1.17	0.95	13	1.15	0.91
14	0.64	1.07	14	0.32	1.76	14	0.97	0.12	14	0.95	0.12
15	0.73	1.95	15	0.35	2.21	15	1.16	2.84	15	0.85	0.81
16	0.66	1.61	16	0.25	1.55	16	1.03	2.32	16	0.73	0.37
17	0.78	2.44	17	0.75	1.93	17	1.15	2.96	17	0.83	0.83
18	0.46	0.95	18	0.67	1.61	18	1.09	2.74	18	0.78	0.7
19	0.58	1.59	19	0.8	2.43	19	1.05	2.94	19	1.16	2.92
20	0.5	1.29	20	0.6	1.4	20	0.95	2.36	20	1.02	2.35
21	0.53	2.64	21	0.6	1.6	21	0.95	2.55	21	1.05	2.55
22	0.37	1.83	22	0.49	1	22	0.59	0.73	22	1.14	2.93
23	0.44	2.58	23	0.89	2.33	23	0.86	1.85	23	1.04	2.91
24	0.22	1.49	24	0.54	0.69	24	0.68	1.01	24	0.95	2.65
25	0.34	2.16	25	0.83	1.85	25	0.78	1.94	25	0.94	2.64
26	0.24	1.76	26	0.75	1.4	26	0.73	1.63	26	0.56	0.7
27	1.21	2.1	27	0.77	1.79	27	0.83	2.48	27	0.84	1.69
28	1.09	1.47	28	0.73	1.64	28	0.52	0.95	28	0.67	1
29	1.19	1.91	29	1.24	2.15	29	0.63	1.61	29	0.79	2.07
30	1.12	1.47	30	1.08	1.32	30	0.52	1.11	30	0.72	1.65
31	1.12	1.37	31	1.18	1.67	31	0.6	2.72	31	0.85	2.72
32	1.09	1.17	32	1.14	1.45	32	0.45	1.88	32	0.5	0.97
33	1.36	2.25	33	1.14	1.4	33	0.54	2.67	33	0.59	1.55
34	1.02	0.68	34	1.08	1.09	34	0.28	1.55	34	0.54	1.28
35	1.09	0.78	35	1.39	2.25	35	0.4	2.22	35	0.57	2.67
36	0.92	0.12	36	1.04	0.69	36	0.31	1.76	36	0.43	1.9
37	1.24	0.85	37	1.12	0.88	37	0.85	0.73	37	0.5	2.62
38	1.07	0.2	38	0.95	0.12	38	0.73	0.26	38	0.33	1.76
39	1.24	0.63	39	0.81	0.75	39	1.32	0.95	39	0.38	2.21
40	1.1	0.08	40	0.69	0.27	40	1.1	0.07	40	0.26	1.55
41	1.31	0.52	41	1.26	0.87	41	1.33	0.71	41	0.43	0.79
42	1.19	0.07	42	1.09	0.16	42	1.16	0.07	42	0.4	0.67
43	0.78	0.72	43	1.26	0.61	43	1.42	0.71	43	1.3	0.97
44	0.67	0.28	44	1.13	0.07	44	1.24	0.06	44	1.08	0.09
45	1.62	1.65	45	1.36	0.68	45	1.67	1.64	45	1.33	0.74
46	1.47	0.89	46	1.21	0.06	46	1.53	0.96	46	1.16	0.07
47	1.58	1.24	47	1.64	1.66	47	1.7	1.57	47	1.36	0.6
48	1.4	0.48	48	1.5	0.92	48	1.45	0.47	48	1.23	0.06
49	1.99	2.91	49	1.67	1.53	49	1.99	2.05	49	1.69	1.57
50	1.74	1.78	50	1.44	0.55	50	1.9	1.52	50	1.45	0.48
51	1.96	2.66	51	1.74	1.43	51	1.86	1.47	51	1.67	1.66

52	1.83	2.07	52	1.62	0.82	52	1.76	0.89	52	1.52	0.95
53	1.77	2.1	53	1.78	1.4	53	1.93	2.11	53	1.99	2.09
54	1.73	1.88	54	1.89	2.05	54	1.8	1.36	54	1.89	1.59
55	1.62	1.66	55	1.97	2.1	55	1.77	1.45	55	1.89	1.55
56	1.47	0.89	56	1.86	1.54	56	1.64	0.73	56	1.76	0.89
57	1.58	1.24	57	1.83	1.46	57	2.06	2.81	57	1.77	1.49
58	1.42	0.56	58	1.73	0.9	58	1.88	2.08	58	1.64	0.85
59	1.87	2.05	59	2	2.79	59	2.04	2.89	59	1.93	2.12
60	1.74	1.33	60	1.84	2.02	60	1.8	1.8	60	1.79	1.39
61	1.71	1.4	61	2.01	2.91	61	1.9	2.35	61	2.04	2.8
62	1.59	0.78	62	1.76	1.76	62	1.78	1.9	62	1.87	2.04
63	1.81	1.47	63	1.93	2.67	63	2.46	2.54	63	2.03	2.9
64	1.71	0.97	64	1.73	1.81	64	2.26	1.7	64	1.76	1.71
65	1.93	1.97	65	2.43	2.52	65	2.36	2.28	65	1.86	2.39
66	1.83	1.52	66	2.26	1.81	66	2.47	2.66	66	1.72	1.71
67	2.37	2.37	67	2.43	2.67	67	2.42	2.61	67	1.96	2.71
68	2.26	1.89	68	2.33	2.29	68	2.36	2.36	68	1.93	2.58
69	2.4	2.66	69	2.38	2.64	69	2.42	2.69	69	2.42	2.38
70	2.23	2	70	2.31	2.32	70	2.35	2.44	70	2.25	1.73
71	2.35	2.64	71	2.36	2.6	71	2.36	2.32	71	2.45	2.56
72	2.22	1.99	72	2.31	2.42	72	2.28	2.05	72	2.42	2.42
73	2.32	2.58	73	2.3	2.28	73	2.33	2.37	73	2.46	2.66
74	2.22	2.13	74	2.25	2.05	74	2.26	2.17	74	2.4	2.43
75	2.59	2.29	75	2.29	2.39	75	2.66	2.25	75	2.4	2.64
76	2.43	1.4	76	2.24	2.17	76	2.48	1.43	76	2.35	2.44
77	2.49	1.9	77	2.61	2.22	77	2.6	2.1	77	2.33	2.3
78	2.42	1.49	78	2.48	1.74	78	2.52	1.73	78	2.28	2.06
79	2.36	1.43	79	2.57	1.94	79	2.42	1.45	79	2.3	2.35
80	2.31	1.16	80	2.45	1.44	80	2.33	1.04	80	2.27	2.19
81	2.36	1.81	81	2.39	1.47	81	2.48	1.27	81	2.64	2.24
82	2.1	0.62	82	2.29	0.97	82	2.32	0.54	82	2.48	1.42
83	2.21	1.33	83	2.45	1.25	83	2.42	1.89	83	2.57	2.03
84	2.03	0.37	84	2.32	0.66	84	2.08	0.44	84	2.47	1.49
85	2.43	1.24	85	2.42	1.97	85	2.23	0.95	85	2.07	1.74
86	2.28	0.62	86	2.06	0.41	86	2.16	0.47	86	2.07	1.67
			87	2.18	0.81	87	2.18	1.03	87	2.42	1.49
			88	2.12	0.46	88	2.16	0.94	88	2.32	1.05
						89	2.09	1.76	89	2.49	1.36
						90	2.07	1.68	90	2.33	0.67
									91	2.44	1.97
									92	2.08	0.47
									93	2.17	1.08
									94	2.15	0.95
									95	2.2	0.86
									96	2.14	0.5
									97	2.29	1.21
									98	2.28	1.15

T=20.7s	X	Y
1	1.43	2.99
2	1.22	1.98
3	1.32	2.9
4	1.26	2.55
5	1.34	2.78
6	1.28	2.48
7	1.18	2.95
8	1.09	2.55
9	1.16	2.95
10	1	2.2
11	1.07	2.94
12	0.98	2.41
13	1.04	2.92
14	0.54	0.6
15	0.9	1.93
16	0.69	1
17	0.83	1.54
18	0.79	1.36
19	0.81	1.81
20	0.78	1.68
21	0.83	2.14
22	0.73	1.68
23	0.88	2.71
24	0.52	0.98
25	0.61	1.54
26	0.51	1.03
27	0.61	2.71
28	0.45	1.9
29	0.52	2.66
30	0.25	1.45
31	0.47	2.23
32	0.37	1.73
33	0.28	1.65
34	0.4	2.27
35	1.29	2.15
36	1.11	1.31
37	1.25	1.83
38	1.19	1.5
39	1.2	1.44
40	1.11	1.08
41	1.42	2.27
42	1.06	0.62
43	1.29	1.44
44	1.48	2.38
45	1.19	0.97
46	0.98	0.1
47	0.89	0.85
48	0.71	0.23

49	0.86	0.87
50	0.79	0.59
51	1.33	0.98
52	1.1	0.07
53	1.35	0.78
54	1.17	0.05
55	1.42	0.74
56	1.25	0.04
57	1.71	1.57
58	1.47	0.47
59	1.69	1.65
60	1.47	0.57
61	1.95	2.1
62	1.81	1.38
63	2.01	2.1
64	1.89	1.52
65	1.88	1.43
66	1.79	0.91
67	1.79	1.48
68	1.64	0.74
69	2.07	2.79
70	1.9	2.07
71	2.06	2.88
72	1.77	1.67
73	1.93	2.52
74	1.74	1.73
75	2.45	2.42
76	2.28	1.71
77	2.44	2.46
78	2.48	2.59
79	2.47	2.65
80	2.36	2.31
81	2.4	2.63
82	2.35	2.4
83	2.33	2.27
84	2.29	2.07
85	2.3	2.31
86	2.28	2.21
87	2.66	2.28
88	2.5	1.45
89	2.59	2.04
90	2.48	1.5
91	2.43	1.5
92	2.31	0.91
93	2.36	1.26
94	2.35	1.17
95	2.46	1.98
96	2.1	0.47
97	2.24	0.95

98	2.17	0.51
99	2.31	1.52
100	2.26	1.33
101	2.22	1.16
102	2.14	0.73
103	2.12	1.81
104	2.09	1.67
105	0.44	0.83
106	0.39	0.65

Appendix 2 Nanowire - End Evolution Code in IGOR

Following code was executed in procedural form in ***IGOR Pro v. 5.0.0.0.*** Code takes inputs of *x, y* coordinates of an end of a nanowire. Code comprise of four distinct functions. First it compares if the point fall in within the radius R from the center. It divides the set in to **in** and **out** (of R) fractions. If **in** (point resides within the radius R) it calculates the displacements from each point to all other points through the entire set: calculates all the displacements for all nanowire ends within R.

Then for the points residing outside of R, the next function calculates the displacements from **in** (point resides within the radius R) point to **out** (point resides outside the radius R) point but never between the two inner points. This proceeds until all in points are exhausted and displacements are measured from each inner point to all outer points. The two sets are combined to get a one set of displacements measurements between nanowire edge points of a single image.

```
#pragmartGlobals=1 // Use modern global access method.
functionWaveDifference(InputWave1, InputWave2) // Returns the set (wave) of radial displacement values after calculating the radial displacement R for one point to all the other points and first point varied through the entre set, For points within R only.
    Wave InputWave1, InputWave2;
        Variable i = 0;
    Variable j = 0;
        Variable k = 0;
        Variable n = 0;
        Variable InputWaveSize = 0;
```

```
n= (numpnts(InputWave1)- 1)*(numpnts(InputWave1))/2;  // Size of the output wave
Make/N = (n)/O PointDisplacement;
InputWaveSize= numpnts(InputWave1);
for (j = 0; j < n; )
    for (k = 0; k <InputWaveSize; k +=1)
        for(i = k + 1; i<InputWaveSize; i +=1)

                PointDisplacement[j]= sqrt((InputWave1[k]- InputWave1[i] )^2 + (InputWave2[k]- InputWave2[i])^2);
                j += 1;
        endfor
    endfor
endfor
returnPointDisplacement;
End
functionWaveSelection(InputWave1, InputWave2) // Returns the only the nanowire edge positions in x and y falling inside (r < R) the designated circle of radius of R measured from the center.
Wave InputWave1, InputWave2;
Variable i = 0;
Variable j = 0;
Variable Xbar = 0;
Variable Ybar = 0;
```

```
        Variable R = 1; //Radious of the selection circle
        Variable rtemp = R ^ 2;
        Variable InputWaveSize = 0;
        InputWaveSize = numpnts (InputWave1);
        Make/N = (0)/O SelectWaveX;
        Make/N = (0)/O SelectWaveY;

    for (i = 0;  i<InputWaveSize; i += 1)
            Xbar = (InputWave1[i]-1.5) ^ 2;// x measure transform to the center.
            Ybar = (InputWave2[i]-1.5) ^ 2;// y measure transform to the center.
        If  ( Xbar + Ybar<rtemp )
                InsertPoints j+1, 1, SelectWaveX;
                InsertPoints j+1, 1, SelectWaveY;
                SelectWaveX[j] =  InputWave1[i];
                SelectWaveY[j] =  InputWave2[i];
                j += 1;
            endif
        endfor
    End
functionWaveDeSelection(InputWave1,  InputWave2)  // Returns only the nanowire edge positions in x and y waves fall outside(r ≥ R) the designated circle of radius of R.
        Wave InputWave1, InputWave2;
        Variable i = 0;
        Variable j = 0;
```

```
        Variable Xbar = 0;
        Variable Ybar = 0;
        Variable R = 1; //Radius of the selection circle
        Variable rtemp = R ^ 2;
        Variable InputWaveSize = 0;
        InputWaveSize = numpnts (InputWave1);
        Make/N = (0)/O DeSelectWaveX;
        Make/N = (0)/O DeSelectWaveY;
    for (i = 0;  i<InputWaveSize; i += 1)
            Xbar = (InputWave1[i]-1.5) ^ 2;
            Ybar = (InputWave2[i]-1.5) ^ 2;
        If  ( Xbar + Ybar>= rtemp )
                InsertPoints j+1, 1, DeSelectWaveX;
                InsertPoints j+1, 1, DeSelectWaveY;
                DeSelectWaveX[j] =  InputWave1[i];
                DeSelectWaveY[j] =  InputWave2[i];
                j += 1;
            endif
        endfor
    End
functionWaveDifferenceSelective(XX, YY, XXOuter,YYOuter, PointDisplacement) // Returns the set (wave) of radial displacement values after calculating the radial displacement R for one point to all the other points residing outside the circle of radius R and first point varied through the entre set of points residing inside the R.
```

```
		Wave XX, YY, XXOuter, YYOuter, PointDisplacement;
		Variable i = 0;
		Variable j = 0;
		Variable k = 0;
		Variable XXYYSize = 0;
		Variable XXOuterYYOuterSize = 0;
		XXYYSize = numpnts(XX);
		XXOuterYYOuterSize = numpnts(XXOuter);
		j = numpnts(PointDisplacement);
			for (k = 0; k <XXYYSize; k +=1)
				for(i = 0; i<XXOuterYYOuterSize; i +=1)
					InsertPoints j+1,  1,  PointDisplacement;
					PointDisplacement[j]= sqrt((XX[k]- XXOuter[i] )^2
+ (YY[k]- YYOuter[i])^2);
					j += 1;
				endfor
			endfor
	End
```

Appendix 3 Time Variation of Gibbs Free Energy and Number of Critical Nuclei

Curve fit formula:

$$J_N = Y_o + A\exp\left(-\frac{1}{Tau}t\right) \quad \text{- (01)}$$

Taking natural logarithms and differentiating with respect to *t*,

$$\frac{1}{J_N}\frac{\partial J_N}{\partial t} = \frac{(J_N - y_0)\left(-\frac{1}{Tau}\right)}{J_N} \quad \text{- (02)}$$

Capillary theory:

$$J_N = Ke^{\left[-\frac{\Delta G(j_{cr})}{kT}\right]} \quad \text{- (03)}$$

Taking natural logarithms and differentiating with respect to *t*,

$$\frac{1}{J_N}\frac{\partial J_N}{\partial t} = \left(-\frac{\partial \Delta G}{\partial t}\right)\left(\frac{1}{kT}\right) \quad \text{- (04)}$$

From 04 and 05:

$$\frac{\partial \Delta G}{\partial t} = \left(1 - \frac{y_0}{J_N}\right)\left(\frac{kT}{Tau}\right) \quad \text{- (05)}$$

And form curve fit (01) alone at t=0:

$$J_N(t=0) = y_0 + A \quad \text{- (06)}$$

Therefore it is possible to find the initial nucleation rate J_N(t=0).

Vita

Indrajith Chandima Senevirathne was born in the western province of Sri Lanka. He received his primary education from St. Josephs College, Anuradhapura, and Raddolugama Primary School, and then continued to Royal College in Colombo, Sri Lanka, for his secondary education. He then entered the University of Sri Jayewardenepura, Sri Lanka, in 1996. During his undergraduate carrier he served as the President of the Physics Society of the University of Sri Jayewardenepura (1999-2000). He received his Bachelor of Science Degree, graduating top of the class with First Class Honors (*Summa cum laude*) in 2000. He entered Louisiana State University (LSU), Louisiana, in 2001 to pursue his graduate studies.

During his graduate career, he served as the President of the International Student Association (ISA) and International Cultural Center (ICC) (2005-2006) at LSU. While serving as president, he led the organization to stage "Sounds of Healing 3", charity concert to provide laboratory equipment for hurricane Katrina – displaced children attending Scotlandville Middle School in Baton Rouge, Louisiana. He also worked with other student and university leaders for student health care reform, resulting in improved health coverage for all the students at LSU. He was also a member of the Student Life and Academic Services Student Advisory Council at Louisiana State University (2005-2006), and served as the Student Representative to the User Committee at CAMD (Center for Advance Microstructures and Devices) at LSU (2003-2004). He was awarded the Charles E. Coates Travel Award from LSU for participation and presentation of research at the 2007 APS March Meeting. He is a member of both the American Physical Society (APS) and the American Vacuum Society (AVS).